Development of Integrated Wireless Power Transfer, Sensing, and Communication Using Compact Reconfigurable RF Structures

by Ali Raza

Thesis submitted in fulfilment of the requirements for the degree of

Doctor of Philosophy

under the supervision of A/Prof. Negin Shariati Moghadam and Dr. Rasool Keshavarz.

University of Technology Sydney
Faculty of Engineering and Information Technology

November 2024

CERTIFICATE OF ORIGINAL AUTHORSHIP

I, Ali Raza, declare that this thesis is submitted in fulfilment of the requirements for the award of Doctor of Philosophy, in the Faculty of Engineering and Information Technology at the University of Technology Sydney.

This thesis is wholly my own work unless otherwise referenced or acknowledged. In addition, I certify that all information sources and literature used are indicated in the thesis.

This document has not been submitted for qualifications at any other academic institution.

This research is supported by the Australian Government Research Training Program.

Signature:

Production Note:
Signature removed
prior to publication.

Ali Raza

11 November 2024

Acknowledgments

I thank ALLAH ALMIGHTY, the most beneficent and most merciful, “Who has taught by the pen, He has taught man he knew not,” for giving me the courage to prosper in the sphere of education. Blessing of ALLAH upon His Holy Prophet (PBUH), “The city of knowledge and blessing for entire creatures,” Who is my greatest inspiration in the world.

I feel indebted for the sympathetic, animate direction, scholarly criticism, and enlightened supervision of A/Prof. Negin Shariati and Dr Rasool Keshavarz. I appreciate their cooperation, valuable instruction and superb guidance. May they succeed in their careers.

Being a Radio Frequency and Communication Technologies (RFCT) Lab member at UTS was a wonderful experience. All my fellow students and lab staff were very cooperative and supported me throughout my PhD journey. As an international student, I was very scared initially; however, the RFCT lab community welcomed me with an open heart. I would like to mention a few lab members who guided me: Eistiak Ahamed, Javad Jafaryahya, Majid Amiri, Md. Amanath Ullah, Nastouh Nikkhah, and Prerna Dhull. I am really thankful to them for their guidance and support.

Words fail in expressing my emotions for my loving parents, wife, daughters, and siblings. I owe my heartiest gratefulness for their support and prayers for my success.

A bundle of thanks to my supervisors, fellows, and seniors for their suggestions and extensive help during my thesis. Finally, I thank all the people around me who have provided confidence in my existence.

ABSTRACT

Recent advancements in Wireless Sensor Networks (WSNs) have transformed various industries, including precision agriculture. In this field, sensors are essential for collecting real-time data on soil moisture, temperature, and other environmental factors, which is vital for optimizing farming practices. As a core element of the Internet-of-Things (IoT), sensor technology enables efficient data collection and transmission; however, these sensors must be highly sensitive, accurate, compact, and autonomous to detect continuous, subtle data changes. Reliance on batteries to power these sensors restricts their operational range and longevity, posing significant challenges for large-scale deployment. This limitation has driven a growing need for Wireless Power Transfer (WPT) technologies to eliminate battery dependency, along with compact, high-precision sensors. The integration of WPT, sensing, and communication technologies is essential to developing a sustainable and efficient smart agriculture system, allowing for continuous sensor operation and reliable data transmission.

This thesis presents an integrated system for WPT, sensing, and communication, utilizing compact and reconfigurable RF structures. Several novel designs are introduced to improve the accuracy, miniaturization, and multifunctionality of RF structures for precision agriculture. Two configurations of miniaturized patch rectennas are proposed for WPT to eliminate battery dependence. These planar and compact structures, with high RF-to-DC conversion efficiencies, are promising candidates for WPT applications.

A novel compact Multi-Service Antenna (MSA) is introduced for smart agriculture. The proposed MSA is versatile and capable of functioning as a single- or dual-band antenna and also measuring the permittivity of materials. A joint sensing and communication system is developed for smart agriculture, integrating an Ultra-compact Soil Moisture Sensor (UCSMS) for sensing and a Pattern Reconfigurable Antenna (PRA) for transmitting information to the base station. Additionally, a compact multi-band soil moisture sensor is proposed for precision farming. By integrating the sensor, directional coupler, and amplifier, a multi-band remote sensing system is realized. The proposed sensors are adaptive and capable of measuring soil moisture within the range of 0–30%. The compact planar geometry, combined with high sensitivity and low resonance frequencies, makes the designs highly suitable for smart farming applications.

Finally, three novel configurations of passive transmit/receive (T/R) switches are presented to integrate WPT, sensing, and communication technologies. These multi-band designs require no biasing voltage to switch signal direction and provide automatic switching between low- and high-power RF signals with low insertion loss. The proposed designs effectively enhance signal routing and enable efficient power management for low-power IoT applications.

LIST OF PUBLICATIONS

Peer-reviewed Journal Papers

1. **A. Raza**, R. Keshavarz, E. Dutkiewicz and N. Shariati, "Compact Multiservice Antenna for Sensing and Communication Using Reconfigurable Complementary Spiral Resonator," in IEEE Transactions on Instrumentation and Measurement, vol. 72, pp. 1-9, 2023, Art no. 8004509, doi: 10.1109/TIM.2023.3300466.
2. R. Keshavarz, E. Majidi, **A. Raza** and N. Shariati, "Ultra-Fast and Efficient Design Method Using Deep Learning for Capacitive Coupling WPT System," in IEEE Transactions on Power Electronics, vol. 39, no. 1, pp. 1738-1748, Jan. 2024, doi: 10.1109/TPEL.2023.3319505.
3. **A. Raza**, R. Keshavarz and N. Shariati, "Precision Agriculture: Ultra-Compact Sensor and Reconfigurable Antenna for Joint Sensing and Communication," in IEEE Transactions on Instrumentation and Measurement, vol. 73, pp. 1-13, 2024, Art no. 8001313, doi: 10.1109/TIM.2024.3350126.
4. **A. Raza**, R. Keshavarz and N. Shariati, "In-Situ Soil Moisture Monitoring Using Compact Multiband Sensing System for Smart Agriculture," in IEEE Transactions on AgriFood Electronics, 2024. (Under-Revision-**Third Round**).
5. R. Keshavarz, **A. Raza**, Md. A. Ullah and N. Shariati, "Efficient Pixelated Rectenna Design Methodology Using Binary Particle Swarm Optimization for WPT Applications," in IEEE Transactions on Circuits and Systems II: Express Briefs, 2024. (Under-Review).
6. **A. Raza**, R. Keshavarz and N. Shariati, "Passive Non-Reciprocal Signal Switching: A Compact Backward Coupler Using a Nonlinear Metamaterial Structure," in IEEE Transactions on Microwave Theory and Techniques, (Under-Review).
7. R. Keshavarz, **A. Raza** and N. Shariati, "Non-Reciprocal and Autonomous Signal Routing Solution: A Power-Agile Passive Multi-Band T/R Switch Using a Nonlinear Metamaterial Network," in IEEE Transactions on Microwave Theory and Techniques, (Under-Review).
8. **A. Raza**, R. Keshavarz and N. Shariati, "A Multi-Band Forward-Backward Non-Linear Metamaterial Network: An Agile Solution for Wireless Power Transfer, Sensing, and Communication," in IEEE Transactions on Microwave Theory and Techniques, (Under-Review).

Peer-reviewed Conference Papers

1. **A. Raza**, R. Keshavarz and N. Shariati, "Miniaturized Patch Rectenna Using 3-Turn Complementary Spiral Resonator for Wireless Power Transfer," 2021 IEEE Asia-Pacific Microwave Conference (APMC), 2021, pp. 455-457, doi: 10.1109/APMC52720.2021.9661674.
2. **A. Raza**, R. Keshavarz and N. Shariati, "Miniaturized Frequency Reconfigurable Patch Rectenna for Wireless Power Transfer," 2025 6th Australian Microwave Symposium (Accepted).

CONTENTS

LIST OF FIGURES

List of Tables

LIST OF ABBREVIATIONS

3-CSR	3-Turns Complementary Spiral Resonator
3-RCSR	3-Turns Reconfigurable Complementary Spiral Resonator
4-CSR	4-Turns Complementary Spiral Resonator
5-CSR	5-Turns Complementary Spiral Resonator
AC	Alternating Current
ADS	Advanced Design System
BPSO	Binary Particle Swarm Optimization
CP	Circularly Polarized
CPBC	Compact Passive Backward Coupler
CPW	Coplanar Waveguide
CSR	Complementary Spiral Resonator
CSRR	Complementary Split-Ring Resonator
CST MWS	Computer Simulation Technology Microwave Studio
CW	Continuous Wave
DC	Direct Current
DiC	Directional Coupler
ESA	Electrically Small Antenna
FDR	Frequency Domain Reflectometry
IoT	Internet-of-Things
JCASA	Joint Communication and Sensing Antenna
M-CSR	Multi-Turns Complementary Spiral Resonator
MSA	Multi-Service Antenna
M-FBNMN	Multi-Band Forward-Backward Non-linear Metamaterial Network
MUT	Material Under Test
PRA	Pattern Reconfigurable Antenna

RF	Radio Frequency
RFEH	Radio Frequency Energy Harvesting
SMS	Soil Moisture Sensor
SR	Spiral Resonator
SRR	Split-Ring Resonator
SUT	Soil Under Test
T/R	Transmit/Receive
TDR	Time Domain Reflectometry
TDT	Time Domain Transmission
UCSMS	Ultra-Compact Soil Moisture Sensor
VNA	Vector Network Analyzer
VUT	Volume Under Test
WPT	Wireless Power Transfer
WSN	Wireless Sensor Network

1

1 Introduction

1.1 Motivation

The use of Internet-of-Things (IoT) devices is increasing rapidly nowadays. The number of IoT devices was 16.6 billion in 2023 [1], and these are increasing by 12 % every year [2]. It is expected that there will be more than 170 billion connected sensor nodes by 2050 [2]. Nowadays, we have smart shopping malls where we just pick up an item, and it automatically goes into the bill, and there is no need to wait in long queues for checkouts. We have smart homes where we can control different appliances using smart devices. We can monitor our kids and pets using IoT devices. Sensors provide the required information, and they are usually powered by batteries with limited lifetimes and power ratings [3]. Hence, they need to be replaced before their time runs out. Besides, the disposal of batteries could also be hazardous to humans and the environment. Every year, around 6 billion batteries are disposed of worldwide [4], and this quantity is dangerous for the human race. With the exponential growth in wireless systems and the increasing demand for Wireless Sensor Networks (WSNs), the power supply is always a bottleneck for large-scale deployment [5].

Sensors in a WSN are the primary element to detect and measure the required parameters. High sensor accuracy, low power consumption, and compactness should be achieved in a WSN. Various applications require autonomous sensors with high accuracy to minimize battery issues or fully passive sensors to eliminate power consumption. In some applications, continuous sensor measurements are required, which increases power consumption, while in others, measurements are needed only at specific time intervals. Sensors can be powered up using wireless and wired power supplies. Power distribution to the sensors using a wired power supply can be costly, impractical and inefficient, especially in remote areas. Therefore, the power supply to WSNs in remote regions, as well as biomedical and wearables, needs to be wireless.

One possible solution to overcome battery issues and build a reliable IoT network is to use sustainable and green energy sources. Harvesting ambient energy is a promising approach to providing sustainable power, with examples including radio frequency (RF) waves, thermoelectric sources, wind, solar, and vibration. Radio Frequency Energy Harvesting (RFEH) is commonly used to power low-profile devices [6]. In RFEH, or Wireless Power Transfer (WPT), power is delivered from an ambient or dedicated source to the receiver without any physical medium. This ambient RF signal should be converted into direct current (DC) voltage to deliver it to the sensor. An antenna is needed to capture the RF signal, and a rectifier is required to convert the RF signal to the DC voltage. This circuit is called a rectenna (rectifying antenna). A well-designed rectenna with high RF-to-DC conversion efficiency can power up the sensor for measurements. Rectenna efficiency can be enhanced by choosing the appropriate antenna and rectifier circuit. An omnidirectional antenna is better for RF energy harvesting, whereas a directional antenna is preferred for WPT. RFEH can power up only low-power electronic devices, e.g., HDC2080 temperature and humidity sensors are low-power consumption sensors [7, 8]. Maximum power consumption of HDC2080 is −27 dBm, suitable for harvested energy [7]. However, RF ambient energy is deficient in powering the Bluetooth TX mode of NxH3670UK [8], where the power range is −10 dBm to +4 dBm [9]. In order to drive a high-power load, the dedicated source can be used in a WPT scenario [10]. This approach is used to transfer a high amount of power and requires directional antennas. Using green energy sources reduces air and water pollution and decreases waste from disposable batteries. This shift helps conserve ecosystems, supports biodiversity, and mitigates climate change. WPT and RFEH ultimately reduce the quantity of toxic waste, carbon footprint, battery disposal and water contamination [10]. There is substantial room for improvement in RFEH and WPT to develop a highly efficient rectenna, with a focus on enhancing RF-to-DC conversion efficiency, optimizing the matching network, and ensuring antenna compactness. This research area has become promising because it offers sustainable, battery-free solutions, especially in remote or hard-to-access locations. This technology can potentially revolutionize fields like IoT, medical implants, and WSNs by reducing the environmental impact of battery disposal.

Demand for food production is increasing due to the rapid rise in the world population. Consequently, primary producers are under significant pressure to develop innovative methods to boost food production. Automation and process efficiency are critical to achieving large-scale production growth, which can only be achieved with a well-designed WSN. Precise soil moisture measurement is indispensable and plays a pivotal role in irrigation resource management. Farmers can optimize water usage for efficient agricultural practices by preventing overwatering and underwatering. Conventional methods for measuring soil moisture rely on manual sampling and are unable to provide real-time data. These traditional methods are not only time-consuming and labor-intensive but also less precise due to spatial and temporal variability issues. WSNs have garnered significant attention in smart agriculture, offering substantial advantages over traditional methods [11]. The cost-effectiveness and scalability of WSNs make them highly suitable for precision farming [12-15]. Multiple techniques and structures have been implemented to measure soil moisture for precision agriculture using metamaterials [16-18]. Split-Ring Resonators (SRRs), Complementary Split-Ring Resonators (CSRRs), Spiral Resonators (SRs), and Complementary Spiral-Resonator (CSRs) have been widely employed due to their simple design and ease of fabrication [16, 19-21]. These metamaterial-based resonators have also garnered significant attention for reducing the size of sensors. In this research, compact metamaterial-based soil moisture sensors with high sensitivity are designed and implemented for smart agriculture. These sensors are compact and can measure soil moisture by detecting the soil's permittivity and transmitting the information to the base station.

Circulators and transmit/receive (T/R) switches play a vital role in remote control, data measurements, and directional control for IoT transceiver modules. They can manage two-way communication in joint sensing and communication, as well as WPT, in smart IoT devices. Although they provide high isolation between the ports, commercially available circulators use ferrite material, which makes them bulky, narrowband, and costly for IoT applications. Magnet-less circulators can also be used for IoT applications, but they require external biasing to control the direction of the signal. Therefore, a smart technique for developing compact, wideband, passive RF switches with high isolation is highly desirable for IoT devices. To address these challenges, this study introduces three configurations of microwave couplers for T/R applications, utilizing non-linear Schottky diodes, transmission lines, and metamaterial-based interdigital capacitors. These designs require no biasing voltage to switch signal direction and provide automatic switching between low and high-power RF signals with low insertion loss and high isolation. The proposed designs are planar to facilitate integration with electronics and meet space constraints.

1.2 Challenges

This research develops an integrated WPT, sensing and communication system for soil moisture sensing and communication in precision agriculture. Different configurations have been designed and tested to address the following challenges in realizing an autonomous sensing and communication system for smart agriculture. A novel nonlinear RF switch is developed to integrate sensing and communication. This research addresses several key challenges, including compactness, sensitivity, multiband capability and system reconfigurability.

1.2.1 Sustainable Energy Source

In a WSN for smart agriculture, different sensors need to be deployed in the agricultural area. These sensors are typically powered by short-lived batteries, which must be replaced or recharged after a certain period. This battery dependency is a major bottleneck for the large-scale deployment of these sensors, especially in remote areas. WPT/RFEH offers a sustainable alternative for WSNs to enable continuous soil data monitoring. In this thesis, various miniaturized patch rectennas with high RF-to-DC conversion efficiency have been developed for WPT applications.

1.2.2 Miniaturization

Different techniques have been developed to achieve compactness of the RF structure, including a magneto-dielectric substrate, Near-Field Resonant Parasitic (NFRP), metamaterials, meandered lines, and inductive/capacitive couplings. A magneto-dielectric substrate is not commercially available and needs to be designed to achieve the required permeability value. Introducing parasitic elements with driven elements in NFRP in structure makes the design procedure complex. Inductive/capacitive coupling introduces additional lumped elements, which can increase the losses due to parasitic effects. These methods make the design geometry complex, and the structure will probably be in 3D geometry. Metamaterials are also useful for size reduction but have narrow bandwidth. In this thesis, various configurations using CSRR and CSR have been developed to reduce the size of the sensors, antennas, and T/R switches.

1.2.3 Sensor Accuracy with Low Resonance Frequency

Soil moisture sensors must be highly sensitive, have a low resonance frequency, and be compact for smart agriculture. Less sensitive sensors with high frequencies can limit the penetration capacity of RF signals into the soil, hindering in-depth analysis and preventing precise soil moisture measurements. High-frequency sensors cover a smaller area of agricultural land, necessitating a large number of sensors to measure moisture across the entire field. Conversely, low-frequency RF sensors can cover a larger volume of soil, significantly reducing the total number of sensors required in a WSN. In this thesis, low-frequency sensors with high sensitivity have been developed using PIN and varactor diodes.

1.2.4 Reconfigurable System

A smart multi-function sensing system is desirable for smart agriculture. The sensor should have the ability to sense the soil parameters and communicate the information to the base station. Two methods can be used to address this challenge: using separate sensors and antennas or using multi-function smart sensors. In this research, the integration of diodes across the CSR has led to the development of a reconfigurable sensing system that functions both as a sensor and an antenna.

1.2.5 Communication Antenna

In smart agriculture, all embedded sensors must have integrated antennas to enable both sensing and communication. For remote sensing systems in diverse geographical structures, it is essential to incorporate an antenna for transmitting sensor data to the base station. This enables real-time, remote soil moisture data monitoring for precise irrigation and enhances resource management efficiency. Agricultural areas have diverse geographical structures, and the positioning of IoT devices can vary. In such areas, a large-coverage antenna is essential to accommodate these variations. An omnidirectional antenna can communicate in all directions and be used for communication with the base station regardless of positioning. However, its gain might be low, making it unsuitable for large agricultural fields. To address this challenge, a directional antenna is required for reliable long-distance communication across various geographical terrains, necessitating pattern reconfiguration. In this thesis, a high-gain reconfigurable antenna is designed for long-distance communication. The radiation pattern of the proposed antenna can be directed in six different directions with different biasing conditions.

1.2.6 Temperature and Humidity Variation

In a real-world environment, environmental conditions such as temperature and humidity change throughout the day, and these variations can significantly affect the frequency response of Frequency Domain Reflectometry (FDR) sensors. The effect of these changes can be reduced by using a multiband soil moisture sensor. Although the design process for single-band sensors is straightforward, these sensors are susceptible to frequency shifts due to environmental factors that compromise measurement accuracy. Measuring frequency responses at multiple bands, however, can significantly reduce measurement uncertainty. However, designing a compact multiband sensor with high accuracy remains very challenging. In this thesis, a dual-band FDR-based remote monitoring system for precision farming is presented. The proposed system comprises a dual-band FDR-based sensor, a Directional Coupler (DiC), and an amplifier. The combination of low resonances, dual bands, high sensitivity, compact size and low cost makes it apt for smart agriculture.

1.3 Research Questions

This thesis will address the following fundamental research questions to overcome the discussed limitations:

1. How can smart agriculture be made sustainable and autonomous?
2. How can an antenna be integrated with a sensor to create a unified sensing and communication system?
3. How can compactness be achieved at low frequencies to reduce the number of sensors and, consequently, the associated costs in a sensor network?
4. How can environmental effects be mitigated in sensor performance?
5. How can WPT, sensing, and communication be effectively integrated?

1.4 Research Objectives

To address the questions outlined above, the following objectives have been established for each stage of the research:

i. Develop a compact rectenna for WPT in smart agriculture.
ii. Design and implement a compact, multi-functional system for sensing and communication.
iii. Integrate a metamaterial-based resonator with the sensor to reduce its size.
iv. Develop a pattern-reconfigurable antenna for communication with the base station, enabling sensing and communication.

v. Create a multiband system using a frequency-reconfigurable structure to mitigate the effects of temperature and humidity variations in soil moisture testing.

vi. Design a compact T/R switch to integrate WPT, sensing, and communication.

1.5 Deliverables

The final deliverables will include the following:

1. A prototype rectenna for WPT to eliminate the need for battery charging and replacement.
2. A multi-functional reconfigurable structure that can be used both as a soil moisture sensor and a communication antenna.
3. A compact multiband sensor for soil moisture measurement with compensation for temperature and humidity effects.
4. A pattern-reconfigurable directional antenna for communication with the base station.
5. A non-linear passive T/R switch for WPT, sensing, and communication.

Stakeholders include the University, the (Food Agility Corporate Research Center, CRC), and, most importantly, farmers. Farmers need frequent monitoring of soil parameters, including temperature and humidity. To get this data, they need to visit the remote locations physically. This process is time-consuming and requires an excessive workforce. Significant time consumption can be reduced if the proposed model is deployed on a large scale in remote agricultural locations. Additionally, the sensors will automatically receive power from the wireless power source, allowing the system to operate autonomously and reducing the need for manual labor. This deliverable will enable farmers to monitor soil parameters continuously without having to visit the fields.

1.6 Contribution and Novelty

Conventionally, it is necessary to visit remote locations to collect and test soil samples. This process is time-consuming and requires significant manual labor. The dual-mode feature of the structure will be used for sensing and information transfer. In addition, pattern reconfiguration antenna will be reliable for long-distance communication in various geographical structures. Without manual labor, this will help the farmers track the field data, e.g., moisture and humidity. Various methods and prototypes have been developed in this research to achieve the objectives.

i. A unique method to realize a miniaturized rectenna system for WPT applications.

ii. A novel method and design for a multi-service structure that functions as both a sensor and an antenna for joint sensing and communication.

iii. A novel approach to developing an ultra-compact passive soil moisture sensor for in-depth moisture analysis and a pattern-reconfigurable antenna for communication, facilitating joint sensing and communication.

iv. A novel methodology to develop a multi-band FDR-based soil moisture sensor to mitigate the environmental effects.

v. A unique method for designing a non-linear passive T/R switch to differentiate between low and high-power levels for the integration of WPT, sensing, and communication.

1.7 Thesis Organization

The following chapters of this thesis are organized as follows:

- *Chapter 2*: This chapter provides a comprehensive literature review on RFEH/WPT, reconfigurable antennas, reconfigurable antenna techniques, miniaturized antenna techniques, soil moisture sensors in precision agriculture, and T/R switches. It summarizes WSN applications, including smart homes, smart offices, and smart agriculture. It also presents the theory of WPT and RFEH, along with the essential components of a WPT system, such as the antenna, matching network, and rectifier. Various antenna types, including wideband and reconfigurable antennas, are discussed, along with techniques to reduce RF structure size. Additionally, comparisons of different antenna types and switching mechanisms are provided. The second section discusses soil moisture sensors in smart agriculture and the implementation of metamaterials for size reduction. Finally, the literature review about various sensing techniques, RFID tags for moisture measurement, different types of microwave sensors, and shortcomings of previously reported works are discussed.

- *Chapter 3*: This chapter presents a miniaturized patch rectennas for WPT.

  The first section describes two basic types of ambient energy harvesting: RFEH and WPT. It also describes the essential components of a WPT system, including the antenna, matching network, rectifier, and the sensor testing procedure in the laboratory.

  In the second section, the designs of a miniaturized patch antenna and rectifier are presented. A design procedure for the CSR is discussed to achieve a miniaturized antenna. The equivalent circuit model of the antenna and rectifier circuit are also presented. The proposed miniaturized antenna is assessed in terms of return loss and radiation patterns, and the results are discussed in the last section. Finally, a comparison of the proposed antenna is presented with the reported antennas.

  The third section presents the design procedure of the rectifier and proposed pixelated antenna using the Binary Particle Swarm Optimization (BPSO) algorithm. Finally, the results, including the radiation pattern of the antenna and RF-to-DC conversion efficiency of the rectifier, are presented.

- *Chapter 4*: A compact multi-service antenna (MSA) is presented in this chapter.

  In the first section, multi-turn CSR and patch antenna are investigated. The modification in the patch geometry and number of turns are addressed.

In the second section, MSA is designed using PIN diodes. MSA operates in three modes: dual-band joint communication and sensing antenna (JCASA), dual-band antenna, and single-band antenna. To achieve miniaturization, a three-turn complementary spiral resonator (3-CSR) is used with a modified patch. Two PIN diodes are integrated with the 3-CSR structure, and three different ON/OFF configurations have been achieved, i.e., 00, 10, and 11, with ‘0’ representing the OFF state and ‘1’ representing the ON state of the diode.

In the third section, different modes are addressed by changing the configuration of diodes, and results are presented. For the ‘00’ case, the structure operates as a dual-band JCASA and has the ability to sense and communicate. This mode is used to measure soil moisture by using FDR in the first band, while the second band is used for communication.

In the fourth section of this chapter, the results of mode-1 are presented to analyze the sensor's performance. Finally, a comparison between the proposed MSA and other reported sensors is provided. The proposed MSA possesses an adaptive nature and can be used to measure the permittivity of any Material Under Test (MUT) within the range of 1–20. Due to its sensing and communication ability, the MSA is a good candidate for soil moisture measurement in precision farming. The proposed MSA is also suitable for standard single and dual-band antenna applications.

- *Chapter 5*: This chapter presents a sensing and communication system for smart agriculture. The proposed system comprises an Ultra-compact Soil Moisture Sensor (UCSMS) and a radiation Pattern Reconfigurable Antenna (PRA) for both sensing and communication.

  The first section explores the miniaturization of the UCSMS by varying the number of turns in the CSR. The impact of different turn numbers is analyzed through simulated results and equivalent circuit models. The UCSMS operates at a low frequency of 86 MHz with a five-turn CSR.

  The second section outlines the design process for the UCSMS and the PRA. A directional antenna with pattern reconfiguration is designed to operate at the 2.45 GHz WLAN band, ensuring reliable long-distance communication across diverse geographical terrains. The integration of PIN diodes to achieve pattern reconfiguration is also addressed. This section further discusses the simulated results of the PRA, including the current distribution.

  The third section investigates the UCSMS's performance in measuring soil moisture, with the results presented. Finally, a comparison between the proposed UCSMS and other reported sensors is provided. The precise sensing capability combined with the multi-directional communication feature makes the proposed system well-suited for precision agriculture applications.

- *Chapter 6*: This chapter presents a dual-band FDR-based remote monitoring system for precision farming.

  The first section explains the sensor's working mechanism for soil moisture sensing in a practical environment, as well as the testing procedures conducted in the laboratory.

  The second section details the design of a miniaturized dual-band sensor on a Rogers substrate. The design process is outlined along with the equivalent circuit model. To eliminate the need for a vector network analyzer (VNA) in the proposed system, a unidirectional Directional Coupler (DiC) and an amplifier have been integrated with the sensor. This section also discusses the necessity of integrating the directional coupler and amplifier. Additionally, three varactor diodes have been incorporated across the complementary spiral resonator (CSR) to enable frequency switching.

  The final section discusses the proposed multiband sensor's performance in measuring soil moisture, with the results presented. A comparison between the proposed sensor and previously reported sensors is also provided. The combination of low resonances, dual-band operation, high sensitivity, compact size, and low cost makes this sensor ideal for smart agriculture applications.

- *Chapter 7*: This chapter introduces a new design for couplers acting as a T/R switch. The chapter discusses three variations of the coupler, with the initial part outlining the fundamental principles of the coupler and its application in various IoT scenarios.

  The following section delves deep into the design process, covering the equations for all three setups. It showcases the proposed circuit and equivalent model using lumped components offering a thorough insight into the coupler's evolution.

  The last segment details the test configurations and outcomes for each configuration. Both low and high-power assessments are conducted to confirm the effectiveness of the proposed coupler.

- *Chapter 8*: The final chapter provides a summary of the thesis and highlights the contributions of the research. Additionally, it offers recommendations for future work.

2

2 Literature Review

2.1 Introduction

The growth of Internet-of-Things (IoT) Wireless Sensor Networks (WSNs) has been rapid in recent years. By 2023, there were 16.6 billion connected IoT devices [1] and this number is increasing by 12% annually [2]. Projections estimate that by 2050, there will be over 170 billion sensor nodes [2]. However, developing IoT devices brings significant challenges depending on the application including security and privacy concerns, real-time data processing, and speed limitations. Various IoT sensor applications are shown in Fig. 2.1 [22]. Today, we have smart environments like shopping malls where products are automatically added to the bill without the need to stand in checkout lines. In smart homes, users can control appliances with their devices, and IoT sensors allow us to monitor children and pets remotely. In smart agriculture, sensors are used for soil moisture monitoring, atmospheric conditions, and animal tracking [23]. Deploying these sensors in outdoor environments enables the remote monitoring of critical parameters like moisture and humidity without the need for physical visits, thereby reducing labor and increasing productivity. This technology also extends to livestock management [24], where wireless sensors track animals and transmit data to base stations, combining communication and sensing. While smart agriculture offers numerous benefits, challenges remain, particularly with power, measurement accuracy and communication reliability.

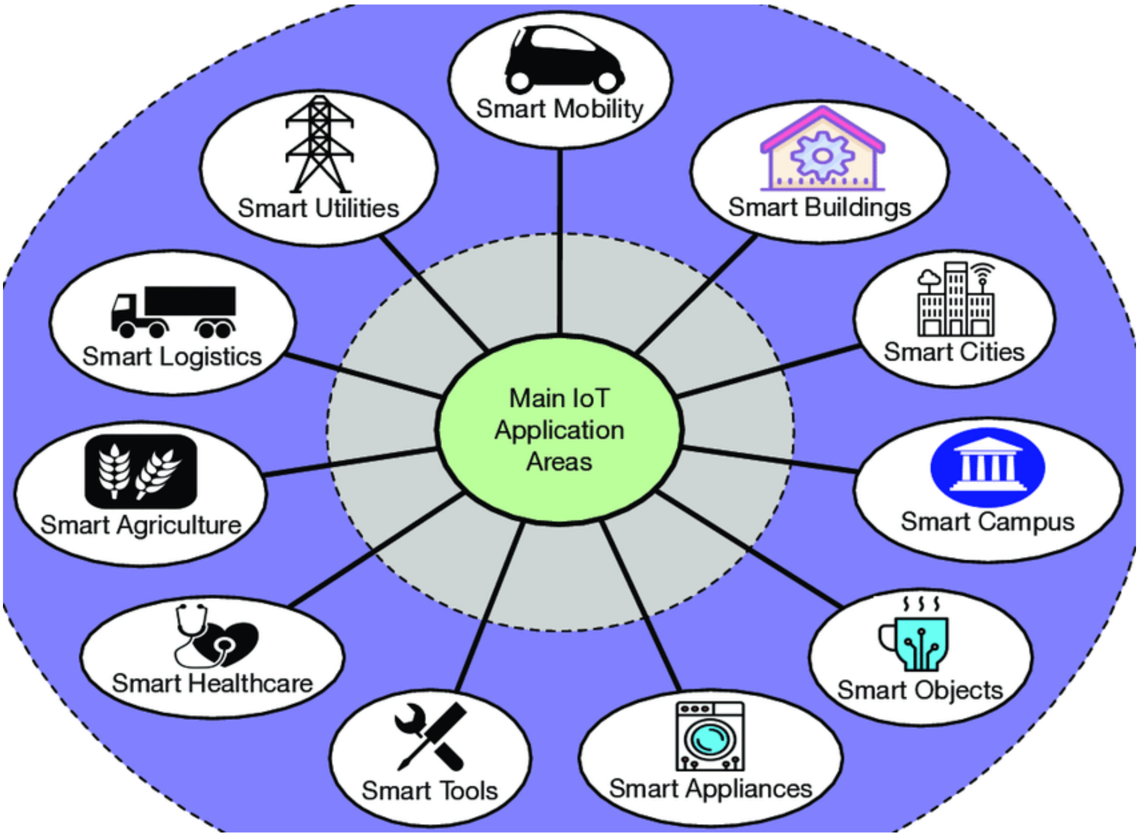

Fig. 2.1. Various applications of IoT sensor networks [22].

2.1.1 Power

Sensors provide essential information but are typically powered by batteries with limited lifespans and power ratings [3]. As a result, batteries must be replaced before they expire. Additionally, battery disposal poses environmental and health hazards, with around 6 billion batteries discarded globally each year [4], which presents a significant risk to humanity. The need for frequent battery replacement is a major obstacle to the large-scale deployment of IoT sensors, especially in remote locations like agricultural fields. To address the challenges of battery dependency in IoT devices, ambient energy sources have become increasingly prominent. Common ambient energy sources include radio frequency (RF) waves [25], thermoelectric [26], wind [27], and solar [25], each suited to different applications. TABLE 2.1 lists various sources along with their available power densities. Ambient RF signals, in particular, carry very low power levels, as illustrated in Fig. 2.2. At a distance of 40 meters, the received power is 7 µW (−20 dBm) for 900 MHz (GSM) and 1 µW (−30 dBm) for 2.4 GHz (Local Area Networks) [28].

TABLE 2.1. AMBIENT SOURCES.

Reference	Energy	Power Density (µw/cm^2)	Source	Availability	Pros	Cons
[25]	Ambient Radio Waves	1	Radio transmitters, mobile base stations, Wi-Fi routers, cell phones, TV broadcasters	Always	Availability is not dependent on time, easy designing of circuit	Power level is very low
[26]	Thermoelectric	60	Electrical system, human body	Depends on the electrical systems operation	Power level is high	Difficult to match impedance, complex circuit
[27]	Wind	1	Air	Weather dependent	Easy circuit design	Power level is low
[25]	Solar	100	Sun	Day time	Power level in high	Not available at nighttime, also depends on weather conditions

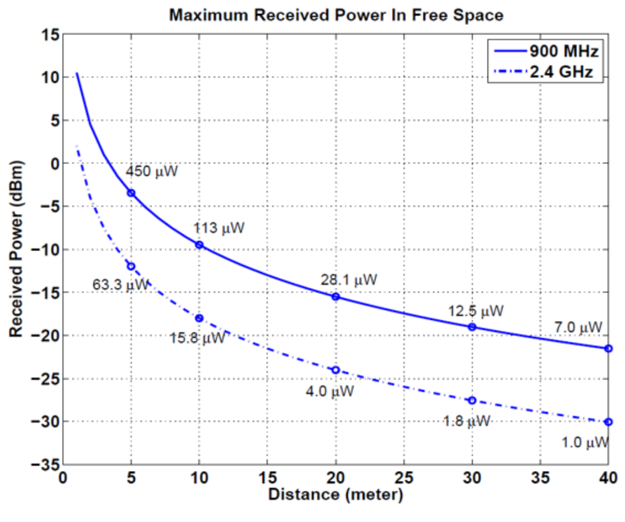

Fig. 2.2. Received ambient power levels vs. distance [8].

2.1.2 Measurement Accuracy and Communication

In a few IoT applications like smart agriculture, the sensor's accuracy is critical to sense or control various soil parameters. Chemical methods can be used to replace conventional sensors with artificially designed sensors with high accuracy. However, the cost of replacing conventional materials with artificially designed materials is a big challenge. In smart agriculture, embedded sensors must have an integrated antenna to enable both sensing and communication. Without communication, a standalone sensor cannot fulfill the purpose of smart agriculture. An antenna should be developed to transmit the measured data to the base station for decision-making. Sensor size, sensitivity, ability to mitigate environmental conditions, and communication antenna in diverse structural areas are key challenges required to develop a precision agriculture system.

2.1.3 Integration of Wireless Power Transfer (WPT) and Sensing

Wireless Power Transfer (WPT) has the potential to revolutionize precision agriculture by providing an eco-friendly power solution for critical sensors that monitor soil conditions, including health and moisture levels. In precision agriculture, interconnected sensors are essential for delivering real-time data to support efficient resource management. However, the reliance on batteries presents challenges related to lifespan, maintenance, and cost, especially in remote agricultural areas.

Components like switches and circulators are essential in IoT WSNs for regulating the flow of RF signals. IoT sensor networks rely on these devices for a wide range of applications, from home automation to industrial automation and control. These devices facilitate remote sensing, data measurement, and communication [29, 30]. RF switches, in particular, are crucial for ensuring signal flow in a single direction while maintaining high isolation and low insertion loss. The sensor measures the required parameters, and an antenna is needed to transmit this information to the base station. For a soil moisture sensor in smart agriculture, the sensor will send moisture data to the base station via an antenna. To create an autonomous system, integrating WPT is crucial to eliminate battery dependency. A switch can be used to combine both WPT and sensing functions, as illustrated in Fig. 2.3, which reduces the number of antennas and simplifies the hardware. However, these RF switches typically require a Direct Current (DC) biasing voltage to operate and to switch between positions 1 and 2, necessitating an additional control mechanism. This added complexity can lead to design challenges and processing delays. To address this issue, a passive RF switch with high isolation is needed. Various RF switches have been investigated and are discussed in Section 2.4.

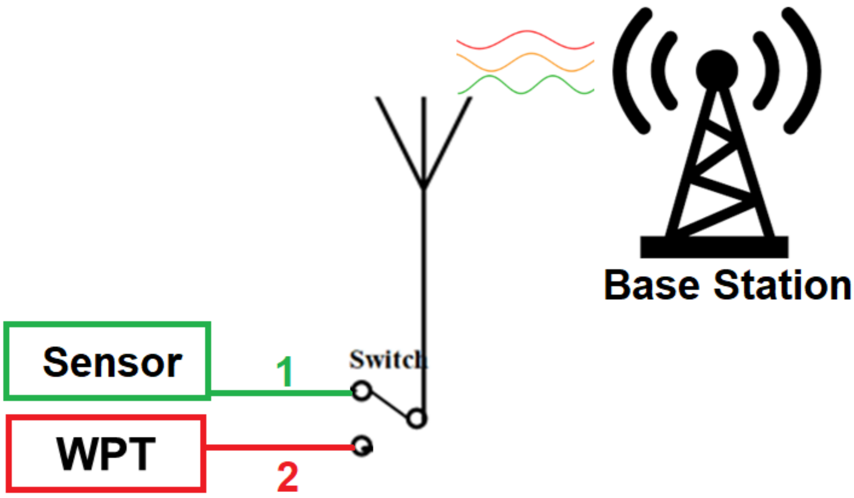

Fig. 2.3. Integration of the WPT and sensing for an autonomous IoT WSN.

2.2 RF Energy Harvesting and Wireless Power Transfer

With the rapid expansion of wireless systems and the rising demand for Wireless Sensor Networks (WSNs), power supply remains a significant barrier to large-scale deployment [4]. A promising solution to address battery limitations is Radio Frequency Energy Harvesting (RFEH) or Wireless Power Transfer (WPT), which captures RF energy to power sensors. In RFEH, ambient RF energy carried by electromagnetic waves is abundantly available from various sources, such as radio transmitters, mobile devices, Wi-Fi routers, cell phones, and television broadcasters [31]. In contrast, WPT refers to RF energy harvesting from a focused beam generated by a dedicated power source [31]. Both RFEH and WPT have the potential to reduce the environmental impact of battery waste, lowering toxic disposal and water contamination risks [10]. Fig. 2.4 illustrates a typical WPT system, which includes an antenna, a matching circuit, and a rectification device (diode), powered by a dedicated source [32].

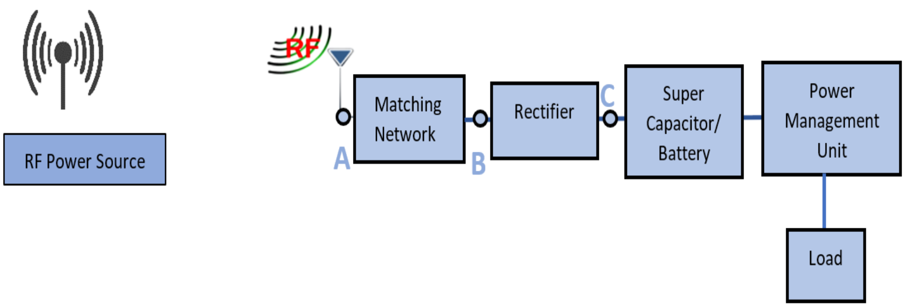

Fig. 2.4. Typical radiating RF WPT [32].

TABLE 2.2. ANTENNA PERFORMANCE PARAMETERS FOR RFEH AND WPT.

Antenna Parameter	RFEH	RF-WPT
Size	Electronics is moving towards miniaturization. Hence, the size of the receiving antenna should also be miniaturized for both EH and WPT	
Radiation Pattern	Omni-Directional	Directional
Polarization	Circular Polarization to capture incident waves at any angle	Linearly Polarized for simple geometry of antenna structure
Bandwidth	Should be wideband or multiband to capture power from multiple sources (GSM, 3G, 4G, Wi-Fi) or frequency reconfigurable antennas	Wideband or multiband to receive from multiple sources having different frequencies
Geometry	Should be planar to integrate with other rectifier circuits in the PCB	

2.2.1 RF Antennas

An antenna is a crucial component for capturing RF energy in WPT and RFEH. The received power is transferred to the rectifier's input. For maximum power transmission, a matching network is also required to transform the impedance of the diode to the 50 Ω impedance of the antenna. The rectification device (e.g., diode) converts the captured RF signal to DC voltage. The DC voltage can be stored in a supercapacitor/battery and consumed by a sensor in a WSN. This complete system is also referred to as rectenna (rectifying antenna) [33]. Different components of rectenna are described in the following subsections [31, 34, 35].

Various antenna types have been discussed in the following subsections. There are multiple factors that are responsible for antenna performance. A comparison of performance parameters such as size, radiation pattern, polarization, bandwidth, and geometry for WPT and RFEH is provided in TABLE 2.2. For example, a circular polarized (CP) antenna is a preferred choice in designing for RFEH, as the direction of the signal's arrival is not known [36, 37]. Linearly polarized antennas have also been reported in RFEH as GSM, TV, and Wi-Fi waves are linear. In WPT, the linear polarized antenna is selected to avoid design complexity because the transmitter location is known. While narrowband antennas dominate WPT due to their efficiency and resonance at specific frequencies, wideband antennas can be beneficial for adaptive WPT systems that adjust to environmental changes or support multi-frequency energy harvesting.

Modern wireless systems need the support of a large number of communication standards, often distributed over very large frequency ranges. For instance, we have mobile phones that can be used for 2G (GSM), 3G, 4G (LTE) and Wi-Fi communication. For RFEH, power is received from multiple sources with different frequencies and in WPT, there could be more than one power source with different frequencies. Hence, the antenna associated with IoT devices needs to be multiband/wideband [38].

2.2.1.1 Multiband and Wideband Antennas

Multiband and wideband antennas cover multiple standards simultaneously, and no external circuitry is required to switch the communication band of the antenna. These antennas have gained significant importance in recent decades. The multiband response is achieved using parasitic strips and slits etched out on the board. Parasitic strips are etched out with the active antenna to achieve other frequency bands. Many types of multiband antennas have been published in the literature [39-44]. The wideband frequency response has been presented in [45-51]. The wideband behavior can be achieved using incomplete ground at the bottom of the board. The distance between the ground and the driven element plays an integral part in achieving adequate frequency response. Multiband antennas are being used in current smartphones and laptops, but because of their wide bandwidth, they are not the preferred choice for RF-WPT with a dedicated source. In this scenario, a single-frequency antenna is a better choice as the power source frequency is fixed. Fig. 2.5 shows wideband behavior of the antenna from 0.79 to 9.16 GHz [46]. In order to achieve wideband behavior, the antenna's geometry becomes complex. As a wideband antenna receives all RF signals within its impedance bandwidth, a filter must be designed to separate these signals. The addition of such a filter reduces the radiation efficiency of the receiving antenna.

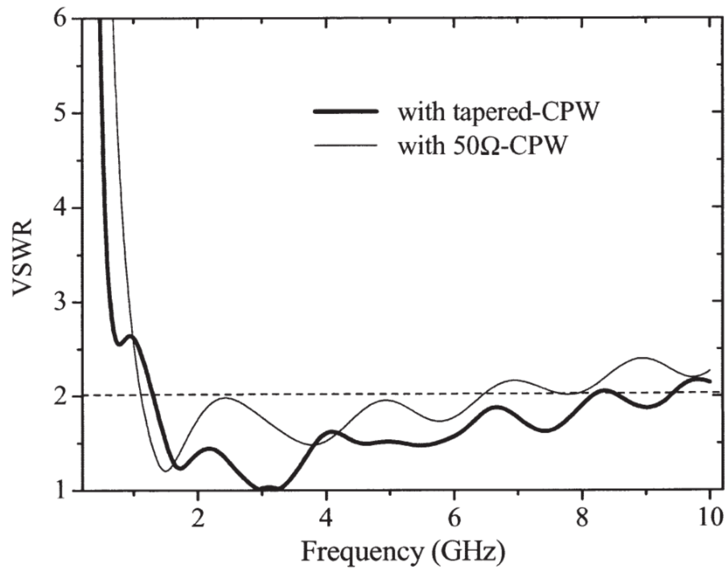

Fig. 2.5. Wideband antenna with bandwidth GHz [46].

2.2.1.2 Frequency Reconfigurable Antennas

The electrical length of the structure defines the resonating frequency of the antenna. In frequency reconfiguration, the antenna changes its resonating frequency using electronic switches. By altering the electrical length of antenna using some switching mechanism frequency reconfiguration can be achieved. Frequency reconfigurable antennas have been reported in [52-57]. These antennas are useful in situations where several frequency bands coverage is required, such as cognitive radios, smartphones and laptops. Some frequency reconfigurable antennas have also been reported to change their bandwidth from multiband to wideband depending on the DC bias voltage [58-61]. In these types of reconfigurable antennas the antenna has the ability to be wideband for EH systems and single-band for WPT with a dedicated source [59, 62], as shown in Fig. 2.6. These frequency reconfiguration features can be extended to develop a multi-function RF structure to serve multiple purposes. TABLE 2.3 shows the comparison of multiband, wideband, and reconfigurable antennas.

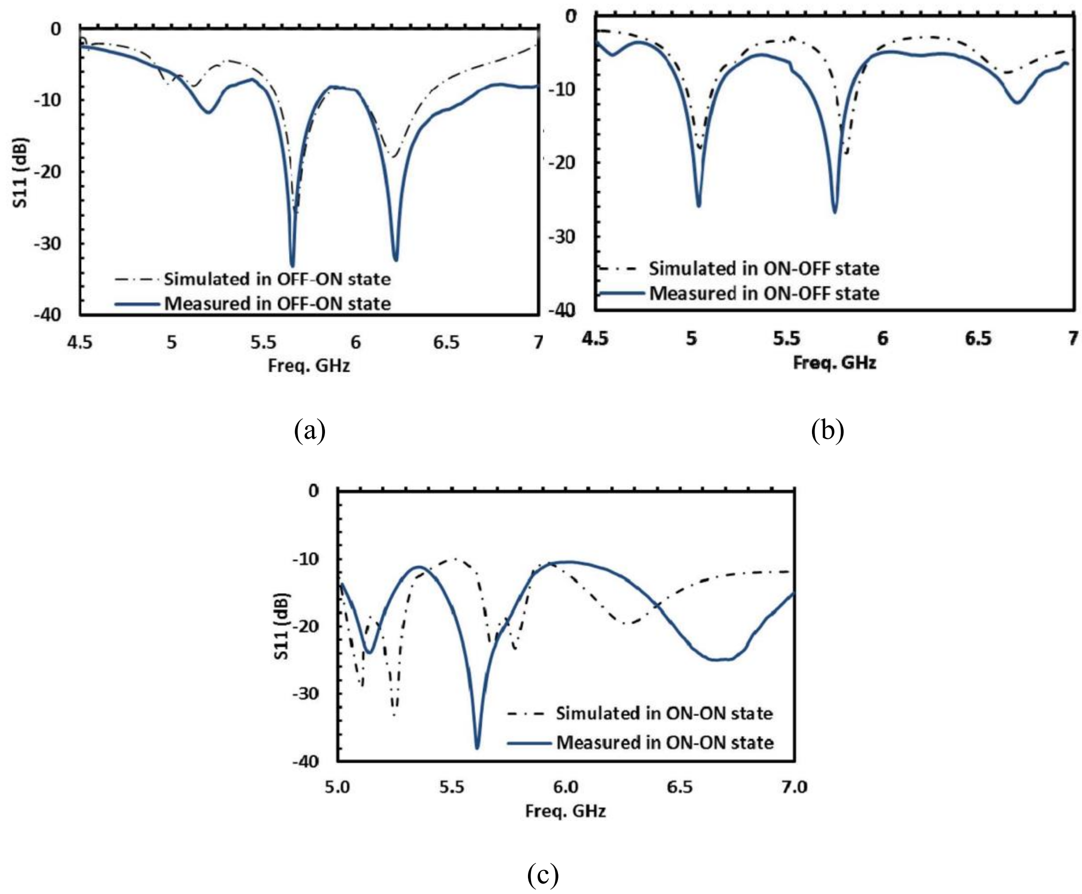

Fig. 2.6. Frequency reconfiguration using electronic switches [62].

TABLE 2.3. COMPARISON OF MULTIBAND, WIDEBAND AND RECONFIGURABLE ANTENNAS.

Characteristics	Multiband	Wideband	Frequency Reconfigurable
Antennas	One antenna can cover multiple bands	One antenna can cover wide frequency bands	One antenna can be switched to different bands
Size	Small space as compared to the number of antennas for different bands	Very compact size	Minimum size required as switching is not a problem
Design Complex	Complex design, sharp filters required	Complex design, sharp filters required	No need for filters but the design is much more complex
Efficiency	Medium performance in terms of power	Less efficiency	Performance is good
Cost	High Cost due to filters	Higher cost due to much complex filtering	High cost due to switches

TABLE 2.4. COMPONENTS COMPARISON.

Component	Advantages	Disadvantages
MEMS	Consumes less Supply voltage, has smaller transmission coefficient, I-V characteristics are linear	Mechanical interface makes it less reliable
Varactor	Very less power consumption	Additional biasing circuitry is needed, there is no use in the forward direction
PIN Diode	High switching speed, cost-effective, less power consumption	Additional biasing circuitry is needed, less sensitive

Various switching components, such as MEMS switches, varactor diodes, and PIN diodes, can be used to achieve frequency switching, with proper biasing required for each type. These switches have been extensively documented in the literature, particularly over the past decade. Frequency reconfiguration using RF MEMS is discussed in [52, 53, 63, 64], highlighting their low power consumption; however, they tend to be bulky and involve mechanical interfaces. Frequency reconfiguration with PIN diodes is explored in [52-54, 65], noted for their high switching speed. Varactor diodes, on the other hand, enable continuous frequency tuning, as shown in [55-57], but they operate only under reverse biasing. A comparison of these switches is provided in TABLE 2.4, indicating that PIN diodes have lower power consumption and faster switching speeds, making them a suitable choice for designing reconfigurable antennas. TABLE 2.5 summarizes frequency-reconfigurable electrically small antennas used in various applications.

TABLE 2.5. COMPARISON OF FREQUENCY RECONFIGURABLE ANTENNAS.

Ref	Freq Tuning (GHz)	No. Of Diodes	Size At Lowest freq.	Lowest Efficiency (%)	Lowest Gain (dBi)	Application
[66]	2.1–3.5 0.41–0.99	2 varactor diodes	0.63λ×0.56λ	<1	–24	Femtocells (Short Distance Communication)
[67]	2.3–2.61, 2.9–3.21, 3.1–3.89, 4.3–7.4,	2 pin diodes	0.16λ×0.115λ	-	-	Heterogeneous Applications
[68]	0.4078–0.463	8 solid state switches	0.07x0.036	5	–10	Portable wireless devices
[69]	0.05925 –0.05975, 0.314–0.398, 0.430–0.496, 0.792–0.950	4 pin diodes	0.06λ×0.06λ	1.5	–23	Public Safety/US
[70]	2.3–2.51, 3.35–3.75, and 4.95–5.53	3 pin diodes	0.154λ×0.154	-	–4.2	Bluetooth, WiMAX, WLAN
[71]	1.98–2.5 3.0–3.5	5 pin diodes	0.33λ×0.33λ	-	0.2	cognitive radio applications
[72]	0.365 – 0.5	4 varactor diodes	0.095 λ×0.046 λ	3	–13.5	Low-frequency applications
[73]	0.0398	-	0.063 λ×0.063 λ	-	–11	Low-frequency applications
[74]	1.575, 2.38–2.5	1 varactor diode	0.22 λ×0.11 λ		–3	GPS, WLAN
[75]	0.470–0.862	2 varactor diodes	0.029x0.0078	-	–9	DVB-H

2.2.1.3 Pattern Reconfigurable Antennas

Radiation pattern reconfiguration depends on the angular orientation of the antenna. In this approach, the beam is adjusted to maximize the signal captured by the receiver. While the antenna plays a key role, the entire digital system connected to the antenna is responsible for optimizing the signal reception. Pattern reconfiguration can be achieved using a movable structure that can be adjusted or rotated through a switching mechanism. Numerous pattern reconfigurable antennas have been reported in the literature, utilizing various technologies such as RF MEMS switches [63], PIN diodes [76-85], and varactor diodes [86] to modify the radiation pattern.

For example, a slot-based electronically steerable pattern reconfigurable array designed for IoT applications is presented in [87]. This design employs six PIN diodes to achieve pattern reconfiguration of a monopole antenna in the WLAN band, but it features a complex and non-planar geometry. Another pattern reconfigurable antenna for the WLAN band, also intended for IoT applications, is described in [88]. This antenna consists of four wire patch elements, with reconfiguration achieved through a single-pole-four-throw (SP4T) switch. However, the design is non-planar and requires a microcontroller to operate the SP4T switch. Additionally, a probe-fed, varactor-loaded pattern reconfigurable antenna is presented for continuous beam steering, using four varactor diodes [89], though the design involves a multi-layered structure.

2.2.1.4 Electrically Small Antennas (ESA)

Electronics is going towards miniaturization, and this miniaturization also requires a small wireless sensor. Therefore, the antenna associated with these sensors needs to be compact. Electrically Small Antennas (ESA) are most widely used in the literature to overcome the compactness issues of electronics. ESA is the antenna within the limits $kr \leq 1$ [90], where $k = \frac{2\pi}{\lambda}$ and r is the minimum radius of the sphere surrounding the antenna. The main features of ESA antennas are:

1. Small size (better option for remote applications (IoT sensors)).
2. Omnidirectional radiation pattern
3. Low input resistance (highly capacitive or inductive because of very small sizes).

According to the antenna gain formula in (2.1), there is a threshold for the antenna aperture value to achieve positive gain. Here, G is the antenna's gain, A_e is the effective area, f is the frequency, and c is the speed of light.

$$G = 4\pi \left(\frac{f}{c}\right)^2 A_e \tag{2.1}$$

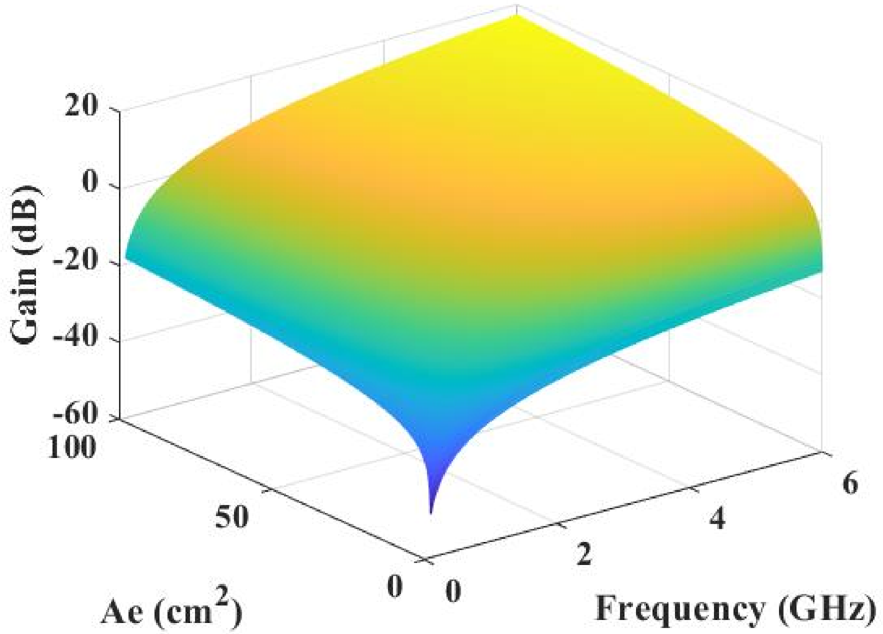

Fig. 2.7. Relationship between gain and effective area of the antenna.

It is clear from Fig. 2.7, when the size of the antenna is below a certain threshold, the gain of the antenna becomes negative. Theoretically, when you select the antenna dimension below this threshold, the gain will be negative. For instance, the gain of an antenna with the dimension of $(\frac{\lambda}{4} \times \frac{\lambda}{4})$ is equal $G = \frac{\pi}{4}$, which will give a negative gain on the decibel scale.

$$A_e = 4\pi \left(\frac{c}{f}\right)^2 \tag{2.2}$$

$$A_e = A_p \times \varepsilon \tag{2.3}$$

Another advantage of ESA is shown in Fig. 2.8. The effective receiving aperture of the antenna is larger than the physical aperture of the substrate, as per the equations (2.2) and (2.3). This leads to a high radiation efficiency and a more efficient RF-to-DC conversion system that is needed to power up sensors [91].

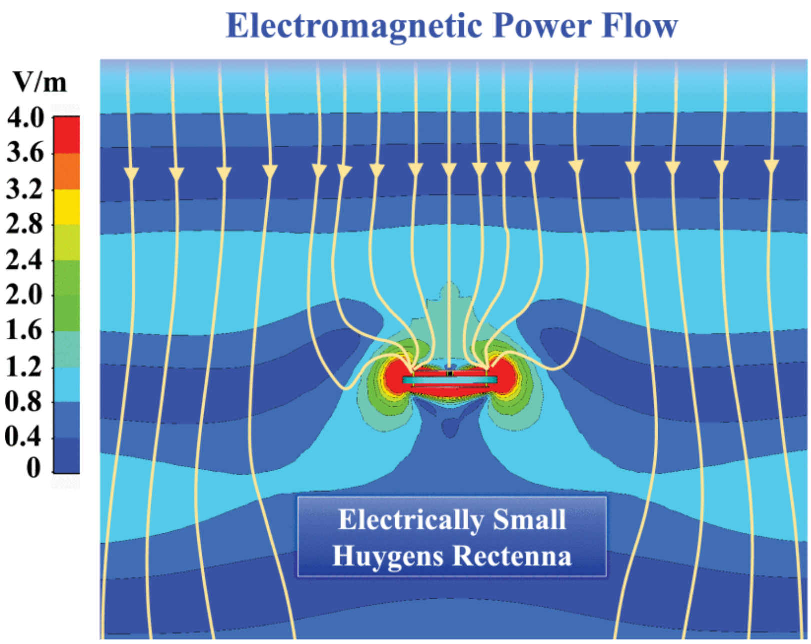

Fig. 2.8. Electromagnetic fields received by ESA [91].

Various ESAs have been reported in the literature [92-96]. Many approaches have been adopted in the literature to miniaturize the size of the antenna, including meandering line [97], inductive coupling [98, 99], folded dipole [100], metamaterials [101-108], Split-Ring Resonator (SRR) [16, 34, 105, 109-111], Capacitively Coupled Loop (CLL), Egyptian Axe Dipole (EAD) [112, 113] and magneto-dielectric substrate. Fig. 2.9 shows the miniaturized structures using meandered lines and inductive coupling.

Commonly, the substrate used to design an antenna has a relative permeability of one (μ_r=1), and the frequency of the structure can be expressed in (2.4) [114].

$$f = \frac{c}{2(l+h)\sqrt{\mu_r \epsilon_r}} \tag{2.4}$$

Where l and h are the dimensions of the antenna element, it is evident from the equation that f is inversely proportional to relative permeability (μ_r). Increasing the value of permeability will decrease the value of frequency f. Hence, to reduce the size of the antenna, the substrate with $\mu_r > 0$ has also been used. These materials are called magneto-dielectric substrates. TABLE 2.6 shows the different antennas using magneto-dielectric substrates with different values of permeability. More generally, the bandwidth of the structure can be enhanced, and the radiation efficiency can be increased if $\mu_r > \varepsilon_r$ [52]. However, these substrates are commercially unavailable and need to be designed in addition to antenna designing, which makes the design process lengthy and complex.

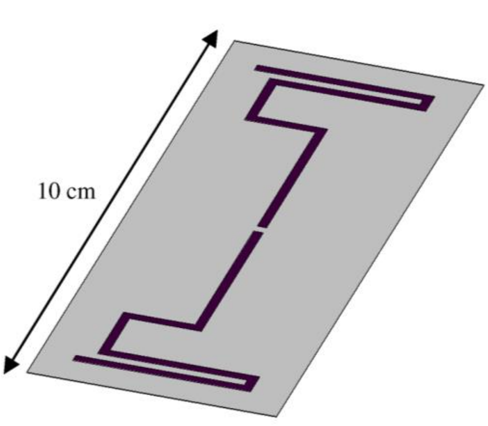

(a)

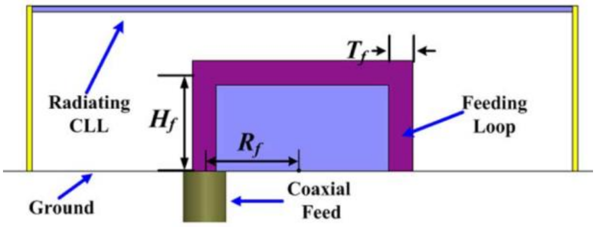

(b)

Fig. 2.9. ESA miniaturization methods, (a) meandering lines [97], (b) inductive coupling [99].

TABLE 2.6. MAGNETO-DIELECTRIC SUBSTRATE TO MINIATURIZE THE SIZE.

Reference	Permeability	Tan δ
[115]	4.35	-
[116]	12	-
[117]	1–9	-
[118]	2	0.01
[119]	Product=10	-
[120]	5	-
[121]	5	0.05
[122]	2.2	-
[123]	2.1	0.1
[124]	2	0.1

Metamaterials have also been used for size reduction. In [125], ESA is designed at 915 MHz (GSM band) with $ka = 0.98$ having a cardioid-shaped pattern. NFPR element is designed to directly match the low impedance of the antenna with the rectification circuit, and 88% efficiency is achieved at +10.4 dBm. Fig. 2.10 is showing the structure of the antenna.

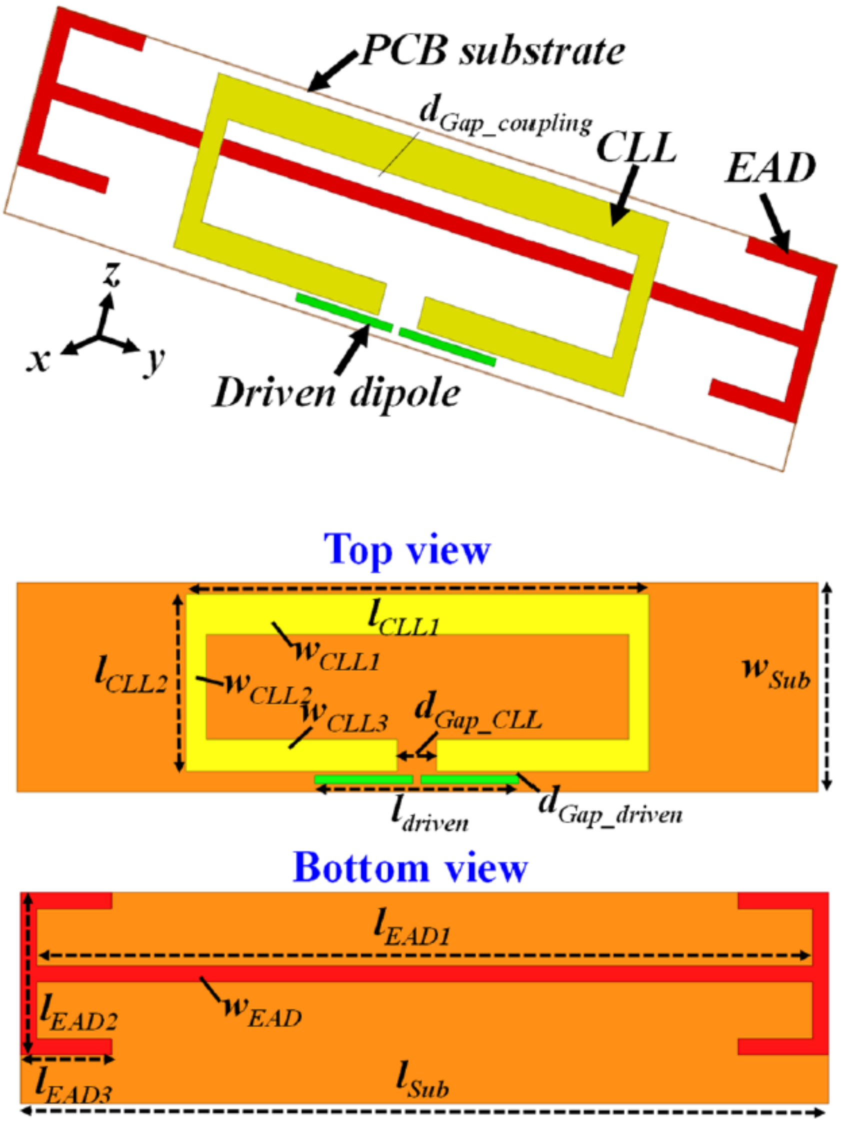

Fig. 2.10. ESA based on NFRP element for impedance matching [125].

In [90] and [126], the ESAs are designed at 868 and 1575.4 MHz with $ka = 0.53$ and 0.611, as shown in Fig. 2.11 and Fig. 2.12, respectively. The radiation patterns are omnidirectional. The input impedance of the antennas is conjugately matched with the impedance of the rectifier using the NFRP element. RF-to-DC conversion efficiency is 22% at –19 dBm and 79.6% at 0 dBm, respectively. ESA is commonly used in remote IoT sensor networks because of its compact size and large effective area compared to physical area. This ensures a high efficiency of the WPT system.

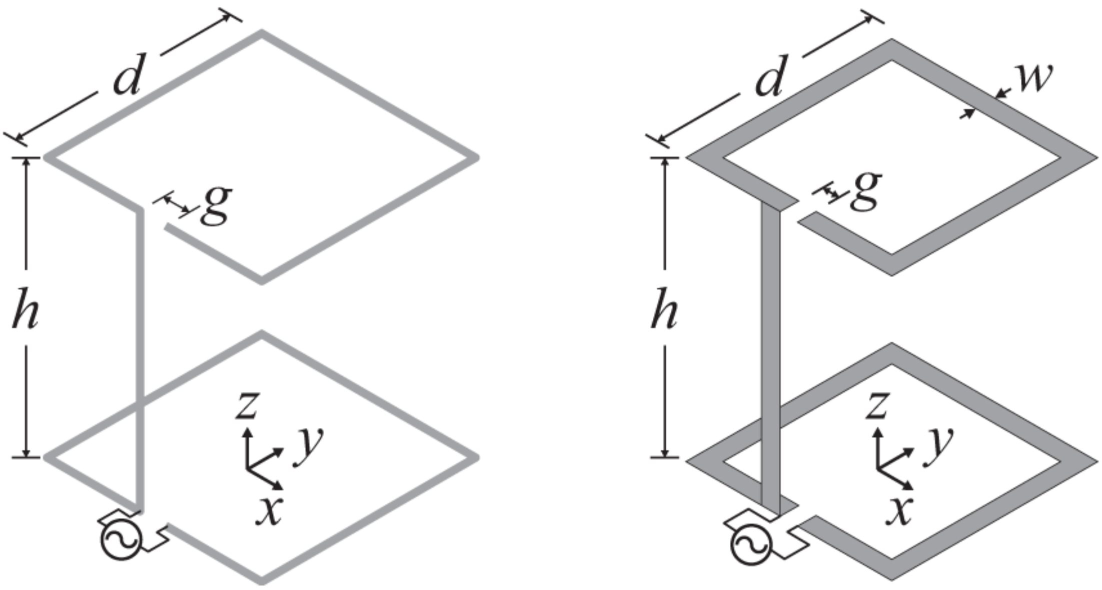

Fig. 2.11. ESA antenna structure for energy harvesting [90].

[Production note: This figure is not included in this digital copy due to copyright restrictions.]

Fig. 2.12. Highly efficient ESA antenna structure for energy harvesting [126].

2.2.2 Matching Network

The matching network sits between the receiving antenna and the rectification circuit to match the antenna's impedance with the rectification circuit. There are several approaches to match the impedances [127].

a) **Lumped element matching:** this technique uses lumped elements (inductor and capacitors) to match the impedances.
b) **Distributed element matching:** in this technique, transmission lines are used to match the impedances. This includes single series/shunt open/short stub matching, multi-stub matching and multi-section matching, tapered matching techniques.
c) **Quarter wavelength transformer:** This technique utilizes transmission lines of length of λ/4 to achieve impedance matching. The geometry of the quarter-wave transformer is shown in Fig. 2.13 [128], where Z_0 is the characteristics impedance and Z_{in} and Z_L are the source and load impedances, respectively.

Any of these methods can be used for matching based on the requirements of the system, such as size, frequency and efficiency.

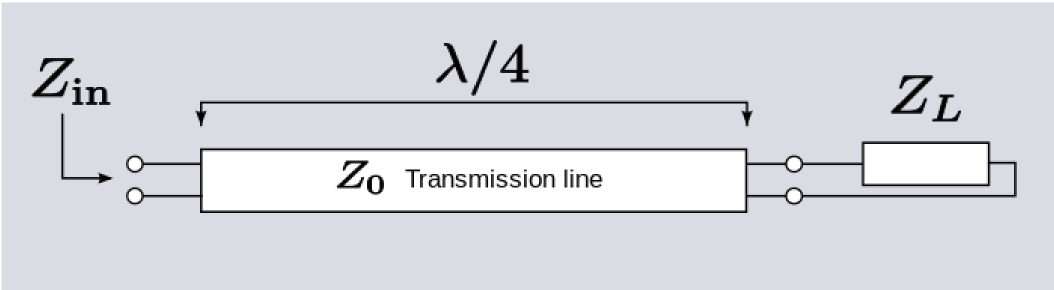

Fig. 2.13. Quarter-wavelength transformer [128].

2.2.3 Rectifier circuit

A rectifier circuit converts an RF signal into DC voltage, which can then be used to power a sensor or recharge batteries. This transformation is a stage in energy harvesting that aims to convert ambient RF energy into a usable form. Various kinds of rectifiers are commonly utilized for RF-to-DC conversion [129].

2.2.3.1 Single Diode Rectifier

The diode rectifier is a basic setup that uses just one diode to convert the RF signal into a usable form by rectifying it [129]. Making it suitable for various applications due to its simplicity and ease of use. However, a major limitation is its low rectification efficiency, especially at low input power levels. The output voltage is relatively low since it only utilizes half of the input signal, leading to poor conversion efficiency. This rectifier is not suitable for high-power scenarios due to its limited ability to handle large voltage swings.

2.2.3.2 Voltage Doubler Rectifier

One common type of circuit used for this purpose is known as a voltage doubler, as illustrated in Fig. 2.14 [130-135]. A voltage doubler rectifier utilizes a combination of two diodes and capacitors to increase the output voltage derived from the RF signal effectively doubling it compared to a diode rectifier setup. The voltage doubler not only converts the AC signal to DC but also amplifies the output voltage by effectively doubling it. This feature is beneficial in low-power scenarios where every increment in voltage is crucial. Typically composed of two diodes and two capacitors, the circuit charges the capacitors during each AC input cycle, resulting in a DC output. This efficient design is widely used for its ability to increase the voltage derived from RF energy. The main drawback is the increased circuit complexity compared to a single diode rectifier. Additionally, higher internal losses may arise due to the presence of two diodes, which introduce more threshold voltage losses. This can reduce overall efficiency, particularly for very low input power levels. Moreover, at higher frequencies, parasitic effects can degrade performance, requiring careful design optimization.

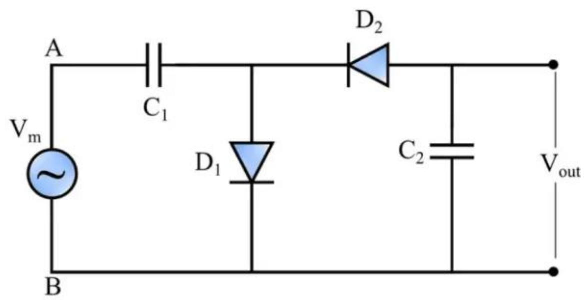

Fig. 2.14. RF to DC voltage doubler circuit [130, 131].

2.2.3.3 Greinacher Voltage Multiplier

The Greinacher voltage multiplier (also known as the Cockcroft Walton voltage multiplier) comprises diode capacitor stages that stack the output of each stage to amplify the DC voltage progressively higher [136]. These rectifiers are well suited for applications that require voltage levels but minimal current flow. The main challenge is that as the number of stages increases, the efficiency drops significantly due to cumulative diode losses and parasitic effects. Additionally, increased circuit complexity requires precise tuning to balance voltage gain versus conversion efficiency. The structure is also sensitive to load variations, meaning that improper load matching can drastically reduce performance.

2.2.3.4 Bridge Rectifier

A bridge rectifier utilizes four diodes arranged in a bridge pattern to convert both negative halves of the RF signal effectively for better conversion efficiency results [137]. Bridge rectifiers work well for medium to RF power levels. A key limitation is the higher conduction losses due to the use of four diodes, which increases threshold voltage drops and reduces efficiency at low input power levels. Additionally, it requires a balanced RF input signal, making its integration more complex in unbalanced RF energy harvesting circuits. The larger component count also increases circuit footprint, making it less suitable for highly compact designs.

2.2.3.5 Differential Rectifier

A differential rectifier usually uses two or more diodes arranged in a setup to improve efficiency in converting power and decrease energy wastage [138]. It is designed to work with low-power radio frequency signals and aims to boost the generated DC output by minimizing the impact of diode threshold voltages. This makes it a good choice for environments, with low radio frequency power levels. The main challenge is that it requires a differential input signal, which may not always be available, adding to circuit design complexity. Additionally, it involves more components than a single-diode rectifier, leading to a larger circuit footprint. Parasitic effects and nonlinearities in diode behavior can also impact performance at very low RF power levels, requiring precise design optimization.

Each of these rectifier types can be selected or modified depending on the input power, frequency, and desired output voltage, aiming for efficient RF-to-DC conversion in energy-harvesting applications.

2.2.4 Efficiency of Complete Rectenna System (Rectifier and Antenna)

The goal of a complete rectenna system is to convert RF energy into DC, and this conversion efficiency of WPT/RFEH depends upon different parameters. Converted DC voltage, DC power and conversion efficiency are represented in (2.5), (2.6), and (2.7), respectively [139].

The main key parameters include the output DC voltage, the power delivered to the load and the conversion efficiency. These equations are important for evaluating and optimizing the performance of a rectenna to achieve maximum efficiency.

$$V_{DC} = \frac{V_{br}}{2} \tag{2.5}$$

$$P_{DC} = \frac{{V_{DC}}^2}{R_L} \tag{2.6}$$

$$\eta = \frac{\frac{V_{DC}^{\ 2}}{R_L}}{P_{in\ EH}} \tag{2.7}$$

V_{DC} is rectified voltage, V_{br} is diode breakdown voltage, P_{DC} is converted DC power, P_{inEH} is delivered RF power from antenna to rectifier, and η is the efficiency of the system. There are multiple parameters that can affect the efficiency of RF-to-DC conversion. These parameters are listed below.

1. **Received Power**: Increasing the transmitted power improves RF-to-DC conversion efficiency. In WPT systems with dedicated sources, we can raise the source power to further enhance efficiency, considering regulations on the level of transmitted power.
2. **Gain:** In WPT, antenna gain can be increased using an array of antenna elements/reflectors. The higher gain of the antenna ensures a high level of received power.
3. **Matching Network:** A poor matching network leads to more losses, which implies less conversion efficiency. Also, the use of resistors in matching networks can decrease the efficiency. Hence, it is recommended to match the impedances with reactive elements (inductor/capacitor).

Fig. 2.15 summarizes the parameters affecting RF to DC conversion efficiency. RF to DC conversion efficiency can be increased by increasing the antenna's gain, increasing the input power level, and reducing the losses of the matching network.

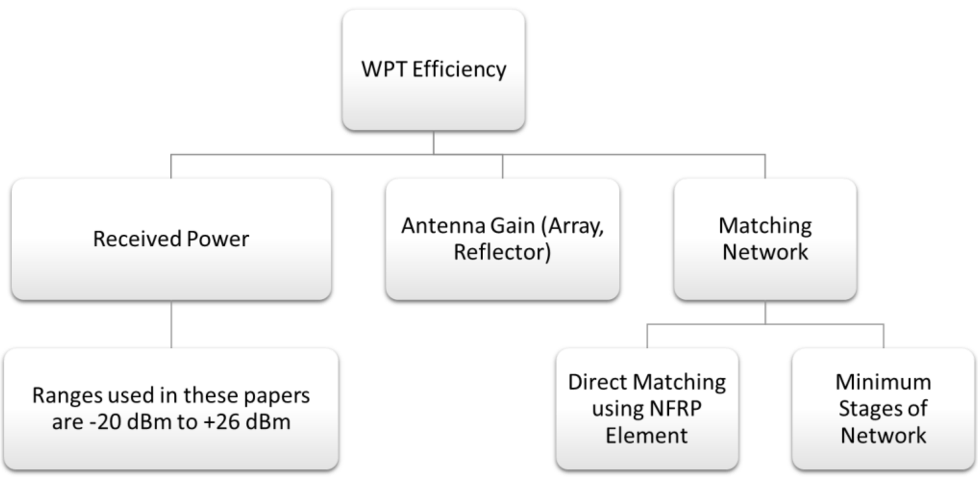

Fig. 2.15. Parameters affecting RF-to-DC conversion efficiency.

Matching the antenna impedance with the rectifier impedance necessitates a matching network. Conventional matching networks involve circuit components that introduce additional complexity into the design and can detrimentally affect overall efficiency [140, 141]. Recently, a patch rectenna is presented for WPT in [142]. The rectenna operates at 915 MHz with a size of $0.305\lambda \times 0.305\lambda$. However, a separate matching network is integrated with the antenna to achieve good impedance matching, which increases the total number of lumped components and the complexity of the structure. Another polarization-insensitive rectenna is presented in [143]. The rectenna comprises an array of octagonal metasurface rings with an overall size of $1.15\lambda \times 1.15\lambda$ and a rectifier circuit with a matching network of size $1.34\lambda \times 0.48\lambda$. Operating at 5.8 GHz, the metasurface array antenna achieves a gain of 10 dBi, but the maximum RF-to-DC conversion efficiency is 66% at a high input power of +13 dBm. Another rectenna at 5.8 GHz is presented in [144]. The antenna employs an array of six patch elements to achieve high gain and uses a separate rectifier based on microstrip transmission lines. Although the rectenna achieves a maximum efficiency of 61% at 382 $\mu W/cm^2$, its size is relatively large. A circularly polarized rectenna is presented at 5.8 GHz in [145]. The proposed rectenna utilizes two separate elements (antenna and rectifier). The maximum RF-to-DC conversion efficiency is 80.6% at an input power of +15 dBm, but the antenna is multilayer, making the geometry complex. Therefore, there is a preference to maintain overall efficiency and reduce design complexities by eliminating the physical matching network. Designing such a circuit for a rectenna poses considerable challenges. Furthermore, the intricate structure of the matching network can potentially reduce efficiency and escalate fabrication costs. Furthermore, avoiding the use of a matching circuit could result in a more compact size for the rectenna. A patch rectenna with an integrated matching network is presented in [146]. Operating at 2.45 GHz, the rectenna achieves conjugate impedance matching between the antenna and the rectifier, and the maximum efficiency is 82.2% at an input power of +22.5 dBm with an overall size of $0.66\lambda \times 0.5\lambda$.

2.3 Precision Agriculture

This section discusses the concept of precision agriculture. The integration of WPT into precision agriculture can enable an autonomous WSN for enhanced agricultural monitoring and management. To improve the yield and quality of the crop it is vital to periodically monitor the soil samples to analyze soil moisture, minerals, nutrients, pests and temperature [11, 147, 148], as shown in Fig. 2.16. Since agricultural areas are in remote locations, physically visiting the site and using the sensing equipment can be challenging due to weather conditions and limited vehicle access. Conventional methods of moisture measurement are labor-intensive and time-consuming. WSNs have been widely used in numerous applications including atmosphere monitoring, animal tracking and healthcare monitoring. This idea can be implemented in the agriculture sector for smart agriculture [23] where wireless sensors can be deployed in outdoor locations to monitor soil parameters without any physical visit to the remote area. This approach can also be applied to livestock [24]. By employing soil moisture monitoring through WSNs on farms, there are opportunities to enhance water efficiency, increase crop productivity, reduce energy costs, and lessen the environmental impact of excessive irrigation and fertilizers [12-15]. Therefore deploying soil moisture sensors in a WSN as a part of the IoT has gained significant attention in smart agriculture [23]. WPT has the potential to revolutionize precision agriculture by offering an eco-friendly power solution for essential sensors and devices used to monitor soil conditions such as health status and moisture levels.

Fig. 2.16. Collecting soil samples for analysis.

The measurement of Volumetric Water Content (VWC), which represents the quantity of water in the soil that's directly accessible to plants, is a crucial indicator. The permittivity of the soil can be correlated to its moisture content [17]. The VWC quantifies the amount of water present in the soil and can be calculated using (2.8), where W_1 and W_2 represent the weights of the dry soil and water, respectively.

$$VWC\ (\%) = \frac{W_2}{W_1 + W_2} \times 100 \tag{2.8}$$

2.3.1 Sensing

In precision agriculture, sensing is divided into remote sensing and remote monitoring, each suited to different agricultural scales and needs. Remote sensing gathers data without physical contact using drones or aircraft [149], and is ideal for extensive data collection across large areas, monitoring crop health and soil conditions effectively. However, it faces limitations in resolution and depth of subsurface information. On the other hand, remote monitoring involves sensors that may be in direct contact with the Material Under Test (MUT), particularly beneficial in environments like greenhouses where precise control over temperature, humidity, and soil moisture is necessary. This approach provides localized, real-time data with high accuracy and resolution, making it better suited for detailed monitoring in controlled settings. The main trade-off is between the extensive coverage of remote sensing and the detailed precision and durability of remote monitoring. In some cases, combining both approaches can yield comprehensive insights, with remote sensing for broader trends and remote monitoring for detailed, actionable data at the field level [150-155]. In [150, 151, 155], paired transmitting and receiving antennas are used to collect soil data. One antenna node is buried within the soil, while the other is above the surface. RF signals are transmitted and received, and soil parameters are determined based on the signal's refraction and reflection. However, accurate antenna placement is crucial, as misalignment can introduce significant errors. Other studies [152-154] utilize soil moisture tags buried in the soil for wireless data collection. In [152], a passive Wi-Fi SoilTag measures soil moisture via relative frequency responses, using two patch antennas and a Wi-Fi transceiver. Although effective, this approach becomes unreliable above 20% VWC, where the response reaches 0 dB, requiring machine learning techniques to interpret values above this threshold. Additionally, relative amplitude measurements are more prone to noise and environmental interference, such as electromagnetic interference (EMI) and soil temperature fluctuations, which can impact signal amplitude. In [153, 154], passive tags reflect RF signals back to the reader, but tag orientation and placement can impact accuracy, as improper alignment may skew data, and reflections from plants may interfere with system performance. Various Radiofrequency Identification (RFID) tags and microwave sensors have been presented in the literature to address these challenges.

2.3.1.1 Radiofrequency Identification (RFID) Tags

RFID tags have gained significant attention in recent years [156, 157]. In smart agriculture, these tags can be used to measure data about growth, water consumption and environmental conditions.

RFID tags and sensors have also been used to monitor soil moisture by measuring soil permittivity in smart agriculture. The basic principle of RFID technology involves using electromagnetic waves in the Ultra-High Frequency (UHF) band (0.840–0.955 GHz) to sense and transmit information from a tag to a base station. The capability to identify, measure, and communicate is crucial for the effective functioning of RFID sensors [158]. To perform these functions, power is required, which can significantly affect the lifespan, cost, sensing range, and complexity of an RFID system [159-162]. Various RFID antenna designs have been proposed in the literature for different applications [163-169]. Recently, a dual-band circularly polarized (CP) crossed dipole antenna has been proposed for RFID applications [163]. The antenna with the size of 0.3×0.3 $\lambda_0{}^2$, operates in the frequency range of 0.77–1.06 GHz and 2.22–2.95 GHz, but it exhibits a large physical size. Another dual-band CP antenna is presented for UHF RFID tag and wireless local area network (WLAN) applications in [164]. The antenna size is 0.18×0.18 $\lambda_0{}^2$ with a gain of –0.6 dBi in the RFID band and 1.2 dBi in the WLAN band, but the geometry is non-planar.

RFID tags can be broadly divided into two categories: chipped and chipless [170]. In chipped RFID, an Application Specific Integrated Circuit (ASIC) chip is integrated with the structure for object identification [165-167]. A chipped UHF RFID tag antenna is presented in [168]. The antenna, with the dimensions of 0.23×0.07 $\lambda_0{}^2$, operates in a single band (913–925 MHz) to detect metallic objects using an ASIC chip. A chipped RFID tag and sensor are presented for fluid detection [169]. The tag and the sensor are separately designed and connected using a circulator to implement the sensing. Another chipped RFID fluid sensor is presented to sense the constitutive parameters of the fluid [171]. Fluid flows between a capacitive gap and affects the capacitance of the sensor, which is then used to categorize the fluid, but the design process is complex. Whereas, in chipless tags, an ASIC chip is not required, and detection is done using resonators [172-174]. Different types of resonators have been used in the literature to engineer chipless tags, including slot resonators [175], Spiral Resonators (SR) [172], QR code-based resonators [173], natural resonance [176], and SRR [177].

2.3.1.2 Microwave Sensors

Microwave sensors have also been used to monitor soil moisture in smart agriculture by measuring soil permittivity. The amount of moisture in the soil is commonly referred to as VWC, and a higher value of VWC in the soil corresponds to a larger value of permittivity. The penetration of the RF signal into the soil depends on the frequency and dielectric properties of the soil [128]. The penetration of the signal can be increased by reducing the sensor's operating frequency. This allows a single sensor to cover a larger volume of soil, thereby reducing the total number of sensors required in a wireless sensor network. However, lower frequencies result in bulkier structures that can be challenging to implement. Microwave sensors can be divided into three categories based on their measurement techniques. The first method is time domain reflectometry/transmission (TDR/TDT) [17, 178], where soil moisture is measured using the time delay in the transmitted and received signal. TDR sensors use a probe to transmit and receive the signals, providing measurements in the vicinity of the probe. However, this limits their ability to measure soil moisture at various depths. The second technique for soil moisture measurement is based on the measurement of the charge/discharge time of a capacitor across a resistor [18, 179-

181]. However, resistance value highly depends on temperature, and temperature variation can lead to inaccurate measurements. The most commonly used technique in microwave sensors is frequency domain reflectometry [111], where soil moisture measurements are performed based on frequency variations. Although this method is simple and can measure VWC at various depths, it requires a portable Vector Network Analyzer (VNA) to determine the frequency response variations to measure soil moisture.

Metamaterial Transmission Lines (MTLs) have garnered significant attention for reducing the size of sensors. SRR, Complementary Split Ring Resonator (CSRR), SR, and Complementary Spiral Resonator (CSR) have been widely employed due to their simple design and ease of fabrication [16, 19, 20, 34, 105, 111, 182].

SRRs:

In the realm of metamaterials, SRRs stand out as structures comprising two metal rings with gaps on opposite sides, as shown in Fig. 2.17(a). These resonators react strongly to frequencies of electromagnetic fields, making them valuable for crafting compact high-frequency components in filters and antennas. SRRs are useful in achieving negative permeability in metamaterial design across various RF and microwave applications.

CSRRs:

As the counterpart to SRRs, CSRRs emerge by etching out an SRR shape from a surface typically a ground plane, as shown in Fig. 2.17(b). CSRRs play a role in attaining negative permittivity within a material. They find their niche in microwave circuits for creating stopbands and enhancing isolation in-band devices through compact filter design.

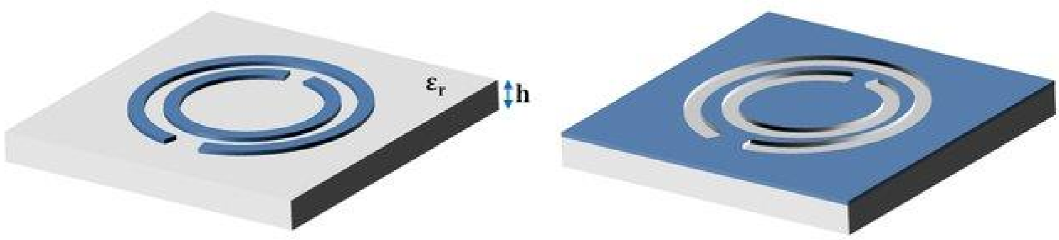

(a) (b)

Fig. 2.17. Geometry of (a) SRR, (b) CSRR [183].

SR:

SRs consist of a coiled conductive path that forms a compact, high-inductance structure, making SRs efficient tools for downsizing resonators within high-frequency circuits [16]. Widely employed in filters, oscillators and selective surfaces spiral resonators resonate at lower frequencies, with smaller footprints compared to conventional counterparts. The geometry of a 2-turns SR is shown in Fig. 2.18(a).

CSRs:

CSRs serve as the inverse or complementary counterparts to spiral resonators [16, 105, 111]. They are formed by eliminating the shape from a conductive surface akin to how CSRRs act as complements to SRRs. CSRs offer a solution for incorporating high permittivity features and finding applications in scenarios where limited space and top-notch performance are crucial. They play a role in crafting antennas, filters and various RF components for efficient manipulation of electromagnetic waves. The geometry of a 3-turns CSR is shown in Fig. 2.18(b)

Each of these resonators is utilized to achieve electromagnetic characteristics, selected based on the specific needs of the application such, as dimensions, frequency range and the intended electromagnetic behavior.

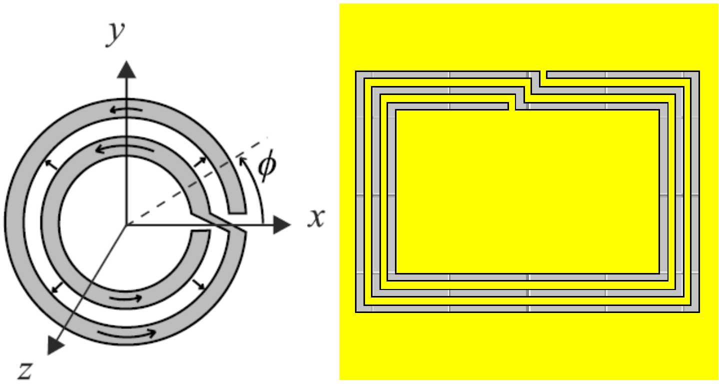

(a) (b)

Fig. 2.18. Geometry of (a) 2-turns SR [184], and (b) 3-turns CSR [34].

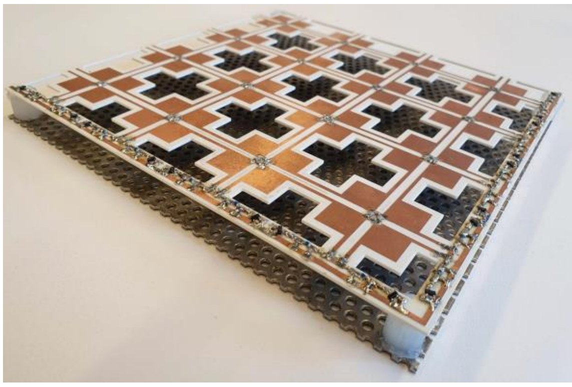

Fig. 2.19. Metamaterial perfect absorber-based soil moisture sensor [185].

A soil moisture sensor based on a metamaterial absorber is presented in [185] and shown in Fig. 2.19. The absorption of the filter varies with different VWC levels in the soil at an operating frequency of 625 MHz. However, the sensor exhibits low sensitivity. Another soil moisture sensor based on Frequency Domain Reflectometry (FDR) is presented in [16]. A combination of spiral and complementary resonators is used to measure soil moisture. However, the resonance frequency of the sensor is 4 GHz, which implies a low penetration capacity of the signal; also, the sensor is very sensitive to the different volumes under test (VUT) of the soil. Sensors for permittivity measurement based on CSRR and Complementary Curved Ring Resonator (CCRR) are presented in [186-188]. These sensors operate at 2.67 GHz, 2.7 GHz, and 3.49 GHz, respectively, and demonstrate high sensitivity. However, the permittivity measurement depends on the thickness of the material under test (MUT) and the distance between the sensor and MUT due to high operating frequency. A Complementary curved ring resonator-based sensor for permittivity detection is shown in Fig. 2.20.

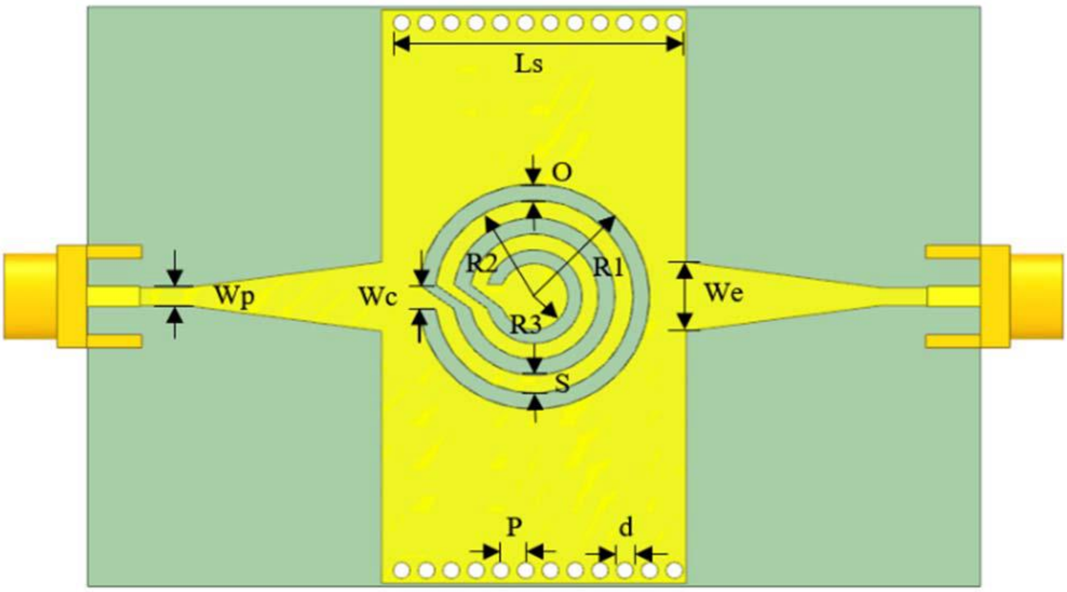

Fig. 2.20. Complementary curved ring resonator-based sensor for permittivity detection [188].

CSRR-based sensors are also used for microfluid characterization [19, 20, 182, 189]. The sensor's resonance frequency changes with different microfluids, but the sensitivity is low. MTLs have been widely used to minimize the size of microwave devices, such as antennas [34, 105, 190], power dividers [191], filters [192], and resonators [177]. Within MTLs, SRRs and CSRRs have been extensively adopted to achieve size reduction [193]. Various SRR and CSRR-based microwave sensors are reported in the literature [16, 19, 182, 186-189]. An FDR-based differential sensor for soil moisture measurements is presented in [16] and shown in Fig. 2.21.

The sensor utilizes both SRR and CSRR on opposite sides of the substrate to measure the permittivity of the MUT. However, the sensor exhibits low sensitivity, and its resonance frequency is high (4 GHz), limiting its coverage area for soil moisture measurements.

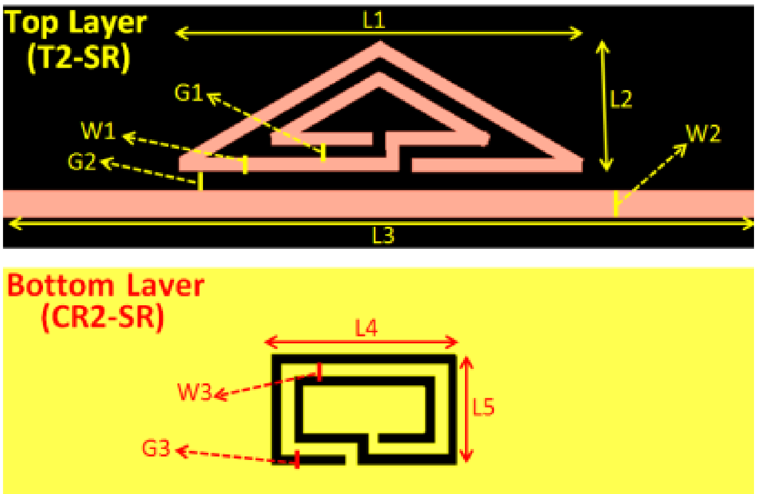

Fig. 2.21. An FDR-based differential sensor for soil moisture detection [16].

Another differential sensor based on SRR is presented in [194], shown in Fig. 2.22. The sensor operates at a high frequency (5.12 GHz), which makes it susceptible to variations in the VUT. Due to these frequency variations with different VUTs, the reported sensor can generate false measurements.

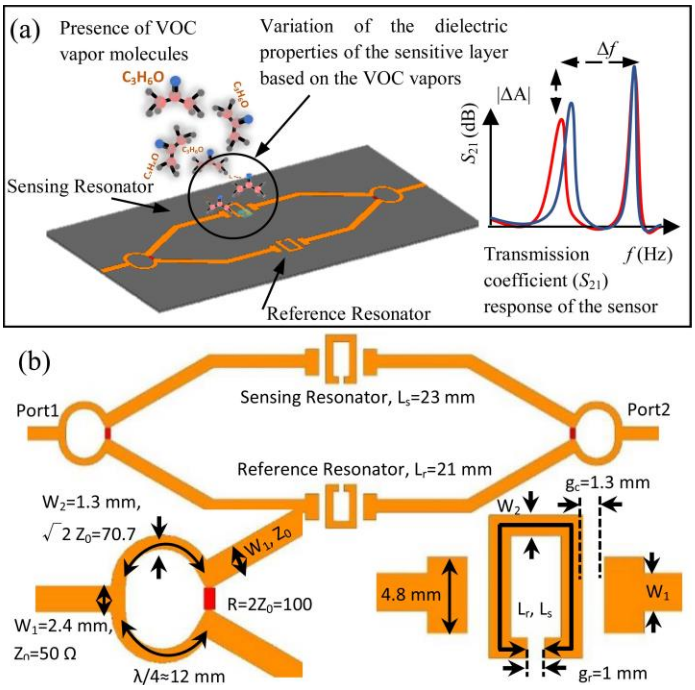

Fig. 2.22. Differential microwave sensor tag for liquid characterization [194].

Low-frequency FDR sensors are presented in [185, 195]. The sensors operate at 560 MHz and 1.017 GHz when unloaded; however, the structures are large, and the sensors have low sensitivity. A low-frequency sensor is shown in Fig. 2.23. Several microwave sensors have been reported for the characterization of microfluids [19, 20, 182, 189]. These sensors operate at frequencies of 2.4 GHz, 2.45 GHz, 2.234 GHz, and 2.38 GHz, respectively. While these sensors have the ability to measure high permittivity values as high as 70, they also exhibit very low sensitivities. Several high-sensitivity CSRR-based sensors have also been proposed for measuring the permittivity of the MUT [186-188]. However, significant frequency variations occur for different heights of the MUT, primarily because of the high resonance frequencies of these sensors.

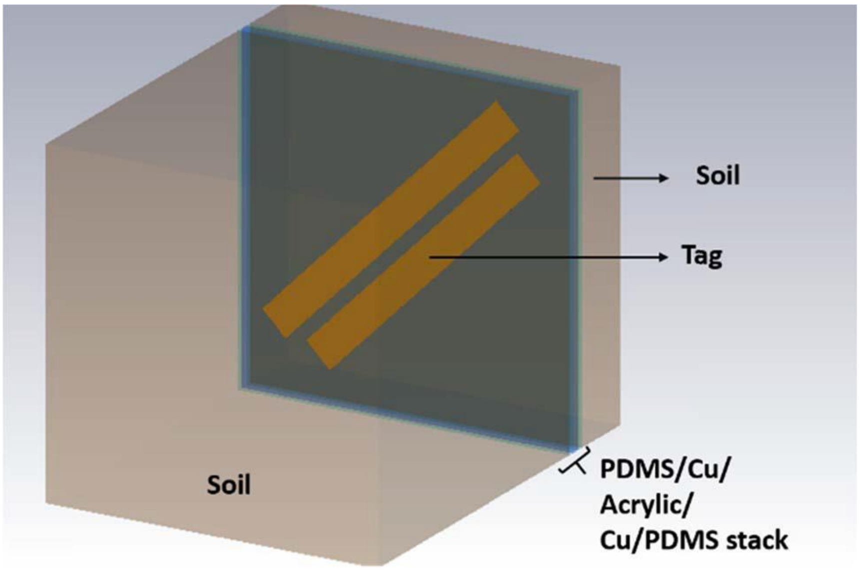

Fig. 2.23. Sensor tag for subsoil moisture detection [195].

2.3.2 Communication

For remote sensing systems in diverse geographical structures, it is essential to integrate an antenna to transmit sensor data to the base station. This enables remote monitoring of real-time soil moisture data for precise irrigation and enhances resource management efficiency. Agricultural areas would have different geographical structures, and the positioning of IoT equipment can vary. A large-coverage antenna becomes particularly essential in agricultural areas where geographical structures vary, and the positioning of IoT equipment may differ. An omnidirectional antenna has the ability to communicate in all directions and can be used for communication with the base station regardless of the positioning. However, the gain of an omnidirectional antenna is very low, which makes it unsuitable for large agricultural fields. Therefore, a directional antenna with pattern reconfiguration is required for reliable long-distance communication in various geographical structures. Various pattern reconfigurable antennas are reported in the literature to switch the radiation pattern of the antenna using radio-frequency microelectromechanical system (RF MEMS) switches [63], PIN diodes [76-85], and varactor diodes [86]. A slot-based electronically steerable pattern reconfigurable array is presented for IoT applications in [87] and shown in Fig. 2.24. It utilizes six-pin diodes to achieve pattern reconfiguration of a monopole antenna in the WLAN band, but the geometry is complex and non-planar. Another pattern reconfigurable antenna is presented in the WLAN band for IoT applications [88]. The proposed structure, shown in Fig. 2.25, consists of 4 wire patch antennas, and the reconfiguration is achieved using a single single-pole-four-throw (SP4T). However, the design is non-planar and requires a microcontroller to control the SP4T switch. A probe-fed varactor-loaded pattern reconfigurable antenna is presented for continuous beam steering, utilizing four varactor diodes [89]. However, the antenna's geometry is multi-layer.

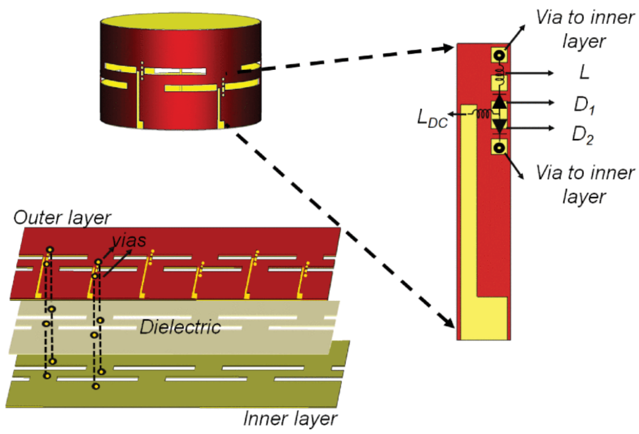

Fig. 2.24. A slot-based electronically steerable antenna for IoT applications [87].

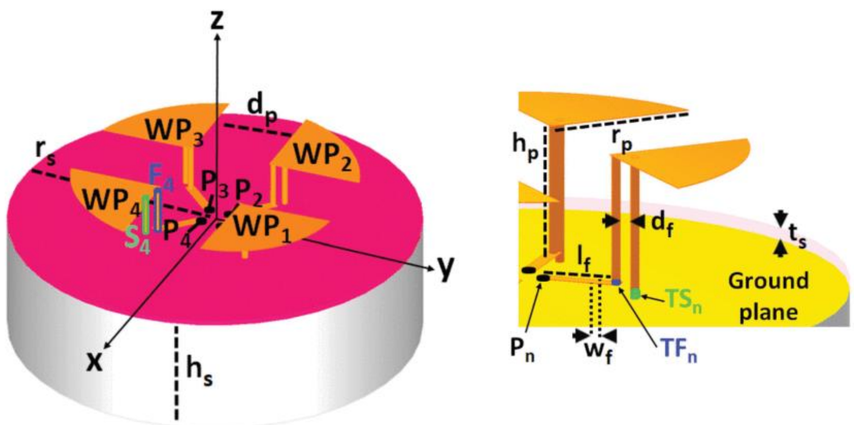

(a) (b)

Fig. 2.25. Electronically pattern reconfigurable antenna for IoT applications, (a) perspective view, (b), wire patch [88].

2.3.3 Integrated Sensing and Communication

Recently, both a permittivity sensor and an antenna have been integrated to enable sensing and communication [196], shown in Fig. 2.26. The antenna is designed to operate at 2.45 GHz Wireless Local Area Network (WLAN) band, while the sensor's resonance frequency is 4.7 GHz. A frequency-selective multipath filter is utilized to measure the permittivity of the MUT to characterize the material. However, the sensor has a high resonance frequency and does not produce narrow resonances, which can lead to false measurements. Designing a sensor with low resonance frequency, compact size, and high sensitivity to cover a large VUT is highly challenging. A comparison of the reported sensors in terms of size, resonance frequency, number of bands, and sensitivity is shown in TABLE 2.7.

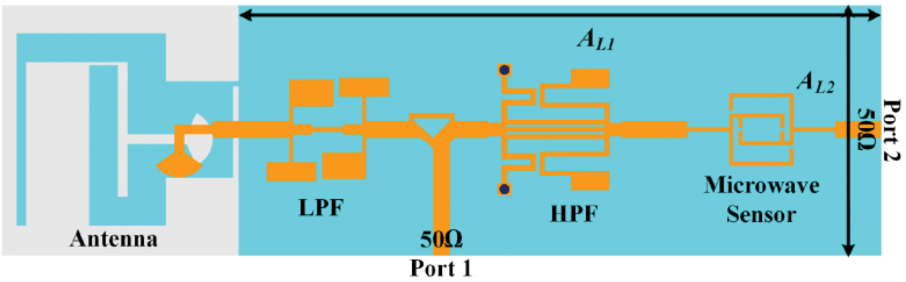

Fig. 2.26. Dual-function system for sensing and communication [196].

TABLE 2.7. COMPARISON OF THE REPORTED SENSORS.

Ref.	Size at f_u ($\lambda_0{}^2$)	f_u (GHz)	Number of Bands	Application	Measurement Technique	Sensitivity at max (ε_r) (%)	Max Measured Permittivity
[185]	0.425×0.425	0.625	1	Sensing	Metamaterial Absorber	0.097	19.1
[16]	0.67×0.13	4	2	Sensing	SRR and CSRR	0.9	16.7
[186]	0.35× –	2.67	3	Sensing	CSRR	1.6	9.2
[189]	–	2.4	1	Sensing	CSRR	0.19	79.5
[19]	0.32×0.2	2.45	1	Sensing	M-CSRR	0.2	70
[20]	0.198×0.198	2.38	1	Sensing	EBG Resonator	0.224	70
[182]	0.184×0.372	2.234	1	Sensing	SRR	0.04476	70
[187]	0.36× –	2.7	1	Sensing	CSRR	1.7	10.2
[196]	0.42×0.44	4.7	2	Sensing+ Communication	Frequency Selective Filter	0.214	26

2.4 Transmit and Receive (T/R) Switch

In smart agriculture, we need devices such as circulators and RF switches to control the flow of RF signals, as shown in Fig. 2.27. These devices play an important role in directing and regulating RF signals within the system [197].

A continuous wave (CW) RF signal is generated by an oscillator and sent to embedded sensors. These sensors will respond with soil moisture information. The purpose of the circulator is to ensure the flow of signal in one direction only [198]. An antenna can transmit moisture data to the base station using a wireless channel. By using a switch, the same antenna can serve as a capturing antenna for WPT to capture ambient RF energy. These components enable effective control and power management in agricultural applications, addressing challenges related to size, bandwidth limitations, and power demands, which are crucial for enhancing system performance and scalability.

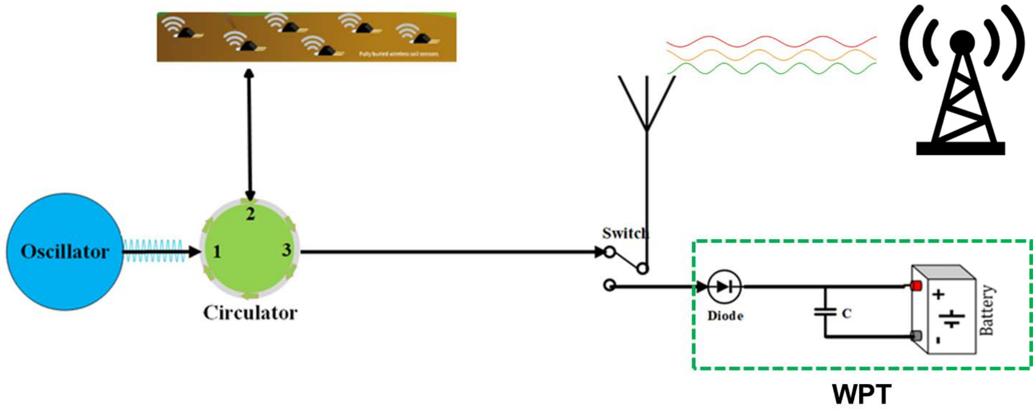

Fig. 2.27. Integration of the WPT, sensing and communication systems.

IoT sensor networks employ devices such as circulators and RF switches across various sectors, from home automation to industrial control systems. These devices are crucial for enabling remote sensing, data measurement, and data communication [29, 30, 111, 199]. Circulators, which are vital for directing signal flow unidirectionally, offer high isolation and low insertion losses. However, their reliance on ferrite materials to achieve non-reciprocal signal propagation results in a narrow bandwidth and limited isolation, typically not exceeding 20 dB. Additionally, ferrite materials add bulkiness, rendering them unsuitable for compact IoT applications. To overcome these limitations, several developments in magnet-less circulators have been reported, which eliminate the need for ferrite and reduce the device size [200-202]. These circulators operate on the principle of spatiotemporal modulation, using modulation to alter the signal's path. Transmit-receive (T/R) switches are also employed to manage signal flow. By utilizing T/R switches, a single antenna can serve both the transmitter and receiver, reducing the need for multiple antennas and thereby simplifying the hardware. T/R switches offer high isolation between the transmit and receive paths and can be categorized as either passive or active [197].

2.4.1 Active T/R Switches

Active T/R switches require a DC bias voltage to switch from OFF to ON, necessitating external biasing circuits. This introduces latency, which can affect switching speed and reduce efficiency. Several active T/R switches have been developed for nuclear magnetic resonance (NMR) applications [203-207]. A broadband active T/R switch was reported in [206], designed to operate from 250 MHz to 1 GHz for pulsed magnetic field NMR. This switch features low insertion loss and high isolation, but its design is complicated by the inclusion of voltage regulators in the biasing circuit. Another active T/R switch for NMR is discussed in [207], covering a wide frequency range from 10 to 330 MHz with low insertion loss. However, the necessity of a control circuit comprising MOSFETs, an RF choke, and a DC bias for switching operation adds complexity and reduces cost efficiency.

Various T/R switch designs for wireless and multistandard applications have also been presented [208-211]. These designs employ complementary metal-oxide-semiconductor (CMOS) T/R switches, covering frequencies from a few MHz to the GHz range. However, due to the nature of CMOS devices, parasitic components values are generally high, which can influence the performance of switching. In [212], a T/R switch utilizing vanadium dioxide (VO_2)-based RF switches at 1.9 GHz is presented. The design, shown in Fig. 2.28, includes a 4-port coupler and two VO_2 switches for forward and backward coupling with low insertion loss. In the OFF state, the switches enable forward coupling, while in the ON state, the signal is directed to the backward coupling port. However, fabricating VO_2 switches requires six layers, adding complexity to the device's geometry. Additionally, a 4-port spatiotemporally modulated circulator with a center frequency of 850 MHz is introduced in [213]. This design incorporates varactor diodes that require a biasing voltage for operation.

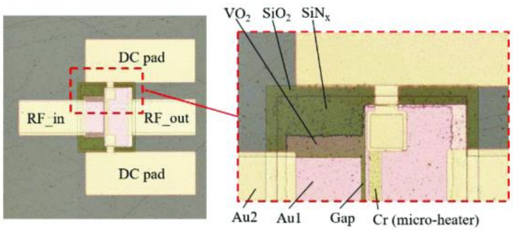

Fig. 2.28. T/R switch using vanadium dioxide (VO_2) [212].

In active T/R switches, an RF choke is essential to isolate RF signals from DC signals. However, there is a trade-off between the inductor value and the RF signal frequency; high inductance at low frequencies can lead to increased transients, limiting the system's bandwidth and reducing its versatility for IoT applications. The additional biasing components required for active switches can also increase circuit size. Compact IoT devices, often powered by limited energy sources such as batteries or energy harvesting, benefit from passive T/R switches. These switches are compact, lightweight, and do not require a biasing voltage, which simplifies the design and implementation and reduces complexity. As a result, passive T/R switches are ideal for energy-constrained IoT devices, enhancing the efficiency and reliability of IoT systems, making them excellent candidates for cost-effective and compact applications. The lack of biasing circuitry also makes passive T/R switches easier to integrate with other circuits and electronics. For instance, a passive narrowband T/R switch operating at 175 MHz is presented in [214], utilizing a quarter-wavelength transmission line and anti-parallel PIN diodes to enable bidirectional signal flow. However, for compact IoT applications, a wideband passive T/R switch is desirable to achieve fast, cost-effective switching without the need for biasing voltage, thereby ensuring a power-efficient design with high isolation and compactness.

2.4.2 Passive T/R Switches

On the other hand, passive RF switches do not require biasing voltage, making them more energy efficient. Nonetheless, they often need help to provide sufficient isolation between transmit and receive paths in IoT setups, especially at higher frequencies or broader bandwidths. Consequently, RF switches encounter challenges at higher frequencies related to insertion loss, isolation quality, and power handling capabilities. Efficient solutions for compact TR systems that balance performance, space, and energy efficiency are in high demand, driven by the trend toward smaller IoT devices that are compatible with semiconductor technology [197]. New designs have emerged to meet this demand, focusing on minimizing size and maximizing power utilization. Researchers are exploring novel materials and advanced semiconductor techniques to create more effective and space-saving TR switches for IoT applications in efficient communication and power management by allowing switching between data transmission and reception using a single antenna [197, 206, 207]. Despite these advancements, current TR switches in IoT networks still face various challenges. Many IoT devices rely on batteries or energy harvesting, making power consumption management a key concern [215, 216]. Achieving low insertion loss with high isolation between transmit and receive paths in compact designs poses a significant challenge. Balancing power consumption, performance, and size often involve trade-offs that complicate the quest for universal solutions. Therefore, developing small yet energy-efficient TR switches tailored for IoT applications remains a significant hurdle. Another critical concern is power efficiency, particularly for battery-operated and energy-harvesting IoT devices, where optimizing switching speed, insertion loss, and power usage demands careful attention.

A passive narrowband T/R switch is presented at 175 MHz in [214]. The switch consists of a transmission line of length λ/4 and anti-parallel PIN diodes to allow signal flow in both directions, as shown in Fig. 2.29. A wideband passive T/R switch is required for compact IoT applications for fast and cost-effective switching without any biasing voltage to realize a power-efficient design, along with high isolation and compactness.

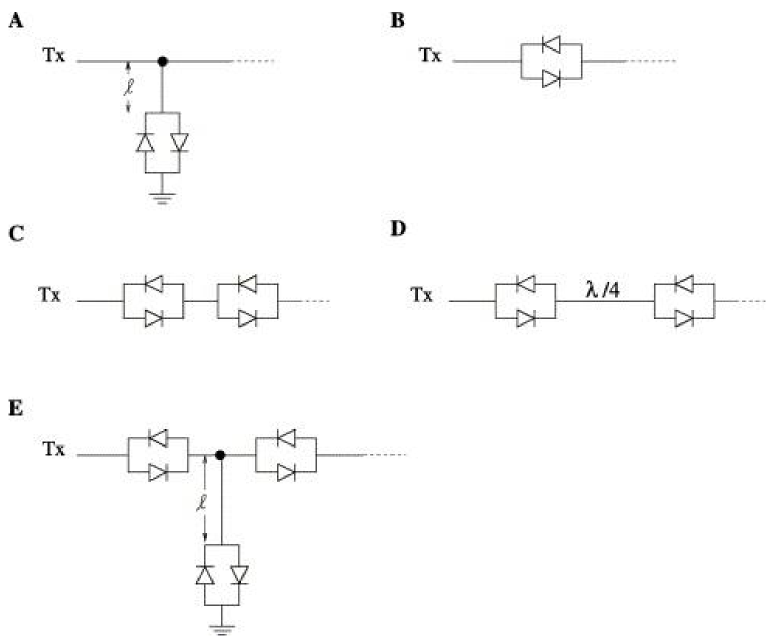

Fig. 2.29. Passive T/R switch using λ/4 transmission lines [214].

Metamaterials have been extensively investigated in designing various microwave circuits, including couplers [217, 218], RF limiters [219], power dividers [191, 220], and filters [105, 192, 221, 222]. A microwave sensor and multi-function structure are presented for precision agriculture in [111, 199]. Both structures comprise a microstrip transmission line and a metamaterial-based complementary spiral resonator to achieve miniaturization. In [220], a 1:4 3-dB power divider is presented using nonlinear metamaterial-based coupled-line couplers at 2.1 GHz with 116 mm width. The structure features four ports and three coupled lines, resulting in a compact circuit. Additionally, a directional coupler utilizing a pair of Split-Ring Resonators (SRRs) for forward and backward coupling is introduced [218], operating at a center frequency of 7.5 GHz with two variable diodes to switch between the coupling modes. However, biasing voltage is needed to achieve switching between forward and backward couplings.

A dual-band T/R calibration switch using metamaterial Composite Right/Left-Handed (CRLH) transmission lines is demonstrated with BiCMOS technology at 24.5 and 35 GHz. Although the design offers good isolation, it suffers from high insertion losses. An RF power limiter based on nonlinear metamaterials, as presented in [219], employs complementary electric inductive resonators and PIN diodes, resonating at 2.5 GHz with limited isolation between low and high power levels.

A Metamaterial-based Interdigital Microstrip Capacitor (MIMC) is a multi-finger recursive microstrip structure that introduces series capacitance into a microstrip transmission line [223] . In recent years, MIMCs have been widely employed in the design and development of various RF and microwave devices. MIMCs can be configured as two- or four-port networks, enabling the creation of microwave components such as oscillators and filters. The characteristics of MIMCs have been explored by She *et al.* and Dib *et al.* in [224, 225]. These capacitors have been utilized in the design of microwave couplers and power dividers s [226-228]. For example, an MIMC-based coupled line coupler operating at 3 GHz is presented in [228]. This coupler uses MIMC to achieve coupling from the input port (port 1) to the forward coupled port (port 4). However, the coupler only provides forward coupling, with no output or backward coupling signal.

2.5 Current Challenges

While there have been many advancements in soil moisture sensor technology, significant challenges remain in achieving miniaturization, high sensitivity, resilience to environmental conditions, and seamless integration with communication technology. Increasing the number of bands, miniaturizing the sensor size, making the design simple and cost-effective, and integrating sensor and antenna to realize joint sensing and communication are general open gaps that have been adopted in this research. Achieving a compact design, high sensitivity, and integration with the antenna to realize both sensing and communication is a significant contribution. Some potential challenges are discussed in the following subsections to achieve a compact yet highly sensitive sensor.

2.5.1 Compactness

The theory behind low-frequency RF signals suggests that they can penetrate deeper into the soil compared to high-frequency signals [128, 229]. Consequently, a low-frequency FDR based sensor can provide measurements of soil moisture at greater depths making it a more suitable choice for practical environments where moisture distribution is uneven across the soil. In high-temperature conditions surface soil moisture tends to be lower while deeper soil layers retain higher moisture levels. Therefore, a high-frequency sensor may produce inaccurate measurements due to its limited signal penetration depth. However, using lower resonance frequencies for the signal necessitates larger sensor structures which can pose handling challenges.

In practical environments, soil moisture is non-homogeneous, with higher water presence beneath the surface than at the surface. To accurately measure VWC in the soil, a sensor with a high penetration depth is necessary. Consequently, a soil moisture sensor with a lower resonance frequency is suitable for precise VWC measurements. However low resonance frequencies necessitate larger structures, posing challenges in handling and installing them in large-scale environments.

2.5.2 Multiband vs. Single Band Sensor

Designing a miniaturized low-frequency sensor to cover a large volume of soil with high sensitivity and accuracy is highly challenging. Various single band FDR based sensors have been presented in the literature for permittivity measurements [19, 20, 185, 195]. Environmental factors such as temperature changes and fluctuations in soil composition can significantly affect the frequency variation in FDR-based sensors. Although the design of single-band sensors is simple, the effect of frequency variations is pronounced reducing flexibility in calibration and resulting in inaccurate measurements.

On the other hand, a multi-band sensor exhibits varying responses at different frequency bands, and a dual-band sensor leverages this diversity, enhancing the accuracy of soil moisture measurement in heterogeneous soil. Environmental effects can be mitigated by measuring the response at different frequencies. Hence a dual-band sensor can provide better accuracy than a single-band sensor in soil moisture measurements.

2.5.3 Moisture Measurements Using FDR-Based Sensor

FDR is widely recognized as the method for measuring soil moisture levels using sensors. This approach determines VWC by studying variations in the frequency response. The simplicity and capability of FDR to assess VWC at various depths make it a versatile tool for agricultural and environmental purposes. The popularity of FDR based sensors stems from their effectiveness in delivering moisture measurements at varying soil depths. However, an important aspect of FDR involves the incorporation of a Vector Network Analyzer (VNA). The VNA plays a role in identifying and analyzing frequency changes resulting from fluctuations in soil moisture levels.

Relying on a VNA can pose challenges, as it increases complexity and costs during the measurement process in field environments, where ease of use and portability are essential.

2.5.4 Integration of WPT, Sensing and Communication

In an autonomous WSN, a continuous power supply is required to avoid battery replacement issues. WPT can be integrated with the WSN to remove battery dependency and make the system autonomous. Sensors collect soil data, which is then transmitted using an integrated antenna. RF switches are useful to enable multi-service operations with the same hardware. These devices play an important role in directing and regulating RF signals within the system as shown in Fig. 2.27. However, these RF switches need DC biasing to change their state from OFF state to ON to change the characteristics of the RF structure which can cause latency in the operation. A passive smart switch is an alternative solution to integrate WPT, sensing and communication, which can change its state automatically without the requirement of any external DC biasing.

2.6 Conclusion

This chapter gives a comprehensive overview of the progress in RFEH/WPT, reconfigurable antennas and their techniques, miniaturized antenna methods, soil moisture sensors for precision agriculture, and T/R switches. The first section explains WPT and RFEH theory, detailing individual components like antennas, matching networks, and rectifiers. It further discusses various antenna types, including wideband and reconfigurable designs, and size miniaturization techniques. Comparisons across different antenna types and switching mechanisms are also presented. The second section delves into the critical role of soil moisture sensors in smart agriculture, highlighting their importance for efficient water management and optimized crop growth. It explores the latest advancements in sensor technology, including the integration of metamaterials to achieve significant size reduction while maintaining high performance. The section also examines various sensor designs, focusing on their sensitivity, accuracy, and resilience in varying environmental conditions. Finally, it reviews diverse sensing techniques, RFID tags for moisture measurement, types of microwave sensors, and current limitations. The last section covers the importance and limitations of current T/R switches in these systems, discussing how they enable seamless integration of sensing and communication functions.

3

3 Miniaturized Patch Rectennas for WPT

(One Journal and one Conference paper have been produced based on this chapter's materials, "Efficient Pixelated Rectenna Design Methodology Using Binary Particle Swarm Optimization for WPT Applications" and "Miniaturized Patch Rectenna Using 3-Turn Complementary Spiral Resonator for Wireless Power Transfer,")

3.1 Introduction

Whilst recent advances in modern sensors and Internet-of-Things (IoT) devices continue to expand, the dependence of their operation on batteries remains a significant weakness, which has imposed restrictions on the range and duration of operation of these portable devices. Energy-autonomous or self-powered devices are poised to become indispensable components within future wireless sensor networks (WSNs) [29, 230]. Wireless Power Transfer (WPT) or Radio Frequency Energy Harvesting (RFEH) is a sustainable, cost-effective, green energy solution to provide an alternative energy source for portable IoT devices and sensors [132, 133, 231], as illustrated in Fig. 3.1. This interest is fueled by several factors: the capability to transmit and receive wireless power over long distances [232], the penetration of radio frequency (RF) signals into various structures such as walls, bridges, and tunnels, the potential for harvesting RF energy throughout the day, the on-demand availability of power through dedicated RF power sources (e.g., WPT), and the growing utilization of IoT devices, wireless sensor nodes, and low-power electronics [105, 222, 233, 234]. One of the pivotal components in wireless power transmission systems is the rectenna, responsible for receiving RF waves and converting them into Direct Current (DC) voltage.

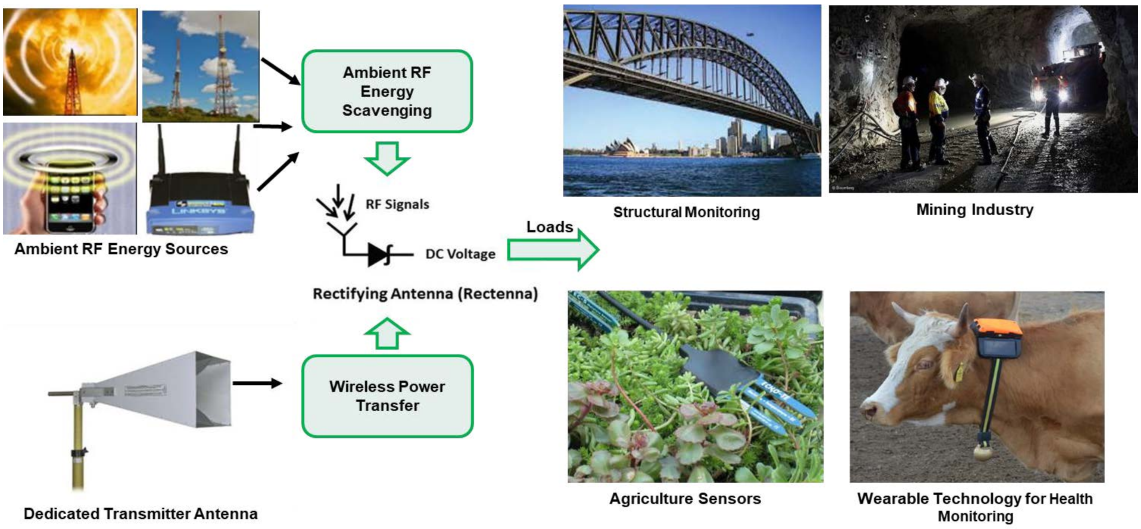

Fig. 3.1. Sustainable energy solution for portable IoT devices.

In this chapter, a rectenna is proposed for the WPT applications at 1.8 GHz. A miniaturized patch antenna is designed and fabricated to receive RF power with an impedance bandwidth of 1.69−2.0 GHz (GSM1800). Miniaturization is achieved by inserting a 3-Turns Complementary Spiral Resonator (3-CSR) structure on the ground plane. A rectifier circuit is also designed for RF-to-DC conversion at −10 dBm (100 μW) input power.

Another pixelated rectenna is presented in this chapter for low-power applications operating at 2.5 GHz. The proposed rectenna uses a pixelated patch antenna that accounts for the complex impedance of the matching network during the design phase. This eliminates the need for an additional matching network in the rectenna structure. An RF-to-DC efficiency of 38% has been achieved at a low input power level of 0 dBm and the maximum efficiency is 64% at +12 dBm.

3.2 Miniaturized Patch Rectenna

This section presents antenna design in the following subsections:

3.2.1 Antenna Design

The top and bottom sides of the proposed miniaturized antenna are shown in Fig. 3.2(a) and Fig. 3.2(b), respectively. The antenna is designed using Computer Simulation Technology Microwave

Studio (CST MWS) on a commercially available FR-4 substrate with a dielectric constant of 4.3, a loss tangent of 0.025, and a thickness of 1.6 mm. The objective was to design a miniaturized patch antenna operating at 1.8 GHz within the GSM1800 band. A conventional patch antenna was initially designed on an FR-4 substrate at this frequency. To achieve size reduction, a 3-Turns Complementary Spiral Resonator (3-CSR) structure was embedded in the ground plane, resulting in an impedance bandwidth from 1.69 GHz to 2.0 GHz. The final design dimensions are 26 × 24.5 mm^2. For comparison, a conventional patch antenna at the center frequency of the proposed antenna is also simulated with patch dimensions of 39.5 mm × 51.6 mm. The size reduction achieved is evident when comparing the conventional patch antenna with the proposed design at 1.8 GHz. Additionally, the impedance bandwidth increased from 43 MHz (1.78−1.83 GHz) to 310 MHz (1.69−2.0 GHz). The inductance and capacitance values can be calculated using the following equations [184].

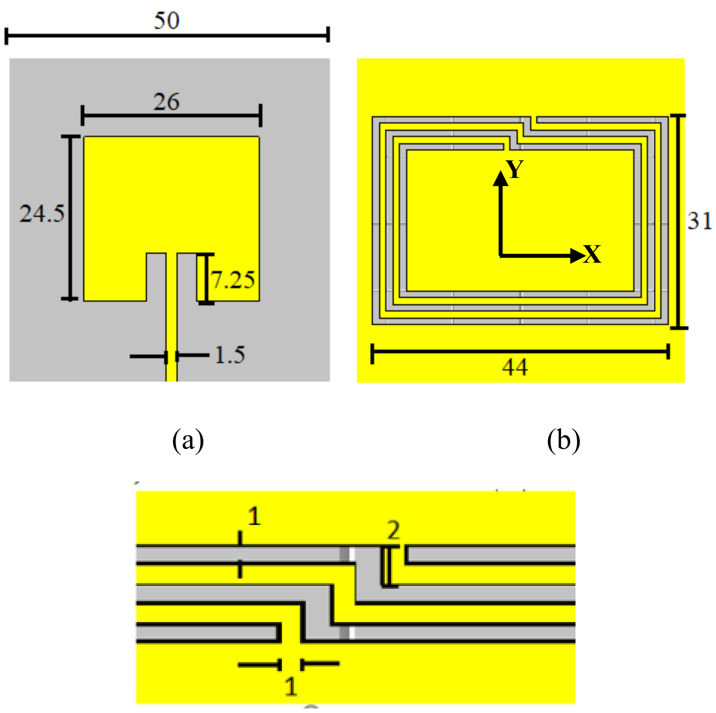

Fig. 3.2. Geometry of the proposed patch antenna. (a) top view, (b) bottom view, (c) magnified view, (all units are in milli-meters).

$$L_0 = 2(L+W)L_{pul} \quad (3.1) \qquad L_s = \frac{L_0}{3} \quad (3.2)$$

$$C_s = 4\frac{\varepsilon_0}{\mu_0}L_s \quad (3.3) \qquad f_0 = \frac{1}{2\pi\sqrt{L_s C_s}} \quad (3.4)$$

Where L_{pul} is the per-unit-length inductance, L and W are the length and width of the 3-CSR rectangle, respectively.

3.2.2 Rectifier Design

After successfully miniaturizing the patch antenna, a simple rectifier circuit is designed and simulated in Keysight Advanced Design System (ADS) to create a rectenna. The rectifier converts the received RF power to Direct Current (DC) voltage, which can be used to drive a low-power load. Low turn-on voltage Schottky diode (HSMS2850) is used as a rectification device, and Large Signal S-Parameters (LSSP) simulation is performed in ADS software with −20 to 0 dBm input power and a load of 10 kΩ. In order to match the impedance of the rectifier with the antenna impedance of 50 Ω, a matching circuit is designed and simulated at 1.8 GHz for −10 dBm. The matching circuit, along with the rectification device is shown in Fig. 3.3. The input impedance of the rectifier is Z_{in} = 62.414–j550.479 Ω at 1.8 GHz for −10 dBm as shown in Fig. 3.4. The rectified output DC voltage and RF-to-DC conversion efficiency are shown in Fig. 3.5. As can be seen, the output DC voltage at –10 dBm is 0.732 V and increases with the input power. The maximum efficiency is 53.6% at –10 dBm, which is a suitable input power range for WPT and ambient RFEH applications.

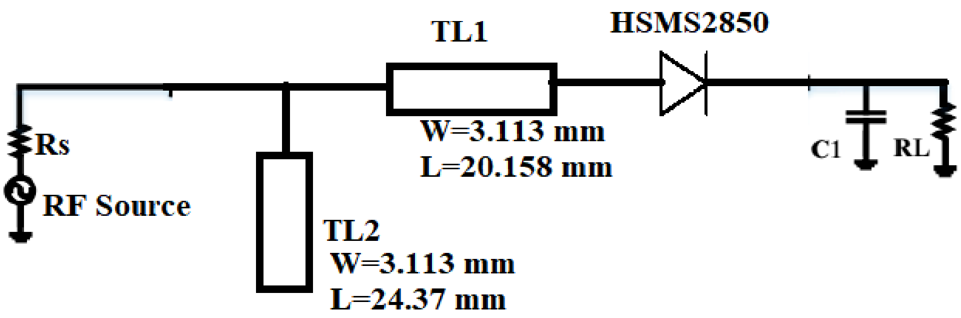

Fig. 3.3. Rectifier circuit with matching network at 1.8 GHz.

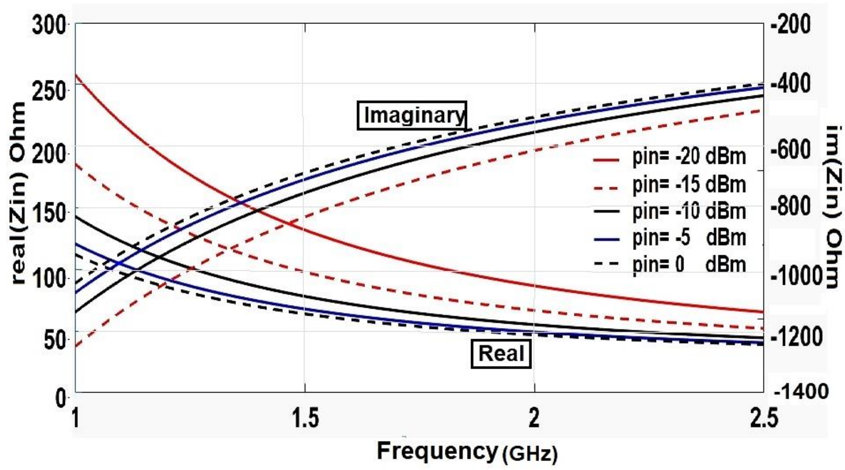

Fig. 3.4. Simulated input impedance of the rectifier over −20 to 0 dBm input power with a 5 dB step.

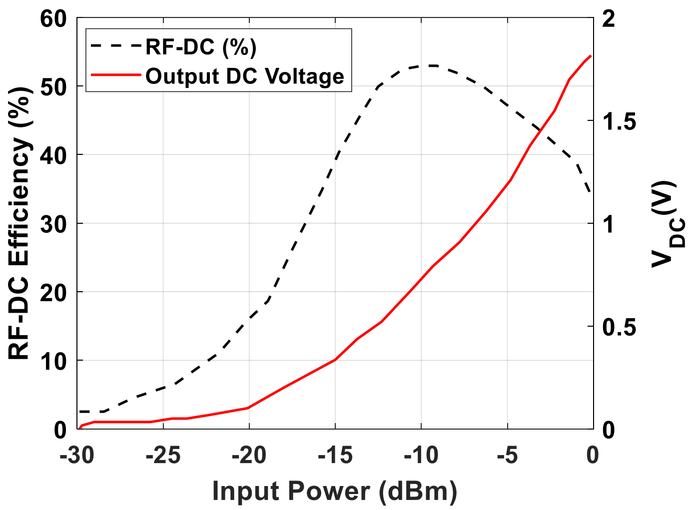

Fig. 3.5. Rectenna simulation results: output DC voltage and RF-to-DC rectification efficiency.

3.2.3 Results and Discussion

The proposed antenna is designed using CST MWS and fabricated on an FR-4 substrate with dimensions of 50 × 50 mm^2 to validate simulation results. A fabricated prototype is shown in Fig. 3.6. Simulated and measured reflection coefficients of the proposed miniaturized antenna are in close agreement. The proposed structure demonstrates good impedance matching at 1.8 GHz. The reflection coefficient of the proposed structure is also compared with the conventional patch in Fig. 3.7. It is clear that two advantages have been achieved using a 3-CSR structure: (1) the proposed antenna has resonance frequency as of conventional antenna, but with smaller dimensions of the patch, and (2) the impedance bandwidth has been increased. The simulated and measured two-dimensional (2D) radiation pattern of the antenna in the *xz* and *yz* planes are shown in Fig. 3.8(a) and Fig. 3.8(b), respectively.

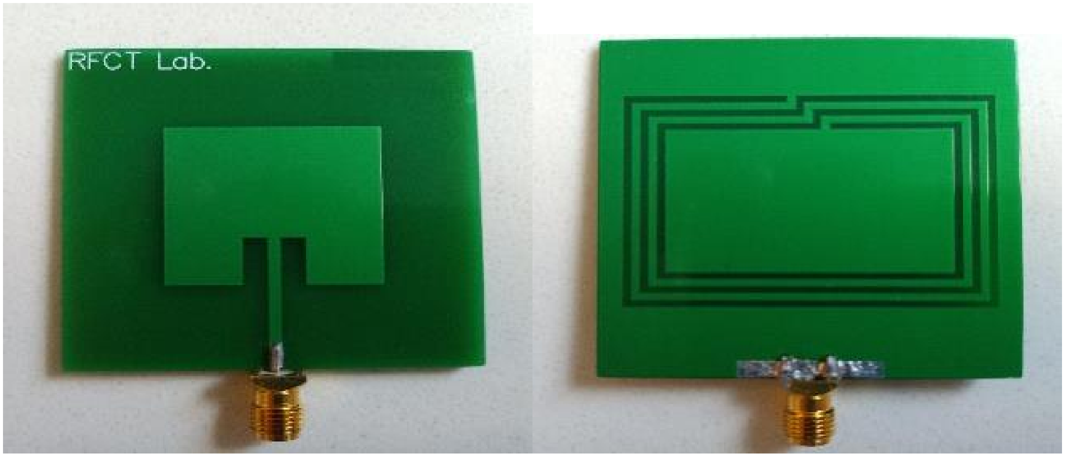

Fig. 3.6. Fabricated prototype of the proposed antenna.

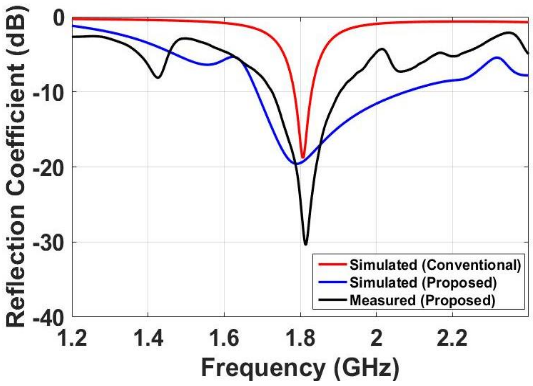

Fig. 3.7. Simulated and measured reflection coefficients of the antenna.

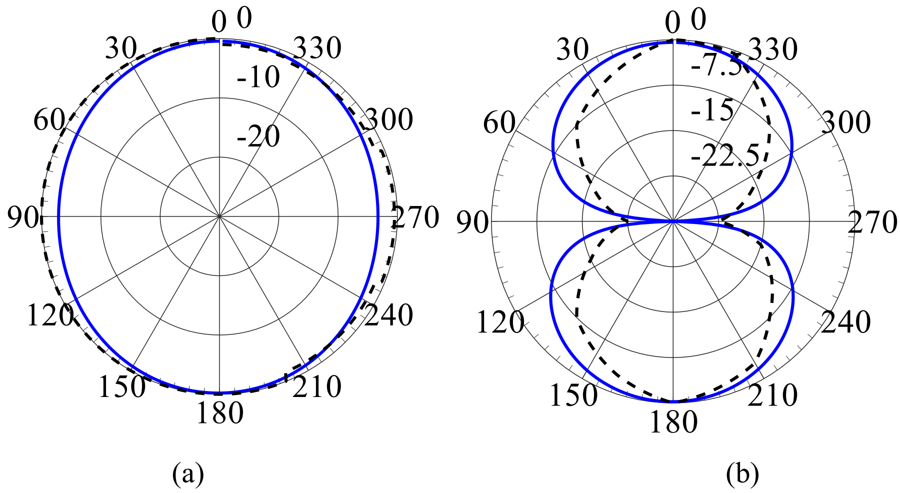

Fig. 3.8. Simulated (solid) and measured (dotted) two-dimensional (2D) radiation patterns of the proposed antenna at 1.8 GHz, (a) *xz-plane*, (b) *yz-plane*.

The bi-directional pattern in the *yz* plane is due to the 3-CSR structure at the bottom side of the substrate. Measured and simulated results are in close agreement as shown in Fig. 3.8, and a maximum measured gain of 2.5 dBi has been achieved. The goal of achieving a compact antenna size does indeed introduce a trade-off with antenna gain. While higher gain is critical for improving RF-to-DC conversion efficiency, smaller antennas inherently tend to have lower gain due to their limited surface area and design constraints. Despite this, the compact size was prioritized to meet the system's space and integration requirements. The gain can be improved by using multilayer structures, which allow for more efficient use of space and can enhance the antenna's performance. By incorporating additional layers, it is possible to increase the effective aperture without significantly increasing the antenna's overall size. This approach can help address the trade-off between compactness and gain, leading to better RF-to-DC conversion efficiency. A comparison of published antennas with this work is provided in TABLE 3.1. It is clear that the proposed antenna is smaller and has a larger bandwidth compared to previously published papers.

TABLE 3.1 COMPARISON OF THE PROPOSED STRUCTURE WITH PUBLISHED ANTENNAS.

Ref	Frequency Band (GHz)	Antenna Size (mm^2)
[235]	5.725–5.875	18.6 × 4.2 ($0.24\lambda_g \times 0.052\lambda_g$)
[236]	0.87–1.05	127 × 127 ($0.195\lambda_g \times 0.195\lambda_g$)
[237]	2.1, 2.4–2.48, 3.3 – 3.8	72 × 68 ($0.29\lambda_g \times 0.23\lambda_g$)
[238]	1.8–2.2	190 × 100 ($0.825\lambda_g \times 0.44\lambda_g$)
Proposed Antenna	1.69–2.0	24.5 × 26 ($0.127\lambda_g \times 0.09\lambda_g$)

3.3 Pixelated Rectenna for WPT

Optimization algorithms play a crucial role in antenna design, especially when balancing factors like gain, operating frequency, input impedance, and size constraints—challenges that are difficult to address using conventional equations alone. By employing optimization algorithms, antenna designers can effectively navigate this intricate design landscape, enabling the creation of highly efficient and compact antennas tailored to specific requirements across various applications [31]. Intelligent optimization algorithms have supplanted traditional electromagnetic simulator optimization techniques in antenna design due to their superior effectiveness in achieving desired outcomes. Optimization algorithms enable the exploration of numerous alternative geometric configurations to design viable structures and meet design constraints. An exemplary instance is Particle Swarm Optimization (PSO) [31, 239-241]. The core PSO approach encounters challenges related to premature convergence and struggles with high-dimensional or multi-objective problems. Researchers have been actively enhancing the performance of standard PSO [242, 243] to mitigate these issues. Additionally, the application of PSO can be extended to antenna designs with discrete shapes using binary PSO (BPSO). Pixelated antenna design offers flexibility in achieving diverse design objectives, such as single or multiband compact antenna design with enhanced BPSO [38, 243]. The utilization of novel patch shapes for receiving antennas can significantly enhance RF energy harvesting or WPT capabilities, as they are not constrained by the conventional length and width limitations of patch rectennas. Fig. 3.9 depicts the design concepts of the conventional and proposed pixelated rectennas.

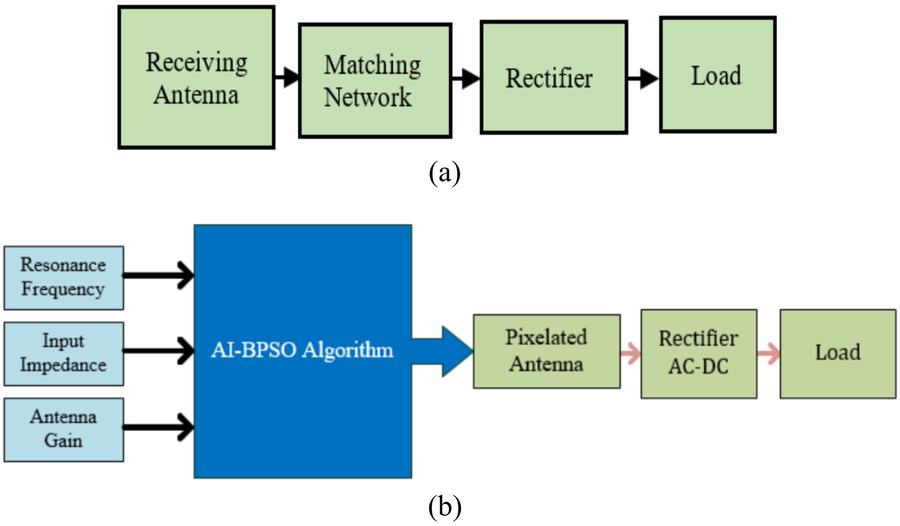

Fig. 3.9. (a) Conventional rectenna configuration with matching network, (b) proposed rectenna design without external matching network.

In conventional rectennas, a matching network sits between the rectifier antenna to match the input impedance of the rectifier to 50 Ω. However, utilizing a binary particle swarm optimization algorithm, the proposed rectenna optimizes the pixelated configuration of the receiving antenna. The antenna is designed with a conjugate-matched input impedance to the rectifier diode. Eliminating the need for a matching network ensures matching across the desired operating frequency. A pixelated antenna is designed to prove the concept with an input impedance at 2.5 GHz. The proposed pixelated rectenna achieved 38% RF-to-DC efficiency at a low input power level of 0 dBm and a maximum efficiency of 64% at +12 dBm. The pixelated design makes the antenna more compact and eliminates the need for a matching network, simplifying the design and reducing additional losses. However, the gain of the antenna is reduced, which in turn lowers its RF-to-DC conversion efficiency. The proposed pixelated rectenna includes two main parts: a pixelated antenna and a rectifier. This section presents the design procedure of the rectifier and proposed pixelated antenna using the BPSO algorithm.

3.3.1 Rectenna Design

A rectifier is developed in Advance Design System 2020 (ADS) utilizing a voltage doubler configuration with two rectifiers (SMS7621). The rectification circuit is meticulously optimized, considering the values of parasitic components of capacitors and the rectifier package. The optimized rectification circuit is shown in Fig. 3.10, where Z_A is the input impedance of the receiving antenna, L_P is parasitic inductance, and C_P is parasitic capacitance. The input impedance (Z_{in}) of the rectifier is analyzed across a range of –30 to +10 dBm input power using Large Signal S-Parameters (LSSP) and Harmonic Balance (HB) simulations in ADS. The input impedance of the rectifier for various power levels is depicted in Fig. 3.11. At 2.5 GHz and an input power of 0 dBm, the optimized rectifier exhibits an input impedance of $0.3 - 37j\Omega$. This Z_{in} value is then utilized to devise a pixel configuration to match the input impedance with the rectifier.

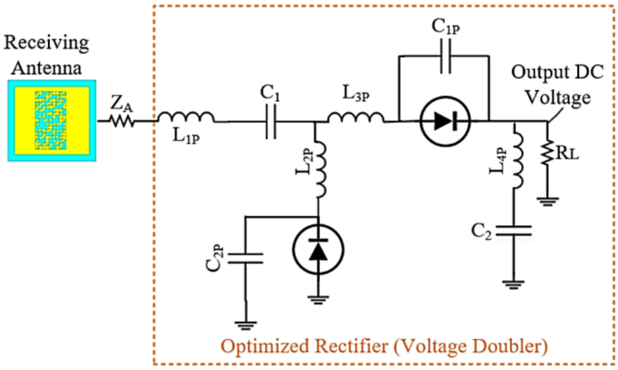

Fig. 3.10. Proposed rectenna (rectifying antenna).

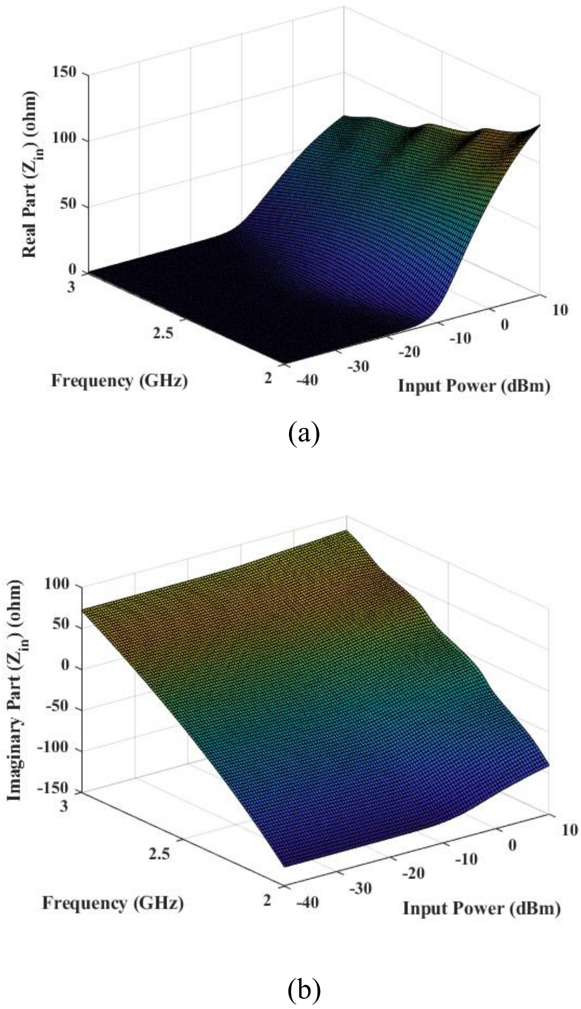

Fig. 3.11. Input impedance of the optimized rectifier, (a) real part, (b) imaginary part.

3.3.2 Pixelated Antenna Design

The proposed pixelated antenna is designed using Rogers RO4003C with a thickness of 1.524 mm and dimensions of L_S X W_S. The design of the receiving antenna commences with a rectangular slot antenna, wherein the slot of the patch antenna is segmented into a triangular array. This triangular array can be substituted with triangular slots or conductors (pixels). Fig. 3.12 illustrates the proposed antenna alongside the division of the geometry into different pixels. The design dimensions are outlined in TABLE 3.2. The optimization objective is to attain optimal positions for these triangular pixels. This enables the antenna to resonate at the desired operating frequency with a specific complex impedance value rather than the standard 50Ω port impedance. This optimization process employs a binary particle swarm optimization algorithm with a V-shaped transfer function [243].

MATLAB is utilized to implement the algorithm, with the simulation module connected to Computer Simulation Technology Microwave Studio (CST MWS) for antenna simulation. The following steps are undertaken for the design and optimization of the receiving antenna.

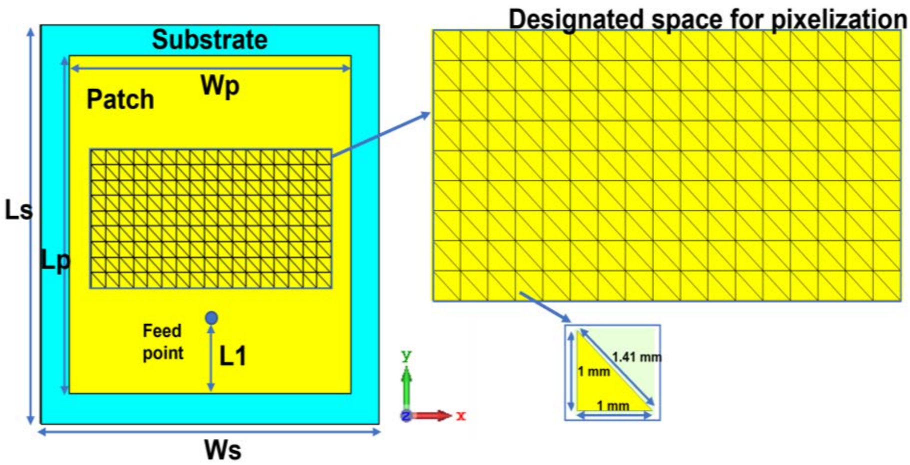

Fig. 3.12. Design of the pixelated receiving antenna, design dimension and layout.

TABLE 3.2. ANTENNA DESIGN DIMENSIONS.

Parameter	L_s	L_p	L_1	W_s	W_p
Value (mm)	26	22	5.2	24	20

Step 1: The electromagnetic simulation tool receives the initial random population generated by the BPSO algorithm via MATLAB. The population's bit values (0 or 1) are then utilized to create the pixel configuration of the antenna.

Step 2: The antenna is simulated, and the resulting reflection coefficient at the desired frequency is fed back to the algorithm to compute the cost function, as depicted in (3.5). This function optimizes the antenna's reflection coefficient value at 2.5 GHz. Subsequently, the algorithm updates the personal best and global best values.

$$\text{Cost function } f = \min(S11_{f_r=2.5\ GHz}) \tag{3.5}$$

Step 3: The velocity value and new position of particles are calculated according to the transfer function [243]. These new particle positions are then employed to generate updated pixel configurations for the antenna. This iterative process continues until a termination criterion is met, such as reaching the maximum number of iterations.

Step 4: After completing all iterations, the global best score from the cost function is determined, and the best position of particles is identified. This best position subsequently defines the optimal pixel configuration for the antenna.

Fig. 3.13 illustrates the convergence curve of the optimization process. The optimization was conducted over 60 iterations, with convergence achieved by the 50th iteration. The final design of the pixelated antenna, with triangular pixels, is presented in Fig. 3.14. The designed rectifier is connected to the pixelated antenna at the ground plane.

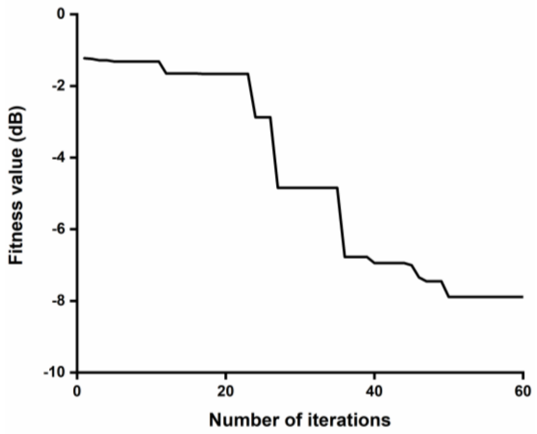

Fig. 3.13. Convergence curve of the antenna design optimization procedure.

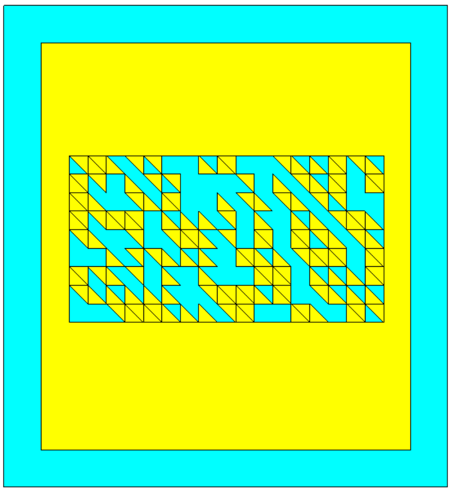

Fig. 3.14. Final pixelated layout of the receiving antenna.

3.3.3 Results and Discussion

The proposed pixelated antenna is designed and simulated in CST MWS 2022 to prove the concept. Moreover, the designed antenna is fabricated using Rogers RO4003C substrate with a thickness of 1.524 mm to validate its performance of WPT, as depicted in Fig. 3.15.

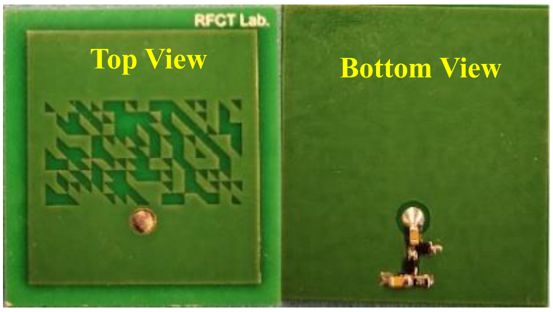

Fig. 3.15. Fabricated prototype of the proposed rectenna.

Fig. 3.16 displays the proposed receiving antenna's return loss and input impedance, optimized with a specific pixel configuration. The antenna does not exhibit matching at any frequency within the 2 to 3 GHz range. However, it achieves an operating band at 2.5 GHz with its input impedance conjugately matched with the rectifier.

The simulated radiation pattern of the proposed antenna is depicted in Fig. 3.17 at 2.5 GHz. The antenna demonstrates an omnidirectional radiation pattern, achieving a maximum simulated gain of 0 dBi with a radiation efficiency of 48%. The relatively low radiation efficiency is attributed to the compact size of the antenna.

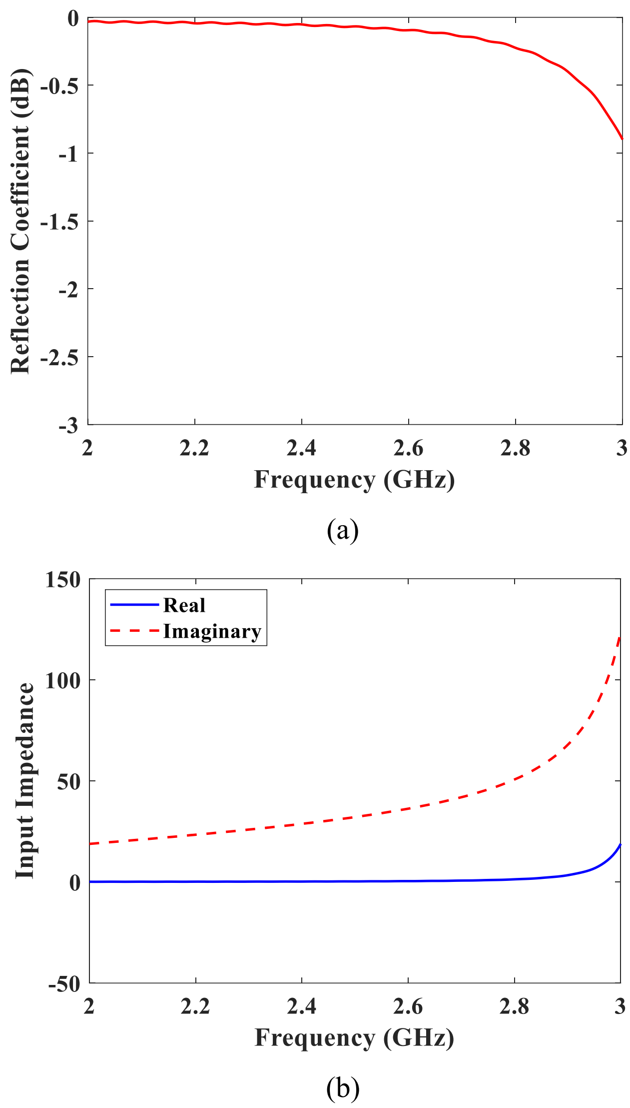

Fig. 3.16. (a) Reflection coefficient of the antenna, (b) input impedance of the antenna.

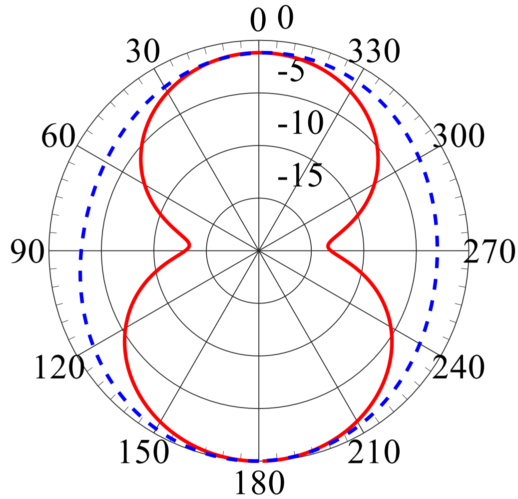

Fig. 3.17. Radiation pattern of the proposed antenna at 2.5 GHz, (solid line represents *xz-plane* and dashed line represents *yz-plane*).

An experimental setup, illustrated in Fig. 3.18, is employed to assess the performance of the proposed rectenna. Utilizing a vector signal generator (R&S SMW200A) as the RF power source, supplemented by a ZHL-15W-422 amplifier to mitigate path loss, ensures accurate power at the antenna's input. A log-periodic antenna with 4.5 dBi gain serves as the transmitter, while the rectenna is positioned at the receiver, maintaining a distance of 30 cm.

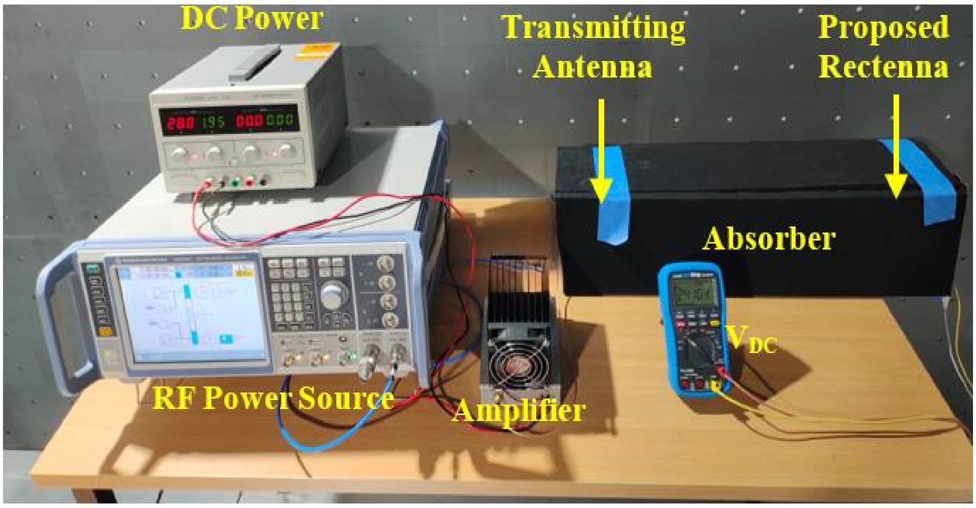

Fig. 3.18. Measurement setup to evaluate the performance of the proposed rectenna.

Fig. 3.19 showcases the results of the proposed rectenna's output DC voltage, RF-to-DC conversion efficiency, and output DC power plotted against input RF power at 2.5 GHz. An efficiency of 38% is attained at a low power level of 0 dBm, with the maximum efficiency peaking at 64% at +12 dBm.

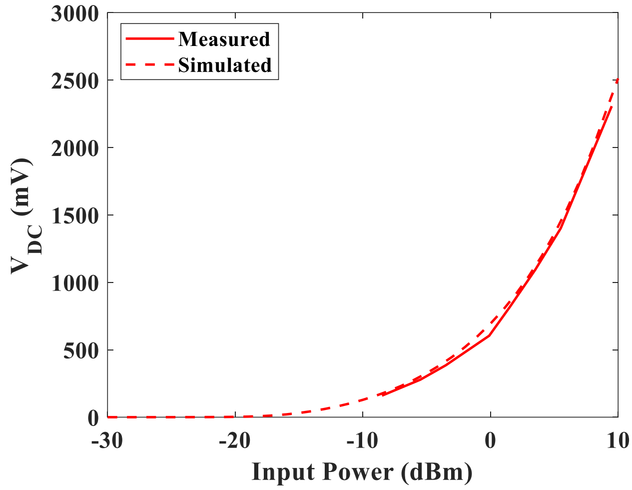

(a)

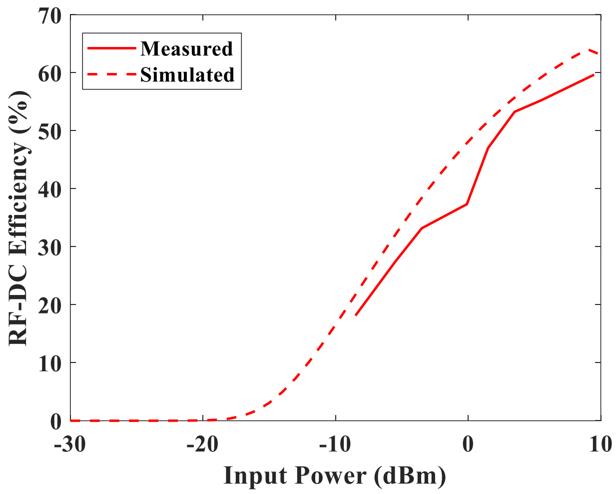

(b)

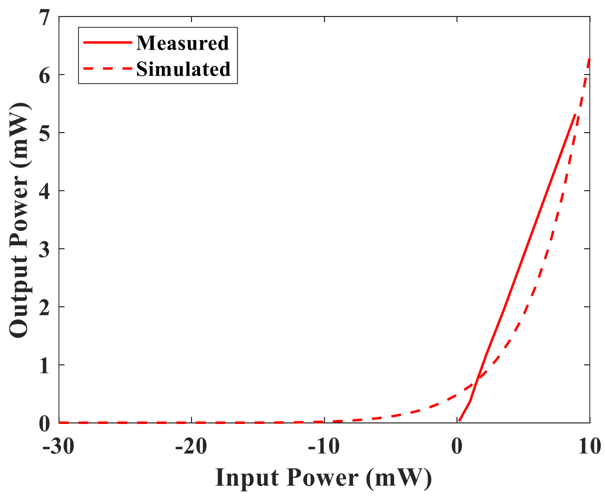

(c)

Fig. 3.19. Performance of the proposed rectenna: (a) output DC voltage vs. input power, (b) RF-to-DC conversion efficiency vs. input power, and (c) output power vs. input power.

3.4 Joint Team Work on WPT

I also collaborated with my supervisors on developing a rectenna for Capacitive Coupling WPT (CCWPT), resulting in the publication of a research paper titled, “Ultra-Fast and Efficient Design Method Using Deep Learning for Capacitive Coupling WPT Systems”.

3.4.1 Capacitive Coupling WPT (CCWPT)

This research proposes a deep learning neural network-based AI-inspired quick and effective design technique for pixelated microstrip structures for Capacitive Coupling WPT (CCWPT). By employing iterative optimization methods (Genetic, BPSO, etc.) instead of EM software (CST, HFSS, etc.) to determine the S-parameter of the pixelated structure in each iteration, this method allows for an automated and flexible design process. Compared to the CST-based technique, the AI-based iterative method design process on CPU is around 3629 times faster, and clearly uses less computational and human resources. The corresponding |S21| and the projected resonance frequency's MAE error are 0.18 dB and 110 MHz, respectively. An AI-based method is used to design and fabricate two parallel pixelated microstrip plates to demonstrate the concept. The success of the suggested approach is demonstrated by the attained consistency of the resonance frequency and |S21| value with the intended aim. Additionally, this approach can be used to develop additional microwave devices and does not require any advanced knowledge of electromagnetic theory.

A rectifier circuit is designed, built, and tested to implement the entire CWPT system. At an input power of –5 dBm, the rectifier's measured efficiency is 50%. The rectifier was then connected to the pixelated parallel plates, and the output DC voltage was measured in relation to the input RF power.

3.5 Conclusion

This chapter introduces patch and pixelated rectenna systems for WPT. A miniaturized linearly polarized patch antenna with a bi-directional radiation pattern is developed at 1.8 GHz. A rectifier circuit, along with the matching network, is designed and simulated at −10 dBm input power for RF-to-DC conversion. The rectenna achieved an efficiency of 53.6% at −10 dBm. The proposed antenna is fabricated, and the measurement results are in good agreement with the simulation.

A pixelated rectenna is also developed at 2.5 GHz using the BPSO algorithm. The proposed rectenna comprises a pixelated receiving antenna that has been meticulously optimized to match the complex impedance of the rectifier diode, thus obviating the necessity for a separate matching circuit. The optimization process is facilitated using a BPSO algorithm. Achieving an efficiency of 37% at a low input power level of 0 dBm and 64% at +12 dBm, the proposed rectenna emerges as a promising candidate for RFEH and WPT applications in low-power devices.

4

4 Multi-Service Structure

(One journal article has been published and one conference paper has been submitted based on the materials in this chapter, "Compact Multiservice Antenna for Sensing and Communication Using Reconfigurable Complementary Spiral Resonator," and "Miniaturized Frequency Reconfigurable Patch Rectenna for Wireless Power Transfer")

4.1 Introduction

In smart agriculture, a system must integrate both sensing and communication capabilities to monitor soil parameters accurately. In this chapter, a multi-function structure is presented, focusing on joint communication and sensing for smart agriculture. The proposed compact multi-service antenna (MSA) operates in three modes. In mode-1, MSA operates as a dual-band joint communication and sensing antenna (JCASA), where the first band is used for sensing and the second band is used for communication. Meanwhile, in mode-2 and mode-3, the MSA acts as a conventional dual-band and single-band antenna.

Various modifications have been made to the conventional patch antenna to achieve the proposed MSA. For instance, two additional patches and two slots are inserted to achieve dual resonance. This modification generated two resonances at 3.2 GHz and 3.4 GHz. In order to reduce the antenna size, a 3-CSR is inserted in the ground plane of the modified patch. To change the resonance frequency of the 3-CSR structure, two PIN diodes are integrated with the 3-CSR to realize a frequency-reconfigurable antenna. Finally, a biasing network for the diodes is designed at the top side of the same substrate, which is connected to the diodes using vias. The biasing circuit for each diode consists of two RF chokes (L1 and L2) and two resistors (R1 and R2).

4.2 Multi-Service Antenna Design, Theory and Methodology

The proposed structure features a compact design with simple planar geometry, yet the resonance frequency of the unloaded sensor is 960 MHz. This characteristic makes it suitable for covering a large Volume Under Test (VUT) of soil. Additionally, the structure includes a communication unit in mode-1 to transfer information to the base station. Besides joint sensing and communication, the integration of 3-CSR and PIN diodes results in a multi-service structure that can function as a standard single/dual band antenna. The proposed structure is adaptive and suitable to measure the permittivity of any Material Under Test (MUT) within the range of 1–20. The design procedure, along with the equivalent model of MSA, is presented as a design guide for future work in joint communication and sensing systems.

The design, theory, and methodology of the proposed MSA are discussed in the following subsections:

4.2.1 Multi-service Antenna Design

The antenna is designed on Rogers RO4003C substrate ($\varepsilon_r = 3.55,\ tan\delta = 0.0027, h = 1.524$ mm) with dimensions of $50 \times 50\ \text{mm}^2$. Initially, a conventional patch antenna was designed and simulated at 3.2 GHz in CST MWS 2019, as shown in Fig. 4.1. Fig. 4.1(a) represents the patch antenna with an inset feed, and Fig. 4.1(b) represents the ground plane of the patch antenna. Two additional patches and two slots are inserted to achieve dual resonance, as shown in Fig. 4.1(c). This modification generated two resonances at 3.2 GHz and 3.4 GHz. In order to reduce the antenna size, a 3-CSR is inserted in the ground plane of the modified patch, as shown in Fig. 4.1(d). The reflection coefficients of the antenna at different stages are shown in Fig. 4.2.

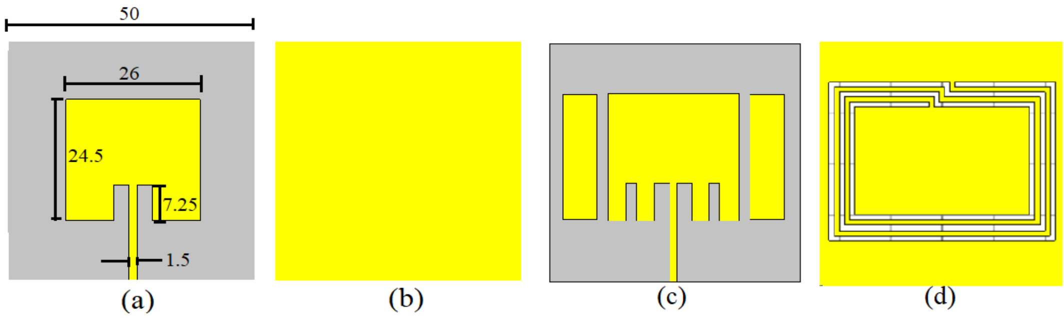

Fig. 4.1. Design steps: (a) top view of the conventional patch, (b) bottom view of the conventional patch, (c) top view of the modified patch, and (d) ground plane of miniaturized patch in (c).

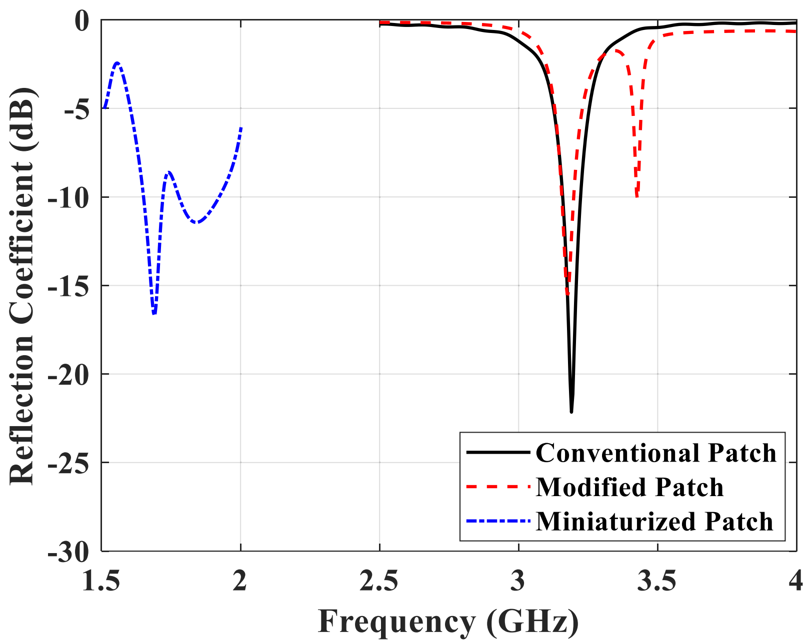

Fig. 4.2. Simulated reflection coefficients of the patch antenna.

The resonance frequency of a resonator depends on the equivalent values of inductance (L) and capacitance (C), and by changing these values, the resonance frequency can be switched. To change the resonance frequency of the 3-CSR structure, two PIN diodes (D1 and D2) are integrated with the 3-CSR to realize a three-turn reconfigurable complementary spiral resonator (3-RCSR). The optimal position for the PIN diodes is selected based on a parametric analysis of the frequency response, which is conducted by placing the diodes at various positions. The integration of the PIN diodes results in the achievement of another operating band at 0.96 GHz, which further reduces the antenna size. The diode model Skyworks SMP1322 is utilized for the design. The simulation and measurement results of the proposed MSA for different diode states are discussed Section 4.3.

The geometry of the proposed MSA is shown in Fig. 4.3, where Fig. 4.3(a) represents the modified patch and Fig. 4.3(b) represents the 3-RCSR. The diode is modeled as a lumped circuit in ON and OFF states. Different antenna applications are achieved by varying the state of the diodes, i.e., 00, 10, and 11. Direct Current (DC) blockers are introduced to prevent the shorting of the positive and negative pins of the DC voltage, as shown in Fig. 4.3(b). A biasing network is also designed for the diodes at the top side of the same substrate, which is connected to the diodes using vias. The biasing circuit for each diode consists of two RF chokes (L_1 and L_2) and two resistors (R_1 and R_2).

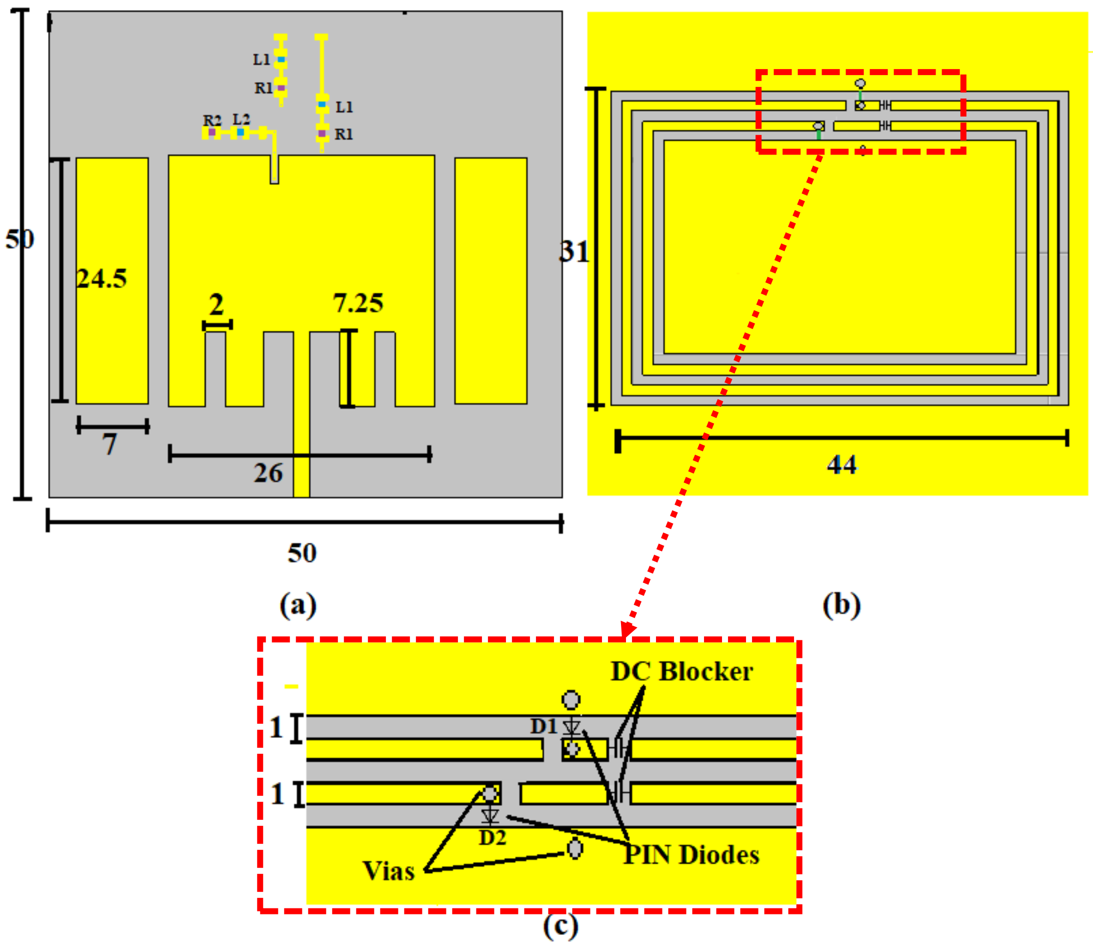

Fig. 4.3. Geometry of the proposed antenna, (a) top view, (b) bottom view, (c) magnified view (all dimensions are in mm).

4.2.2 MSA Theory

The equivalent circuit (EC) of a 3-CSR consists of an LC circuit with two series inductors (L_0) and a capacitor (C_c), as shown in Fig. 4.4(a) [244]. The ECs of the PIN diode are shown in Fig. 4.4(b) and Fig. 4.4(c). The resonance frequency can be calculated using (4.1), where L_C is the equivalent inductance. The value of inductance (L_0) depends on the line impedance (Z_0), effective permittivity (ε_{re}), speed of light (c), and line length (l) as represented by (4.2) [223]. The values of Z_0 and ε_{re} can be calculated using (4.3)-(4.6) [245]. The lengths (l) of the smallest and largest turns are 125 mm and 140 mm, respectively. The width (W) of a single turn is 1 mm, and the thickness of the substrate (h) is 1.524 mm.

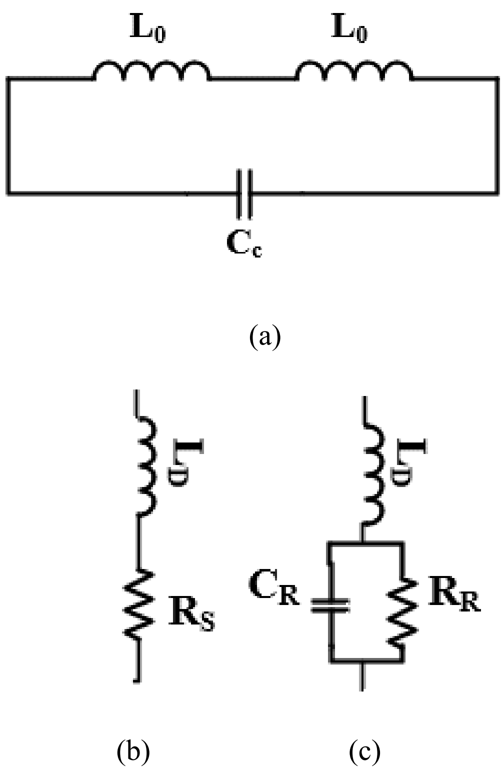

Fig. 4.4 Equivalent circuits, (a) 3-CSR, (b) PIN diode in ON state, and (c) PIN diode in OFF state.

$$f = \frac{1}{2\pi\sqrt{L_c C_c}} \tag{4.1}$$

$$L_0 = \frac{Z_0\sqrt{\varepsilon_{re}}}{c} l \tag{4.2}$$

$W < h$:

$$\varepsilon_{re} = \frac{\varepsilon_r + 1}{2} + \frac{\varepsilon_r + 1}{2}\left[\frac{1}{\sqrt{1 + 12\left(\frac{h}{W}\right)}} + 0.04\left(1 - \frac{W}{h}\right)^2\right] \tag{4.3}$$

$$Z_0 = \frac{60}{\varepsilon_{re}} log_2\left[8\frac{h}{W} + 0.25\frac{W}{h}\right] \tag{4.4}$$

$W > h$:

$$\varepsilon_{re} = \frac{\varepsilon_r + 1}{2} + \frac{\varepsilon_r + 1}{2}\left[\frac{1}{\sqrt{1 + 12\left(\frac{h}{W}\right)}}\right] \tag{4.5}$$

$$Z_0 = \frac{120\pi}{\varepsilon_{re}\left[\frac{W}{h} + 1.393 + \frac{2}{3}log_2\left(\frac{W}{h} + 1.444\right)\right]} \tag{4.6}$$

The integration of the PIN diodes with the 3-CSR modifies the behavior of the LC circuit, resulting in a dual-band (0.96/1.55 GHz) structure. The modified EC of the 3-RCSR is shown in Fig. 4.5 and the diodes can be modeled as lumped components, as shown in Fig. 4.4. Different states of the diodes modify the values of inductance and capacitance and change the resonance frequency according to (4.1).

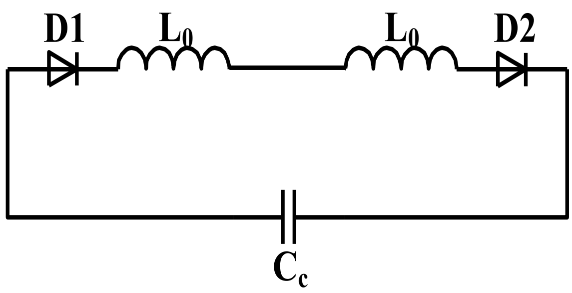

Fig. 4.5. Equivalent circuit of the 3-RCSR.

Patch antenna at the top side of the substrate can be considered as a right-handed transmission line of physical length, consisting of series inductances and parallel capacitances. A complete circuit of the patch antenna with 3-RCSR is shown in Fig. 4.6, where the inductance of the patch can be calculated using (4.2).

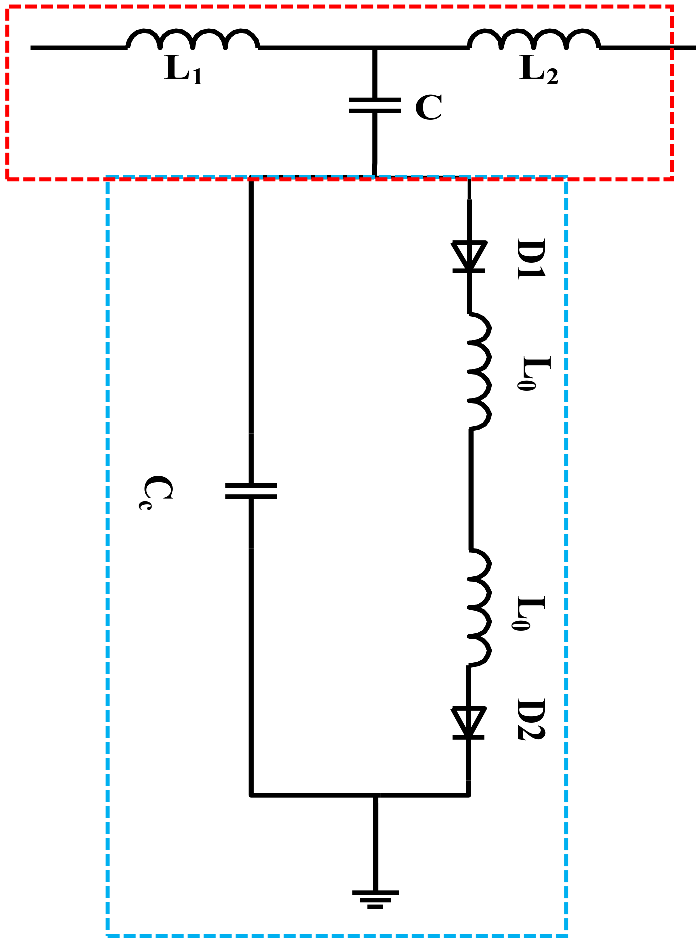

Fig. 4.6. Equivalent circuit of the proposed JCASA.

4.2.3 Working Principle of the JCASA

In RFID tags, a radio frequency (RF) reader sends a continuous wave (CW) interrogating signal for a short period of time. This interrogating signal is captured by the tag which encodes the signal and sends it back to the reader.

The proposed MSA structure has a frequency-tuneable feature, and the antenna mode can be changed by switching the state of the PIN diodes. A specified state of the diodes can be used to select a required mode of the antenna. In the JCASA mode, the proposed structure is used for sensing as well as communication. A high-level block diagram of the proposed system is shown in Fig. 4.7. A CW signal is sent from an oscillator to the JCASA using a 3-port circulator, and the reflected signal is measured using a power detector. The real value of permittivity is measured using Frequency Domain Reflectometry (FDR). For the experimental purpose, the oscillator and power detector are replaced by a vector network analyzer, as shown in Fig. 4.7(b). The frequency shift in the first band is analyzed to measure the permittivity [16, 186], while the second band is used to transfer the information to the base station. In general, the proposed JCASA can sense the permittivity of any object from 1 to 20.

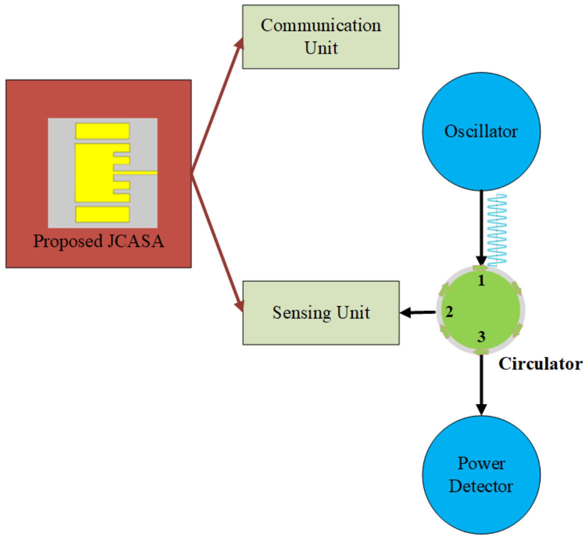

(a)

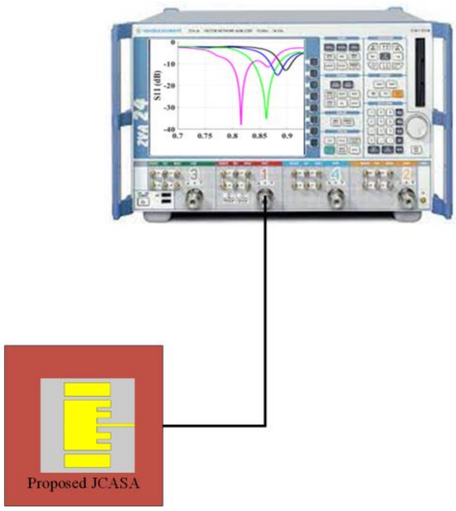

(b)

Fig. 4.7. Working principle of the proposed JCASA, (a) practical setup, (b) experimental lab setup.

4.3 Results and Discussion

To demonstrate the performance of the MSA, the proposed antenna is simulated, designed, and optimized using CST MWS 2019. The MSA is fabricated on a Rogers RO4003C substrate, and the fabricated prototype is shown in Fig. 4.8.

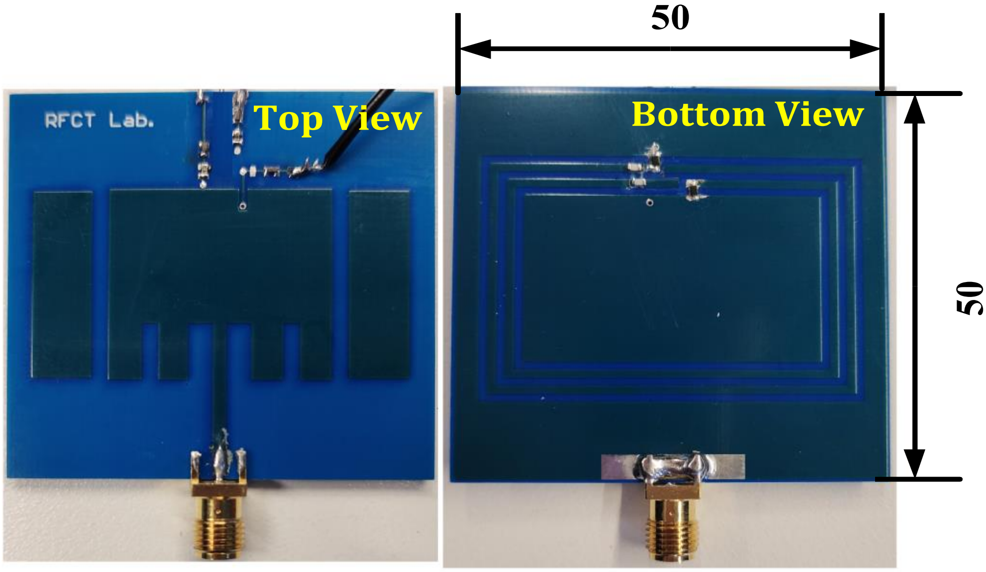

(a) (b)

Fig. 4.8. Fabricated prototype of the antenna on Rogers substrate ($\varepsilon_r = 3.55,\ tan\delta = 0.0027, h =$ 1.524 mm) with dimensions of 50×50 mm^2.

4.3.1 Simulated and Measured MSA Results for Different States

The proposed MSA can be used as a JCASA, dual-band antenna, and single-band antenna. Simulated and measured reflection coefficients of the antenna for different diode states are shown in Fig. 4.9. Both simulation and measurement results represent similar behavior, indicating the validity of the structure. Measured impedance bandwidths of the MSA are summarized in TABLE 4.1 against each state. The proposed MSA operates in three modes by switching the state of the PIN diodes. For the '00' case (mode-1), the antenna operates as dual-band JCASA, where the first band (0.95–0.97 GHz) is used for sensing to measure the permittivity (1–20) and the second band (1.53–1.56 GHz) is allocated to communication. For '10' and '11', the proposed antenna operates in dual-band mode (0.91–0.94 GHz, 1.54–1.57 GHz) and single-band mode (0.83–0.85 GHz), respectively. The proposed MSA operates passively and does not require any biasing voltage for JCASA mode. However, a CW oscillator is necessary to generate a frequency sweep for the sensor, with a power meter used to measure the received data. A low-power radio module, such as the Semtech SX1276, which has a maximum power consumption of 400 mW, can be employed to transmit the frequency sweep signal in the range of 0.8 to 1 GHz.

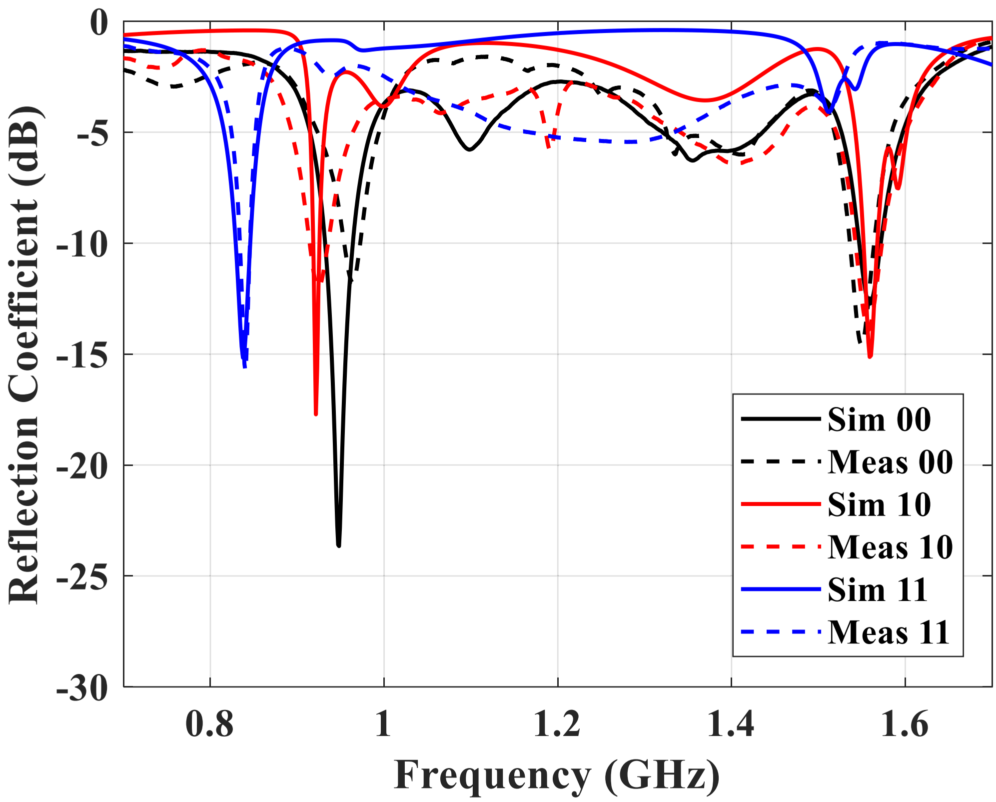

Fig. 4.9. Simulated and measured reflection coefficients of the antenna for different states.

TABLE 4.1. MEASURED BANDWIDTHS OF THE PROPOSED MSA FOR DIFFERENT STATES.

Mode	Diodes State (D2, D1)	Band 1 (GHz)	Band 2 (GHz)	Application
1	00	0.95–0.97	1.53–1.56	Dual-band JCASA
2	10	0.91–0.94	1.54–1.57	Dual-band antenna
3	11	0.83–0.85	–	Single-band antenna

To validate the antenna performance, two-dimensional (2D) gain patterns of the MSA are measured in the *xz* and *yz* planes. Simulated and measured 2D patterns at 0.93 GHz and 1.55 GHz are shown in Fig. 4.10. The proposed antenna shows an omnidirectional radiation pattern, and the maximum gain of the unloaded antenna is 1.5 dBi at 1.55 GHz. The Co-pol traces follow the same pattern in both the simulated and measured results. However, in Cross-pol, the measured results show power levels 10 dB lower than the Co-pol, while the simulated results also indicate power levels below -35 dB. This discrepancy in Cross-pol power levels is attributed to the reactive components of the antenna structure, which introduce polarization impurities. The resonance frequency in the communication band changes from 1.54 to 1.35 GHz with the Volumetric Water Content (VWC) of the soil. The radiation pattern of the antenna remains omnidirectional at all resonances, but a higher VWC reduces the antenna gain.

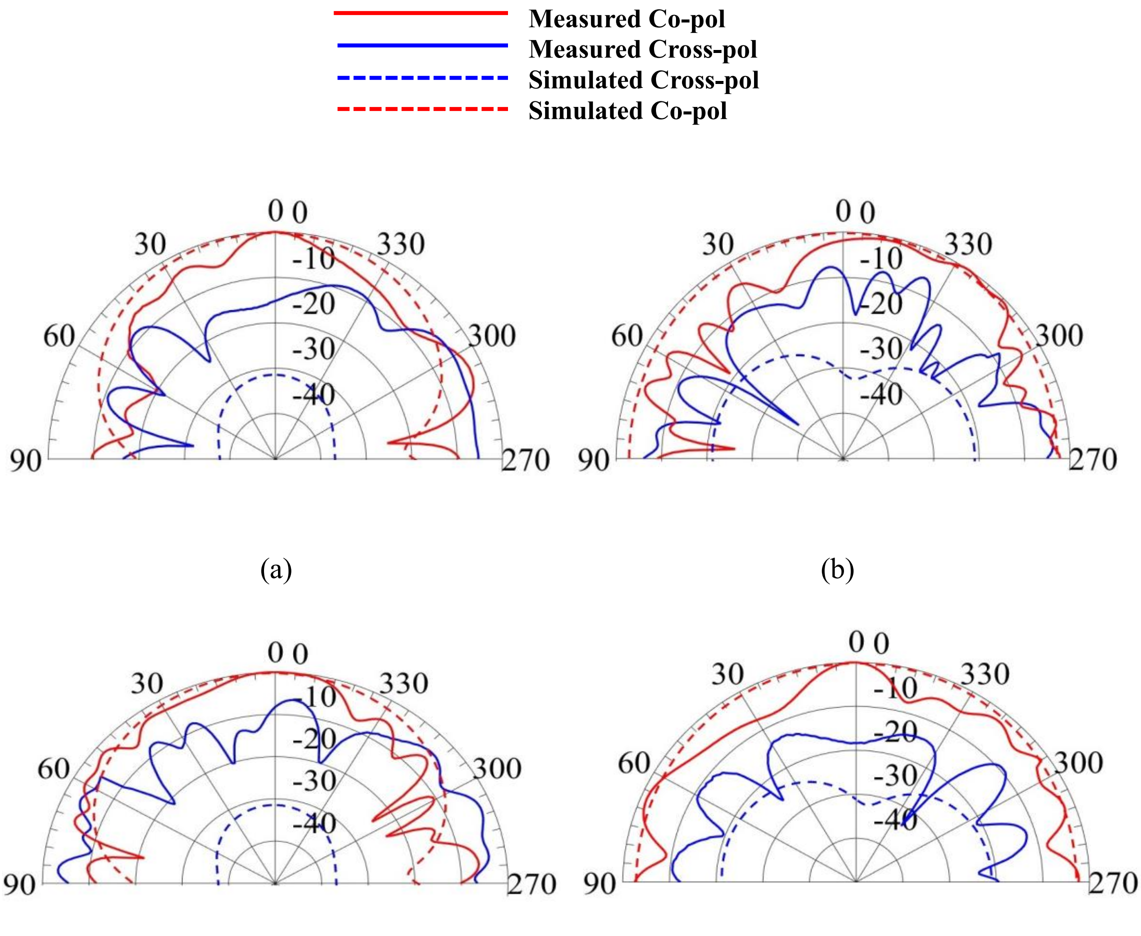

(a) (b)

(c) (d)

Fig. 4.10. Simulated and measured 2D gain patterns of the proposed antenna, (a) *yz* at 0.93 GHz, (b) *xz* at 0.93 GHz, (c) *yz* at 1.55 GHz, and (d) *xz* at 1.55 GHz.

4.3.2 Sensing Unit Results and Analysis

To verify the performance of the sensing unit in mode-1 for the ‘00’ case, an experimental setup shown in Fig. 4.11 was used to examine the fabricated prototype. The frequency responses of the structure are measured using a calibrated 4-port vector network analyzer (VNA-ZVA40) with different VWC levels in the soil. The VNA is calibrated using an SOLT (short, open, load and through) standard before executing the frequency responses. The proposed structure is placed in a non-metallic holder and the sensor depth is adjusted to 3 mm from the top of the holder to put soil on the structure. A sweep of RF signals is sent to the sensor and the reflected signal is measured in terms of S11 to estimate the permittivity of the MUT. The permittivity of the soil increases with the VWC and the value of permittivity (ε'_r) changes from 3.7 to 19 with a VWC range of 0 to 30 %, as shown in TABLE 4.2. Fig. 4.12 shows the simulated and measured results for the ‘00’ case. As the water content in the soil increases, the permittivity of the soil also increases, resulting in a significant leftward shift in the resonance frequency. Hence, the frequency responses from 0.93 GHz to 0.83 GHz reflect the change in permittivity from 3.7 (VWC=0 %) to 19 (VWC=30 %). The communication band also varies due to different VWCs, however, it stays within the L-band for communication.

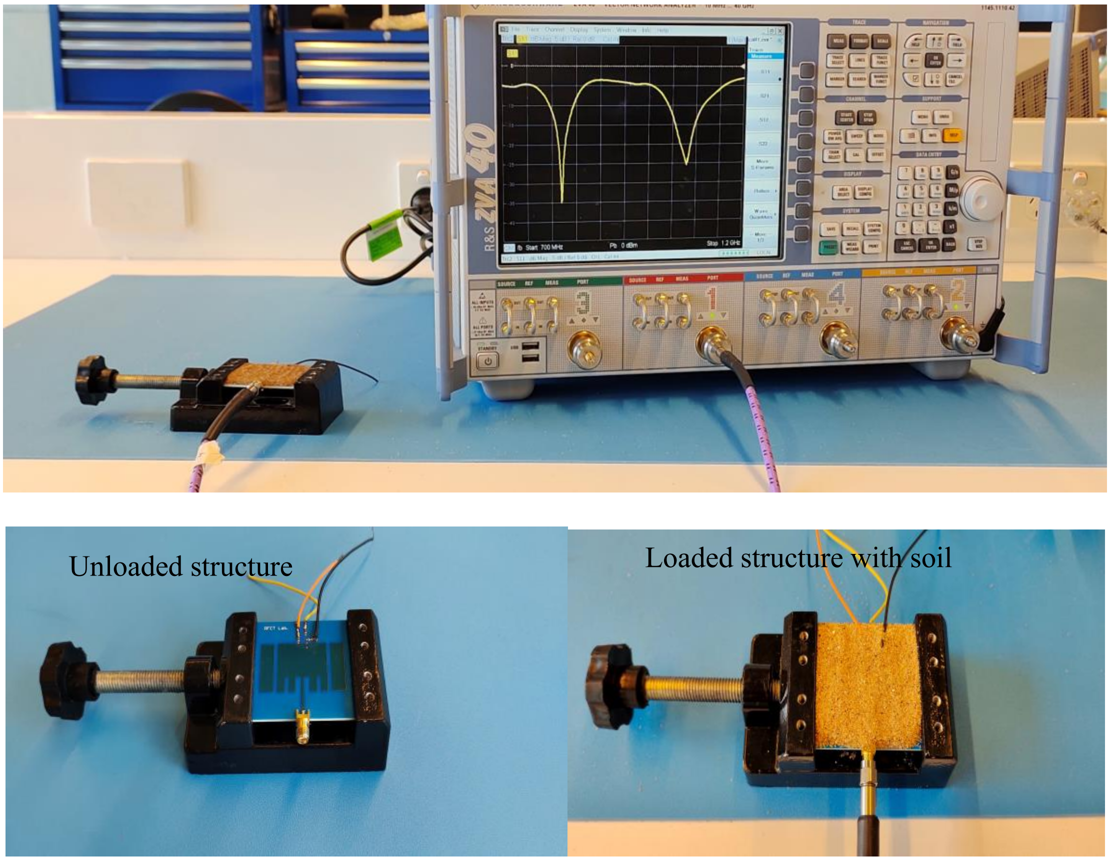

Fig. 4.11. Measurement setup for the sensing unit with unloaded and loaded structure.

TABLE 4.2. REAL PERMITTIVITY OF SOIL FOR DIFFERENT VWCS [229].

VWC (%)	0	5	10	15	20	25	30
ε'_r	3.7	4.4	5.8	8.4	12	15.8	19

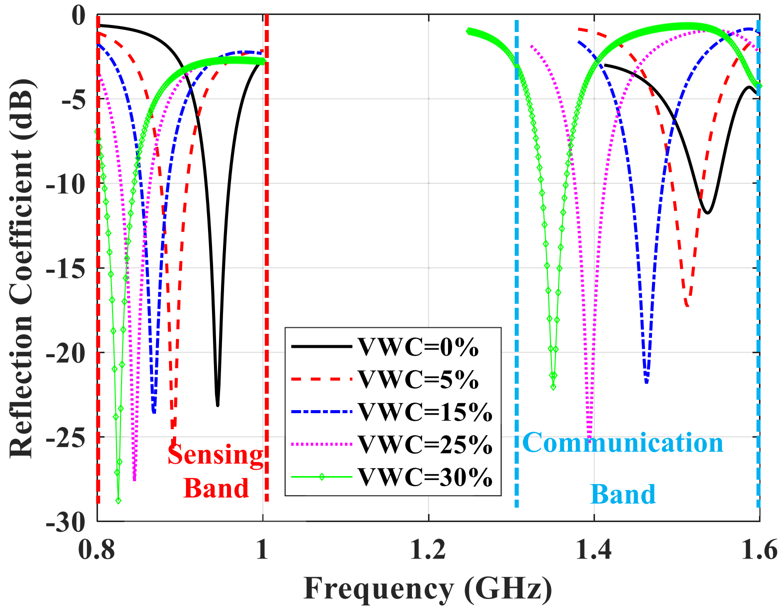

(a)

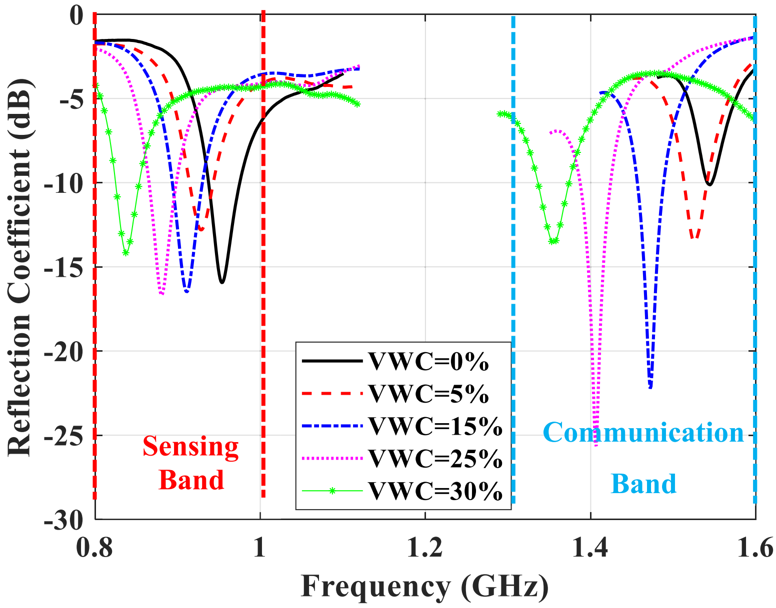

(b)

Fig. 4.12. Frequency response of MSA in mode-1 (JCASA) for different values of VWC, (a) simulated, (b) measured.

To assess the accuracy of the sensor, the measurement is repeated four times, and a maximum variation of 10 MHz is observed in the frequency responses. A linear relationship between ε'_r and frequency shift (Δf) for different tests is shown in Fig. 4.13. The frequency shift (Δf) is calculated using (4.7),

$$\Delta f = f_m - f_u \tag{4.7}$$

where f_u is the resonance frequency of the unloaded structure and f_m is the resonance frequency of the structure with the material under test (MUT).

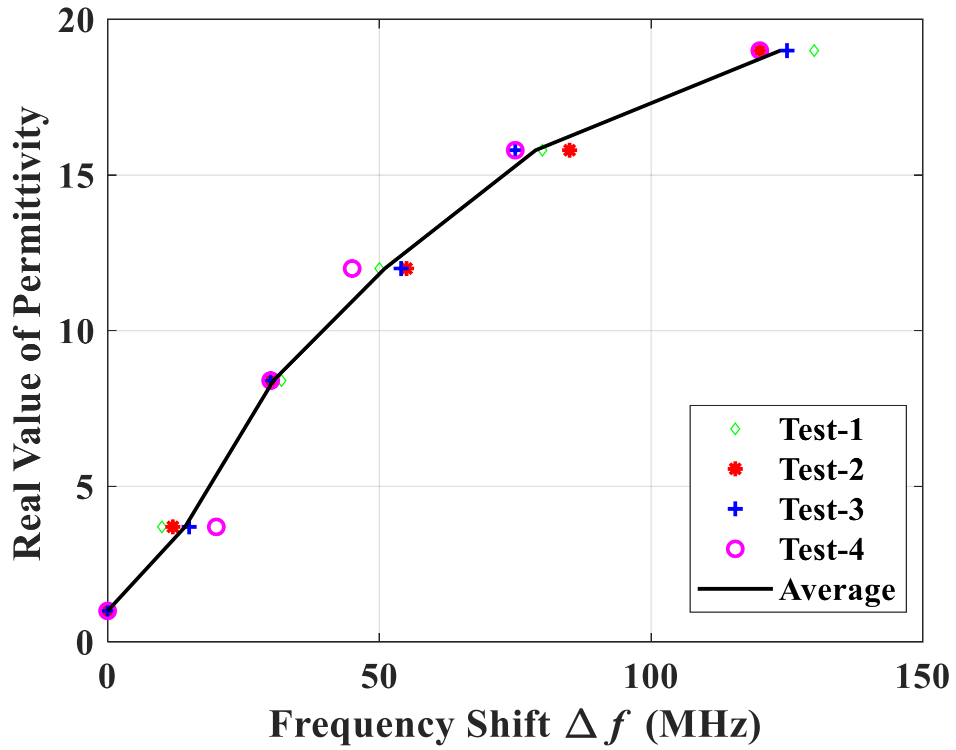

Fig. 4.13. Real value of permittivity (ε'_r) vs. frequency shift (Δf).

The sensing ability of the MSA is also examined in mode-2 and mode-3 to validate the simulation results. Measured frequency responses of the antenna for '10' (mode-2) and '11' (mode-3) are shown in Fig. 4.14. In modes-2 and -3, the frequency shift does not exhibit a consistent pattern across varying VWC levels, as shown in Fig. 4.14. Therefore, these modes are not suitable for soil moisture sensing.

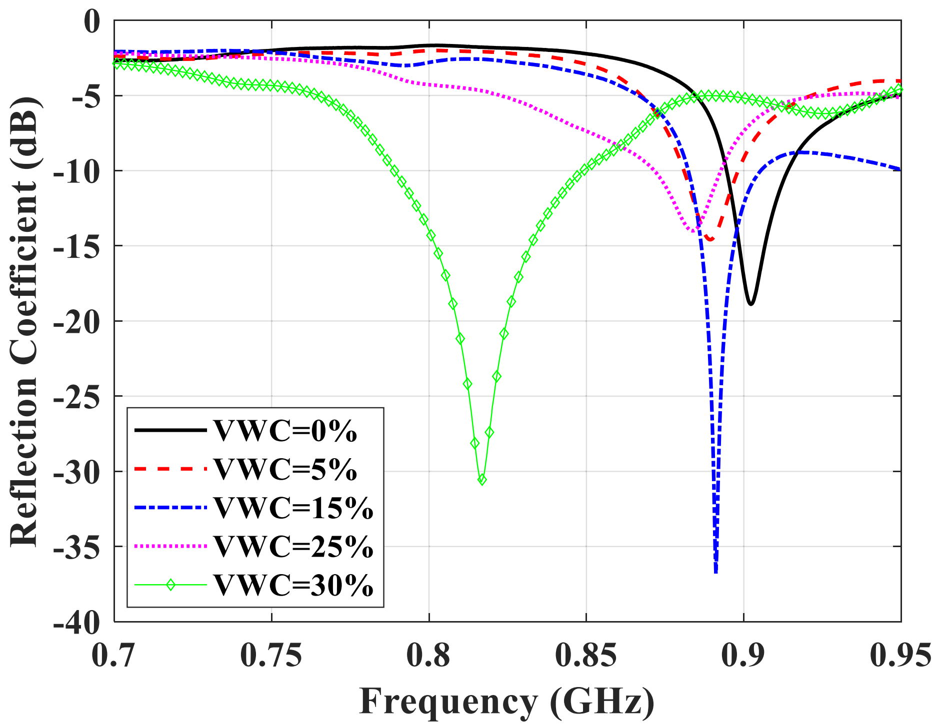

(a)

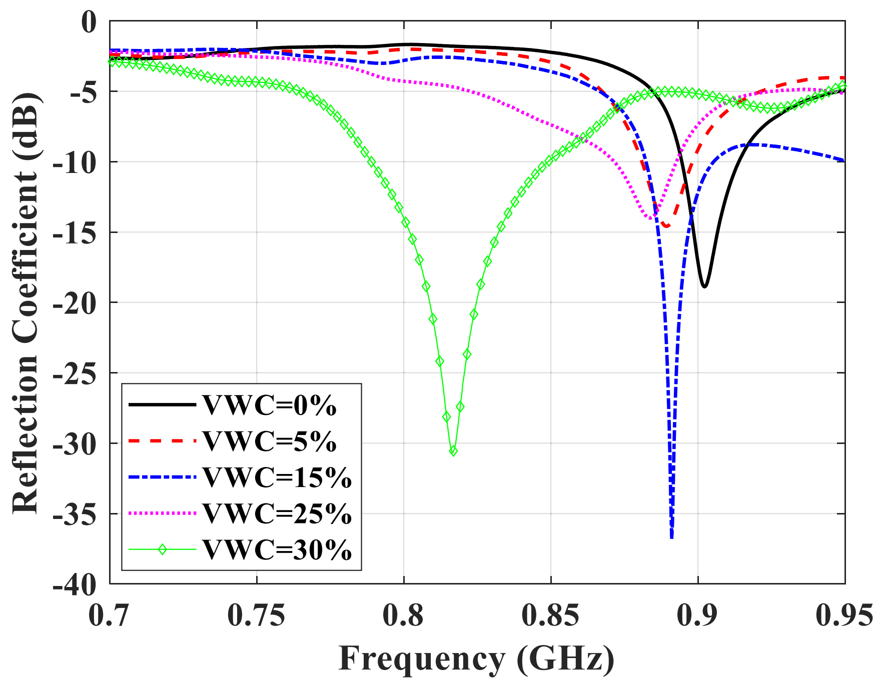

(b)

Fig. 4.14. Measured frequency response of the MSA for different values of VWC, (a) mode-2, (b) mode-3.

To further evaluate the performance of the sensing unit, the sensitivity of the proposed structure is calculated using (4.8),

$$Sensitivity = \left|\frac{f_1 - f_2}{f_u(\varepsilon_{r1} - \varepsilon_{r2})}\right| \times 100 \tag{4.8}$$

where f_1 is the current resonance frequency, f_2 is the updated resonance frequency due to a new material, ε_{r1} is the relative permittivity at f_1, ε_{r2} is the relative permittivity at f_2 and f_u is the resonance frequency of the unloaded structure. A comparison of the proposed antenna in mode-1 (sensing) with those reported in the literature is summarized in TABLE 4.3. In comparison to previously reported sensors [16, 19, 20, 182, 185-187, 189, 196], the proposed structure boasts a compact design with enhanced sensitivity. Furthermore, the proposed structure exhibits a dual-mode behavior and is capable of functioning as a JCASA and a standard single/dual band antenna.

TABLE 4.3. COMPARISON OF THE PROPOSED STRUCTURE WITH REPORTED WORKS.

Ref.	Size at f_u (λ_0^2)	f_u (GHz)	Number of Bands	Application	Design Technique	Sensitivity at max (ε_r) (%)	Max Measured Permittivity
This Work	0.158×0.158	0.95	2	Sensing + Communication	3-RCSR	1.7	16.7
[185]	0.425×0.425	0.625	1	Sensing	Metamaterial Absorber	0.097	19.1
[16]	0.67×0.13	4	2	Sensing	SRR and CSRR	0.9	16.7
[186]	0.35× –	2.67	3	Sensing	CSRR	1.6	9.2
[189]	–	2.4	1	Sensing	CSRR	0.19	79.5
[19]	0.32×0.2	2.45	1	Sensing	M-CSRR	0.2	70
[20]	0.198×0.198	2.38	1	Sensing	EBG Resonator	0.224	70
[182]	0.184×0.372	2.234	1	Sensing	SRR	0.04476	70
[187]	0.36× –	2.7	1	Sensing	CSRR	1.7	10.2
[196]	0.42×0.44	4.7	2	Sensing+ Communication	Frequency Selective Multipath Filter	0.214	26

4.4 Conclusion

This chapter presents a compact multi-service antenna (MSA) for sensing and wireless communication using a 3-RCSR. The antenna design incorporates a modified patch and a 3-CSR, with two PIN diodes integrated into the 3-CSR to achieve an MSA. The proposed MSA can operate in three modes: dual-band joint communication and sensing antenna (JCASA), dual-band antenna, and single-band antenna. In the JCASA mode, the first band (0.95–0.97 GHz) is used for sensing to precisely measure the permittivity, while the second band (1.53–1.56 GHz) is allocated for communication. In mode-2 and -3, the proposed MSA operates as a dual-band and single-band antenna, respectively. The proposed structure is fabricated and measured to validate its performance, and a favorable agreement is observed between the simulation and measurement results. Based on the experimental results, the proposed design is suitable for measuring soil moisture in precision farming, determining the permittivity of materials within the range of 1–20, and implementing single or dual-band antenna applications. Hence, the MSA is versatile and adaptable to a range of applications.

5

5 Ultra-Compact Sensor and Reconfigurable Antenna

(One journal paper has been produced based on the material in this chapter, "Precision Agriculture: Ultra-Compact Sensor and Reconfigurable Antenna for Joint Sensing and Communication")

5.1 Introduction

Designing a sensor with a low resonance frequency to cover a large volume under test (VUT) while maintaining a compact size and high sensitivity is highly challenging. For practical remote sensing systems in diverse geographical structures, it is also essential to integrate a pattern reconfigurable antenna for transmitting sensor data to the base station. This dissertation is to discuss a compact sensor with both low resonance frequency and high sensitivity for precise sensing, along with a pattern reconfigurable antenna for effective data transmission in various geographical locations.

The proposed system comprises an Ultra-Compact Soil Moisture Sensor (UCSMS) and a radiation Pattern Reconfigurable Antenna (PRA) for both sensing and communication purposes. The proposed UCSMS operates at a low resonance frequency to cover a larger VUT and provide in-depth soil moisture sensing. The sensor is designed using a multi-turn complementary spiral resonator (MCSR) in the ground plane of a microstrip transmission line to realize a miniaturized and planar structure. The UCSMS operates at a low frequency of 86 MHz with a 5-turn complementary spiral resonator (5-CSR). The sensor is tested in an environmental chamber, with temperature and humidity adjustments made to assess its performance under real-world conditions. This results in a sensor with compact size (0.028×0.028 $\lambda_0{}^2$), low resonance frequency, and high sensitivity, making it well-suited for soil moisture measurements. A directional antenna with pattern reconfiguration is designed at a 2.45 GHz WLAN band for reliable long-distance joint communication for diverse geographical structures. The proposed PRA is designed using CSRR and U-shaped slots, and to achieve pattern reconfiguration, four varactor diodes are integrated with the CSRRs. By changing the biasing voltage of the diodes, six different radiation patterns can be achieved. Moreover, this design enables the utilization of the proposed PRA for Wireless Power Transfer (WPT) or energy harvesting (EH) in the 2.45 GHz WLAN band to store power in a battery. This stored power can then be utilized to power the varactor diodes. The precise sensing capability and multi-directional communication feature of the proposed system make it suitable for precision agriculture applications.

5.2 Design Methodology

The working principle, design, and theory of the proposed system are discussed in the following subsections:

5.2.1 Working Principle of the System

The proposed joint sensing and communication system comprises a UCSMS and a PRA designed for smart agriculture. Fig. 5.1. illustrates the working principle of the proposed system. A practical setup for sensing and communication is shown in Fig. 5.1(a), where a continuous wave radio frequency (RF) signal is transmitted to the UCSMS through a circulator, and the reflected signal is then measured at port 3 of the circulator using a power detector. The frequency of the reflected signal is used to measure the complex permittivity of the MUT, which corresponds to a specific Volumetric Water Content (VWC). This information is transmitted to the base station using a directional pattern reconfigurable antenna. The PRA is designed with the capability to change the directions of the radiation pattern for various geographical structures. In standby mode, the PRA can be utilized for WPT or EH. In the experimental setup shown in Fig. 5.1(b), a vector network analyzer (VNA) is utilized to measure the frequency responses at different VWC levels using UCSMS. This proposed UCSMS can be utilized to measure the permittivity of various materials by configuring the system as depicted in Fig. 5.1.

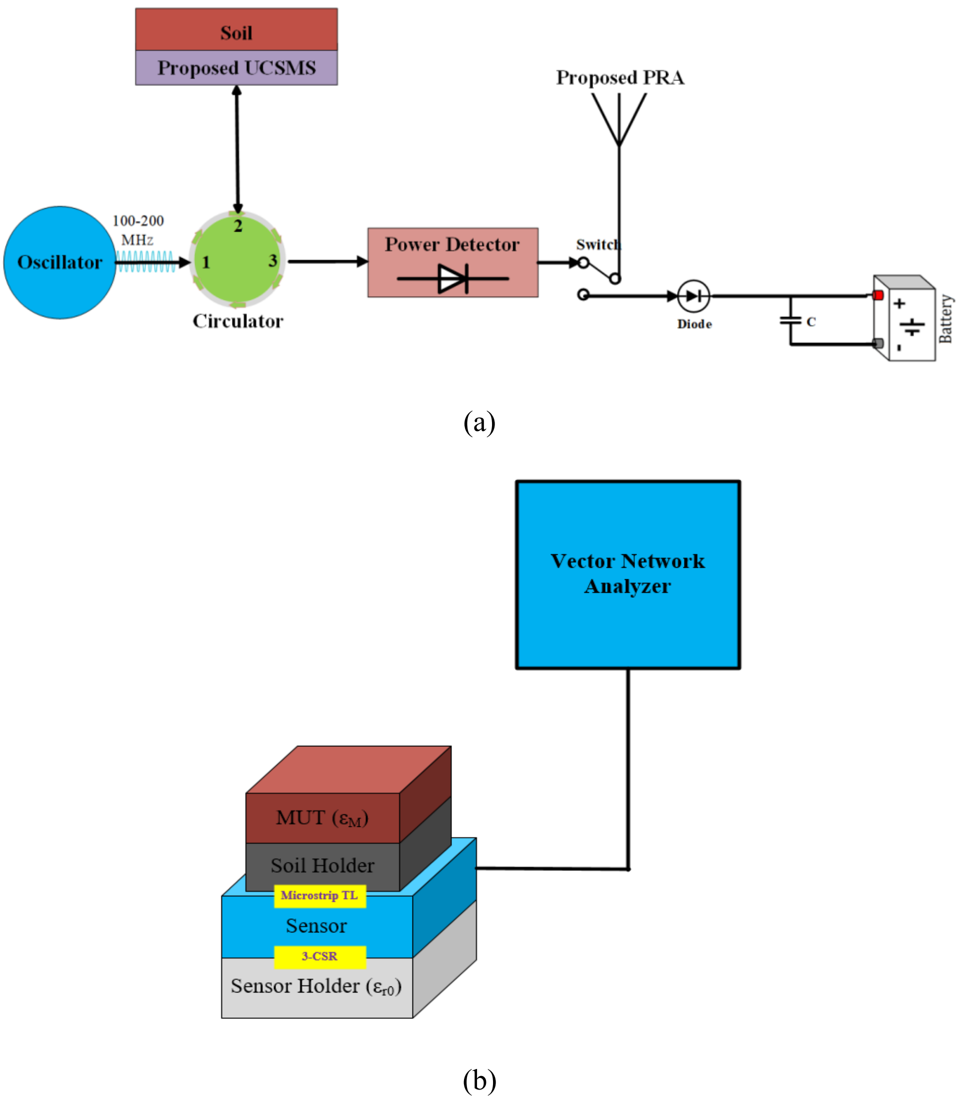

Fig. 5.1. Working principle of the proposed system, (a) working principle of the combined system, (b) laboratory setup for testing the UCSMS.

5.2.2 UCSMS Design

The proposed ultra-compact soil moisture sensor (UCSMS) is designed using an FR-4 substrate ($\varepsilon_r = 4.3,\ tan\delta = 0.025, h = 1.6$ mm) and has dimensions of 50×50 mm^2 as shown in Fig. 5.2. The proposed sensor incorporates an MCSR and a microstrip feed line for exciting the resonator. An open circuit stub of 5 mm length is connected at a distance of 16 mm with the transmission line to achieve a better impedance matching for a wide range of permittivity (ε'_r) values. The reflection coefficients of the proposed structure with and without the open circuit stub are shown in Fig. 5.3.

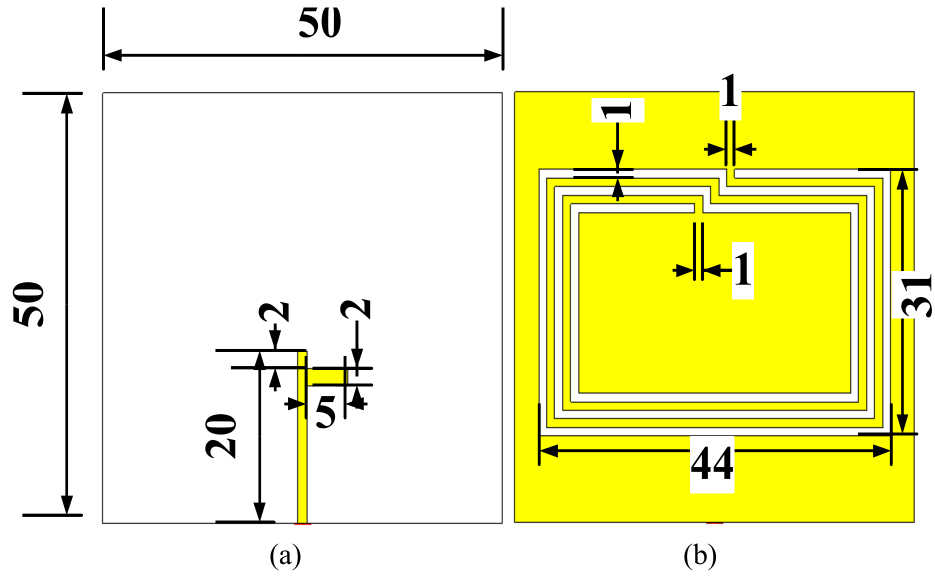

Fig. 5.2. Geometry of the proposed UCSMS, (a) top view, (b) bottom view, (all dimensions are in mm).

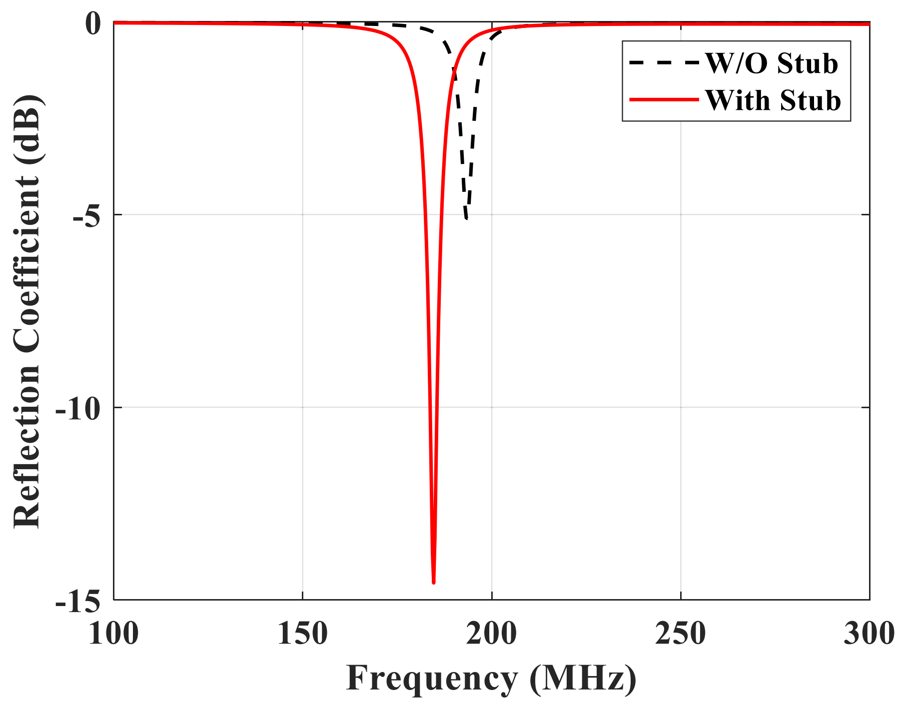

Fig. 5.3. Reflection coefficient of the proposed UCSMS without and with open stub.

The resonance frequency of the spiral resonator can be calculated using equivalent inductance and capacitance (5.1). Increasing the number of turns in the resonator results in a corresponding increase in the equivalent inductance, while reducing the width of the turns increases the equivalent capacitance [193]. Simulations were conducted to analyze different configurations of the spiral resonator by varying the number of turns and the width of the turns.

$$f = \frac{1}{2\pi\sqrt{L_e C_e}} \tag{5.1}$$

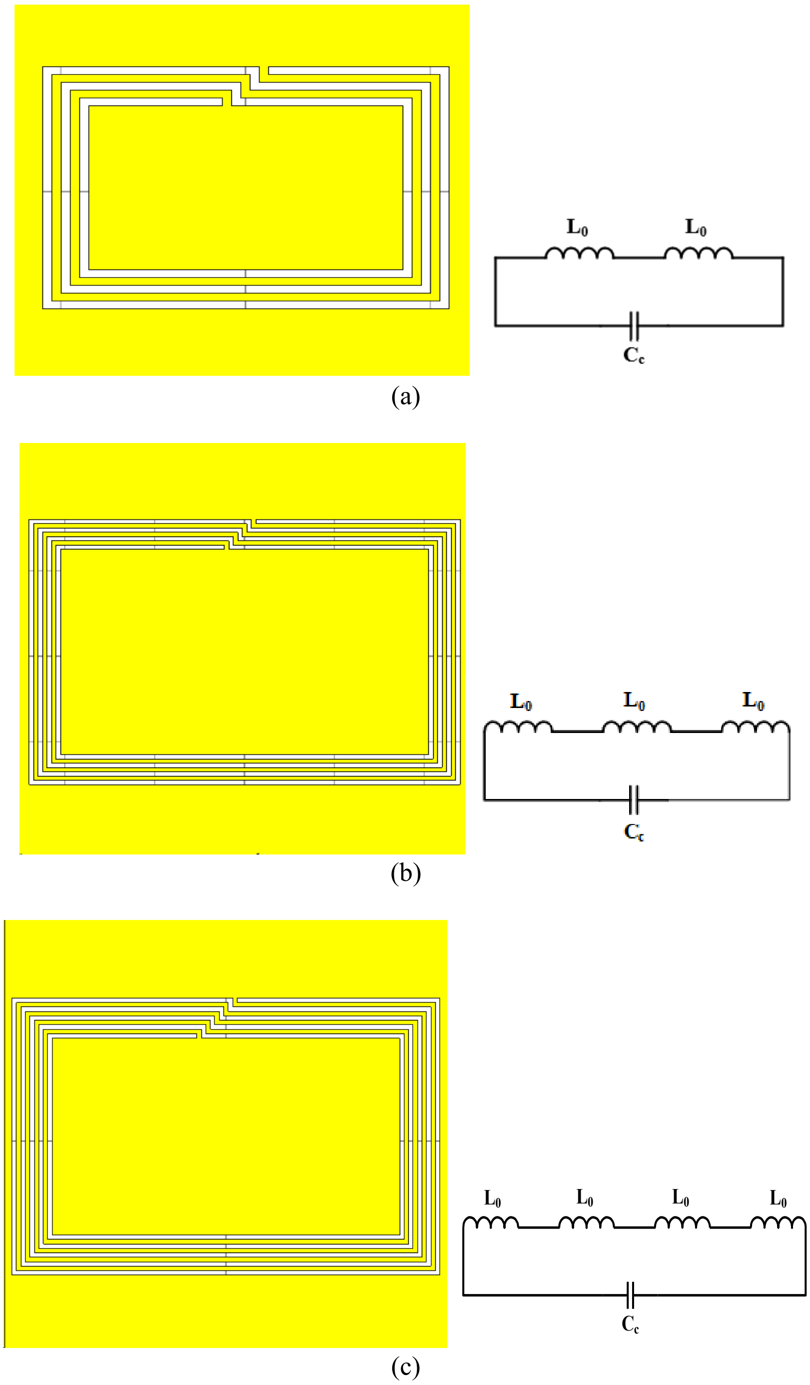

Fig. 5.4. Geometry and equivalent circuits of different complementary spiral resonators, (a) 3-CSR, (b) 4-CSR, (c) 5-CSR.

Fig. 5.4 illustrates three different configurations of the spiral resonator, along with their corresponding equivalent circuits. It can be observed from the equivalent circuits that increasing the number of turns and/or decreasing the width of the turns will increase the equivalent inductance and/or capacitance, resulting in the reduction of the resonance frequency. However, the practical limitation of the fabrication equipment makes it challenging to reduce the width and spacing beyond a certain limit. A comparison between the 3-Turns Complementary Spiral Resonator (3-CSR) with a turn width (w_t) of 1 mm, the 4-turn complementary spiral resonator (4-CSR) with a w_t of 0.5 mm, and the 5-turn complementary spiral resonator (5-CSR) with a w_t of 0.5 mm is presented in Fig. 5.5. The simulated resonance frequencies of 3-CSR, 4-CSR, and 5-CSR are 180 MHz, 102 MHz and 86 MHz, respectively, which validates the aforementioned theory. For this study and to prove the concept, the 3-CSR was selected, fabricated, and tested as a soil moisture sensor.

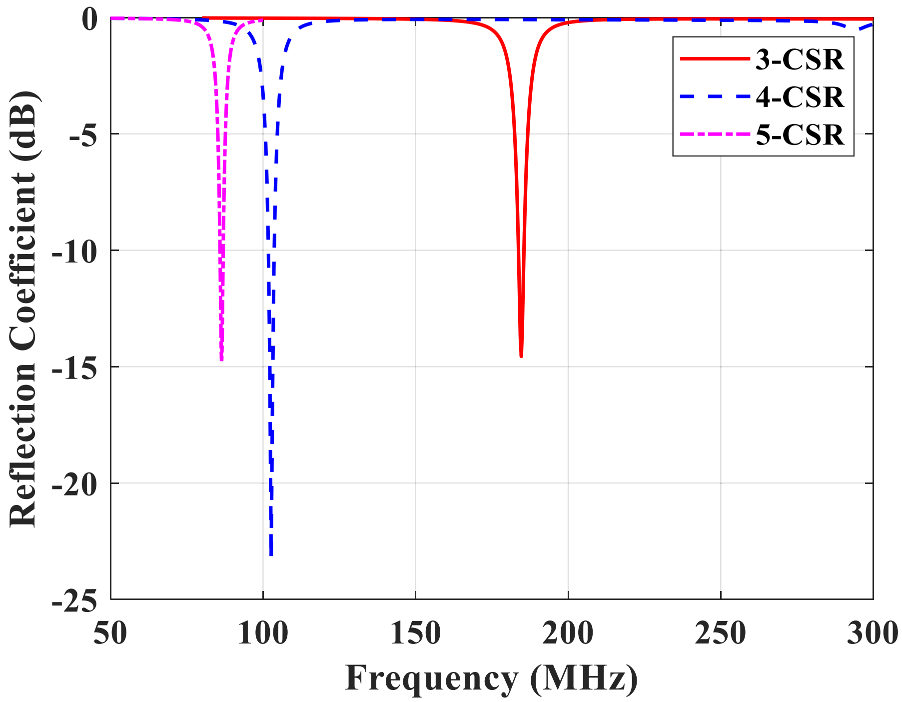

Fig. 5.5. Comparison of different complementary spiral resonators.

The equivalent circuit of a spiral resonator is an *LC* tank circuit, as illustrated in Fig. 5.4. For instance, the equivalent circuit of 5-CSR consists of four inductances and a capacitance connected in series. The inductance value of the resonator can be calculated using (5.2) [223], where Z_0 is the line impedance, ε_e is the effective permittivity, *c* is the speed of light, and *l* is the line length.

$$L_0 = \frac{Z_0\sqrt{\varepsilon_e}}{c} l \tag{5.2}$$

The line impedance (Z_0) and the effective permittivity (ε_e) can be calculated using (5.3)-(5.6) [245], where h represents the thickness of the substrate and w_t is the width of a single turn. The thickness of the substrate is 1.6 mm.

$w_t < h$:

$$\varepsilon_e = \frac{\varepsilon_r + 1}{2} + \frac{\varepsilon_r + 1}{2}\left[\frac{1}{\sqrt{1 + 12\left(\frac{h}{w_t}\right)}} + 0.04\left(1 - \frac{w_t}{h}\right)^2\right] \tag{5.3}$$

$$Z_0 = \frac{60}{\varepsilon_e} log_2\left[8\frac{h}{w_t} + 0.25\frac{w_t}{h}\right] \tag{5.4}$$

$w_t > h$:

$$\varepsilon_e = \frac{\varepsilon_r + 1}{2} + \frac{\varepsilon_r + 1}{2}\left[\frac{1}{\sqrt{1 + 12\left(\frac{h}{w_t}\right)}}\right] \tag{5.5}$$

$$Z_0 = \frac{120\pi}{\varepsilon_e\left[\frac{w_t}{h} + 1.393 + \frac{2}{3}log_2\left(\frac{w_t}{h} + 1.444\right)\right]} \tag{5.6}$$

5.2.3 PRA Design

After measuring the soil moisture using UCSMS, an antenna is required to transmit this information to the base station to realize smart agriculture. A directional pattern reconfiguration antenna is designed for reliable long-distance communication in various geographical structures.

The proposed PRA is designed on a Rogers RO4003C substrate (ε_r = 3.55, $tan\delta$ = 0.0027). The PRA geometry consists of a coaxial probe-fed circular patch, two CSRRs, and two U-shaped slots. Each CSRR slot has a commentary split-ring resonator and a coplanar waveguide (CPW) stub. The circular patch is positioned on the top side of the substrate, while the CSRRs and U-shaped slots are located on the bottom side. The structure is symmetrical along the *x-axis* and *y-axis* and the size of the substrate is $L_s \times W_s \times H$ mm^3. Both left and right CPW-based CSRRs are responsible for the radiation pattern in the *xz-plane*, while top and bottom U-shaped slots are employed for the radiation pattern in the *yz-plane*. To achieve pattern reconfiguration in the *xz-plane* while maintaining the same *yz* pattern, two varactor diodes are integrated across each symmetrical CPW-based CSRR. The PRA is excited using a coaxial probe at a distance of L4 to achieve better impedance matching.

The detailed geometry of the proposed PRA is shown in Fig. 5.6, with Fig. 5.6(a) depicting the top view, Fig. 5.6(b) showing the bottom view, and Fig. 5.6(c) providing a magnified view. Four varactor diodes are integrated across both symmetrical CPW-based CSRRs at an optimized position to achieve pattern reconfiguration in the *xz-plane*. A biasing network is designed and connected to the varactor diodes using vias, as shown in Fig. 5.6(a). The antenna is designed for the 2.45 GHz WLAN band, and the optimized dimensions of the structure are provided in TABLE 5.1.

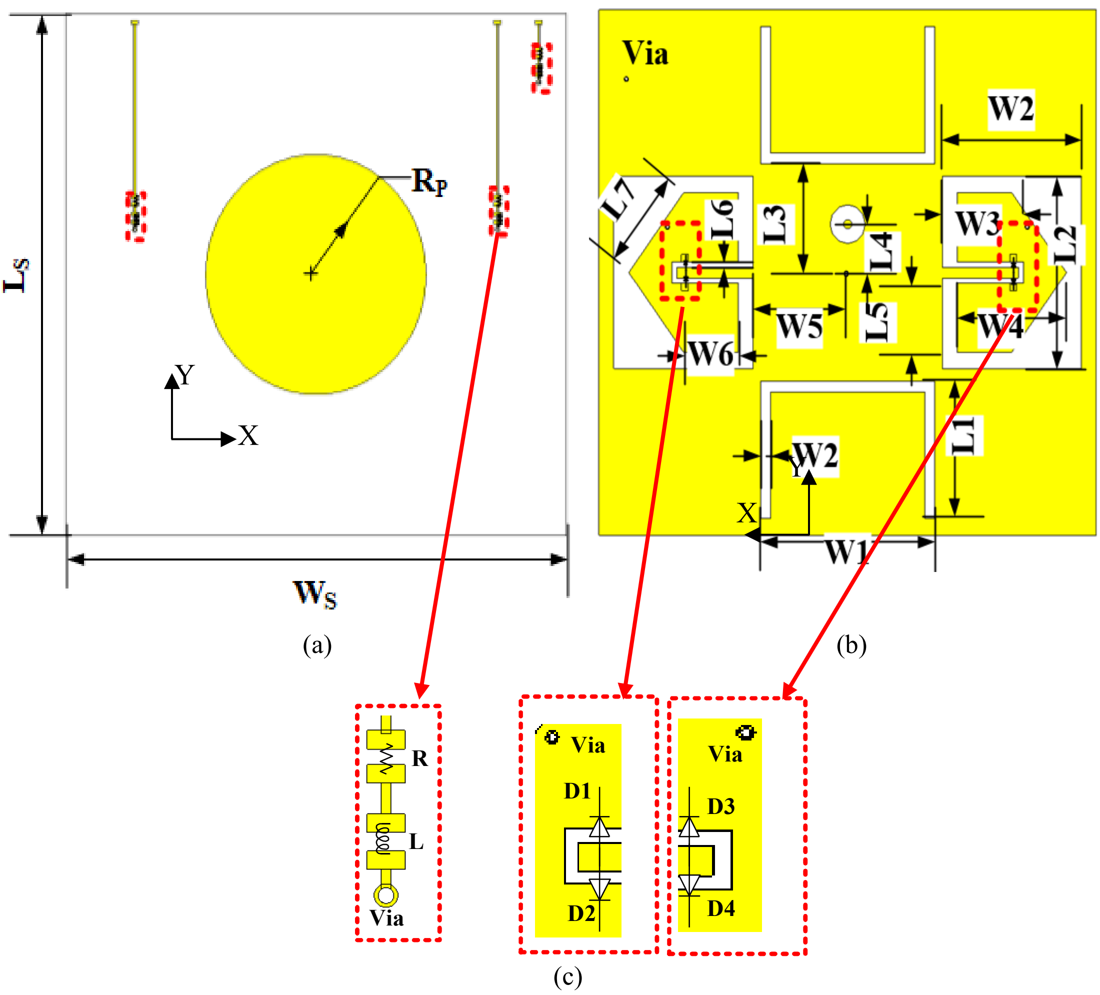

Fig. 5.6. Geometry of the proposed antenna, (a) top view, (b) bottom view, (c) magnified view.

TABLE 5.1. DIMENSIONS OF THE PROPOSED PATTERN RECONFIGURABLE ANTENNA (ALL UNITS ARE IN MM).

L_S	W_S	R_P	$L1$	$W1$	$W2$	$L2$
81.175	85	18.7	21.25	29.75	1.7	29.75
L3	***L4***	***W2***	***W3***	***W4***	***L5***	***W5***
16.8	7.53	23.8	13	18.7	10.625	16.15
L6	***W6***	***L7***	***H***			
0.85	9.35	15.47	1.524			

By selecting suitable biasing voltages, six different radiation patterns have been generated in various directions, named 'front', 'back', 'upper left', 'left', 'upper right', and 'right', as shown in Fig. 5.7.

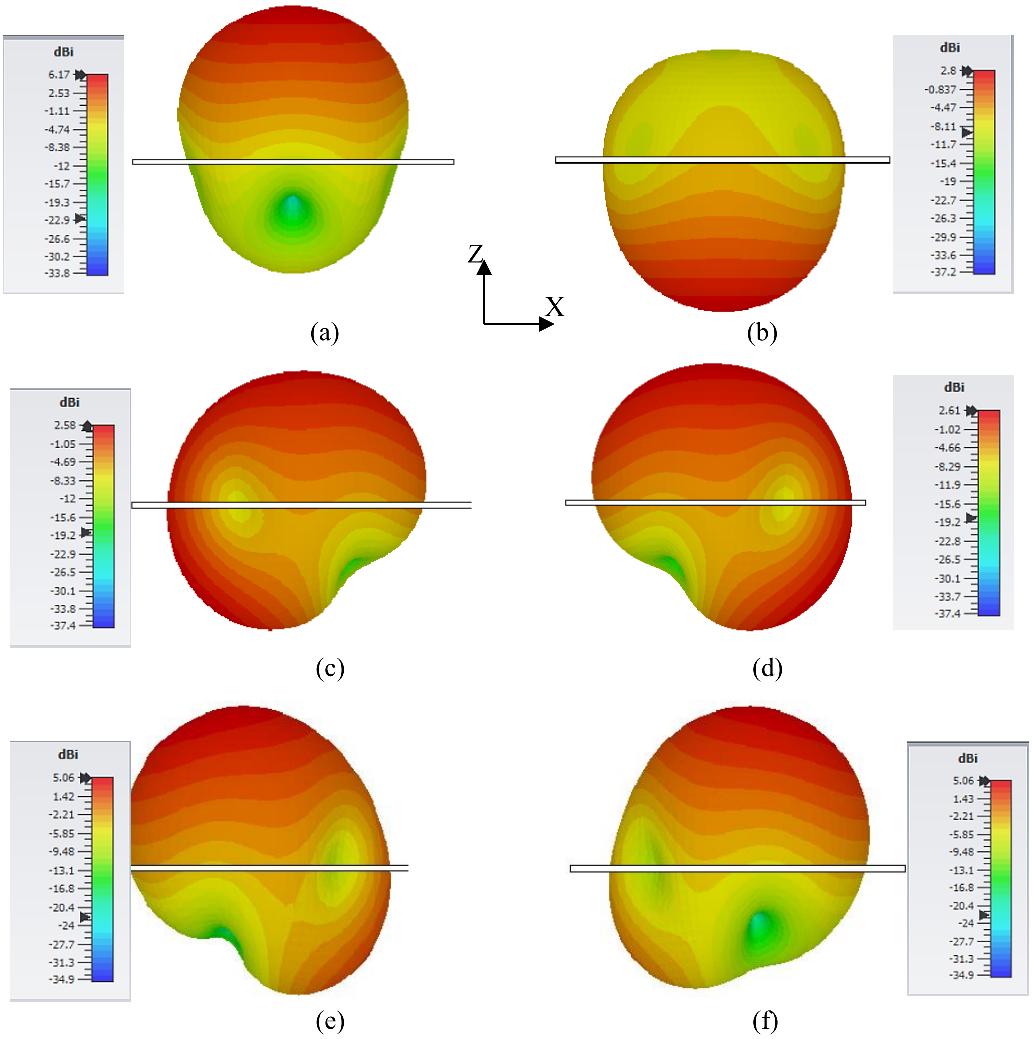

Fig. 5.7. Radiation patterns of the proposed PRA at 2.45 GHz: (a) front, (b) back, (c) left, (d) right, (e) upper left, (f) upper right.

TABLE 5.2 summarizes the biasing voltages and corresponding capacitance values for the six different radiation patterns of the proposed PRA. In the simulation, the varactor diode is modeled as a non-linear circuit and a parametric sweep is utilized to change the value of the capacitance.

TABLE 5.2. BIASING VOLTAGES AND CAPACITANCE VALUES OF VARACTOR DIODES FOR DIFFERENT RADIATION PATTERNS

Varactor Diodes (D1, D2)		Varactor Diodes (D3, D4)		Radiation Pattern
Bias Voltage (V)	**Capacitance (pF)**	**Bias Voltage (V)**	**Capacitance (pF)**	-
0	2.35	0	2.35	Front
0	2.35	3	0.970	Upper left
0	2.35	15	0.466	Left
3	0.970	0	2.35	Upper right
15	0.466	0	2.35	Right
15	0.466	15	0.466	Back

The surface current distributions for the 'left' and 'right' directions are shown in Fig. 5.8. For the 'left' case, the diodes D1 and D2 have a capacitance value of 2.35 pF, resulting in low reactance at 2.45 GHz. Due to this low reactance value, the current bypasses the right CSRR and instead travels through the diodes as shown in Fig. 5.8(a). However, the diodes D3 and D4 have a capacitance value of 0.466 pF, resulting in a higher reactance value for the current at 2.45 GHz. As a result, the current flows through the left CSRR and produces the 'left' radiation pattern. For the 'right' case, diodes D1 and D2 have a capacitance value of 0.466 pF, while diodes D3 and D4 have a capacitance value of 2.35 pF. This configuration results in the generation of the 'right' radiation pattern.

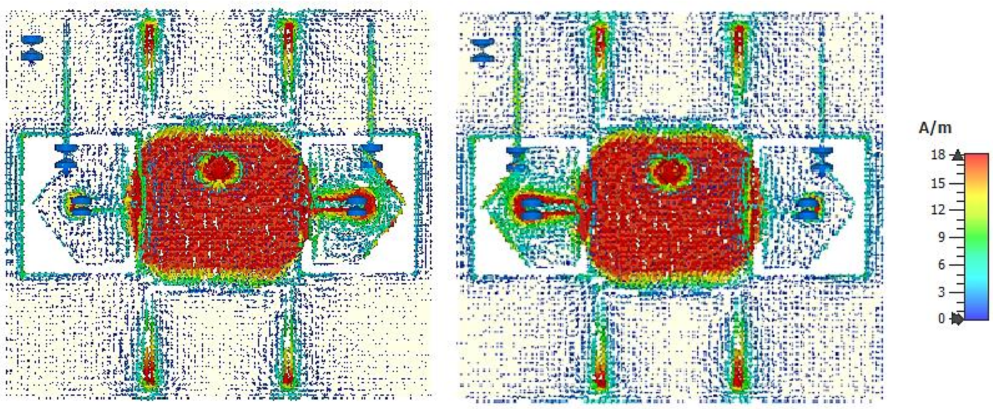

(a) (b)

Fig. 5.8. Current distribution of the PRA, (a) 'left' radiation pattern, (b) 'right' radiation pattern.

5.3 Simulation and Measurement Results

5.3.1 Simulated and Measured Results of UCSMS

To showcase the performance of the proposed UCSMS, the MCSR sensor is designed and simulated using CST MWS 2019. Furthermore, the optimized UCSMS with 3-CSR is fabricated on an FR-4 substrate, and the prototype is shown in Fig. 5.9. The simulated and measured reflection coefficients of the unloaded UCSMS with 3-CSR are shown in Fig. 5.10. The measured resonance frequency of the sensor is 170 MHz with a narrow bandwidth, and a close agreement between the simulated and measured results indicates the validation of the structure.

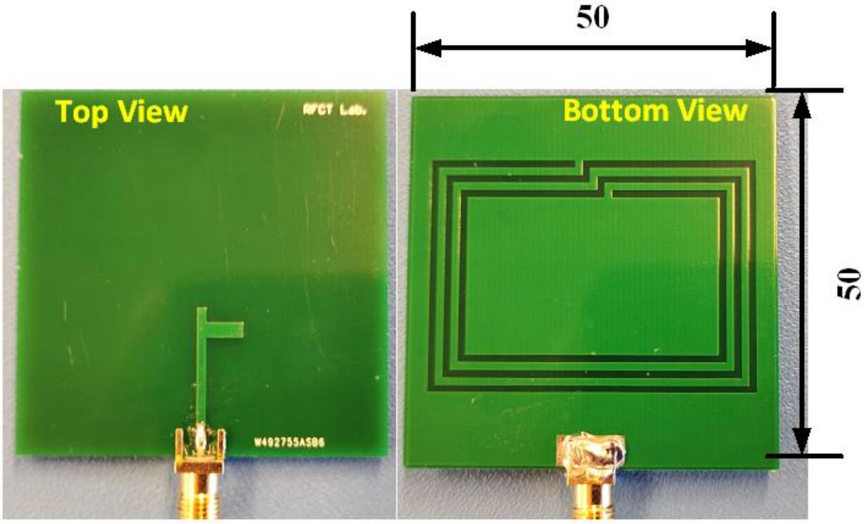

Fig. 5.9. Fabricated prototype of the proposed UCSMS on FR4 substrate ($\varepsilon_r = 4.3,\ tan\delta = 0.025, h = 1.6$ mm).

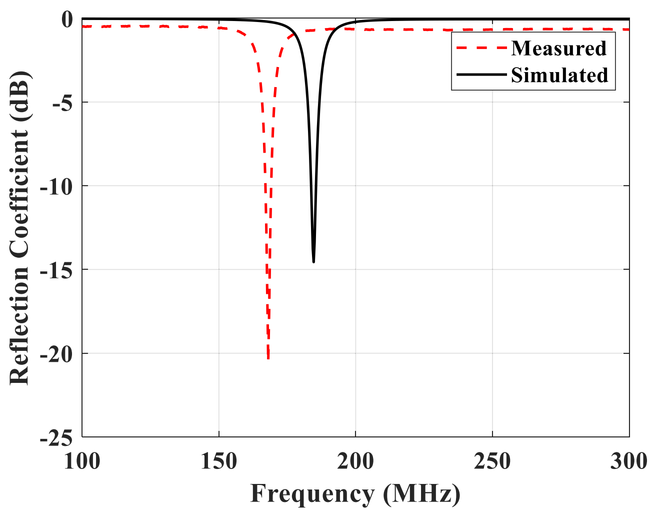

Fig. 5.10. Reflection coefficients of the unloaded UCSMS with 3-CSR.

To analyze the performance of the UCSMS, a measurement setup, as depicted in Fig. 5.11, was utilized. Pure-washed fine sand from Bagged Product Supplies [246] was used to measure the frequency responses for different VWCs. Various types of soil exhibit different permittivity values at different VWCs, and the presence of various materials can also alter the permittivity of soil. For instance, the concentration of potassium chloride can increase the soil's permittivity. The proposed system requires calibration each time for different soil types and various material concentrations to establish the relationship between permittivity and VWC for each specific case. After calibration, the proposed UCSMS can measure VWC on a specific soil type with constant material concentration.

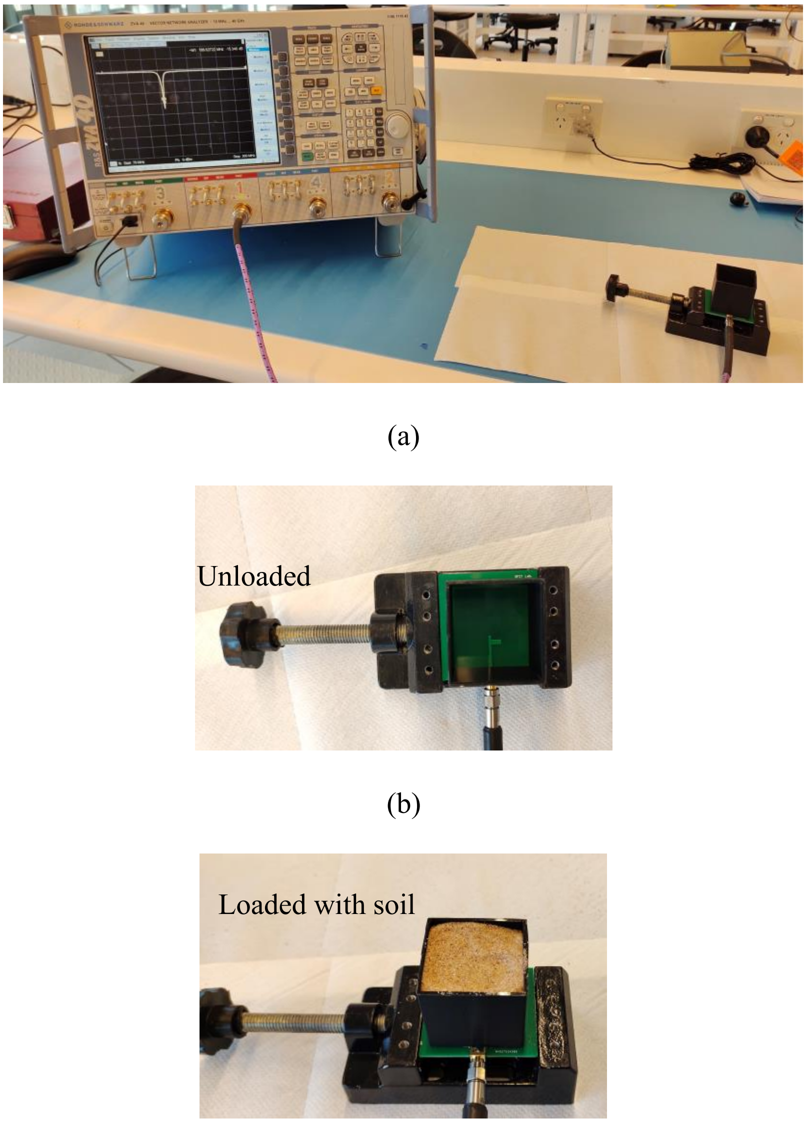

(a)

(b)

(c)

Fig. 5.11. Experimental setup to measure soil moisture, (a) measurement setup, (b) unloaded UCSMS, (c) loaded UCSMS with soil.

Calibration of the system was conducted using pure sand without any impurities, as outlined in TABLE 5.3. The frequency responses of the proposed sensor were measured using a 4-port R&S VNA (VNA-ZVA40) and a standard SOLT (short, open, load, and through) calibration was performed before conducting each test. . A cube with dimensions 40 × 40 × 40 mm is 3D printed and used as a soil container. The simulated and measured frequency responses of the proposed UCSMS are shown in Fig. 5.12. As the VWC in the soil increases, the frequency response of the UCSMS shifts leftwards with a significant frequency difference. The frequency of the sensor shifts from 158 MHz to 115 MHz as the VWC increases from 0 to 30 %. This frequency transition is used to measure the permittivity of the soil, which can be correlated to the VWC. The complex permittivity of the soil at 130 MHz for different VWCs is provided in TABLE 5.3. A close agreement between simulation and measurement results can be observed, validating the design of the proposed UCSMS.

TABLE 5.3. PERMITTIVITY OF SOIL FOR DIFFERENT VWCS AT 130 MHZ [229].

VWC (%)	**0**	**5**	**10**	**15**	**20**	**25**	**30**
ε'_r	2.5	6	8	14.5	18	21	23
ε''_r	0.05	0.5	0.9	1.8	2.5	3.1	3.5

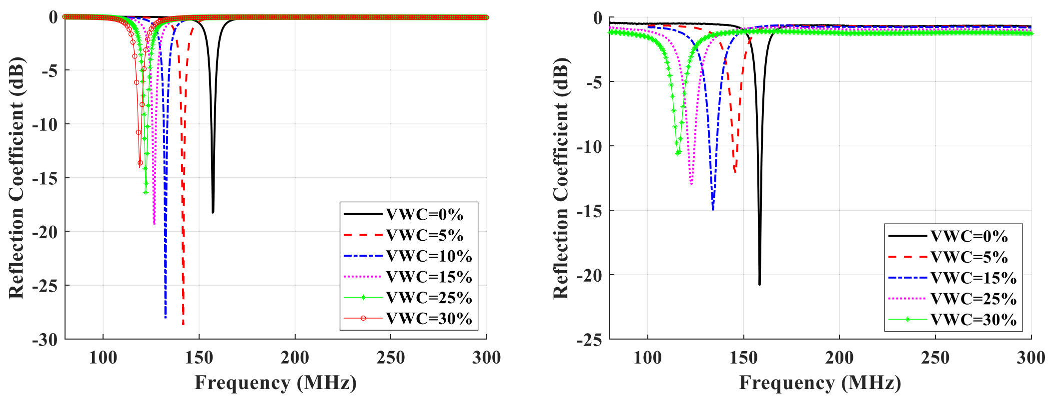

(a

(b)

Fig. 5.12. Frequency responses of the proposed UCSMS with 3-CSR at different VWCs in the soil, (a) simulated, (b) measured.

Three tests are performed separately to evaluate the precision of the measurement and frequency shifts have been measured with a maximum variation of ± 5 MHz. The relationship between the frequency shift (Δf) and the complex permittivity is shown in Fig. 5.13, indicating a linear change. The proposed UCSMS is also analyzed with different heights of soil as depicted in Fig. 5.14(a) and corresponding frequency responses are measured. The frequency responses of the UCSMS for different heights are shown in Fig. 5.14(b), clearly indicating that the proposed UCSMS is not sensitive to the variation in the height of the soil under test. Hence, the proposed sensor can cover a larger VUT of the soil.

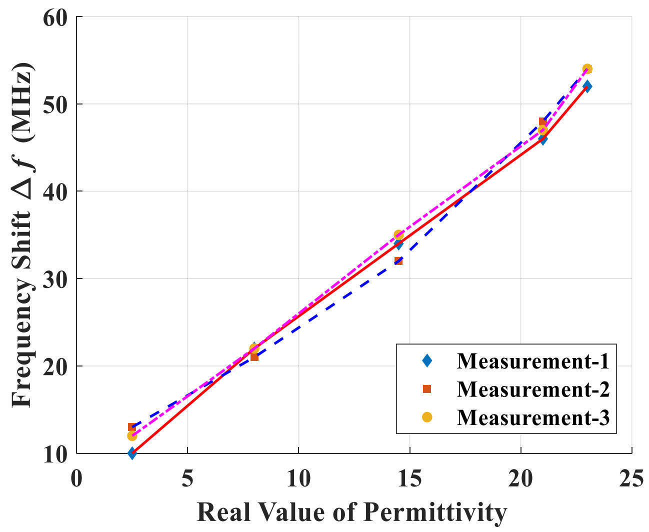

(a)

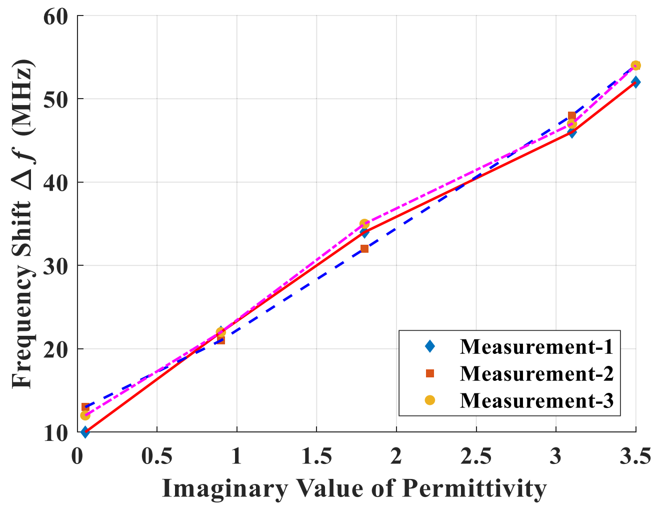

(b)

Fig. 5.13. Frequency shift vs. permittivity, (a) real value, and (b) imaginary value.

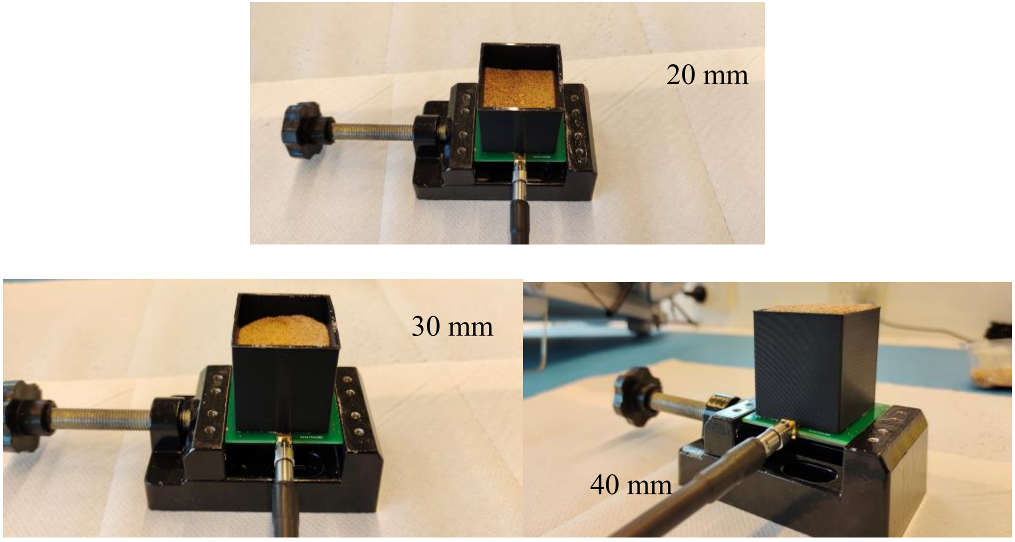

(a)

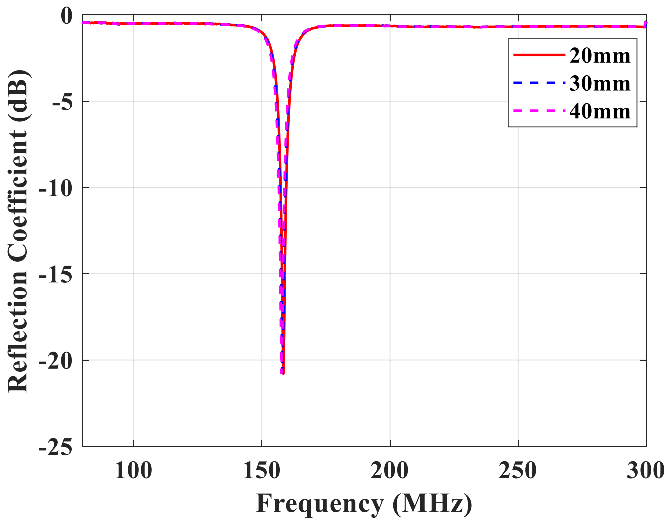

(b)

Fig. 5.14. Frequency Analysis for different soil heights, (a) different soil thicknesses, (b) frequency responses.

To analyze the sensor's accuracy, two reference devices, Dielectric Assessment Kit (DAK 12) [247] and TDR-315L [248], were used to measure the permittivity and VWC of the soil. Fig. 5.15 displays the soil measurements using the DAK 12 and TDR-315L sensor.

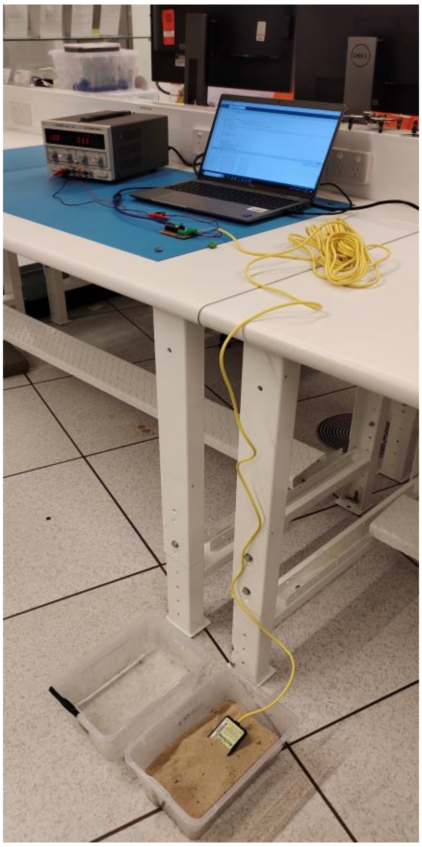

(a)

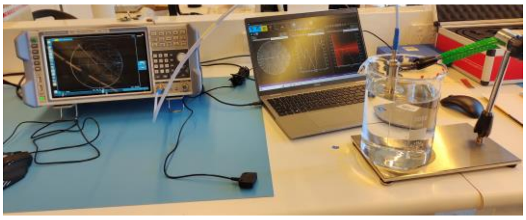

(b) (c)

Fig. 5.15. Soil measurements using reference devices, (a) TDR-315L measurement, (b) DAK 12 calibration, (c) DAK 12 measurement.

To evaluate the sensor's performance in real-world conditions, additional tests have been conducted in a controlled Vötschtechnik Environmental Climate Chamber (Temperature and Humidity) to measure the frequency responses under various environmental conditions. The laboratory setup for analyzing the sensor's performance under different environmental conditions is shown in Fig. 5.16. In a real-world environment, temperatures can drop as low as 0 °C during the nighttime and rise as high as 45 °C in summer, while humidity levels can vary from 40 % to 70 % at different times. To characterize the sensor in real-world conditions, temperature (0 to

45°C) and humidity (40 to 70%) are varied in the chamber to create extreme weather scenarios for 15 % and 30 % VWC values. For temperature variations, a constant humidity of 50 % is used, and for humidity measurements, a constant temperature of 25 °C is maintained. In the case of

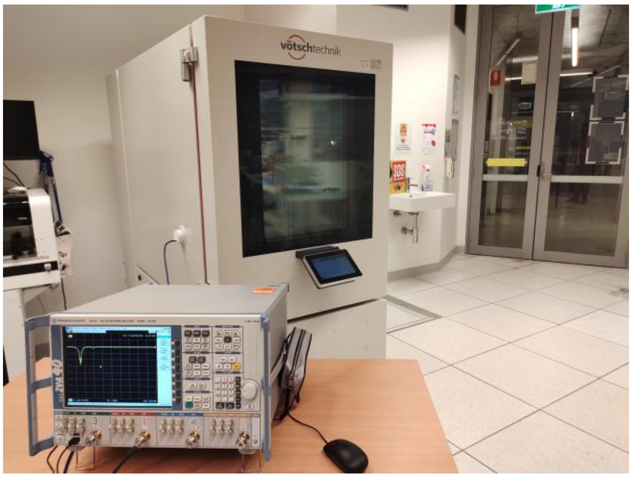

(a)

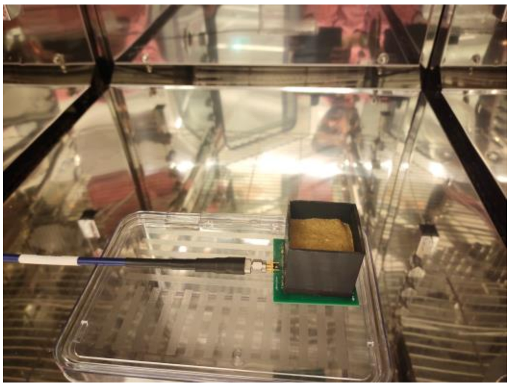

(b)

Fig. 5.16. Sensor performance analysis in the climate chamber, (a) test setup, (b) loaded UCSMS inside chamber.

30% VWC, the measured results as depicted in Fig. 5.17, indicate that there is no significant difference in the frequency response readings with varying humidity values, as the sand is already saturated. However, for 15% VWC, the resonance frequency shifts towards the left side, indicating higher soil moisture with increased humidity. At 0 °C, where water exists in both liquid and solid forms, the VWC decreases due to the formation of ice, causing the resonance frequency to shift to the right. The frequency variation due to temperature is higher for 30 % VWC compared to 15% VWC. Similarly, at a high temperature of 45 °C, soil moisture decreases over time due to water vaporization, thereby validating the accuracy of the sensor. It should be noted that there is no significant difference in the resonance frequency between 10 and 30 °C.

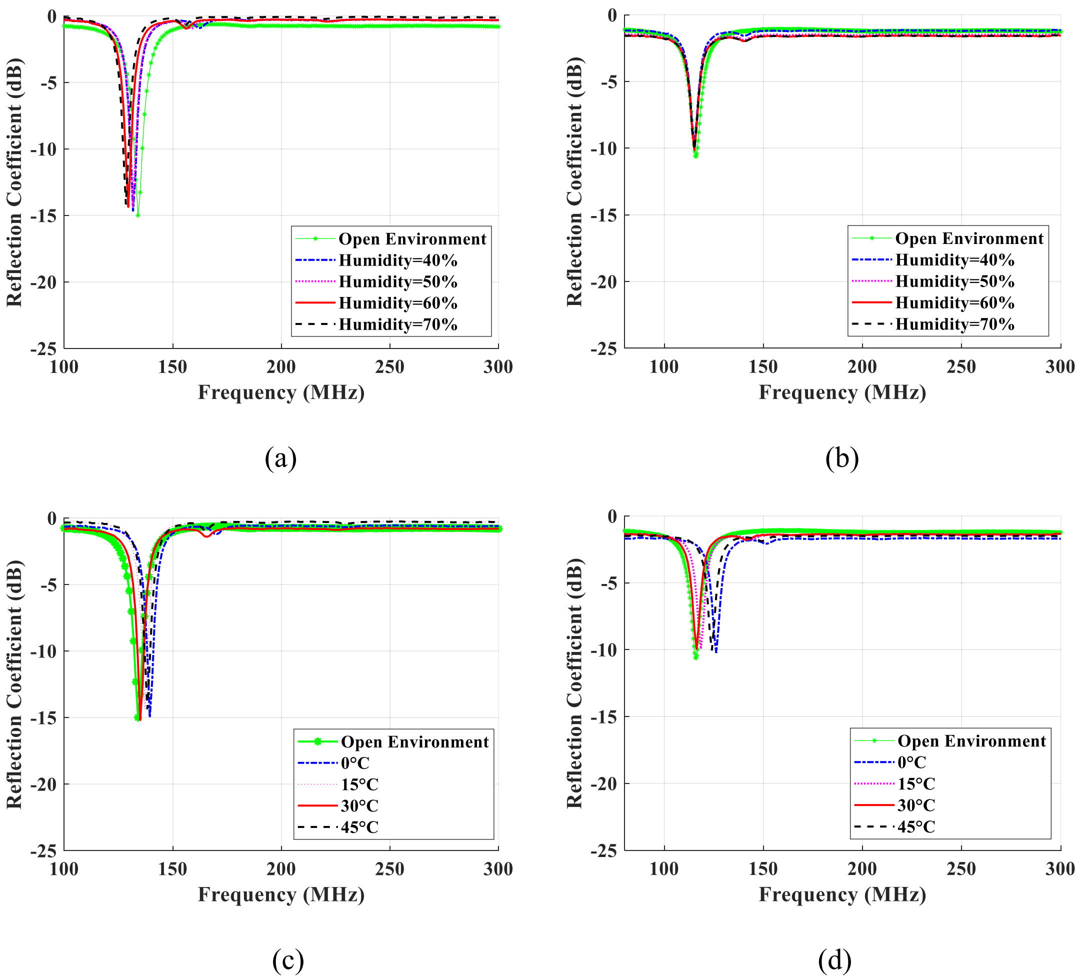

Fig. 5.17. Frequency response variations for different climate conditions in the environmental chamber, (a) 15 % VWC at 25 ^{0}C, (b) (a) 30 % VWC at 25 ^{0}C, (c) 15 % VWC at 50 % humidity, (d) 30 % VWC at 50 % humidity.

5.3.2 Simulated and Measured Results of PRA

The PRA is designed and simulated using CST MWS 2019. The optimized structure is fabricated on a Rogers RO4003C substrate, and the fabricated prototype is illustrated in Fig. 5.18. The Skyworks SMV1231-079LF varactor diode is utilized, offering a capacitance range of 0.466 – 2.35 pF. In the simulation, a non-linear diode model has been utilized and various capacitance values have been achieved using a parametric sweep. A biasing network is designed to bias the diodes which consists of two RF chokes, each with a value of 390 nH, and two resistors with a resistance of 1.2 kΩ, connected in series with the varactor diode.

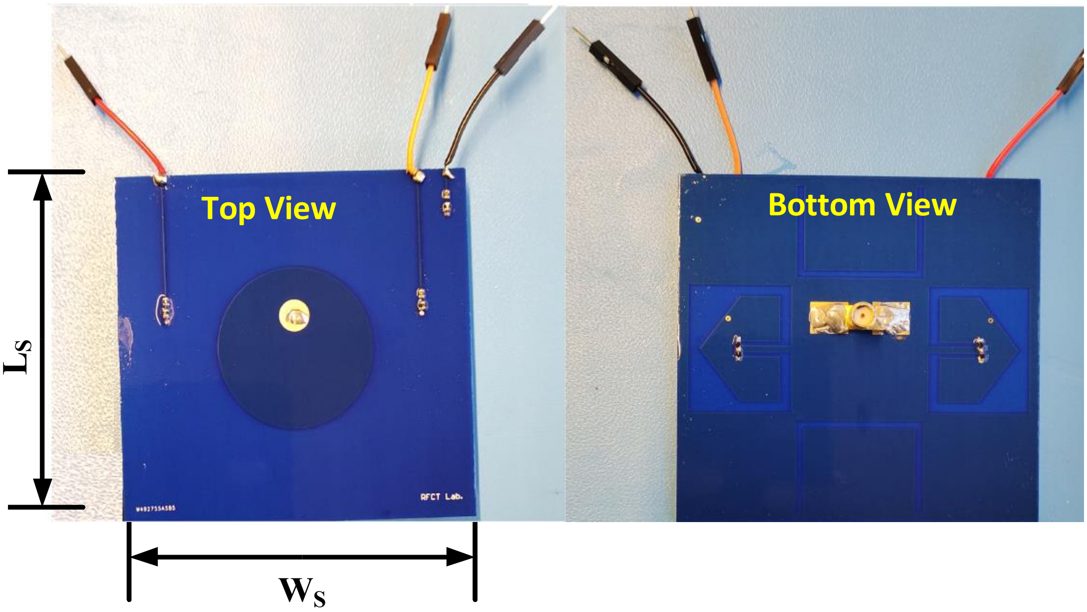

Fig. 5.18. Fabricated prototype of the proposed PRA on Rogers substrate ($\varepsilon_r = 3.55,\ tan\delta = 0.0027, h = 1.524$ mm).

The simulated and measured reflection coefficients of the proposed PRA are shown in Fig. 5.19. The antenna resonates at 2.45 GHz, with a minimum measured bandwidth of 20 MHz for the 'upper left' and 'upper right' configurations. There is a slight variation in the resonance frequency of the PRA under different bias conditions of varactor diodes, with a maximum difference of 20 MHz between the 'front' and 'back' resonances. The simulation and measurement results exhibit good agreement, validating the successful realization of the antenna.

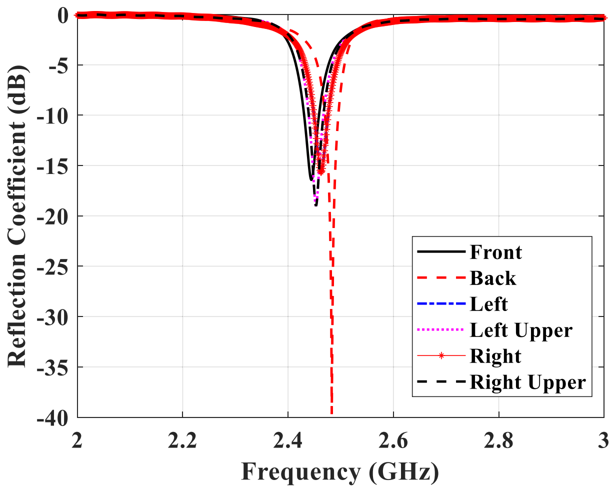

(a)

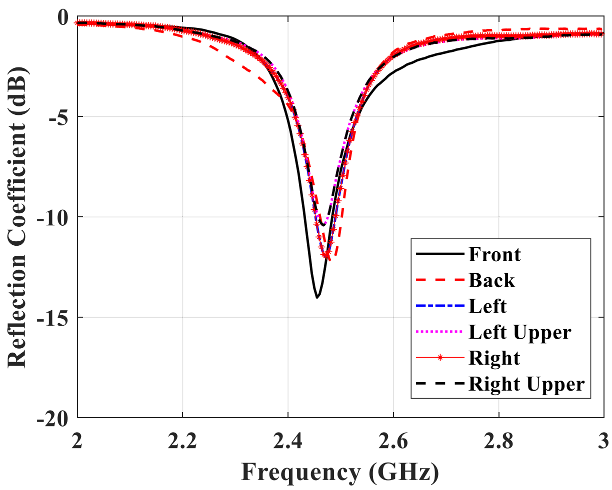

(b)

Fig. 5.19. Reflection coefficients of the proposed PRA, (a) simulated, (b) measured.

To analyze the far-field parameters, 2D radiation patterns of the proposed PRA are measured in an anechoic chamber at different basing voltages. A Direct Current (DC) power supply was used to bias the varactor diodes to achieve various biasing conditions, and a standard gain horn antenna was utilized to measure the gain of the proposed PRA. The measurement setup for evaluating the far-field characteristics is shown in Fig. 5.20 and the simulated and measured 2D radiation patterns of the proposed PRA at 2.45 GHz are displayed in Fig. 5.21. Due to the presence of a DC power supply and biasing leads connected to the antenna for varactor diodes biasing, noise is introduced in the 'left' and 'right' radiation patterns. Nevertheless, for other biasing conditions, Fig. 5.21 illustrates a close agreement between the simulated and measured radiation patterns. Six different radiation patterns have been achieved with different biasing voltages across the diodes.

Due to the symmetry of the structure in the *x-axis*, the patterns are symmetrical in the *xz-plane* as shown in Fig. 5.21. The patterns in the *yz-plane* are directional, with a constant 0^0 lobe for all biasing conditions, as there are no varactor diodes across the U-shaped slots. The gains and directions of the maximum lobe in the *xz-plane* are summarized in TABLE 5.4. The antenna achieves a maximum measured gain of 5.63 dBi in the ʻfrontʻ case. The directions of the maximum lobes are 6^0, 185^0, 10^0, 25^0, 340^0, and 254^0 for ʻfrontʻ, ʻbackʻ, ʻleftʻ, ʻupper leftʻ, ʻrightʻ, and ʻupper rightʻ, respectively.

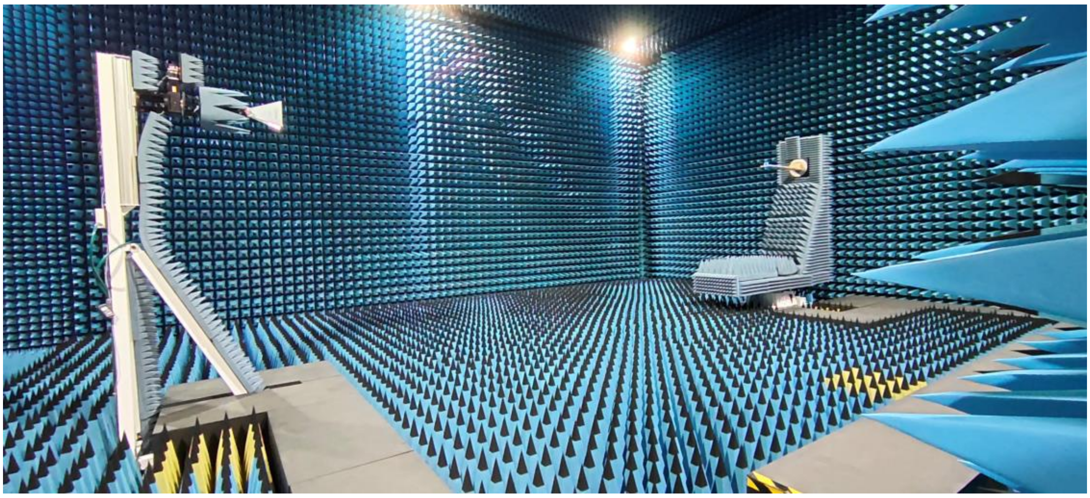

Fig. 5.20. Measurement setup to test the far-field characteristics.

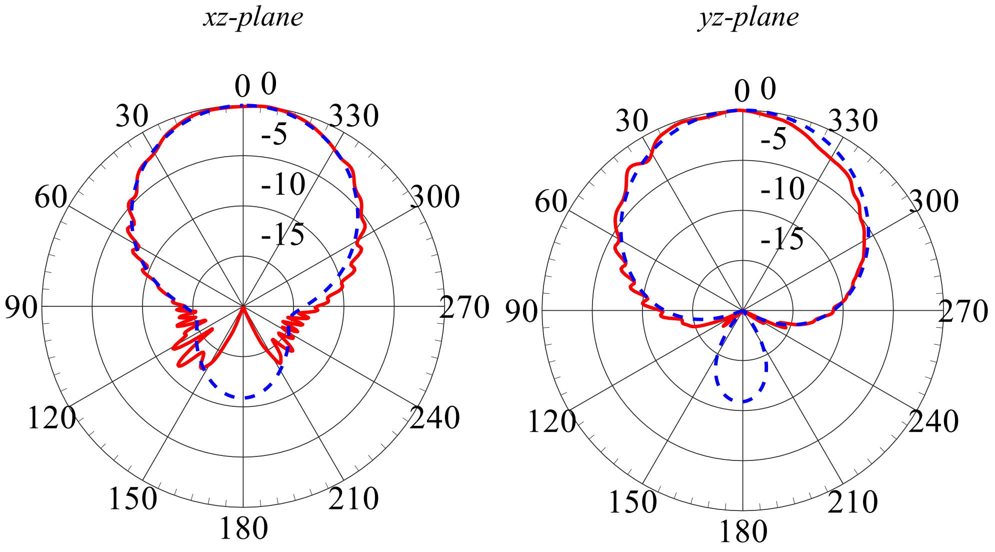
xz-plane
yz-plane
0
0
30
330
60
300
90
270
120
240
150
210
180
-5
-10
-15

(a)

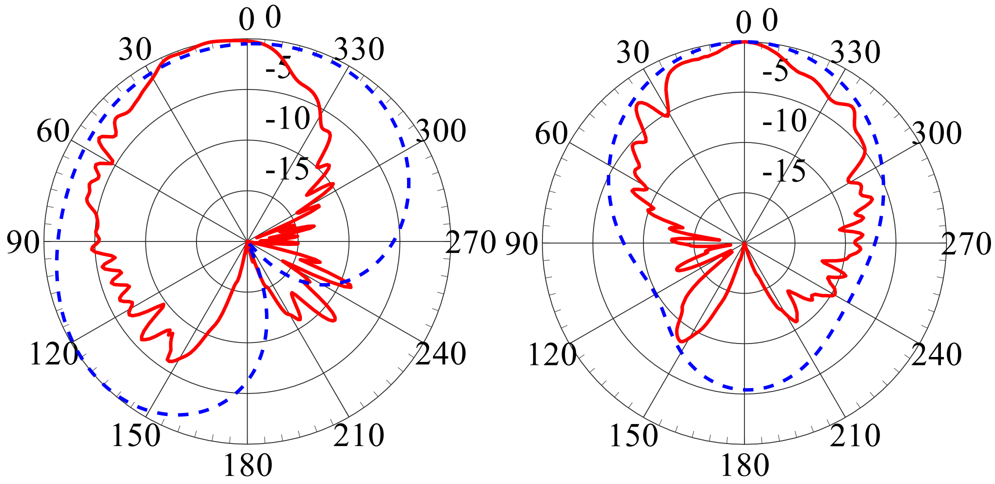
0
0
30
330
60
300
90
270
120
240
150
210
180
-5
-10
-15

(b)

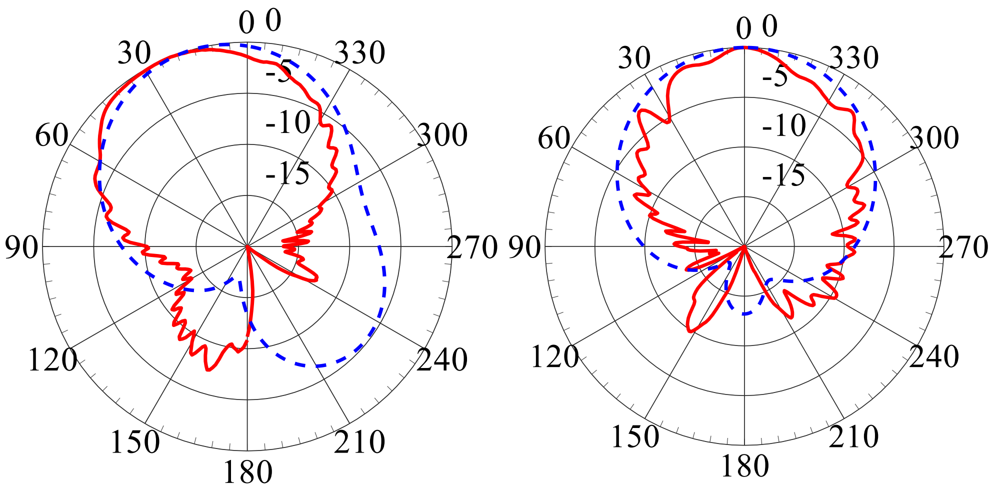
0
0
30
330
60
300
90
270
120
240
150
210
180
-5
-10
-15

(c)

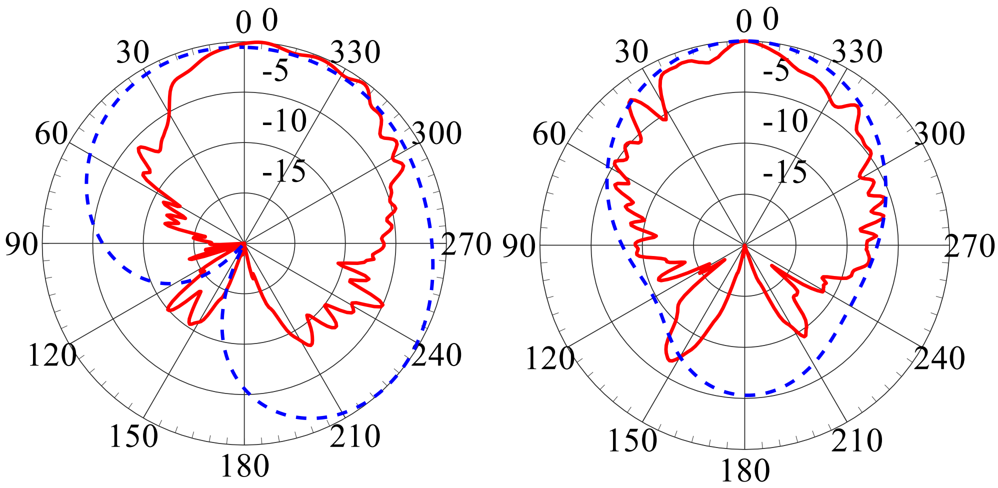

(d)

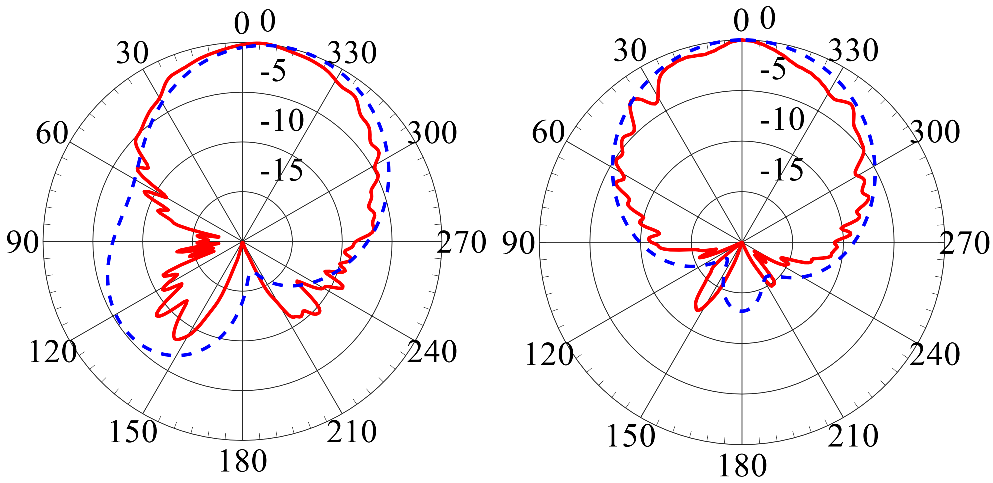

(e)

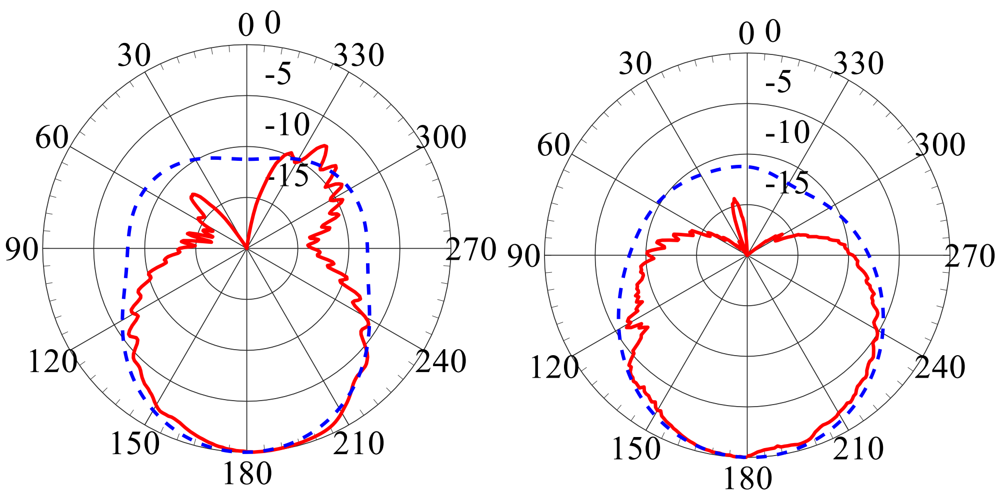

(f)

Fig. 5.21. Simulated and measured 2D radiation patterns at 2.45 GHz, (a) front, (b) left, (c) upper left, (d) right, (e) upper right, (f) back (solid line represents measured and the dotted line represents simulated plots).

TABLE 5.4. FAR-FIELD CHARACTERISTICS OF THE PROPOSED PRA.

Pattern Type	**Gain (dBi)**		**Maximum Lobe Direction (θ_m) in the *xz* plane**	
	simulated	**measured**	**simulated**	**measured**
Front	6.17	5.63	0^0	6^0
Back	4.45	4.14	180^0	185^0
Left	2.7	2.54	132^0	10^0
Upper left	5.117	5.08	15^0	25^0
Right	2.73	2.62	220^0	340^0
Upper right	5.08	4.923	345^0	354^0

5.3.3 Figure of Merit

To compare the performance of the proposed sensor, the sensitivity of the UCSMS is calculated using (5.7),

$$Sensitivity = S = \left|\frac{f_1 - f_2}{f_u(\varepsilon_{r1} - \varepsilon_{r2})}\right| \times 100 \tag{5.7}$$

where f_u is the resonance frequency of the unloaded sensor, f_1 and f_2 are the resonance frequencies due to different materials, ε_{r1} and ε_{r2} represent relative permittivity of materials at f_1 and f_2, respectively. Additionally, a figure of merit (FOM) is defined in (5.8) taking into account the sensitivity (S), maximum electrical length of the sensor (l), and maximum measurable permittivity (ε_{rm}).

$$Figure\ of\ Merit = \frac{S \times \varepsilon_{rm}}{l} \tag{5.8}$$

Based on these evaluations, a comparison of the proposed UCSMS with the reported sensors is summarized in TABLE 5.5. Furthermore, the proposed system possesses the ability to communicate with the base station to transfer information.

TABLE 5.5. COMPARISON OF THE UCSMS (ULTRA-COMPACT SOIL MOISTURE SENSOR) WITH REPORTED SENSORS

Ref.	Size at f_u ($\lambda_0{}^2$)	f_u (GHz)	Number of Sensing Bands	Measurement Technique	Sensitivity @ $max(\varepsilon_r)$ (%)	Max Measured Permittivity	FOM $\frac{1}{\lambda_0}$
This Work	0.028×0.028	0.170	1	MCSR (3-CSR)	2.05	23	1683.92
[16]	0.67×0.13	4	2	SRR and CSRR	0.9	16.7	22.43
[186]	0.35× –	2.67	3	CSRR	1.6	9.2	42.05
[189]	–	2.4	1	CSRR	0.19	79.5	-
[19]	0.32×0.2	2.45	1	M-CSRR	0.2	70	43.75
[187]	0.36× –	2.7	1	CSRR	1.7	10.2	48.167
[195]	0.34×0.034	1.017	1	Shorted-Dipole	0.614	19	34.31
[196]	0.42×0.44	4.7	1	Frequency Selective Multipath Filter	0.214	26	12.65
[20]	0.198×0.198	2.38	1	EBG Resonator	0.224	70	79.19
[182]	0.184×0.372	2.234	1	SRR	0.04476	70	8.42
[188]	0.6×0.4	3.49	1	Complementary Curved Ring Resonator	4.47	4.4	32.78
[185]	0.38×0.38	0.56	1	Metamaterial Absorber	0.109	19.1	5.47

5.4 Conclusion

This chapter presents a joint sensing and communication system for smart agriculture. The proposed system consists of an ultra-compact sensor for soil moisture measurement and a PRA for communication. An MCSR is used with a microstrip transmission line to achieve miniaturization. The proposed UCSMS operates at low frequencies, 180 MHz for 3-CSR, 102 MHz for 4-CSR, and 86 MHz for 5-CSR, making it suitable for covering a large volume of soil. The sensor is evaluated in an environmental chamber by varying temperature and humidity to analyze its performance under real-world conditions. The PRA operates at the 2.45 GHz WLAN band, facilitating the transmission of information to the base station. Integration of four varactor diodes with the communication antenna enables pattern reconfiguration, generating six distinct radiation patterns with different bias conditions. This feature makes the system suitable for smart agriculture across diverse geographical landscapes. In standby mode, the PRA can also be utilized for WPT and EH applications to store power in a battery. This stored power can be utilized to bias the diodes to achieve reconfiguration. The UCSMS with 3-CSR and the PRA have been fabricated and measured, demonstrating a close agreement between the simulated and measured results. The sensor is adaptive and capable of measuring the permittivity of various materials within the range of 1–23.

6

6 Multiband Soil Moisture Sensor

(One journal paper has been generated based on this chapter's material, "In-Situ Soil Moisture Monitoring Using Compact Multiband Sensing System for Smart Agriculture".)

6.1 Introduction

Environmental factors such as temperature changes can significantly affect the frequency variation in Frequency Domain Reflectometry (FDR) sensors. Single-band sensors are simple, but the effect of frequency variations is pronounced, resulting in inaccurate measurements. Conversely, a multi-band sensor can mitigate these effects by measuring responses at different frequencies. Therefore, a multi-band sensor can provide improved accuracy compared to a single-band sensor in soil moisture measurements.

In this chapter, a dual-band FDR-based remote monitoring system for precision farming is presented. An FDR-based sensor typically requires a handheld VNA to measure the frequency responses. Therefore, to eliminate the need for a VNA in the proposed system, a unidirectional Directional Coupler (DiC) and an amplifier have been integrated with the sensor. The proposed system comprises a dual-band FDR-based sensor, a DiC, and an amplifier. A Three-turn Complementary Spiral Resonator (3-CSR) has been employed in the ground plane of a modified patch to achieve miniaturization. Three varactor diodes have been integrated across the spiral resonator to achieve frequency switching. The sensor operates at low resonance frequency bands (500 MHz and 900 MHz) to cover a large Volume Under Test (VUT), and the resonance frequency can be switched using external Direct Current (DC) biasing. The DiC is employed in the opposite direction to realize a dual-port structure, where the output pin of the DiC is used for the input to the sensor, and the input pin is connected to the sensor. The reflected signal from the sensor is coupled from the input pin to the coupled pin, and the coupled pin is connected to the sensor output. A 20 dB gain amplifier is utilized to compensate for coupling and free space losses. The combination of low resonances, dual bands, high sensitivity, compact size and low cost makes it apt for smart agriculture.

6.2 Design Methodology

The subsequent subsections delve into the working mechanism, design, and theory of the proposed system:

6.2.1 Working Mechanism of the Proposed Sensing System

The proposed miniaturized sensing system consists of three subsystems: a Radio Frequency (RF) reader, receiving and transmitting sensor antennas, and the proposed SMS, as shown in Fig. 6.1(a). The proposed structure is an FDR-based dual-port miniaturized sensor designed to measure the Volumetric Water Content (VWC) in the soil. The sensor operates in dual bands (500 MHz and 900 MHz), and varactor diodes have been used to switch between the bands.

In a practical setup (Fig. 6.1(a)), a Continuous Wave (CW) RF signal is wirelessly transmitted using an RF reader. The receiving end employs a vertically polarized antenna positioned at a distance of 1.5 m to capture the transmitted signal. To compensate for path loss, the received signal is fed into an amplifier with a gain of 20 dB. The amplifier's output is then connected to the output pin of a unidirectional DiC, while the input port of the DiC is linked to the sensor, as illustrated in Fig. 6.1(a). The sensor's frequency response varies with different VWCs, and the reflected signal from the sensor is measured at the coupling port of the DiC. This coupled signal is then transmitted back to the reader using a transmitting antenna with horizontal polarization.

In a laboratory setup designed to measure the sensor's performance, the RF reader is replaced with a Vector Network Analyzer (VNA), as illustrated Fig. 6.1(b). The output port of the DiC is connected to port 1 of the VNA, and the coupling port of the DiC is linked to port 2. Frequency responses in terms of transmission coefficient (S21) are then measured for different VWCs.

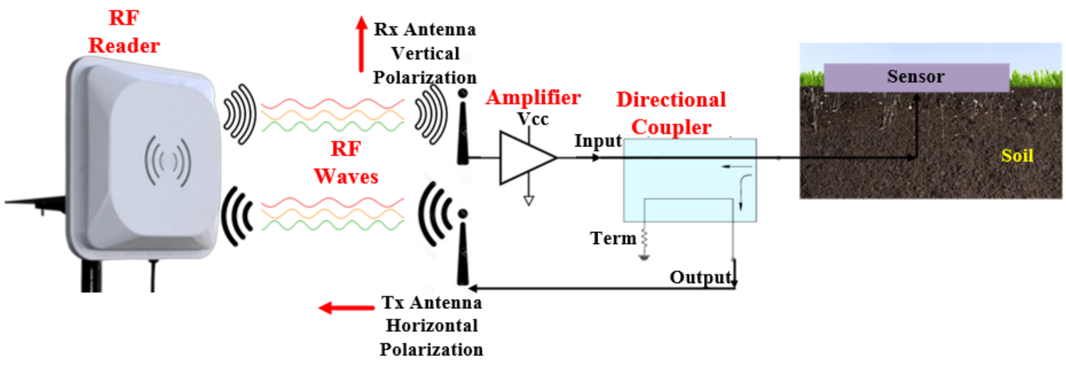

(a)

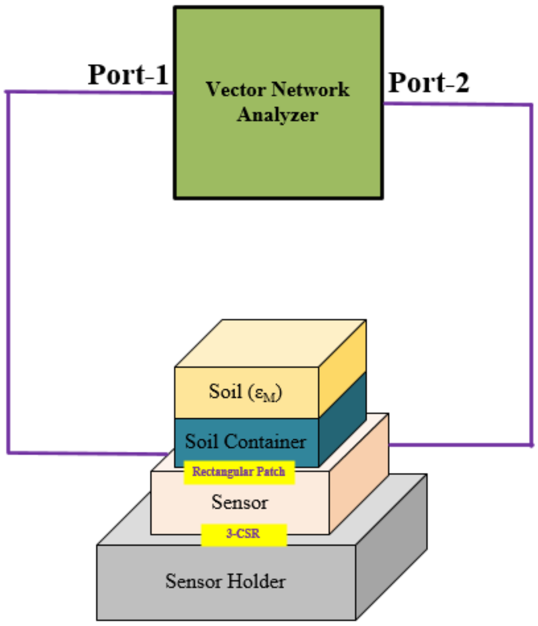

(b)

Fig. 6.1. (a) Working Mechanism of the proposed sensing system, (b) lab setup for measurement of VWCs.

6.2.2 Miniaturized Dual-band Sensor Design

The proposed miniaturized dual-band sensor is designed using Rogers RO4003C (ε_r=3.55, $tan\delta$=0.0027, h=1.524 mm) and has dimensions of 50 × 50 mm^2. The detailed geometry of the sensor is depicted in Fig. 6.2. The proposed sensor comprises a modified patch, two parasitic patches, and a multi-turn complementary spiral resonator (M-CSR). Initially, a conventional patch antenna was designed with dimensions of 24.5×26 mm², resonating at a single frequency. To achieve dual resonance, six rectangular slots are inserted in the patch, and two parasitic patches are added on either side of the modified patch, as shown in Fig. 6.2(a). For a compact sensing structure, a three-turn complementary spiral resonator (3-CSR) is etched into the ground plane of the modified patch, as illustrated in Fig. 6.2(b).

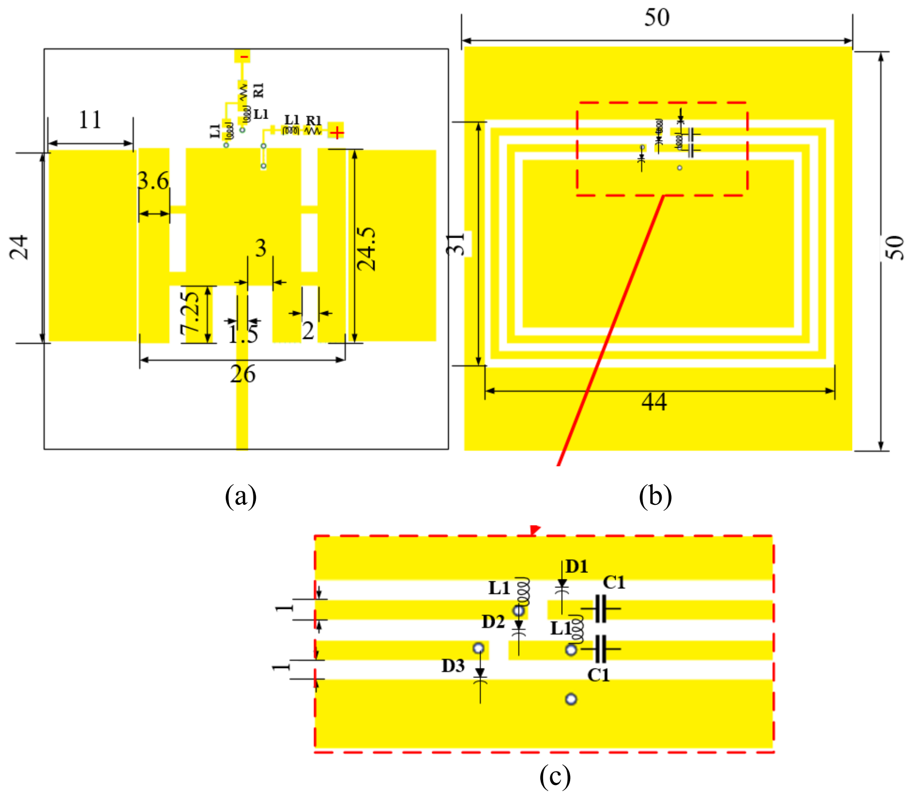

Fig. 6.2. Geometry of the proposed miniaturized dual-band sensor, (a) top view, (b) bottom view, (c) varactor diodes setup (all dimensions are in mm).

The 3-CSR can be modeled as an equivalent LC circuit, and the resonator's resonance frequency relies on the values of the equivalent inductance (L) and capacitance (C). The equivalent circuit of 3-CSR comprises two series inductances (L_0) and an equivalent capacitance, as shown in Fig. 6.3(a). The resonance frequency can be calculated using (6.1). Changing the width of the turns and the number of turns allows for adjustment of the resonance frequency. However, modifying the geometry of the structure is not possible after fabrication.

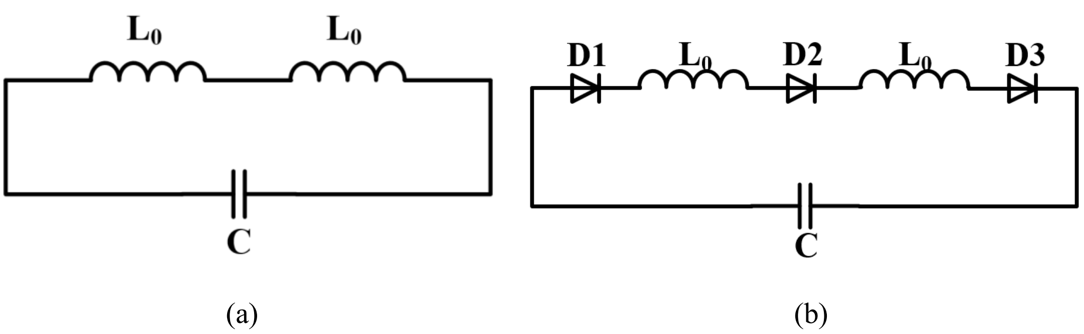

Fig. 6.3. (a) Equivalent circuit of 3-CSR, (b) equivalent circuit of reconfigurable 3-CSR.

$$f = \frac{1}{2\pi\sqrt{LC}} \tag{6.1}$$

To dynamically adjust the resonance frequency of the 3-CSR, an alternative approach involves employing electronic switching to modify the values of L and C. For real-time frequency reconfiguration of the 3-CSR, three varactor diodes (D1, D2, D3) are intricately integrated across the resonator, as depicted in Fig. 6.2(c). The modified circuit is composed of a series connection involving varactor diodes, inductances, and capacitance, as illustrated in Fig. 6.3(b). By manipulating the reverse bias voltage applied to the varactor diodes, changes in diode capacitance occur, thereby influencing the resonance frequency of the structure across the 500 MHz and 900 MHz bands. A biasing network is additionally devised on the top side of the substrate, interconnected to the varactor diodes through shorting vias. Two 10 pF DC blockers (C1) are integrated to prevent the shorting of DC voltage, and two inductors (L1) of 390 nH each are employed to short the DC pins. The biasing circuit is configured as a series RL circuit intended for the reverse biasing of the varactor diodes. Within this biasing circuit, the inductors (L1) act as RF chokes, and resistors (R1) of 2.2 kΩ are employed to prevent diode damage in the forward bias direction. The proposed reconfigurable sensor utilizes the varactor diode SMV1231-079LF model. In simulations, a nonlinear model of the varactor diode is employed to produce accurate results, and a parametric sweep is conducted to modify the diode's capacitance, facilitating frequency reconfiguration. The single-turn inductance (L_0) is contingent upon various factors, including the length and width of the turn, the dielectric constant of the substrate, and the substrate thickness. The calculation of L_0 can be performed using (6.2), where Z_T is the turn impedance, ε_e is the effective dialectical constant of the substrate, L_T is the turn length, and c is the speed of light. The values of Z_T and ε_e can be determined utilizing conventional microstrip line equations outlined in (6.3)-(6.6), where H signifies the substrate thickness, and W_T is the turn width.

$$L_0 = \frac{Z_T\sqrt{\varepsilon_e}}{c}L_T \tag{6.2}$$

$W_T < H$:

$$\varepsilon_e = \frac{\varepsilon_r + 1}{2} + \frac{\varepsilon_r + 1}{2}\left[\frac{1}{\sqrt{1 + 12\left(\frac{H}{W_T}\right)}} + 0.04\left(1 - \frac{W_T}{H}\right)^2\right] \tag{6.3}$$

$$Z_T = \frac{60}{\varepsilon_e} log_2\left[8\frac{H}{W_T} + 0.25\frac{W_T}{H}\right] \tag{6.4}$$

$W_T > H$:

$$\varepsilon_e = \frac{\varepsilon_r + 1}{2} + \frac{\varepsilon_r + 1}{2}\left[\frac{1}{\sqrt{1 + 12\left(\frac{H}{W_T}\right)}}\right] \tag{6.5}$$

$$Z_T = \frac{120\pi}{\varepsilon_e\left[\frac{W_T}{H} + 1.393 + \frac{2}{3}log_2\left(\frac{W_T}{H} + 1.444\right)\right]} \tag{6.6}$$

To establish a dual-port sensing system, modifications are made to the top side of the substrate, and a DiC (Mini-Circuits ADC-6-13+) is inserted in the reverse direction. The RF source is connected to the output of the DiC, while the input is linked to the proposed sensor. The reflected signal from the sensor is captured from the coupling port of the DiC and subsequently connected to the sensor's output, as depicted in Fig. 6.4(a). DC blockers are integrated at the sensor's input and output ports to prevent RF and DC signal coupling. This proposed structure is completely passive and doesn't require any DC biasing voltage. However, in a practical sensing system, the presence of an RF reader is essential for wirelessly sending and receiving RF signals. An amplifier is incorporated at the sensor input port to counteract the impact of free-space path loss. The *Mini-Circuits* GALI-74+ amplifier model is employed, providing a gain of 20 dB. The entire system, comprising the sensor, DiC, and amplifier, is illustrated in Fig. 6.4(b). The power consumption of the amplifier is 384 mW, which may be excessive for low-power applications. In such cases, an alternative approach is to use a high-sensitivity receiver instead of a power-hungry amplifier. A high-sensitivity receiver can detect weak signals more efficiently, reducing the need for amplification and lowering overall power consumption. This approach enhances the energy efficiency of the system, making it more suitable for battery-operated or energy-harvesting applications where power availability is limited.

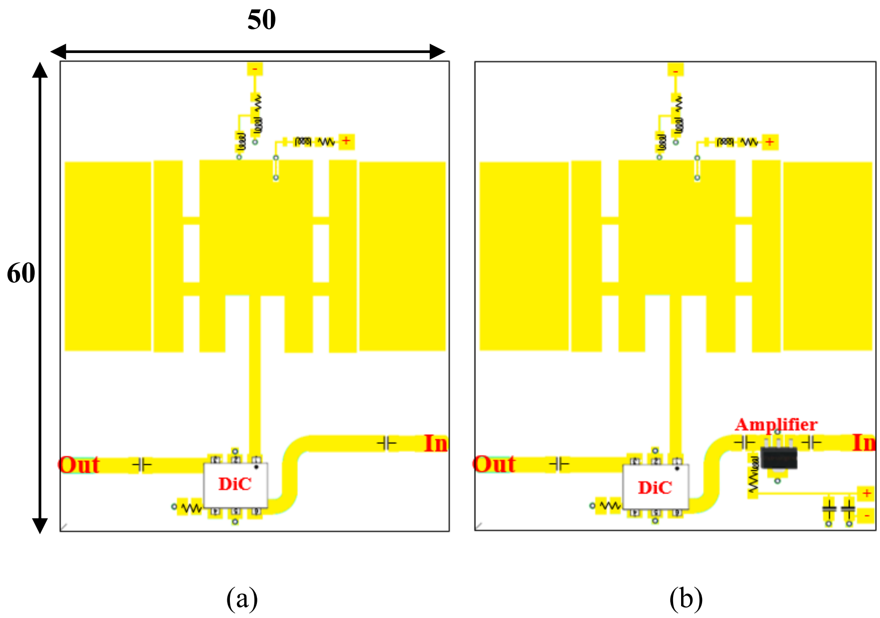

Fig. 6.4. Modified miniaturized dual-band sensor for a complete system, (a) integration of a DiC, (b) integration of a DiC and an amplifier.

6.3 Sensor Results and Performance Analysis

To validate the concept and assess the performance of the miniaturized dual-band sensor, the proposed sensing system is meticulously designed and simulated using the Rogers RO4003C substrate in CST MWS 2019. Furthermore, physical prototypes of the proposed sensor, both with and without the amplifier, are fabricated and depicted in Fig. 6.5.

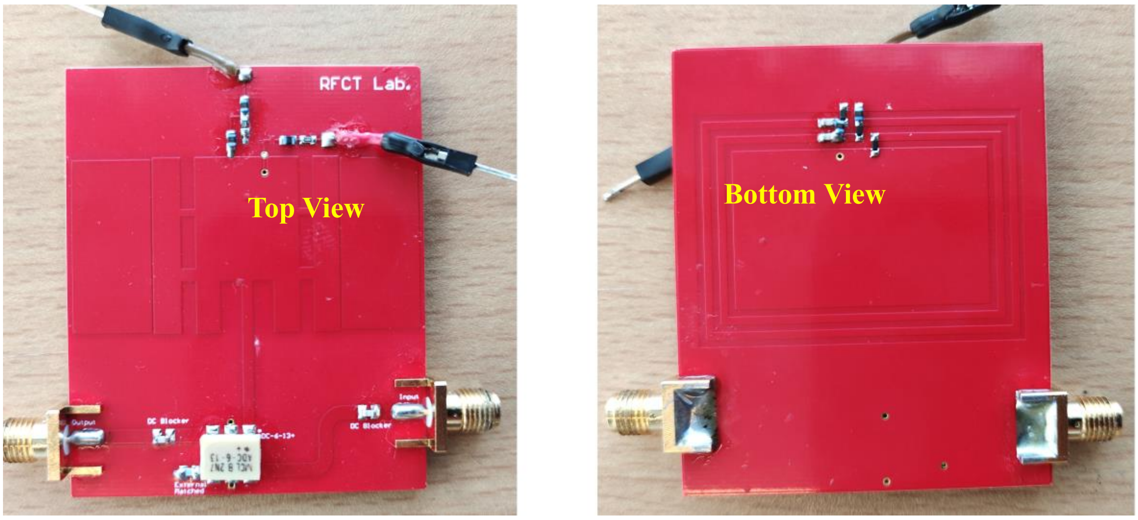

(a)

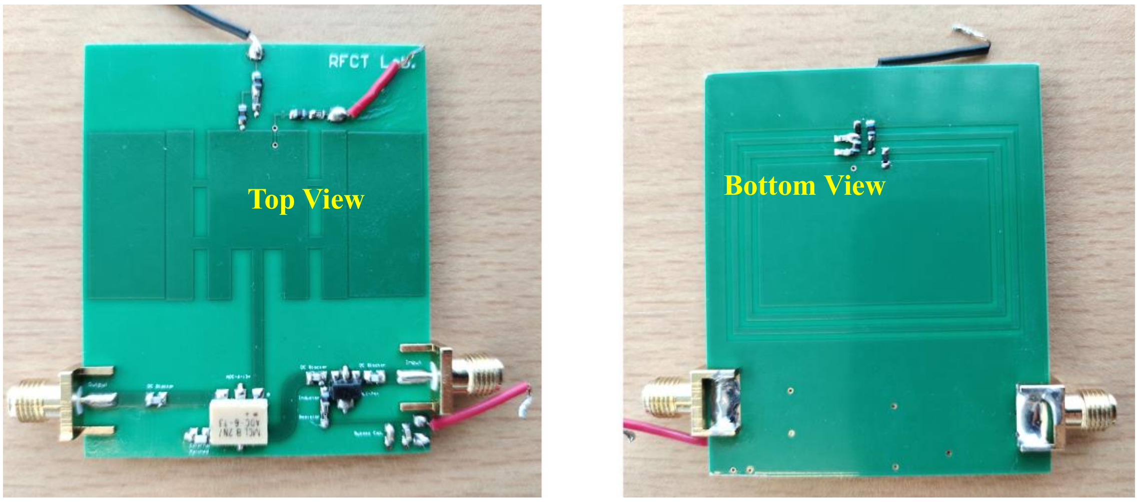

(b)

Fig. 6.5. Fabricated prototypes of the proposed dual-band sensing system on Rogers substrate, (a) without amplifier, (b) with amplifier.

6.3.1 Simulated and Measured Results of the Proposed Sensor

The proposed sensor is dual-band, and its resonance frequency can be adjusted using varactor diodes. This sensor is designed to measure the VWC in the soil through FDR, where the measurement is based on the frequency variation in the reflection coefficient (S11). In the measurement setup, an additional DiC is employed at the input of the sensor, as shown in Fig. 6.4(a), to create a dual-port sensor. The frequency variation in the transmission coefficient (S21) is subsequently used to measure the VWC in the soil.

To analyze the performance of the proposed system and validate the results, the measurement setup as illustrated in Fig. 6.6 was employed. A $40 \times 40 \times 40$ mm^3 block, printed with a 3D printer, serves as the soil container. To measure the variations in the frequency response, a 4-port R&S VNA (VNA-ZVA40) is utilized, as depicted in Fig. 6.6. To guarantee precise frequency response readings, the VNA underwent calibration using a Short-Open-Load-Through (SOLT) standard before initiating the measurement. The acquired frequency responses can be employed to deduce the permittivity values, subsequently correlating them with the soil's VWC. Soil permittivity is affected by multiple factors, including soil type, moisture content, and the concentration of various materials [199]. For example, soil permittivity typically rises with elevated moisture levels, and the presence of potassium chloride can further amplify this effect. To achieve accurate VWC measurements, maintaining consistency in other parameters becomes imperative. This implies the necessity of calibrating the system for a particular soil type and material concentration, requiring a new calibration for a different soil type and changed materials concentration. To validate the concept in the laboratory, pure washed fine sand from Bagged Product Supplies [246], devoid of impurities, is utilized. The correlation between VWC and permittivity can be established by referencing a calibration lookup table, as illustrated in TABLE 6.1 and TABLE 6.2. The imaginary part of permittivity can be neglected at 1.3 GHz as the maximum value is 1.4 at 30% VWC. The proposed sensor is versatile and adaptable for different soil types such as sand, loam, and clay. The sensor's data can be converted into soil permittivity, which can be correlated to VWC using TABLE 6.1 and TABLE 6.2. For a broader range of soil sets, the proposed sensor is also trainable, and Artificial Intelligence (AI) techniques can be applied in the future to convert RAW data to the VWC.

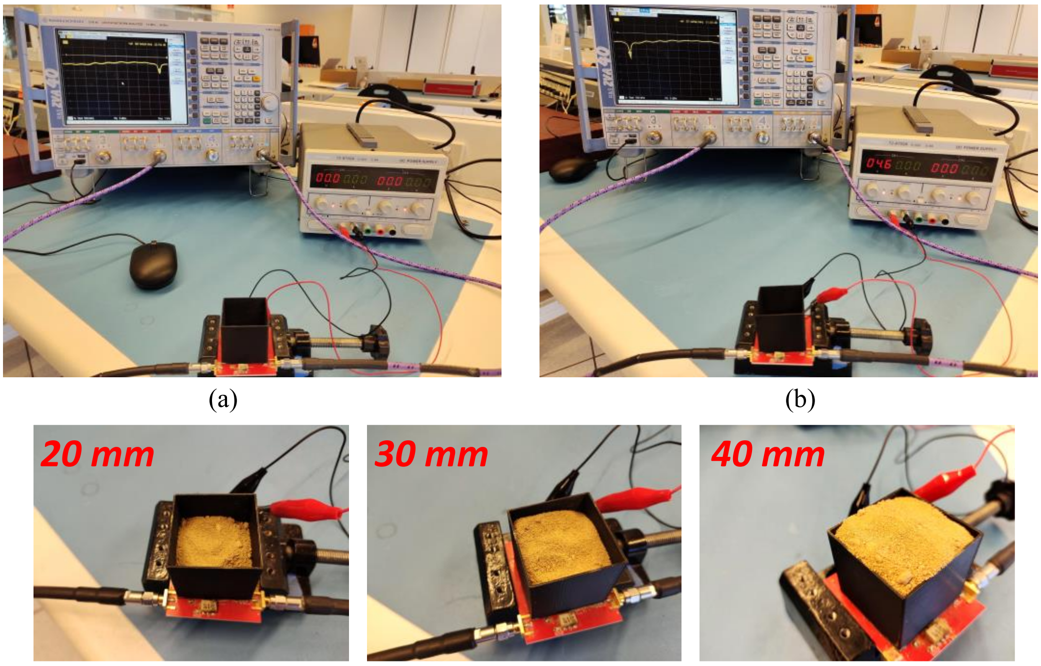

(a) (b) (c)

Fig. 6.6. Soil moisture measurement setup, (a) 0 V biasing, (b) 4.6 V biasing, (c) soil with different VUTs.

TABLE 6.1. COMPLEX SOIL PERMITTIVITY FOR VARIOUS VWCS AT 1.3 GHZ [229].

	VWC (%)	0	5	10	15	20	25	30	40
Sand	ε'_r	3.7	4.3	6.4	9	12	15.8	19	-
	ε''_r	0	0.2	0.6	0.7	0.8	1	1.4	-
Loam	ε'_r	3.4	4.5	6	7.6	9.8	12.6	16.5	24.5
	ε''_r	0	0.1	0.8	1	1.3	1.5	1.9	3
Clay	ε'_r	3	4	5.2	6.6	8.3	10.6	13.8	21
	ε''_r	0	0.5	1	1.2	1.8	2.5	3	4.6

TABLE 6.2. COMPLEX SOIL PERMITTIVITY FOR VARIOUS VWCS [229, 249].

MHz	VWC (%)	0	5	10	15	20	25	30
Sand	ε'_r	2.2	6	10	14	19.6	23	25
0.3 GHz	ε''_r	0	0.2	1	1.2	2	-	-
Loam	ε'_r	2.8	5.8	10	16	22	26	-
0.3 GHz	ε''_r	0	1.8	6	10	16	20	-
Clay	ε'_r	3.2	4.5	8.5	11	13	16	-
0.5 GHz	ε''_r	0	0.15	0.3	0.5	1	1.8	-

Soil moisture sensors are typically designed to measure up to a VWC of 30%, which covers the range most relevant for agriculture [16, 185, 195, 196, 250, 251]. Beyond this threshold, soil permittivity increases rapidly, potentially leading to saturation and waterlogging that can impair root function and reduce oxygen availability in the soil [252-254]. Maintaining a VWC below the threshold is essential for optimal irrigation and avoiding oversaturation, a crucial strategy in arid regions like Australia, where water conservation is vital. This approach effectively prevents conditions detrimental to plant health while maximizing water use efficiency. The simulated and measured results of the proposed dual-band sensor are depicted in Fig. 6.7. The measured frequency of the unloaded sensor is 960 MHz with 0V biasing and 575 MHz with 4.6V biasing. As the soil moisture content rises, the resonance frequency in both bands shifts to lower values. Across a spectrum of soil moisture levels, from 0% (representing dry soil) to 30% (indicating fully wet soil), the measured resonance frequencies exhibit variations. In the upper band, the frequencies range from 942 to 900 MHz, while in the lower band, they vary from 562 to 513 MHz. In the experimental outcomes, the inclusion of the Directional Coupler (DiC) has resulted in an approximate 6.5 dB coupling loss. However, for a fair comparison between simulated and measured results, normalized values have been presented in Fig. 6.7(b) and Fig. 6.7(c). Fig. 6.7 reveals a strong correlation between the simulated and measured results, affirming the validity of the proposed sensor. Multiple tests have been conducted to assess the sensor's accuracy across a range of VWC scenarios. In each test, the frequency response is recorded, revealing a maximum variation of ±4 MHz across three distinct tests. Notably, a linear relationship has been observed between permittivity and frequency variation (Δf), as shown in Fig. 6.8. The imaginary part of the permittivity has been disregarded, considering a maximum value of 1.4 for 30% VWC at 1.3 GHz, as outlined in TABLE 6.1. To validate the sensor's results, two standard devices, namely the Dielectric Assessment Kit (DAK 12) [247] for measuring soil permittivity and the TDR-315L sensor [248] for assessing VWC, were employed. The sensor exhibited similar behavior to the standard devices, affirming the authenticity of its results.

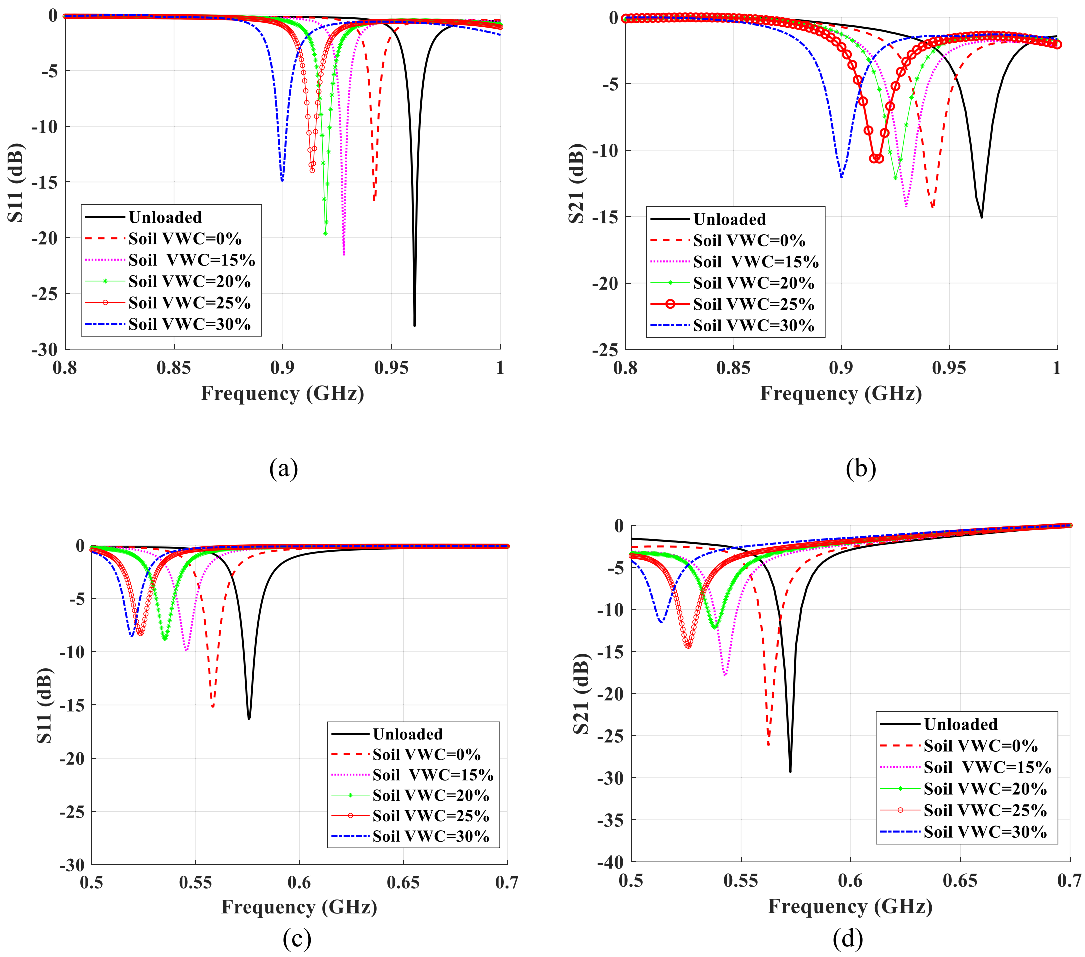

Fig. 6.7. Simulated and measured responses of the sensor for different VWCs, (a) simulated at 900 MHz, (b) measured at 900 MHz, (c) simulated at 500 MHz, (d) measured at 500 MHz.

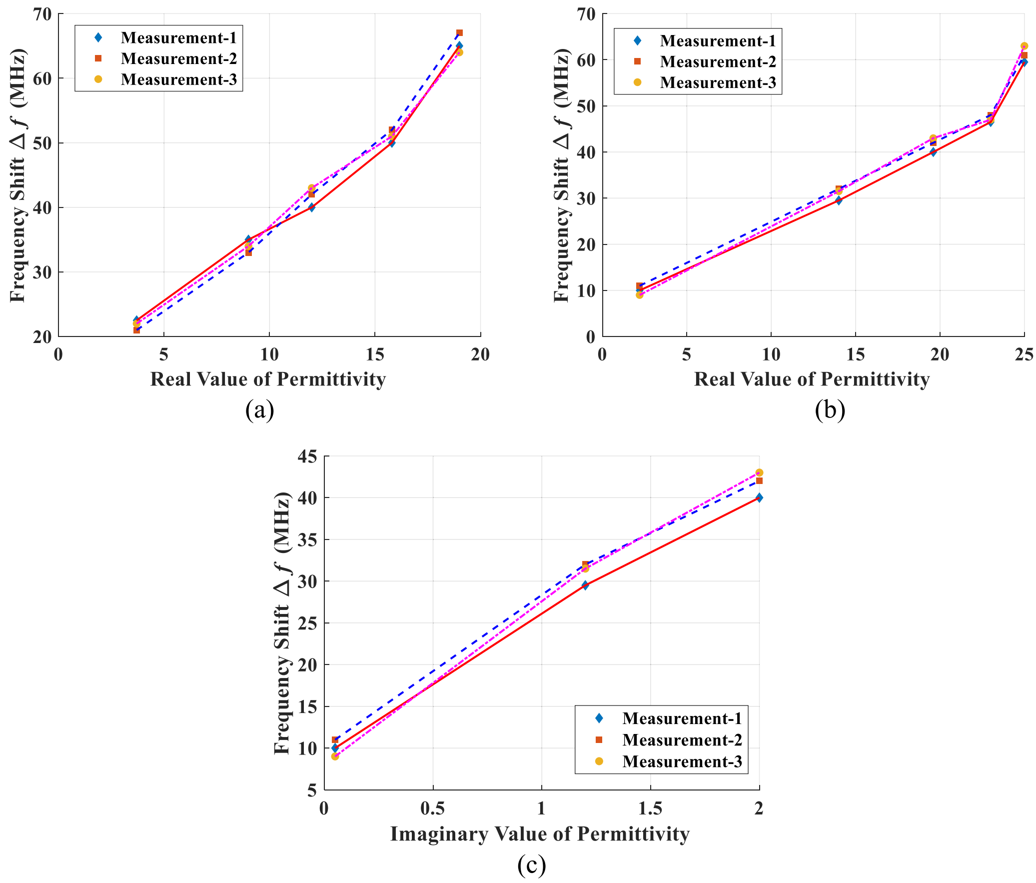

Fig. 6.8. Relationship between frequency variation and permittivity, (a) real permittivity at 900 MHz, (b) real permittivity at 500 MHz, (c) imaginary permittivity at 500 MHz.

In specific scenarios, the water content at the soil surface may be different than that within the soil, introducing the possibility of inaccurate VWC measurements. Thus, a sensor capable of covering a larger VUT is essential for precise measurements. The penetration depth (δ) of an RF signal into the soil, which depends on the signal's frequency and the soil's dielectric properties, can be increased by using lower frequencies as defined in (6.7), where f is the resonance frequency, μ is the relative permeability and σ is the soil conductivity. A dual-band low-frequency sensor enhances soil moisture assessment, allowing for selecting either frequency to assess moisture at different depths. For assessment, a reference device, the DAK 12 (Dielectric Assessment Kit), was utilized to measure soil conductivity, as shown in Fig. 6.9(a). The depth limits of the proposed system at both frequency bands are illustrated in Fig. 6.9(b). At 900 MHz, the penetration depth of the signal in dry sandy soil (0 to 10% VWC) ranges from 15 to 25 cm but decreases in wet soil (15 to 30% VWC). Similarly, at 500 MHz, the signal's penetration depth in dry sandy soil spans from 30 to 45 cm but decreases in wet soil.

$$\delta = \frac{1}{\sqrt{\pi f \mu \sigma}} \tag{6.7}$$

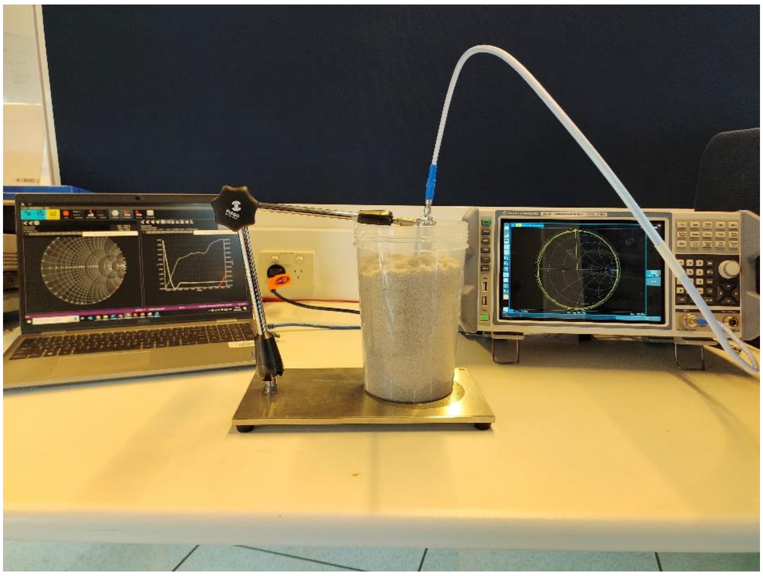

(a)

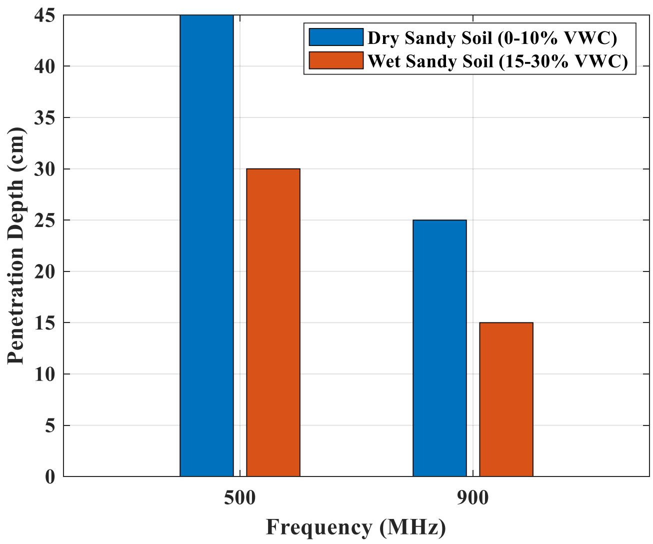

(b)

Fig. 6.9. (a) DAK 12 conductivity measurement for different VWCs, (b) Depth limits of the proposed sensing system.

To assess the dependency of the frequency response on the volume of the soil, different heights of sand are utilized in the test setup, as illustrated in Fig. 6.6(c). The frequency responses for three different heights (20 mm, 30 mm, and 40 mm) have been recorded for dry soil, and the measured results are displayed in Fig. 6.10. It is evident from these results that the proposed sensor exhibits zero sensitivity to variations in the VUT of the soil, showcasing its capability to cover a large soil volume for accurate VWC measurements.

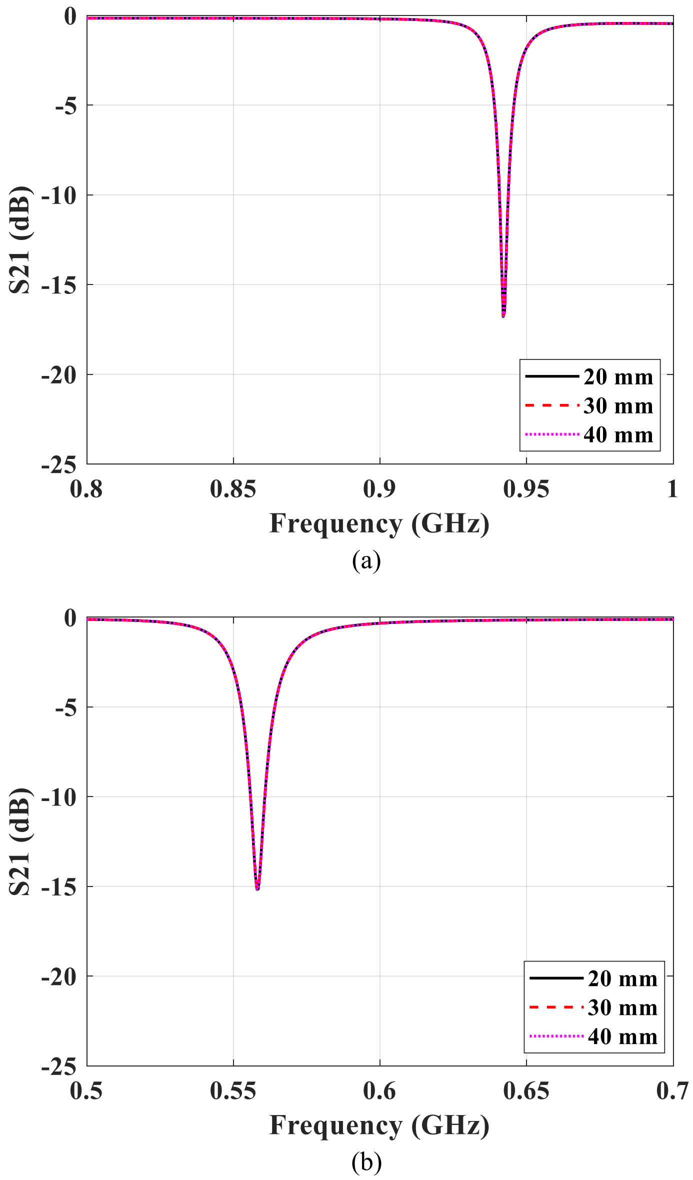

Fig. 6.10. Frequency responses of the proposed sensor for different VUTs of soil, (a) 900 MHz band, (b) 500 MHz band.

To validate the sensor's performance, the TEROS 12 sensor is employed, a standard device for measuring VWC [255]. Sensor's readings are closely aligned with those from the TEROS 12, affirming the accuracy of the results. Fig. 6.11 displays the estimated errors for the two devices. Across various tests, a maximum frequency variation of ±4 MHz resulted in an error margin of less than 4% for different VWC levels. This consistency demonstrates the precision of the system relative to the standard device.

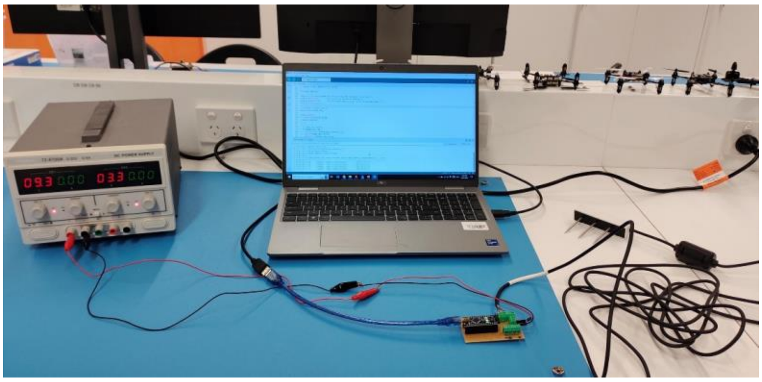

(a)

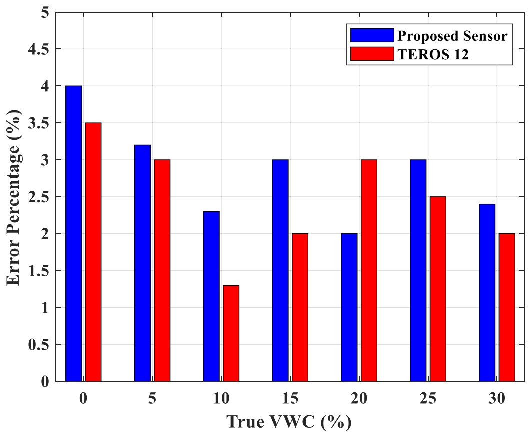

(b) (c)

Fig. 6.11. (a) Measurements setup, (b) soil sample, and (c) error percentage (%) of sensors for different VWC levels.

To assess the proposed sensor in a real-world setting, frequency responses were measured in a vötschtechnik Environmental Testing Chamber [256]. The measurement setup illustrating the assessment of frequency variations under various atmospheric conditions is demonstrated in Fig. 6.12. In real scenarios, temperatures may decrease below freezing point during winter nights and significantly rise to 45 °C on summer days, while humidity may vary between 40% and 70%. To evaluate the frequency variation of the sensor, both temperature and humidity have been varied to replicate real environment conditions for 15% VWC. The sensor's performance is evaluated by varying temperature and humidity. For temperature variation measurements, a constant humidity of 55% was maintained, and for humidity variation measurements, 25 °C was maintained inside the chamber. The measured results are presented in Fig. 6.13.

(a)

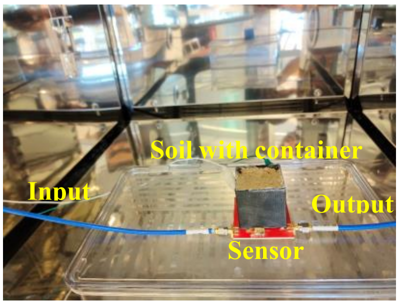

(b)

Fig. 6.12. (a) Measurement setup in the Environmental Testing Chamber (Temperature and Humidity), (b) sensor placement inside the chamber.

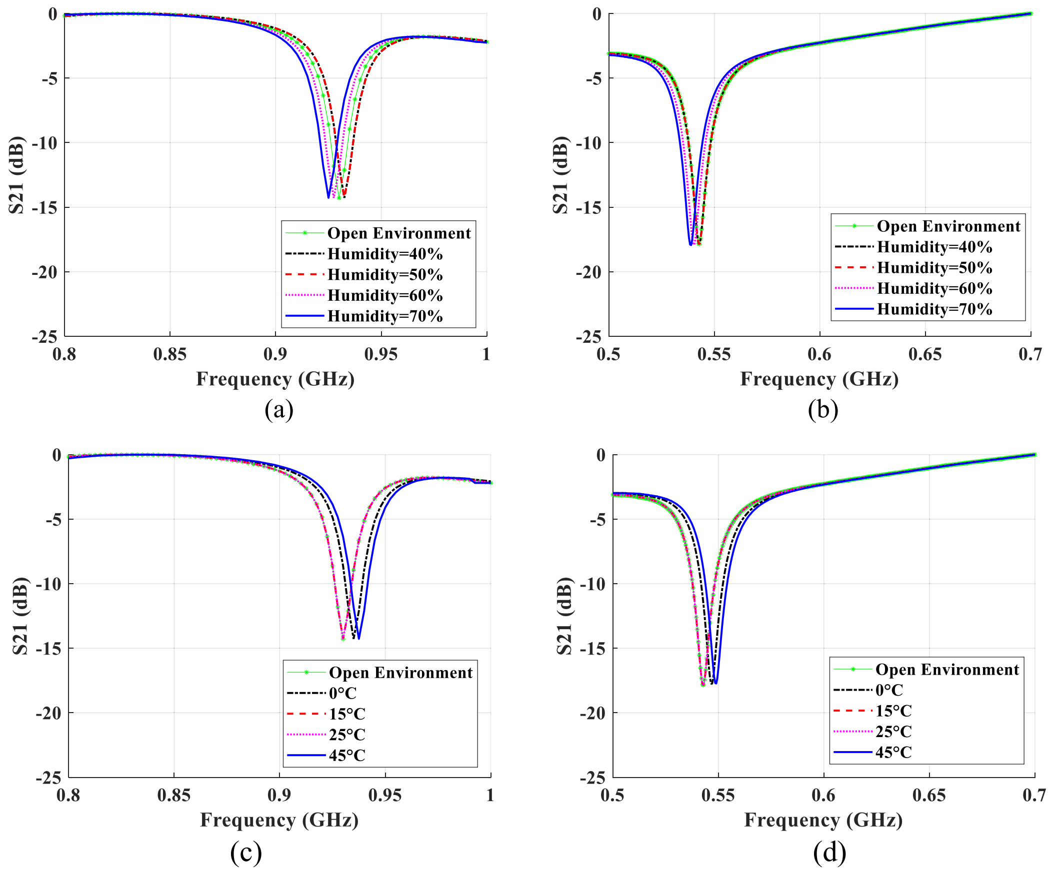

Fig. 6.13. Frequency responses of the proposed sensor for 15% VWC in different environmental conditions, (a) 900 MHz with various humidity levels, (b) 500 MHz with different humidity levels, (c) 900 MHz with different temperature values, (d) 500 MHz with different temperature values.

The presence of moisture in the air (humidity) can influence soil moisture, with higher water content in the air elevating soil moisture at the surface. Therefore, the frequency shifts to the left with increasing humidity, representing higher VWC, as depicted in Fig. 6.13(a) and Fig. 6.13(b). An increase in temperature can impact soil moisture, with higher temperatures leading to a reduction in soil moisture due to vaporization. Conversely, at extremely low temperatures, water in the soil exists in both liquid and solid forms, which can also decrease the VWC in the soil, as illustrated in Fig. 6.13(c) and Fig. 6.13(d). However, under normal weather conditions, the VWC in the soil remains unchanged.

6.3.2 Measured Results of the Proposed Sensor with Amplifier

To implement a practical sensing system for real-world application, an RF reader needs to transmit a CW signal to the sensor, and the sensor responds back with the information signal. This system requires wireless connectivity, and antennas are essential for transmitting and receiving RF signals. The practical implementation of the proposed sensor is depicted in Fig. 6.5(b), where an amplifier is employed to compensate for path loss.

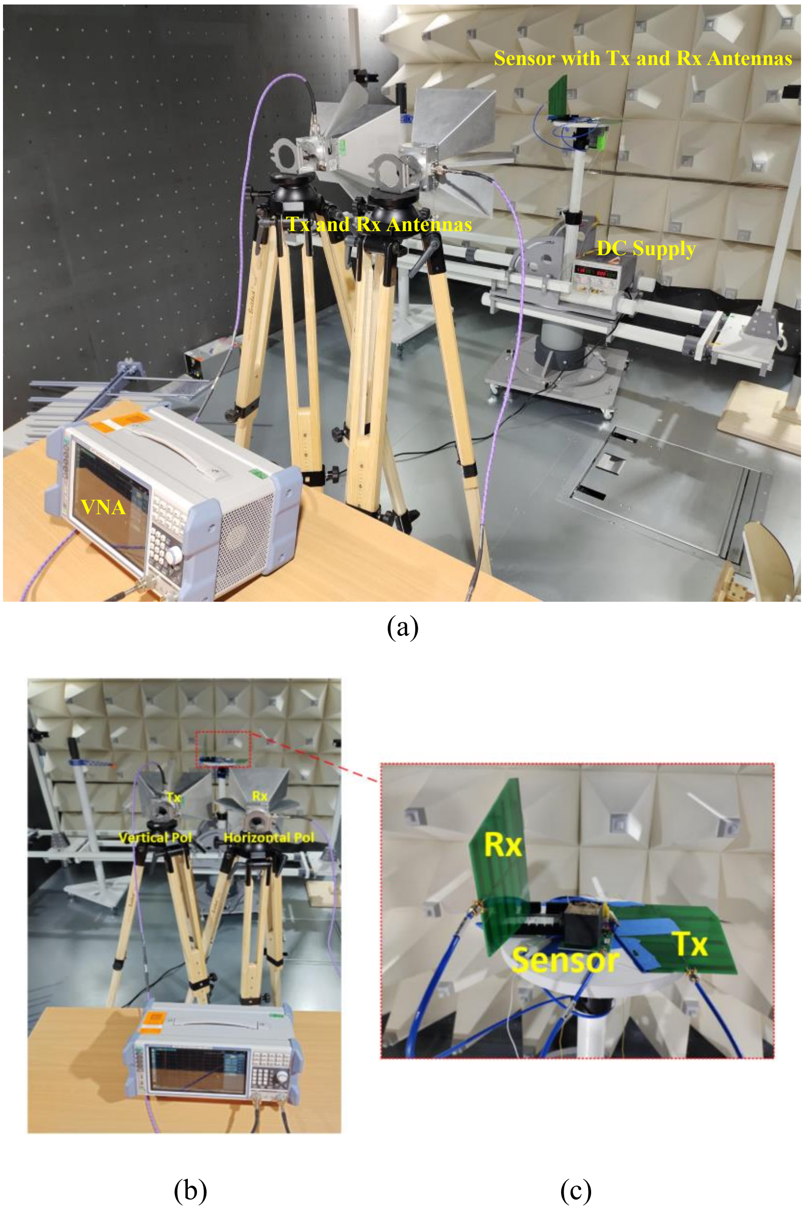

Fig. 6.14. (a) RF measurement of the proposed dual-band antenna in RFCT Laboratory, (b) reader view, (c) magnified view of the sensor.

A laboratory measurement setup, as illustrated in Fig. 6.14, is utilized to measure diverse soil moisture levels in a practical application. A 2-port R&S VNA (ZNLE6), along with two R&S horn antennas (HF907), served as the RF reader. Both antennas were positioned orthogonally to minimize the coupling between transmitted and received signals. At the sensor side, two end-fire planar log-periodic antennas, with a gain of 5 dBi each, are utilized for receiving the CW and transmitting the information signals. The distance between the reader and the sensor was maintained at 1.5 m, and a 20 dB amplifier was employed in combination with the 20 dB antenna gains to compensate for the path loss. Fig. 6.15 presents measured results for various VWCs at 900 MHz, providing a conclusive validation of the proposed sensor's performance, as illustrated in Fig. 6.7.

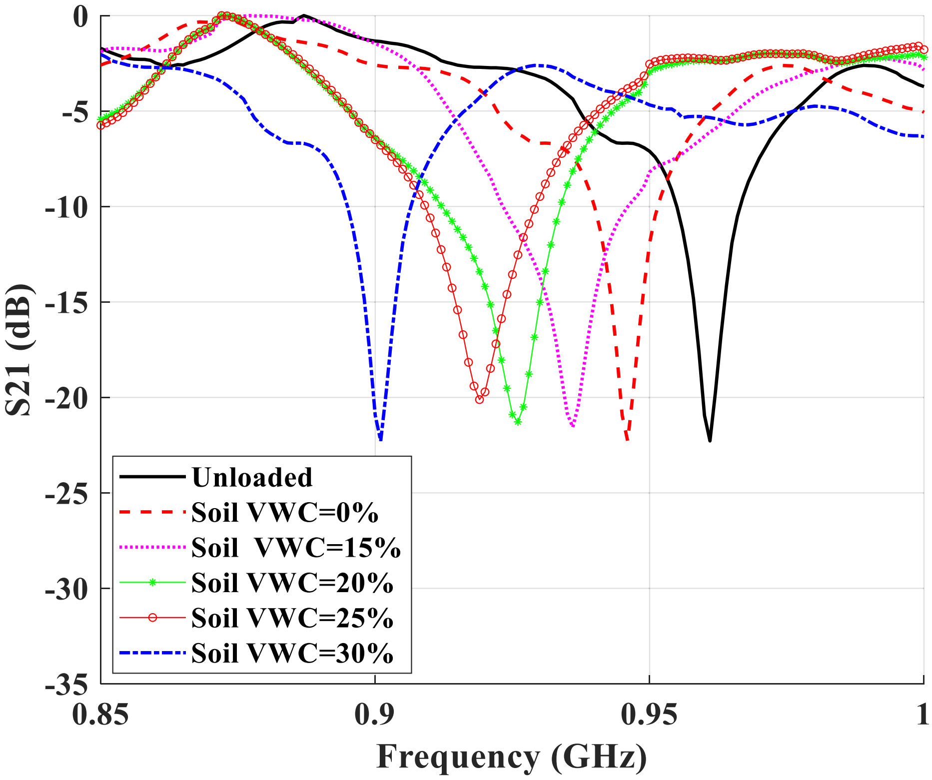

Fig. 6.15. Measured RF results for different VWCs at 900 MHz.

To assess the accuracy of the proposed sensor, the sensitivity of the dual-band sensor is computed using (6.8),

$$Sensitivity = \theta_s = \left| \frac{f_{m1} - f_{m2}}{f_{l0}(\varepsilon_{rm1} - \varepsilon_{rm2})} \right| \times 100 \tag{6.8}$$

here f_{l0} is the lowest unloaded resonance frequency, f_{m1} and f_{m2} are the resonances of different materials, ε_{rm1} and ε_{rm2} denote the relative permittivity of the materials. Furthermore a benchmark is used, indicated in (6.9), as a performance indicator to assess the overall sensor's performance, considering the parameters such as θ_s, the highest length of the sensor (l_m), the highest measured permittivity (ε_m), and number of bands (N).

$$Performance\ Indicator = \varphi = \frac{\theta_s \times \varepsilon_m}{l_m} \times N \tag{6.9}$$

Taking these evaluations into account, a comparative summary of the proposed sensor performance against reported sensors is presented in TABLE 6.3.

TABLE 6.3. COMPARISON OF THE REPORTED SENSOR WITH OTHER STRUCTURES

Ref.	Size at f_{l0} (λ_0^2)	f_{l0} (GHz)	Number of Sensing Bands	Sensing Method	Remote Monitoring	Environment Compensation	θ_s (%)	ε_m	φ $\left(\frac{1}{\lambda_0}\right)$
This Work	0.095×0.095	0.572	2	3-CSR	YES	YES	1.7	25	894.6
[16]	0.67×0.13	4	2	SR and CSR	NO	NO	0.9	16.7	44.8
[19]	0.32×0.2	2.45	1	M-CSRR	NO	NO	0.2	70	43.8
[20]	0.198×0.198	2.38	1	EBG Resonator	NO	NO	0.22	70	79.2
[182]	0.18×0.37	2.234	1	SRR	NO	NO	0.044	70	8.4
[111]	0.158×0.158	0.95	1	CSR	NO	NO	1.7	16.7	179.7
[195]	0.34×0.034	1.017	1	Shorted-Dipole	YES	NO	0.614	19	34.3
[185]	0.38×0.38	0.56	1	Metamaterial Absorber	YES	NO	0.109	19.1	5.5
[250]	1.23×-	1.01	1	Open-End Microwave Coaxial Cable Resonator	NO	NO	0.13	15.8	1.7
[257]	0.35×0.59	1.32	1	Microstrip Open-Loop Resonator	NO	NO	11.2	4	75.9
[188]	0.6×0.4	3.49	1	Complementary Curved Ring Resonator	NO	NO	4.47	4.4	32.8
[251]	0.25×0.117	1	1	CSRR	YES	NO	0.5	35	149.6
[196]	0.42×0.44	4.7	1	Frequency Selective Filter	NO	NO	0.214	26	12.6

The proposed sensor demonstrates dual resonances for environmental compensation, offering superior sensitivity and accuracy, a compact size, and a notably high-performance indicator compared to reported sensors. Furthermore, the sensor is versatile and capable of operating in either a single-band mode (500 and 900 MHz) or a dual-band configuration. Multiband analysis independently examines frequency responses at various frequencies enabling the development of a calibration procedure that accounts for environmental effects. The proposed remote monitoring system is capable of covering a large VUT, resulting in cost-effectiveness as fewer sensors will be required to cover a large farming area.

6.4 Conclusion

This chapter introduces a compact dual-band SMS for smart agriculture applications. The versatility of the proposed wireless sensor allows it to operate in both single and dual-band configurations. In the single-band configuration the 900 MHz band is employed for homogenous soil VWC analysis while the 500 MHz band is utilized for dual-band analysis, facilitating precise measurements and environmental compensation in heterogeneous soil. The proposed sensor comprises a 3-CSR, achieving compactness at a low resonance frequency, rendering the design apt for covering larger soil volumes. Three varactor diodes have been incorporated across 3-CSR to enable switching between the frequency bands. A DiC is integrated to the input port of the sensor to create a dual-port configuration, and a 20 dB gain amplifier is connected to the input port to offset DiC and path losses. The integration of a dual-band sensor, DiC, and amplifier enhances the system's suitability for accurate VWC measurements eliminating the need for an external portable VNA. Furthermore, the low resonance frequencies of the sensor enable it to cover a large VUT, resulting in cost efficiency as a smaller number of sensors will be needed to cover the farming area. Sensors with and without amplifiers were fabricated and tested. A close agreement between simulated and measured results suggests the validity of the sensor's performance. A vötschtechnik Environmental Chamber is employed to create a realistic environment for evaluating the sensor's performance in real-world conditions. The integration of a dual-band SMS, DiC, and amplifier enables the realization of precise remote monitoring for smart farming in a real-world scenario.

7

7 Non-Linear Passive RF Switches

(Three Journal papers have been generated based on this chapter's material, "Passive Non-Reciprocal Signal Switching: A Compact Backward Coupler Using a Nonlinear Metamaterial Structure", "Non-Reciprocal and Autonomous Signal Routing Solution: A Power-Agile Passive Multi-Band T/R Switch Using a Nonlinear Metamaterial Network", and "A Multi-Band Forward-Backward Non-Linear Metamaterial Network: An Agile Solution for Wireless Power Transfer, Sensing, and Communication".)

7.1 Introduction

Circulators have been used as a core component along with transmitter and receiver in various IoT applications including smart homes, industrial automation and monitoring and smart sensing. Circulators control the flow of radio frequency (RF) signal in a particular direction, providing high isolation in the other direction and facilitating joint sensing and communication for remote control and data collection [30, 111, 199].

These devices play a vital role by controlling the RF signal flow in two-way communication and provide good isolation, e.g., 20 dB, between the transmitter and receiver devices. Although the high isolation without any control mechanism and the passive nature of these devices makes them very useful in IoT applications, they require a magnetic ferrite material to achieve this high isolation. Although the high isolation without any control mechanism and the passive nature of these devices make them very useful in IoT applications, they require a magnetic ferrite material to achieve this high isolation [29]. Few magnetless devices have been introduced, but they comprise active elements and require an external biasing network to change the direction of the RF signal.

To address these challenges, this chapter introduces a novel technique to develop symmetrical output-backward and forward-backward couplers that can control the direction of the RF signal based on the power applied at the input. The 4-port coupler consists of multiple unit cells (UCs), and each UC comprises non-linear Schottky diodes and interdigital capacitors. Input is applied to port 1 of the coupler, which can be directed to port 2/port 3 in case of output-backward configuration and port 4/port 3 in forward-backward configuration. When the power level is low, all the power can be delivered to port 2 or port 4, while at a high-power level, the power will be delivered to port 3. The proposed couplers are magnetless, compact, wideband, and no external biasing is required to change the direction of the RF signal. The proposed structures are simulated and fabricated to validate their performance, and the measurement results show strong agreement with the simulations. The designs effectively enhance signal routing and isolation performance for passive switching applications and enable efficient communication and power management by allowing seamless switching between data transmission and reception using a single antenna.

7.2 Working Mechanism

To overcome the narrowband, bulkiness, and voltage-basing challenges, a new technique has been proposed to realize a T/R switch. Fig. 7.1 shows the block diagram of the proposed transmit/receive (T/R) switch consisting of four ports: ‘Input’, ‘Output’, ‘Backward Coupled’, and ‘Forward Coupled’.

When a low-power RF input is applied at port 1, the signal is transmitted to port 2 with minimal insertion loss. Depending on the design parameters, the low-power signal may also be transmitted to port 4. Either of these ports can be connected to the receiver. However, if a high-power signal is applied to port 1, all of the signal is transferred to port 3 without the need for an external DC voltage, which can then be connected to the transmitter. The proposed T/R switch is entirely passive and can integrate low and high-power receivers and transmitters.

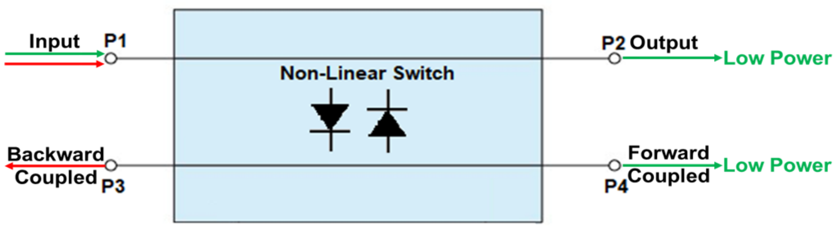

Fig. 7.1. Block diagram of the proposed compact non-linear T/R passive switch.

7.2.1 2-Unit Cell (2-UC) Configuration

For the 2-unit cell (2-UC) configuration, a practical arrangement is shown in Fig. 7.2(a), wherein a receiving antenna is linked to the 'Input Port' (port 1), a receiver (Rx) is connected to the 'Output Port' (port 2), a transmitter (Tx) is connected to the 'Backward Port' (port 3), and a termination is connected to the 'Forward Port' (port 4). The antenna receives the RF signal, which it then transmits to either port 2 or port 3, depending on the power level at port 1. If the received power is low, the signal is broadcast to port 2 with low insertion loss for a low-power Rx; other ports will have substantial insertion losses. The signal will be routed to port 3 with minimal insertion loss for a high-power Tx, whereas other ports will have significant insertion losses, if the received power is high.

For the 2-UC cell configuration, another setup in a bi-directional transceiver (Tx/Rx) is depicted in Fig. 7.2(b). Two Tx/Rx connections are made to ports 2 and 3, and two antenna connections are made to ports 1 and 4. The signal transmission is in the right direction if antenna-1 (A1) captures the RF signal. The signal is sent to Rx for low-power levels; for high-power, it is shifted to Tx at the backward port. The antenna-2 (A2) signal follows the same principles but travels in the leftward direction. The proposed coupler can be cascaded to further increase isolation, as shown in Fig. 7.2(c).

7.2.2 16-Unit Cell (16-UC) Configuration

For the 16-unit cell (16-UC) configuration, a receiving antenna is connected to port 1, a termination is connected to port 2, a Tx is connected to port 3, and a Rx is connected to port 4, as shown in Fig. 7.2(d). The RF signal is captured by the antenna and based on the power level at port 1, the signal is delivered to port 4 or port 3. If the received power is low, the signal is transmitted to port 4 with low insertion loss for a low-power Rx, while other ports will provide high insertion losses. However, if the received power is high, the signal will be forwarded to port 3 with low insertion loss for a high-power Tx, while other ports will have high insertion losses. In a bi-directional Tx/Rx for the 16-UC configuration, another configuration is shown in Fig. 7.2(e). Two antennas are connected at port 1 and port 2, and two Tx/Rx are connected to port 3 and port 4. If A1 captures the RF signal, the signal transmission is in the right direction, delivered to Rx for low-power levels and is switched to the backward port for a high-power Tx. For A2, the signal flows in the left direction with the same principles. The isolation can further be improved by cascading the proposed coupler.

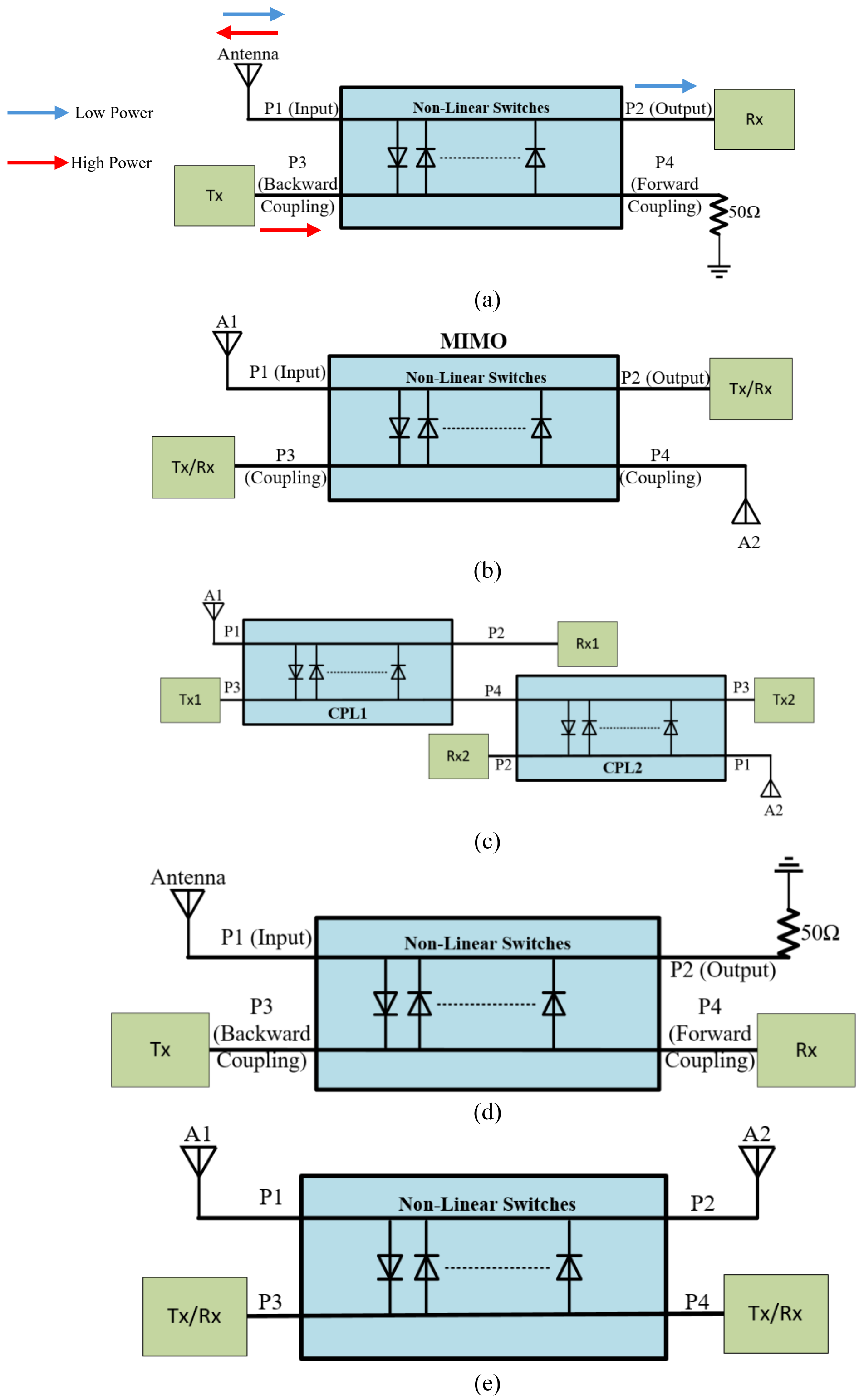

Fig. 7.2. Working principle of the proposed T/R switch, (a) single frequency transceiver (output-backward coupling), (b) bi-directional transceiver (output-backward coupling), (c) high isolation configuration (output-backward coupling), (d) single frequency transceiver (forward-backward couplings), and (e) bi-directional transceiver (forward-backward couplings).

7.3 Design Methodology

The proposed passive T/R couplers are designed using Rogers RO4003C, a substrate with a dielectric constant of 3.55 and a thickness of 1.524 mm. The coupler's dimensions are $L_S \times W_S$, and 2-UC and 16-UC circuit diagrams are illustrated in Fig. 7.3 and Fig. 7.4, respectively. Fig. 7.3 depicts a switch design with a 2-UC configuration, while Fig. 7.4 shows the 16-UC configuration. This four-port coupler integrates metamaterial-based interdigital capacitors, microstrip transmission lines, and Schottky diodes to achieve its functionality.

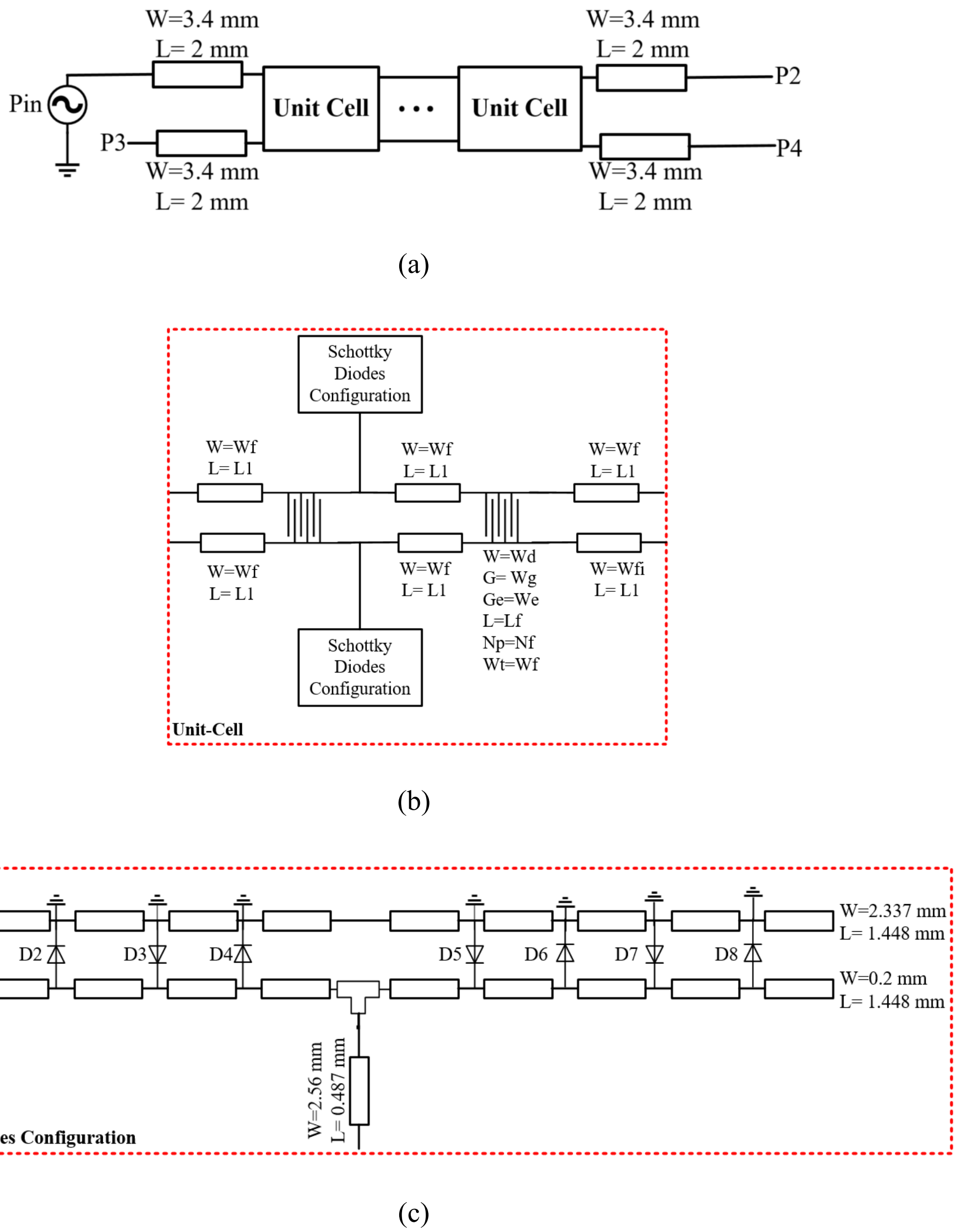

Fig. 7.3. The circuit diagram of the proposed 2-UC coupler, (a) 2-UC design, (b) each UC circuit, and (c) diode connections.

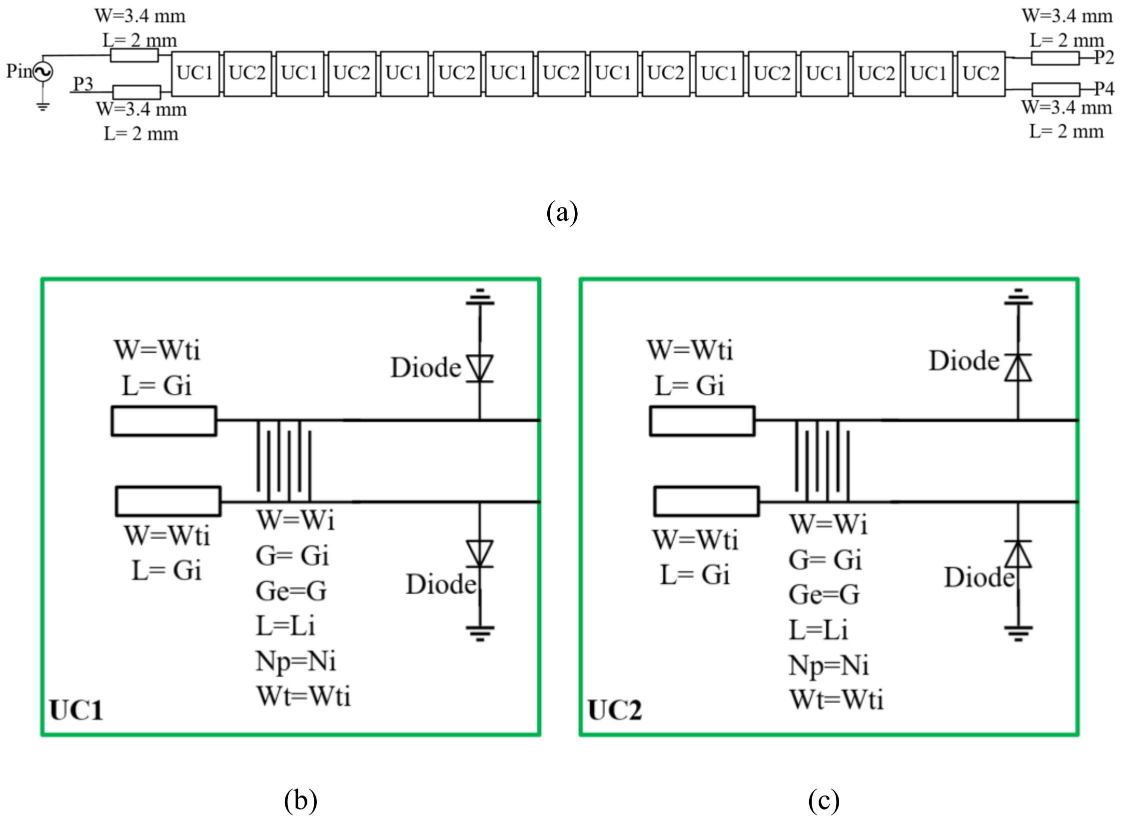

Fig. 7.4. The circuit diagram of the proposed 16-UC coupler, (a) 16-UC circuit, (b) UC1 circuit, and (c) UC2 circuit.

7.3.1 2-UC Design

A 2-UC configuration is developed to realize a Compact Passive Backward Coupler (CPBC) with minimum insertion losses. The design parameters of the interdigital capacitor are listed in TABLE 7.1, where *Wd* is the finger width, *Wg* is the gap between fingers, *We* is the gap at the end of the fingers, *Lf* is the length of the overlapped region, *Nf* is the number of the finger pairs, and *Wf* is the width of the interconnect. The resonance frequency of this configuration is 2.43 GHz. At low-power levels, all signal is transferred to port 2; at high-power, the signal is transferred to port 3. Each UC has two metamaterial-based interdigital capacitors (MIMCs) and 16 Schottky diodes connected symmetrically to both transmission lines. Transmission lines are utilized to prevent DC short between the two conductors of the interdigital capacitor. The directions of the diodes are kept anti-parallel to allow signal flow in both directions, and a total of 32 diodes are used to ensure minimum insertion loss and high isolation between the ports.

TABLE 7.1. PARAMETRIC VALUES IN MM OF METAMATERIAL-BASED INTERDIGITAL CAPACITORS FOR OUTPUT AND BACKWARD COUPLING (2-UC).

Wd	***Wg***	***We***
0.79	0.22	0.2
Lf	***Nf***	***Wf***
4.12	8	1.372
Ls	***Ws***	***L1***
77	16	1.5

The diodes are connected in pairs, where each pair has anti-parallel diodes, as shown in Fig. 7.3(c). The resistance of the diodes can be reduced by increasing the number of diode pairs (n) in parallel. The addition of more diodes can also reduce nonlinear distortion effects in RF applications. With more diodes conducting in parallel, the transition between conduction and non-conduction states becomes smoother. This smoother transition can help in reducing harmonics and intermodulation distortion in RF signals, leading to cleaner signal handling, especially in sensitive RF circuits. Adding more diodes in parallel also improves power dissipation capabilities. Each diode dissipates power based on its forward current and forward voltage drop. With more diodes, the current is shared, reducing the power dissipated by each diode. This distribution can prevent individual diodes from overheating and increase the overall thermal management of the circuit. However, each diode junction has a small capacitance, and with more diodes, the total parasitic capacitance (C_{DE}) may increase. Hence, there is a trade-off between the parasitic capacitance and effective diode resistance (R_{DE}). R_{DE} and C_{DE} can be calculated using below equations, where $\widehat{R_D}$ and $\widehat{C_D}$ are the non-linear resistance and capacitance of a single diode, respectively, and n is the total number of anti-parallel diodes. These non-linear parameters are a function of applied voltage and changes with the incident voltage.

$$R_{DE} = \frac{\widehat{R_D}}{n}$$

$$C_{DE} = n.\widehat{C_D}$$

The effective diode resistance (R_{DE}) is plotted in Fig. 7.5 for different numbers of diode (n). As the value of n increases, R_{DE} decreases. In the beginning, there is an abrupt decrease in the value of R_{DE} but after $n = 8$, increasing the value of n doesn't have any significant effect on R_{DE} (Fig. 7.5).

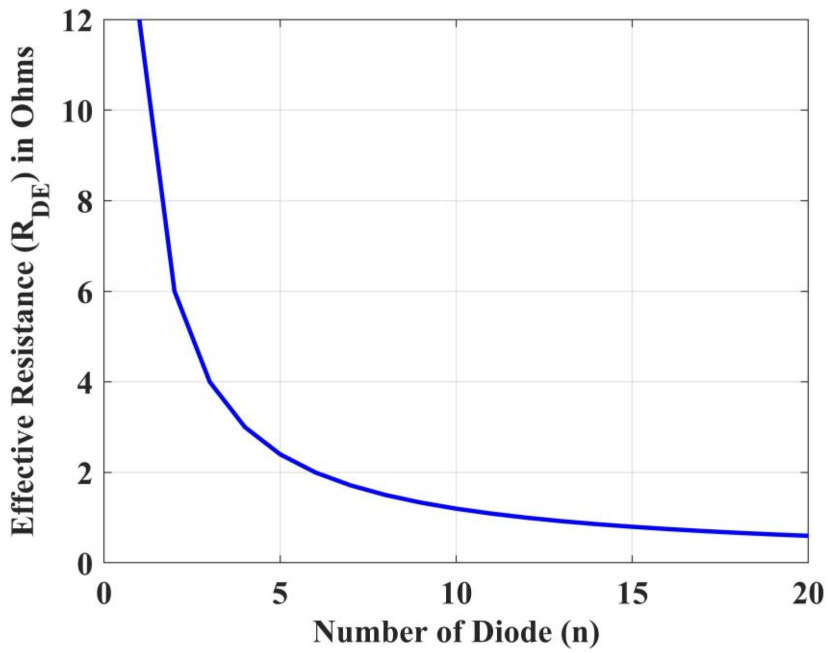

Fig. 7.5. Number of diode pairs vs effective resistance.

The values of R_{DE} and C_{DE} are shown in Fig. 7.6 for different numbers of diodes using the SMS7621 diode model. The value of R_{DE} is decreasing, and after $n = 8$, there isn't any significant difference in the value. Therefore $n = 8$ is selected for the development of the proposed CPBC, where parasitic capacitance is not significant, and the resistance value is small.

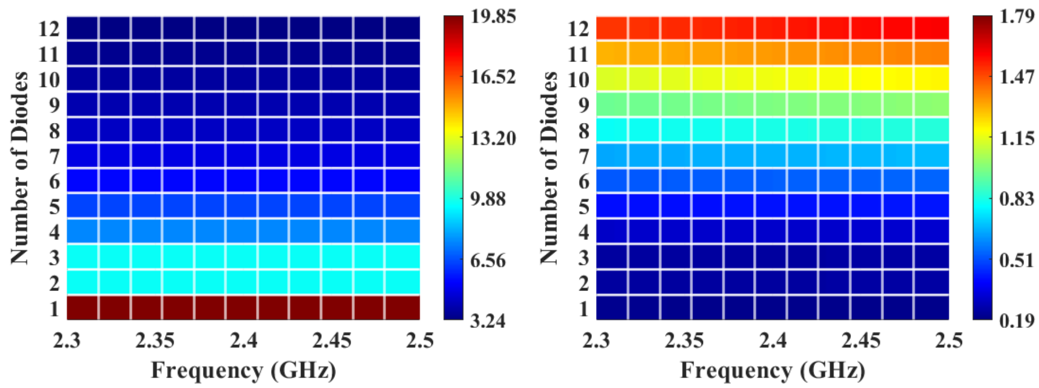

(a) (b)

Fig. 7.6. Number of anti-parallel diodes vs. (a) R_{DE}, (b) C_{DE}.

7.3.2 16-UC Design

A 16-UC configuration is also developed to realize a T/R switch with minimum insertion losses, as shown in Fig. 7.4. Two design configurations have been developed using different parameters, i.e., forward and backward coupling and output and backward coupling.

The design parameters of interdigital capacitors of the Multi-Band Forward-Backward Non-linear Metamaterial Network (M-FBNMN) are listed in TABLE 7.2, where *Wi* is the finger width, *Gi* is the gap between fingers, *G* is the gap at the end of the fingers, *Li* is the length of the overlapped region, *Ni* is the number of the finger pairs, and *Wti* is the width of the interconnect. The configuration operates at 1.9 and 2.52 GHz. At low-power levels, all signal is transferred to port 4; at high power, the signal is transferred to port 3.

Each UC has a Metamaterial-based Interdigital Microstrip Capacitor (MIMC) and 2 Schottky diodes connected symmetrically to both transmission lines. Transmission lines are utilized to prevent DC short between the two conductors of the interdigital capacitor in adjacent UCs. Each adjacent UC has a different orientation of diodes to enable signal flow in both directions. This configuration comprises 16 interdigital capacitors and 32 diodes to ensure high isolation and low insertion loss.

TABLE 7.2. PARAMETRIC VALUES IN MM OF METAMATERIAL-BASED INTERDIGITAL CAPACITORS FOR FORWARD AND BACKWARD COUPLINGS (16-UC).

Wi	***Gi***	***G***
0.**66**	0.68	0.2
Li	***Ni***	***Wt***
5.84	5	0.2
Ls	***Ws***	
218	12	

TABLE 7.3. PARAMETRIC VALUES IN MM OF METAMATERIAL-BASED INTERDIGITAL CAPACITORS FOR OUTPUT AND BACKWARD COUPLING (16-UC).

Wi	***Gi***	***G***
0.755	0.2	0.2
Li	***Ni***	***Wt***
6.7856	3	0.24
Ls	***Ws***	
96	13	

To achieve output and backward coupling with minimal insertion loss, another 16-UC configuration is developed. The design parameters for the MIMC used in output and backward coupling are detailed in TABLE 7.3. The circuit operates at frequencies of 1.6 and 2.1 GHz. Port 2 is enabled at low-power input, while port 3 is enabled at high-power levels.

Each UC includes an MIMC and two symmetrically connected Schottky diodes, which are attached to the transmission lines. The transmission lines in adjacent UCs are designed to prevent a DC short between the two conductors of the interdigital capacitor. To enable bidirectional signal flow, the diodes in neighboring UCs are oriented in opposite directions. This configuration utilizes 32 diodes and 16 interdigital capacitors with varying design parameters to ensure high isolation and low insertion loss.

7.4 Theoretical Analysis

The theory and step-by-step design procedure are outlined in this section. This section also presents a generic model of a 4-port directional coupler, the equivalent circuit of the proposed structures, and their theoretical equations. A general block diagram of a symmetrical 4-port coupler with characteristics impedance (Z_0) is shown in Fig. 7.7. The coupler has four ports, and the circuit is symmetrical around the dotted line. This model can be analyzed using even and odd modes, and the S-parameters can be evaluated to analyze the circuit. The subscript 'e' represents even mode, and 'o' represents odd mode in this work. Considering the symmetry of the circuit, even and odd modes can be defined in equations (7.1)-(7.9).

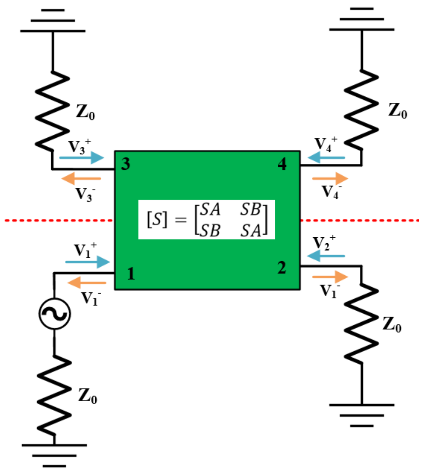

Fig. 7.7. S-parameters of a 4-port coupler.

Even Mode:

$$V_3^{\pm} = V_1^{\pm} = V_{1e}^{\pm} \tag{7.1}$$

$$V_4^{\pm} = V_2^{\pm} = V_{2e}^{\pm} \tag{7.2}$$

$$\begin{bmatrix} V_{1e}^- \\ V_{2e}^- \end{bmatrix} = [[SA] + [SB]] \begin{bmatrix} V_{1e}^+ \\ V_{2e}^+ \end{bmatrix} \tag{7.3}$$

$$S_e = [SA] + [SB] \tag{7.4}$$

Odd Mode:

$$V_1^{\pm} = -V_3^{\pm} = V_{1o}^{\pm} \tag{7.5}$$

$$V_2^{\pm} = -V_4^{\pm} = V_{2o}^{\pm} \tag{7.6}$$

$$\begin{bmatrix} V_{1o}^{-} \\ V_{2o}^{-} \end{bmatrix} = [[SA] - [SB]] \begin{bmatrix} V_{1o}^{+} \\ V_{2o}^{+} \end{bmatrix} \tag{7.7}$$

$$S_o = [SA] - [SB] \tag{7.8}$$

$$[SA] = \frac{S_e + S_o}{2},\ [SB] = \frac{S_e - S_o}{2} \tag{7.9}$$

A typical MIMC is illustrated in Fig. 7.8 with a different number of fingers. The MIMC consists of a series of parallel capacitances, and the equivalent capacitance can be increased by incorporating a greater number of fingers of the same length. The forward and backward couplings of the proposed switches can be calculated using circuit parameters.

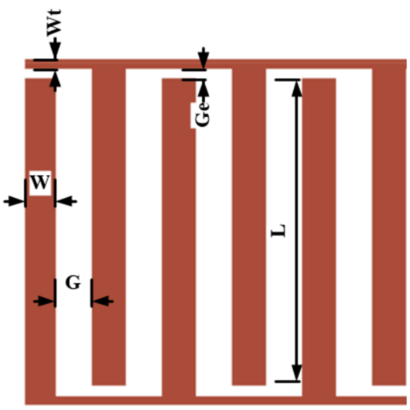

Fig. 7.8. PCB layout of a 14-fingers MIMC.

7.4.1 2-UC Configuration

This section discusses the theory and design variables of the proposed UC. The equivalent circuit of the proposed UC is shown in Fig. 7.9(a), consisting of microstrip transmission lines (MTLs), metamaterial-inspired interdigital capacitors (MICs), and parallel combinations of eight diodes. MTL is modeled as series inductance (L_m) and capacitance (C_m), while diode is modeled as a parallel combination of non-linear equivalent resistance (R_{DE}), capacitance (C_{DE}), and a series equivalent resistance (R_{SE}). MIC is modeled as parasitic capacitance (C_{cp}), series inductance (L_c), and capacitance (C_c). The circuit is symmetrical around point 'P,' allowing for investigation using even- and odd-mode analysis, as shown in Fig. 7.9(b, c). In both even and odd modes, Z_{Lm} and Y_m

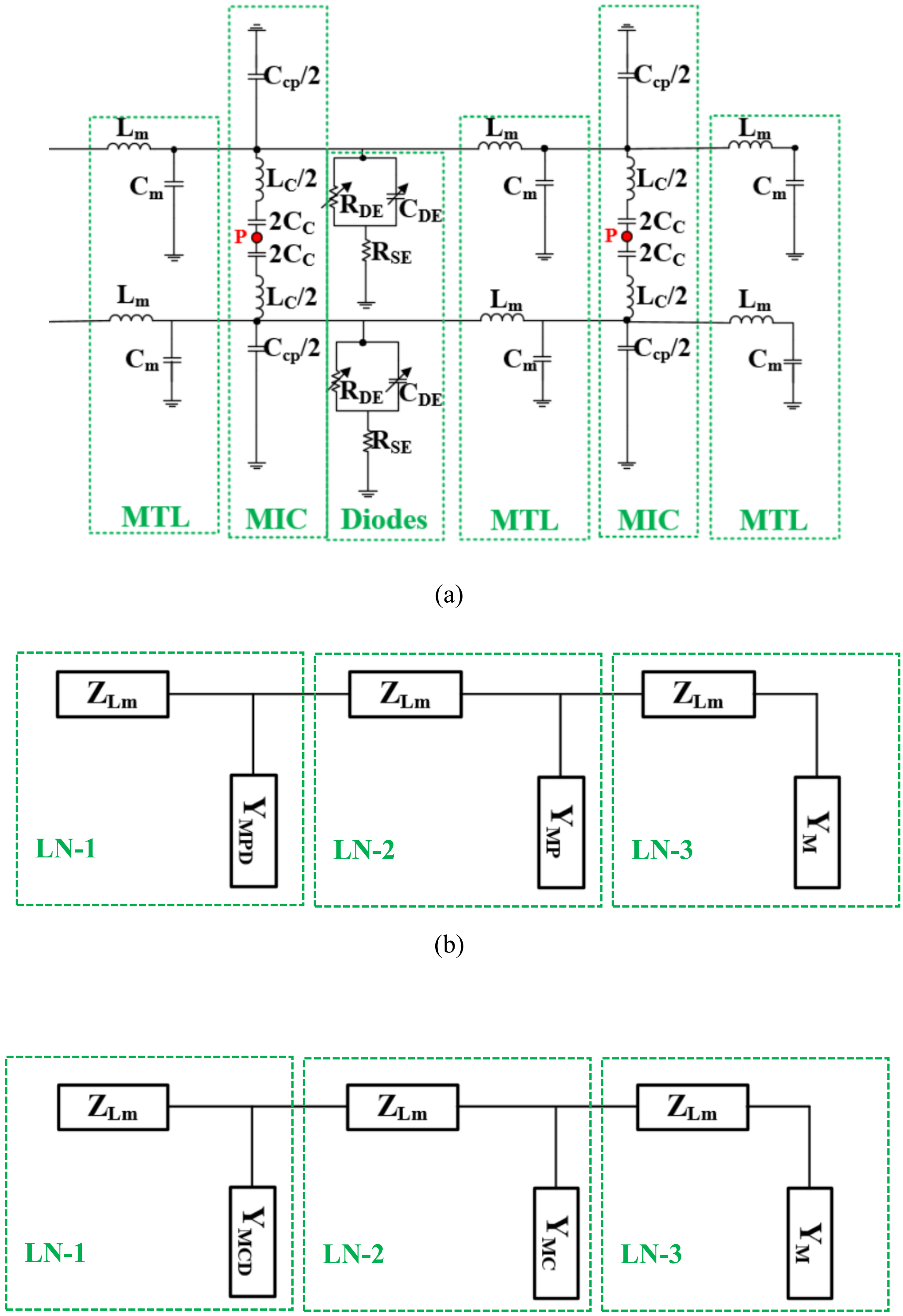

(a)

(b)

(c)

Fig. 7.9. (a) Equivalent circuit model of the proposed UC, (b) even mode circuit, (c) odd mode circuit.

represent MTL impedance and admittance, respectively. Y_{MPD} represents equivalent admittance of MTL, C_{cp} and diode, while Y_{MCD} represents equivalent admittance of MTL, MIC, and diodes. Similarly, Y_{MP} represents equivalent admittance of MTL and C_{cp}, and Y_{MC} represents equivalent admittance of MTL and MIC. The even and odd mode circuits of the proposed UC can be divided into three individual L-networks (*LN-1*, *LN-2* and *LN-3*), as shown in Fig. 7.9(b, c). The equivalent impedances and admittances of these networks are summarized in the equations below.

$$Y_M = j\omega C_m \tag{7.10}$$

$$Y_{MP} = j\omega\left(\frac{C_{cp}}{2} + C_m\right) \tag{7.11}$$

$$Z_{LM} = j\omega L_m \tag{7.12}$$

$$Y_{MPD} = j\omega\left(\frac{C_{cp}}{2} + C_m\right) + \frac{\frac{1}{R_{DE}} + j\omega C_{DE}}{1 + (\frac{1}{R_{DE}} + j\omega C_{DE})R_{SE}} \tag{7.13}$$

$$Y_{MCD} = j\omega\left(\frac{C_{cp}}{2} + C_m\right) + \frac{1}{\frac{j\omega L_c}{2} + \frac{1}{2j\omega C_c}} + \frac{\frac{1}{R_{DE}} + j\omega C_{DE}}{1 + \left(\frac{1}{R_{DE}} + j\omega C_{DE}\right)R_{SE}} \tag{7.14}$$

$$Y_{MC} = j\omega\left(\frac{C_{cp}}{2} + C_m\right) + \frac{1}{\frac{j\omega L_c}{2} + \frac{1}{2j\omega C_c}} \tag{7.15}$$

The subscript 'e' is used for even mode and 'o' is used for odd mode variables in this section. In even mode, the point 'P' is open, and the effect of L_c and C_c can be neglected, as shown in Fig. 7.9(b). Three cascaded L-networks can be analyzed using ABCD matrices individually and the combined circuit can be investigated by multiplying individual matrices [128]. The ABCD matrix for Fig. 7.9(b) is calculated in (7.16).

$$\begin{bmatrix} A & B \\ C & D \end{bmatrix}_Z = \begin{bmatrix} 1 & Z \\ 0 & 1 \end{bmatrix}$$

$$\begin{bmatrix} A & B \\ C & D \end{bmatrix}_Y = \begin{bmatrix} 1 & 0 \\ Y & 1 \end{bmatrix}$$

$$\begin{bmatrix} A & B \\ C & D \end{bmatrix}_{LN-1e} = \begin{bmatrix} 1 & Z_{Lm} \\ 0 & 1 \end{bmatrix} \cdot \begin{bmatrix} 1 & 0 \\ Y_{MPD} & 1 \end{bmatrix} = \begin{bmatrix} 1 + Y_{MPD}Z_{Lm} & Z_{Lm} \\ Y_{MPD} & 1 \end{bmatrix}$$

$$\begin{bmatrix} A & B \\ C & D \end{bmatrix}_{LN-2e} = \begin{bmatrix} 1 & Z_{Lm} \\ 0 & 1 \end{bmatrix} \cdot \begin{bmatrix} 1 & 0 \\ Y_{MP} & 1 \end{bmatrix} = \begin{bmatrix} 1 + Y_{MP}Z_{Lm} & Z_{Lm} \\ Y_{MP} & 1 \end{bmatrix}$$

$$\begin{bmatrix} A & B \\ C & D \end{bmatrix}_{LN-3e} = \begin{bmatrix} 1 & Z_{Lm} \\ 0 & 1 \end{bmatrix} \cdot \begin{bmatrix} 1 & 0 \\ Y_M & 1 \end{bmatrix} = \begin{bmatrix} 1 + Y_M Z_{Lm} & Z_{Lm} \\ Y_M & 1 \end{bmatrix}$$

$$\begin{bmatrix} A & B \\ C & D \end{bmatrix}_e = \begin{bmatrix} A & B \\ C & D \end{bmatrix}_{LN-1e} \cdot \begin{bmatrix} A & B \\ C & D \end{bmatrix}_{LN-2e} \cdot \begin{bmatrix} A & B \\ C & D \end{bmatrix}_{LN-3e} \tag{7.16}$$

Similarly, in odd mode, point 'P' is short-circuited, and the corresponding equivalent circuit, including the effect of MIC, is shown in Fig. 7.9(c). Similarly, the ABCD matrices can be derived to analyze the equivalent circuit.

$$\begin{bmatrix} A & B \\ C & D \end{bmatrix}_{LN-1o} = \begin{bmatrix} 1 & Z_{Lm} \\ 0 & 1 \end{bmatrix} \cdot \begin{bmatrix} 1 & 0 \\ Y_{MCD} & 1 \end{bmatrix} = \begin{bmatrix} 1 + Y_{MCD} Z_{Lm} & Z_{Lm} \\ Y_{MCD} & 1 \end{bmatrix}$$

$$\begin{bmatrix} A & B \\ C & D \end{bmatrix}_{LN-2o} = \begin{bmatrix} 1 & Z_{Lm} \\ 0 & 1 \end{bmatrix} \cdot \begin{bmatrix} 1 & 0 \\ Y_{MC} & 1 \end{bmatrix} = \begin{bmatrix} 1 + Y_{MC} Z_{Lm} & Z_{Lm} \\ Y_{MC} & 1 \end{bmatrix}$$

$$\begin{bmatrix} A & B \\ C & D \end{bmatrix}_{LN-3o} = \begin{bmatrix} 1 & Z_{Lm} \\ 0 & 1 \end{bmatrix} \cdot \begin{bmatrix} 1 & 0 \\ Y_{M} & 1 \end{bmatrix} = \begin{bmatrix} 1 + Y_{M} Z_{Lm} & Z_{Lm} \\ Y_{M} & 1 \end{bmatrix}$$

$$\begin{bmatrix} A & B \\ C & D \end{bmatrix}_{o} = \begin{bmatrix} A & B \\ C & D \end{bmatrix}_{LN-1o} \cdot \begin{bmatrix} A & B \\ C & D \end{bmatrix}_{LN-2o} \cdot \begin{bmatrix} A & B \\ C & D \end{bmatrix}_{LN-3o} \quad (7.17)$$

For a symmetrical and reciprocal two-port network, the characteristics impedance (Z_0) and propagation constant (β) can be calculated using ABCD parameters as below:

$$Z_0 = \sqrt{\frac{B}{C}} \quad (7.18)$$

$$\theta = \beta l = cos^{-1}\left(\frac{A+D}{2}\right) \quad (7.19)$$

7.4.1.1 Forward Coupling

For low-power input, the signal can be transferred to either port 2 or port 4. The coupling of the proposed CPBC can be adjusted based on the number of UCs, and the proposed circuit can be realized for either output (S_{21}) or forward coupling (S_{41}) at low power. For output power transfer, the S_{21} should be very low, while S_{31} and S_{41} should have high insertion losses. For output, S_{21} of a matched network can be calculated using the following equation. The β can be calculated using (7.19).

$$S_{12} = S_{21} = cos\frac{(\beta_e - \beta_o)l}{2}$$

$$max|S_{21}| = \frac{(\beta_e - \beta_o)l_m}{2} = \pi$$

$$l_m = \frac{2\pi}{(\beta_e - \beta_o)}$$

$$\Delta\beta l_m = |\beta_e - \beta_o| l_m = F(L_c, C_c, C_{cp}, C_m, L_m, C_{DE}, N_A) \quad (7.20)$$

To ensure the compact length of the CPBC, $\Delta\beta$ has seven variables, and many solutions exist to balance the equation to achieve minimum S_{21}. Solving this equation involves complex computations. To estimate the unknown parameters, optimization techniques such as random search and gradient-based algorithms are applied. A random algorithm selects a value from within a defined range and based on the calculated error, a new set of values is generated, and the error function is recomputed until the error reaches a minimum threshold. After this step, the gradient-based optimizer is used to fine-tune the parameters through a gradient search method. Since the gradient algorithm evaluates several functions, it requires more computation time compared to the random search method. The above parameters are calculated at low power, and corresponding results are shown in Fig. 7.10. For instance, for 2 UCs, S_{21} is very small at 2.43 GHz, while for 3-UCs, the S_{41} is small, as shown in Fig. 7.10(b, d). To prove the concept, an optimum value of 2 UCs is selected for the power transfer to the output port for low-power signals at 2.43 GHz. It is also evident from the Fig. 7.10(c, d) that backward and forward-coupled ports show high isolation.

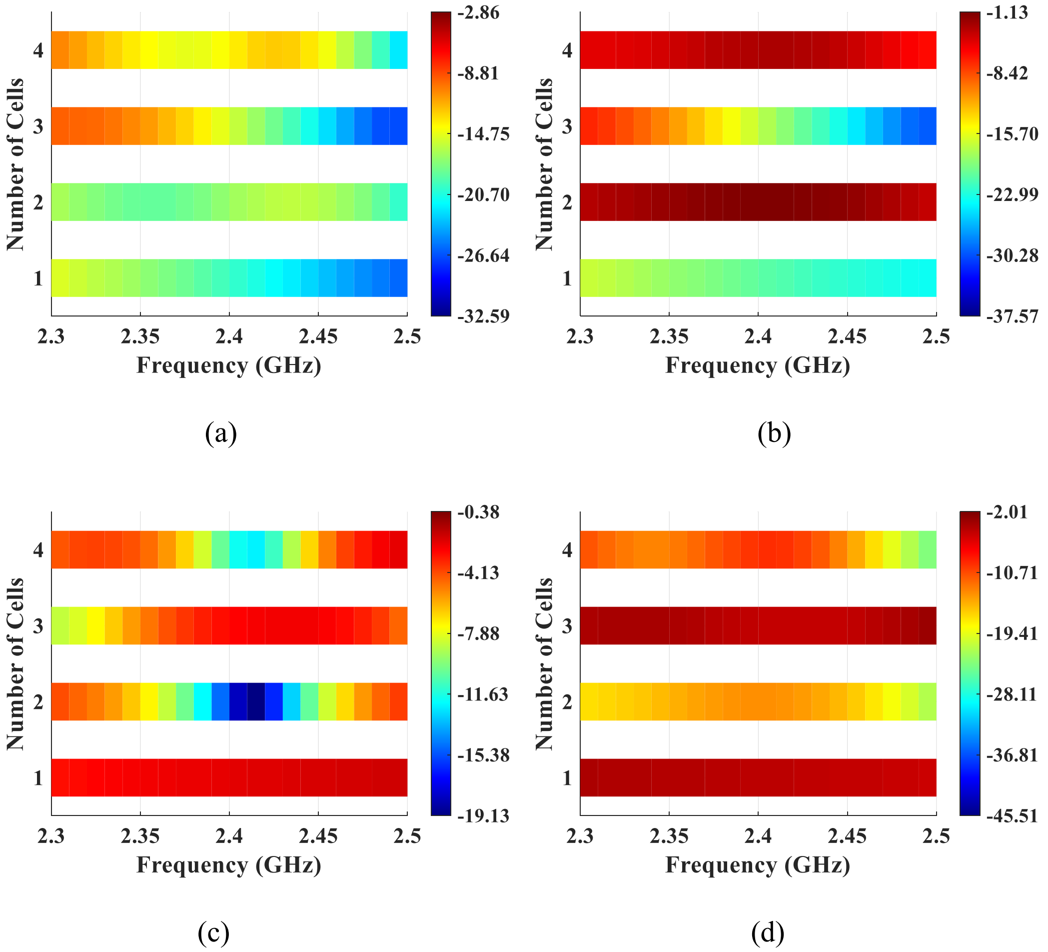

Fig. 7.10. Low power couplings for different numbers of UCs in dB, (a) S_{11}, (b) S_{21}, (c) S_{31}, and (d) S_{41}.

7.4.1.2 Backward Coupling

For a high-power input signal, the signal is transferred to a backward coupled port with low insertion loss. Due to high power, the diodes act as short-circuit switches with high conductance and prevent power from going to the output port. When input is applied at port 1, the backward coupling can be calculated using S_{31}, where a is the coupling coefficient.

$$S_{31} = \frac{ja\sin(\theta)}{\sqrt{1-a^2}\cos(\theta)+j\sin(\theta)}$$

To achieve backward coupling, the S_{31} should be a and θ should be a multiple of $\frac{\pi}{2}$.

$$|S_{31}| = a$$

$$a = \frac{Z_{0e} - Z_{0o}}{Z_{0e} + Z_{0o}}$$

Using (7.18), a can be calculated as,

$$a = \frac{\frac{Z_{0e}}{Z_{0o}} - 1}{\frac{Z_{0e}}{Z_{0o}} + 1} = \frac{\frac{\sqrt{\frac{B_e}{C_e}}}{\sqrt{\frac{B_o}{C_o}}} - 1}{\frac{\sqrt{\frac{B_e}{C_e}}}{\sqrt{\frac{B_o}{C_o}}} + 1}$$

$$a = F(L_c, C_c, C_{cp}, C_m, L_m, C_{DE}, N_A) \tag{7.21}$$

The equation (7.21) has many variables, and many solutions can be true to achieve backward coupling with a maximum coupling coefficient. The values are calculated using design tools in simulation, and Fig. 7.11 shows simulated power couplings for all four ports at high power. For high power, power is transferred to port 3 while maintaining high isolation between other ports at 2.43 GHz. When increasing the number of cells beyond two, there is no significant difference in the S_{31} value, as shown in Fig. 7.11(c).

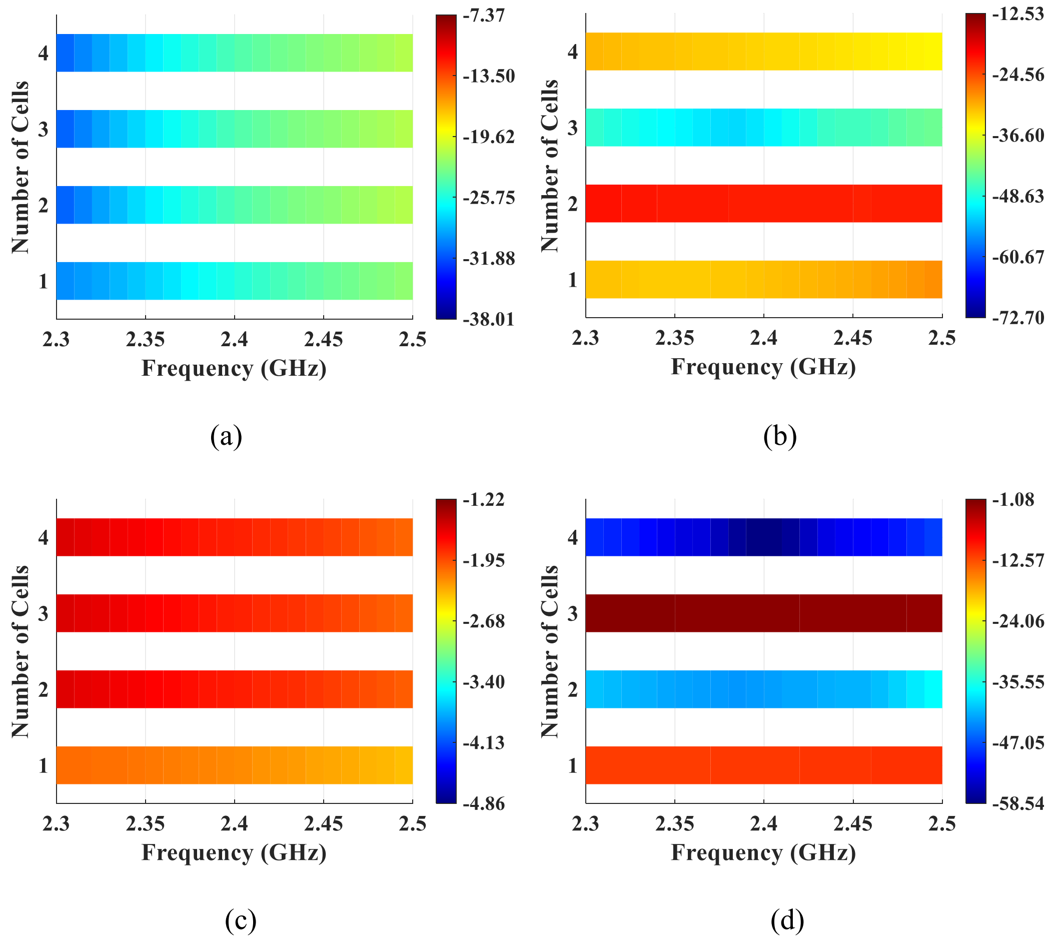

Fig. 7.11. High power couplings for different numbers of UCs in dB, (a) S_{11}, (b) S_{21}, (c) S_{31}, and (d) S_{41}.

7.4.2 16-UC Configuration

The design process begins by developing the equivalent circuit for the UC of the 16-UC configuration, incorporating transmission lines, MIMC, and diodes. The equivalent circuit of the UC, shown in Fig. 7.4(b), is depicted in Fig. 7.12. It consists of three main components: coupled transmission lines, an MIMC, and two Schottky diodes. The transmission line is represented by a series inductance (L_T) and a parallel capacitance (C_T). The MIMC is modeled with a series inductance (L_i), series capacitance (C_i), and parasitic capacitance (C_{ip}). The non-linear circuit model of the Schottky diode includes non-linear resistance ($\widehat{R_D(v)}$), non-linear capacitance ($\widehat{C_D(v)}$), and series resistance (R_{SD}). When the parasitic elements are ignored, the Schottky diode can be represented by non-linear equations [258].

$$i_D = I_s e^{\alpha v} - \frac{C_0}{\sqrt{1-\frac{v}{V_0}}}\frac{dv}{dt} \tag{7.22}$$

where C_0 is the capacitance due to the DC biasing, I_s is the saturation current, and $\alpha = \frac{1}{nV_T}$ (V_T is the thermal voltage, and n is the identity factor of the diode). The $\widehat{C_D(v)}$ is a function of applied voltage and changes with the voltage. The circuit is symmetrical around point ‘A’ and can be divided into even and odd modes to analyze the proposed UC, as depicted in Fig. 7.13.

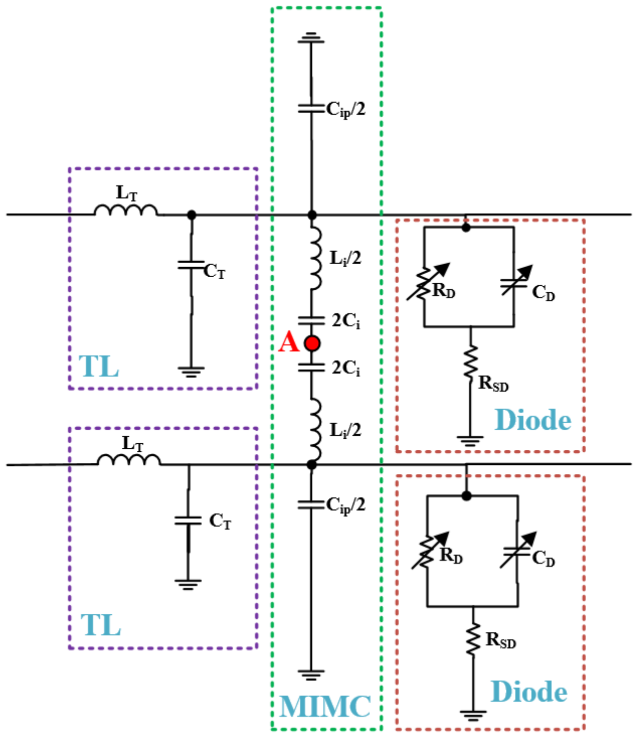

Fig. 7.12. Equivalent circuit of the proposed UC.

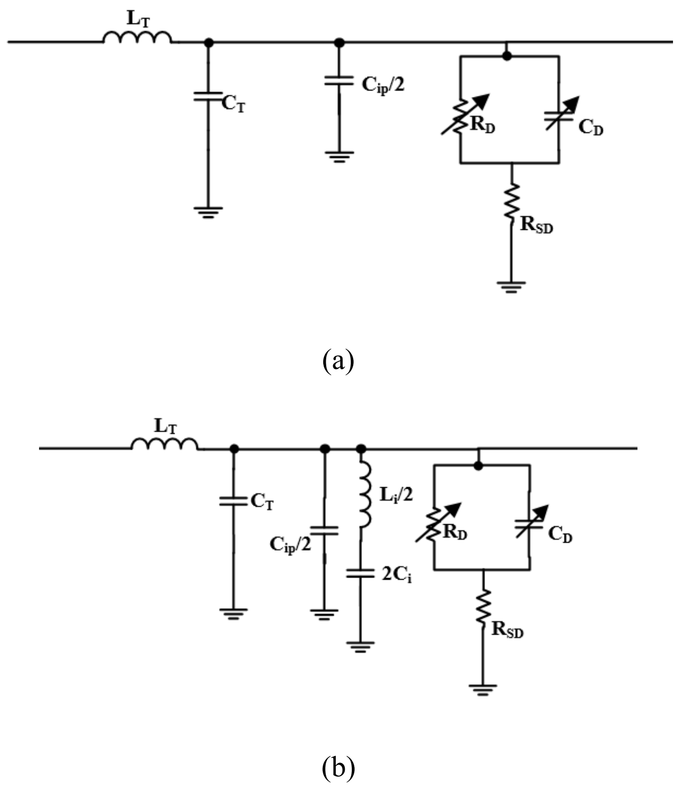

Fig. 7.13. (a) Even mode circuit of the proposed UC and (b) odd mode circuit of the proposed UC.

In the even mode, point A in Fig. 7.12 is treated as an open circuit, resulting in the simplified circuit shown in Fig. 7.13(a). This approach removes the coupling path between the two transmission lines, leaving only the parasitic capacitance ($C_{ip}/2$) in the even mode. The equivalent even impedance (Z_e) and even admittance (Y_e) can be calculated using (7.23) and (7.24), respectively, where Y_D represents the equivalent admittance of the diode.

$$Z_e = j\omega L_T \tag{7.23}$$

$$Y_e = Y_1 + Y_D \tag{7.24}$$

$$Y_D = \frac{\frac{1}{R_D(v)} + j\omega \widehat{C_D(v)}}{1 + (\frac{1}{R_D(v)} + j\omega \widehat{C_D(v)})R_{SD}} \tag{7.25}$$

$$Y_1 = j\omega\left(\frac{C_{ip}}{2} + C_T\right) \tag{7.26}$$

For the odd mode analysis, point A in Fig. 7.12 is treated as a short circuit, resulting in the circuit configuration shown in Fig. 7.13(b). This configuration establishes a coupling path represented by $L_i/2$ and $2C_i$, along with the parasitic capacitance. The equivalent odd impedance (Z_o) and admittance (Y_o) can be calculated using (7.27) and (7.28).

$$Z = Z_o = Z_e = j\omega L_T \tag{7.27}$$

$$Y_o = Y_e + Y_i \tag{7.28}$$

$$Y_i = \frac{1}{\frac{j\omega L_i}{2} + \frac{1}{2j\omega C_i}} \tag{7.29}$$

The equivalent capacitance and inductance of the MIMC UC can be calculated using the equations (7.30) and (7.31) [128].

$$C_i \approx F(N_i - 1)\varepsilon_0 \varepsilon_r \frac{L_i}{G_i} \tag{7.30}$$

$$L_i = \frac{\mu_0 \mu_r {N_i}^2 L_i}{W_i G_i} \tag{7.31}$$

where ε_0 and μ_0 are the permittivity and permeability of free space, ε_r and μ_r the relative permittivity and permeability of the substrate, F is the correction factor. The propagation constant (β) and characteristics impedance (Z_0) can be calculated using the below equations [259].

$$\beta l = \sqrt{ZY} \tag{7.32}$$

$$Z_0 \cong \sqrt{\frac{Z}{Y}} \tag{7.33}$$

7.4.2.1 Backward Coupling (High-Power)

For backward coupling, the power is delivered to port 3 with low insertion loss and high isolation between other ports. The output (S_{21}) and backward coupling (S_{31}) of the coupler can be evaluated using equations (7.34) and (7.35), respectively.

$$S_{11} = S_{22} = S_{33} = S_{44} = 0$$

$$S_{14} = S_{41} = S_{23} = S_{32} = 0$$

$$S_{21} = \frac{\sqrt{1-k^2}}{\sqrt{1-k^2}\,cos(\beta l) + jsin(\beta l)} \tag{7.34}$$

$$S_{31} = \frac{jksin(\beta l)}{\sqrt{1-k^2}\,cos(\beta l) + jsin(\beta l)} \tag{7.35}$$

$$k = \frac{Z_{0e} - Z_{0o}}{Z_{0e} + Z_{0o}}$$

Maximum backward coupling (k) will occur when $\beta l = \frac{\pi}{2} \rightarrow l = \frac{\lambda_g}{4}$. Using $\beta l = \frac{\pi}{2}$, equations (7.34) and (7.35) can be written as

$$|S_{31}| = k$$

$$|S_{21}| = \sqrt{1-k^2}$$

$$k = \frac{\frac{Z_{0e}}{Z_{0o}} - 1}{\frac{Z_{0e}}{Z_{0o}} + 1} = \frac{\sqrt{1 + \frac{Y_i}{Y_1 + Y_D}} - 1}{\sqrt{1 + \frac{Y_i}{Y_1 + Y_D}} + 1}$$

To validate the above equation, Y_i should be infinite.

$$Y_i = \infty$$

$$Y_i = \frac{1}{\frac{j\omega L_i}{2} + \frac{1}{2j\omega C_i}} = \infty$$

$$\omega_B = \frac{1}{\sqrt{L_i C_i}}$$

ω_B is the frequency at which backward coupling will occur and is a function of Li and Ci. Another condition to achieve backward coupling is related to the reflection coefficient at the input port.

$$S11_e = -S11_o$$

$$Z\left(\frac{1}{1+Y_oZ}+\frac{1}{1+Y_eZ}\right)=0$$

β is a key parameter to analyze the forward and backward couplings. For backward coupling, β_e should be the same as β_o, and $|\beta_e - \beta_o|$ should be zero.

$$\beta_e = \beta_o$$

$$ZY_e = ZY_o \rightarrow Y_e = Y_o$$

$$Y_e = Y_e + Y_i \tag{7.36}$$

To balance the above equation (7.36), two solutions exist i.e., $Y_i = 0, \infty$. However, $Y_i \neq 0$ and to hold the solution, $Y_i = \infty$. Y_e is infinite implies $Y_D = \infty$.

$$Y_e = Y_1 + Y_D = \infty \rightarrow Y_D = \infty \tag{7.37}$$

This implies that diodes should be ON with infinite conductance. β is simulated for different power levels to ensure the dependency for both backward and forward coupling. Fig. 7.14 shows the per-unit length phase difference ($|\beta_e - \beta_o|$) for various power levels. $|\beta_e - \beta_o|$ is high for low power (-30 dBm), which indicates forward couping at 2.52 GHz. The same phenomenon can also be observed for 0 dBm, indicating forward coupling. However, the difference is zero for +30 dBm, showing backward coupling at 2.52 GHz at high power.

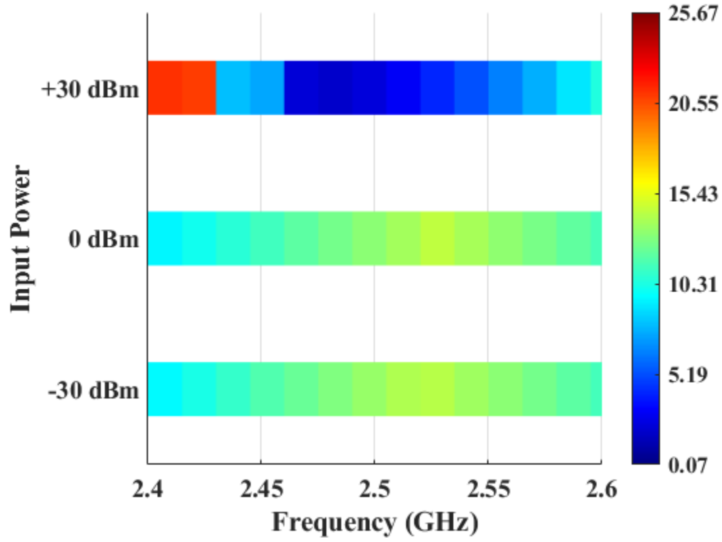

Fig. 7.14. The difference in propagation constants for even and odd modes ($|\beta_e - \beta_o|^{\circ}$).

As a summary for backward coupling, the following criteria should be met:

$$k = 1 \rightarrow \omega_B = \frac{1}{\sqrt{L_iC_i}} \tag{7.38}$$

$$\beta_e = \beta_o \tag{7.39}$$

$$S11_e = -S11_o \tag{7.40}$$

$$\beta l = \frac{\pi}{2} \rightarrow l = \frac{\lambda_g}{4} = \frac{2\pi c}{4\omega_B} = \frac{\pi c}{2}\sqrt{L_i C_i} \tag{7.41}$$

7.4.2.2 Forward Coupling (Low-Power)

The signal is delivered to port 4 for low power while maintaining high isolation between other ports. The forward coupling can be calculated using the following S-parameters.

$$S_{13} = S_{31} = S_{42} = S_{24} = 0 \tag{7.42}$$

$$S_{41} = S_{14} = S_{32} = S_{23} = sin\frac{(\beta_e - \beta_o)l}{2} \tag{7.43}$$

$$S_{12} = S_{21} = S_{34} = S_{43} = cos\frac{(\beta_e - \beta_o)l}{2} \tag{7.44}$$

$$S_{11e} = S_{11o} = 0 \tag{7.45}$$

$$\frac{Z\left(\frac{1}{1+Y_e Z}\right)}{Z+Z\left(\frac{1}{1+Y_e Z}\right)} = 0 \tag{7.46}$$

$$\frac{Z\left(\frac{1}{1+Y_o Z}\right)}{Z+Z\left(\frac{1}{1+Y_o Z}\right)} = 0 \tag{7.47}$$

$$max|S_{41}| = \frac{(\beta_e - \beta_o)l_m}{2} = \frac{\pi}{2} \tag{7.48}$$

$$l_m = \frac{\pi}{(\beta_e - \beta_o)} \tag{7.49}$$

In this case, l_{max} and $\Delta\beta$ can be calculated as below:

$$\beta_e l = \sqrt{ZY_e} = \sqrt{(j\omega L_T) \times (Y_1 + Y_D)} \tag{7.50}$$

$$\beta_o l = \sqrt{ZY_o} = \sqrt{(j\omega L_T) \times (Y_1 + Y_i + Y_D)} \tag{7.51}$$

$$\Delta\beta l = |\beta_e - \beta_o| l_{max} = \left|\sqrt{ZY_e} - \sqrt{ZY_o}\right| \tag{7.52}$$

$$\Delta\beta l = \left|\sqrt{(Z)(Y_1 + Y_D)} - \sqrt{(Z)(Y_1 + Y_D + Y_i)}\right| \tag{7.53}$$

$$\Delta\beta = F(C_T, C_{ip}, C_i, L_i, l) \tag{7.54}$$

Equation (7.53) shows that $\Delta\beta$ depends on Yi, a higher value of Yi will lead to a smaller length of MIMC. For low-power analysis, the diodes act as open circuits due to the availability of a small current, and Y_D can be considered negligible. By increasing the number of MIMC fingers, Y_i will increase, resulting in low Z_i and high $\Delta\beta$.

In conclusion, calculating forward and backward couplings requires six variables—$(C_T, L_T, C_{ip}, C_i, L_i, l, \widehat{C_D(v)})$—necessitating seven equations for a closed-form solution.

1. $k = 1 \rightarrow \omega_B = \frac{1}{\sqrt{L_i C_i}}$
2. $S11_e = -S11_o \rightarrow F\left(C_T, C_{ip}, \omega_B, L_T\right)$
3. $l = \frac{\lambda_g}{4} = \frac{2\pi c}{4\omega_B} = \frac{\pi c}{2}\sqrt{L_i C_i}$
4. $\Delta\beta = \frac{\pi}{l}\Big]_{F1} \rightarrow F(C_T, C_{ip}, C_i, L_i, l)$
5. $\Delta\beta = \frac{\pi}{l}\Big]_{F2} \rightarrow F(C_T, C_{ip}, C_i, L_i, l)$
6. $S11_e = S11_o = 0]_{F1}$
7. $S11_e = S11_o = 0]_{F2}$

Solving these equations requires complex computations. Optimization algorithms, such as random and gradient methods, have been used to determine the unknown parameters. Initially, a random algorithm is used to select a value within a specified range. Based on the resulting error, a new set of values is generated, and the error function is recalculated until the error is minimized. Afterward, a gradient optimizer is employed to further refine the values using a gradient search method. The gradient algorithm evaluates various functions during each iteration, making it more time-consuming compared to the random algorithm.

7.5 Simulation and Measurement Results

To validate the performance of the proposed passive couplers, four-port couplers were designed and simulated using the Rogers RO4003C substrate in Advanced Design System (ADS) 2020. The designs were analyzed in ADS using Harmonic Balance (HB) and Large-Signal S-Parameter (LSSP) simulators to accurately model the non-linear behavior of the Schottky diodes. The non-linear model of the SMS7621 diode was incorporated into the simulations, including series parasitic inductance and parallel capacitance, to create a realistic circuit representation. Prototypes were then fabricated on the Rogers substrate, with the Schottky diodes SMS7621 model assembled, to experimentally validate the proposed couplers.

7.5.1 Simulated and Measured Results of the Proposed 2-UC Design

The PCB layout and fabricated prototype of the 2-UC design are shown in Fig. 7.15. The proposed CPBC operates at 2.43 GHz for output and backward coupling. The circuit consists of 2 UCs, each incorporating two Schottky diode configurations, microstrip transmission lines, and metamaterial-based interdigital capacitors. Each diode configuration includes eight diodes arranged in an anti-parallel orientation to enable bidirectional signal flow, as depicted in Fig. 7.4(a).

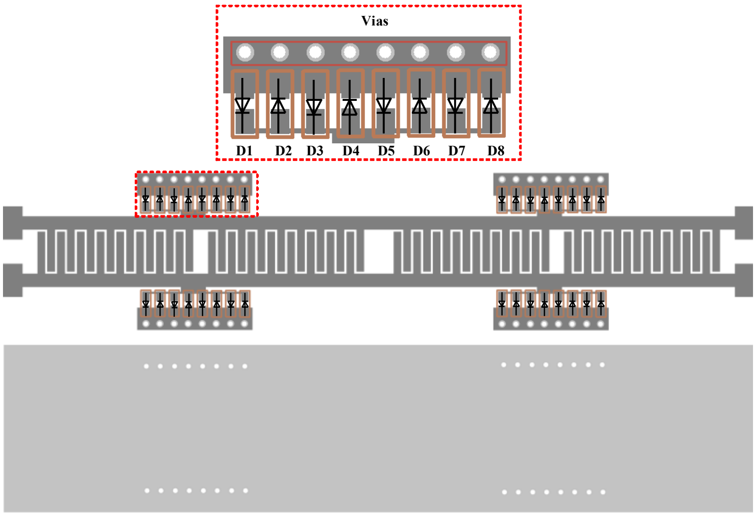

(a)

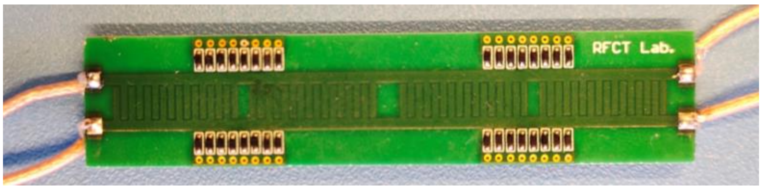

(b)

Fig. 7.15. (a) PCB layout, (b) fabrication prototype of the proposed CPBC (2-UC configuration).

The proposed Compact Passive Backward Coupler (CPBC) operates at 2.43 GHz for both output and backward coupling. The designed circuit comprises 2 UCs containing two Schottky diode configurations, MTLs and MICs. Each diode configuration includes eight diodes arranged in an anti-parallel orientation to facilitate bidirectional signal flow. The proposed CPBC is a four-port network, and sixteen elements of S-matrix are required to analyze the performance, as shown below.

$$\begin{bmatrix} S_{11} & S_{12} & S_{13} & S_{14} \\ S_{21} & S_{22} & S_{23} & S_{24} \\ S_{31} & S_{32} & S_{33} & S_{34} \\ S_{41} & S_{42} & S_{43} & S_{44} \end{bmatrix}$$

Due to symmetry of the proposed CPBC, $S_{11} = S_{22} = S_{33} = S_{44}$, $S_{21} = S_{12} = S_{34} = S_{43}$, $S_{31} = S_{13} = S_{42} = S_{24}$, $S_{41} = S_{14} = S_{23} = S_{32}$. Hence, only S_{11}, S_{21}, S_{31}, and S_{41} are reported in this subsection. To evaluate the performance of the proposed CPBC under low and high-power conditions, the test setup illustrated in Fig. 7.16 was utilized.

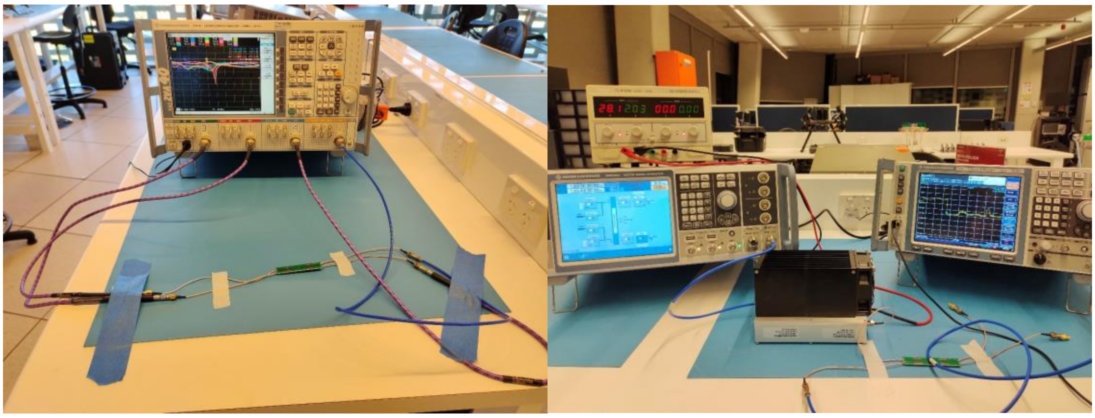

(a) (b)

Fig. 7.16. Test setup to measure the performance of the proposed CPBC (2-UC configuration), (a) low-power analysis, (b) high-power analysis.

A 4-port R&S Vector Network Analyzer (VNA-ZVA40) is utilized for low-power analysis to measure the S-parameters from –30 to 0 dBm, as illustrated in Fig. 7.16(a). To measure precise S-parameter data, a 4-port calibration using Short-Open-Load-Through (SOLT) was carried out prior to testing. The proposed CPBC ports connected to the VNA, and different power levels were used to record frequency responses. A vector signal generator (R&S SMW200A), a signal analyzer (R&S FSV 10 Hz to 40 GHz), and an amplifier (ZHL-15W-422) were utilized for high-power analysis, as Fig. 7.16(b) illustrates. The signal generator created a Continuous Wave (CW) RF signal fed into the amplifier to produce high-power CW output signals in the +30 dBm to 0 dBm range. The amplifier's output was connected to port 1 of the CPBC, and the output power at other ports was measured using the signal analyzer. A 20 dB attenuator was connected to the signal analyzer's input to protect it from high-power RF signals. To evaluate the low and high-power performance of the proposed CPBC, power is swept from –30 to +30 dBm. The corresponding simulated and measured results are shown in Fig. 7.17. The proposed T/R switch resonates at 2.43 GHz for both output and backward coupling. At low power (–30 dBm), the signal is delivered to the output port (port 2) with low insertion loss, while the other ports experience high insertion losses. The insertion loss at 2.43 GHz at port 2 is 1.5 dB, with isolation better than 20 dB. The signal is directed to the backward coupling port at high power while the other ports maintain high insertion losses.

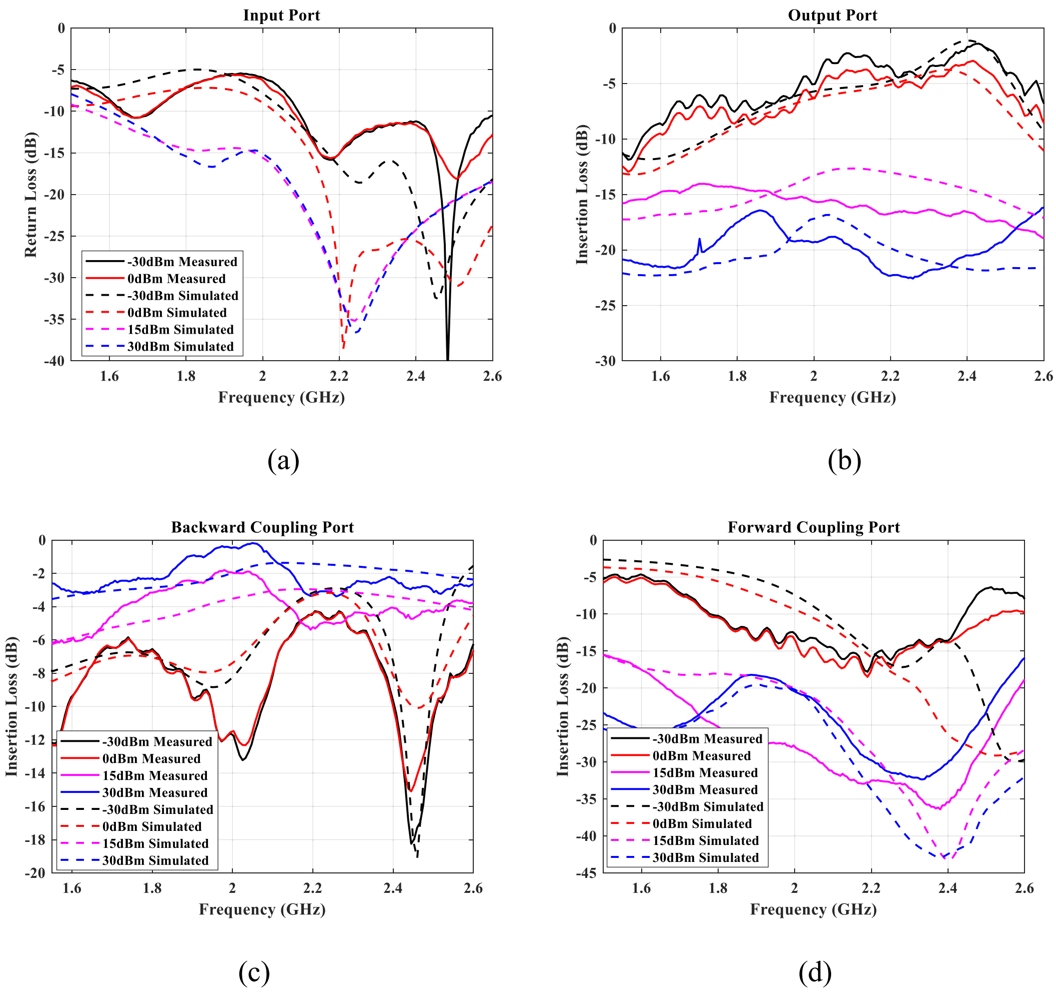

Fig. 7.17. Simulated and measured results of the proposed CPBC (2-UC configuration), (a) return loss at the input port, (b) insertion loss at port 2, (c) insertion loss at port 3, and (d) insertion loss at port 4

The insertion loss is 2.2 dB, and the isolation is high for low-power levels. Fig. 7.17 illustrates the insertion losses for low and high powers at port 2 and port 3, respectively, as well as the isolation between the ports. A good agreement can be observed between simulation and measurement results, showing the validity of the structure. The proposed CPBC is compact, passive and does not need biasing and control circuitry to operate, making it more energy-efficient and suitable for IoT devices running on batteries. Its compact size and planar geometry decrease the system's overall footprint, which is crucial for applications with limited space. Furthermore, it has low insertion loss, guaranteeing improved signal quality and performance in comparison to larger switches.

7.5.2 Simulated and Measured Results of the Proposed 16-UC Design

The proposed 16-UC designs are four-port devices and can be analyzed using sixteen elements S-matrix, as shown below.

$$\begin{bmatrix} S_{11} & S_{12} & S_{13} & S_{14} \\ S_{21} & S_{22} & S_{23} & S_{24} \\ S_{31} & S_{32} & S_{33} & S_{34} \\ S_{41} & S_{42} & S_{43} & S_{44} \end{bmatrix}$$

Due to symmetry of the structure, $S_{11} = S_{22} = S_{33} = S_{44}$, $S_{21} = S_{12} = S_{34} = S_{43}$, $S_{31} = S_{13} = S_{24} = S_{42}$, $S_{41} = S_{14} = S_{23} = S_{32}$. Hence, only S_{11}, S_{21}, S_{31}, and S_{41} are presented in this subsection.

7.5.2.1 Forward and Backward Coupling

The PCB layout and fabricated prototype of the 16-UC design for forward and backward couplings are shown in Fig. 7.18. The top side features MIMCs, MTLs, and diodes, while the bottom side consists of a ground (GND) plane. The proposed M-FBNMN is dual-band, operating at 1.9 GHz and 2.52 GHz for forward and backward couplings. The circuit is composed of 16 UCs, with each UC incorporating non-linear Schottky diodes and MIMC. The diodes in each adjacent UC are oriented differently to facilitate signal flow in both directions.

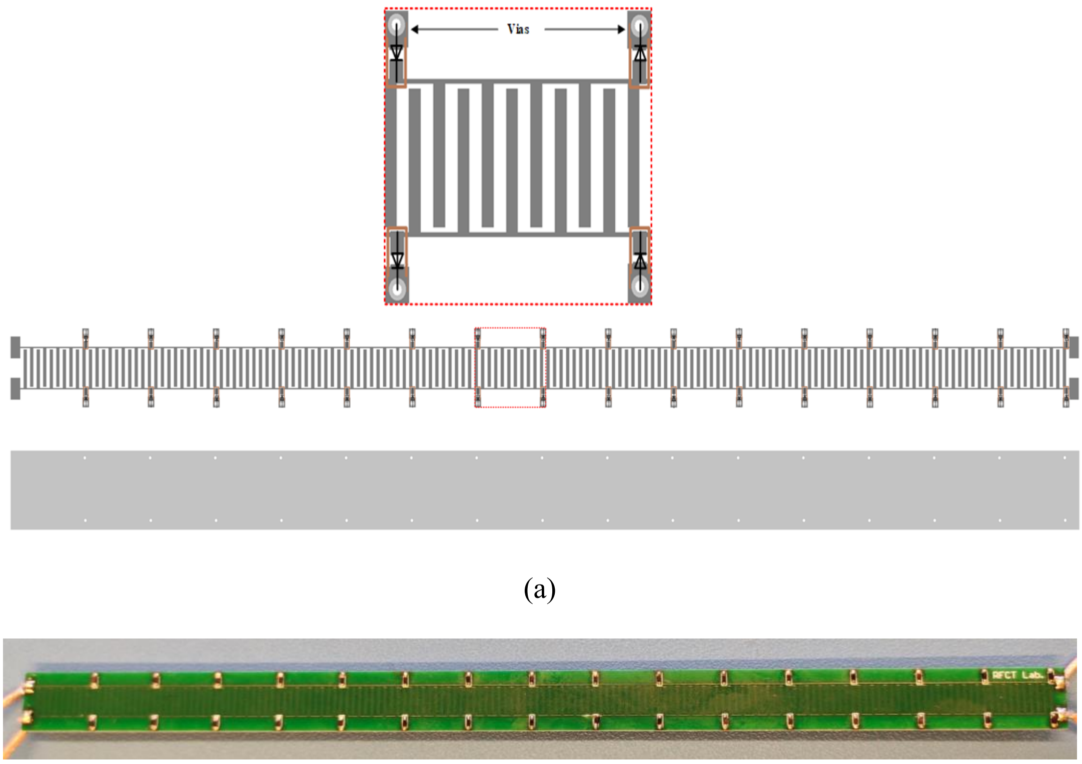

(a)

(b)

Fig. 7.18. PCB layout and fabrication prototype of the proposed M-FBNMN (16-UC configuration).

To evaluate the performance of the proposed M-FBNMN under low and high-power conditions, a test setup was utilized, as shown in Fig. 7.19. For low-power analysis, a 4-port VNA is utilized to measure the s-parameters for –30 to 0 dBm, as shown in Fig. 7.19(a). To measure precise values of S-parameters, a 4-port calibration was performed before measurements. All ports of the proposed M-FBNMN were connected to the VNA, and frequency responses were recorded for different power levels. For high-power analysis, the measurement setup is shown in Fig. 7.19(b). A CW RF signal was generated using a signal generator and fed to the amplifier with high gain to achieve high-power CW output signals with a power range from 0 to +30 dBm. The output of the amplifier was connected to port 1 of the M-FBNMN, and the output power was measured at other ports of the M-FBNMN using the signal analyzer. A 20 dB attenuator is connected to the input of the signal analyzer to protect the equipment from a high-power RF signal.

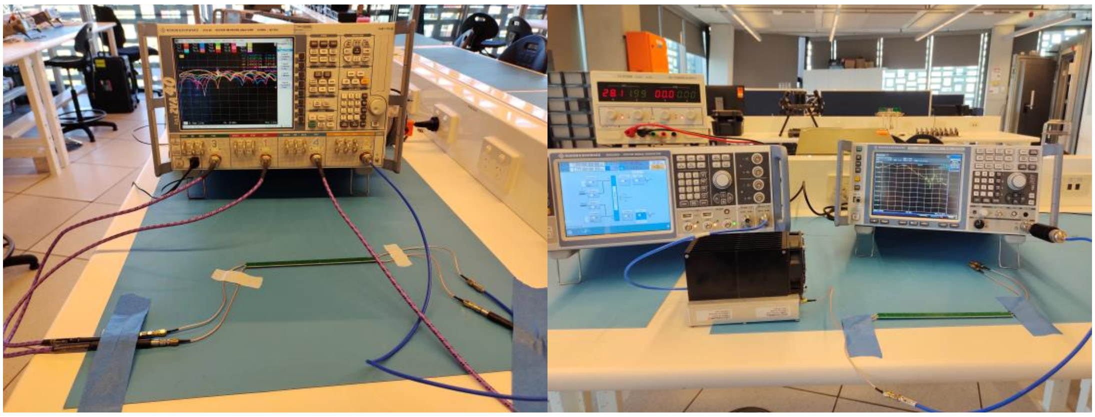

(a) (b)

Fig. 7.19. Test setup to measure the performance of the proposed M-FBNMN (16-UC configuration), (a) low-power analysis, (b) high-power analysis.

To assess the proposed M-FBNMN's low and high-power performance, power is swept from –30 to +30 dBm and corresponding simulated and measured results of the proposed M-FBNMN are shown in Fig. 7.20. The proposed M-FBNMN operates as a multi-band coupler at 1.9 GHz and 2.52 GHz for forward coupling, while it functions as a single-band coupler at 2.52 GHz for backward coupling, along with high isolation between the ports. At low power (–30 dBm), all the power is available at the forward coupling port (port 4) with low insertion loss, while other ports have high insertion losses at both 1.9 and 2.5 GHz. The insertion losses at 1.9 GHz and 2.52 GHz at port 4 are 1.4 and 2 dB, respectively, while the isolation is better than 30 dB. Sine and cosine functions can be observed at port 2 and port 4 (Fig. 7.20). However, at high power, all the power is available at the backward coupling port at 2.52 GHz. For high power, the insertion loss at port 3 is 3 dB, while other ports have high insertion losses. Fig. 7.20(b-d) show the insertion losses for low and high powers at port 4 and port 3, respectively and high isolation between the ports.

Both simulation and measurement results show good agreement, validating the performance of the structure. Therefore, the proposed M-FBNMN is suitable for a dual-band T/R switch for low-power IoT applications.

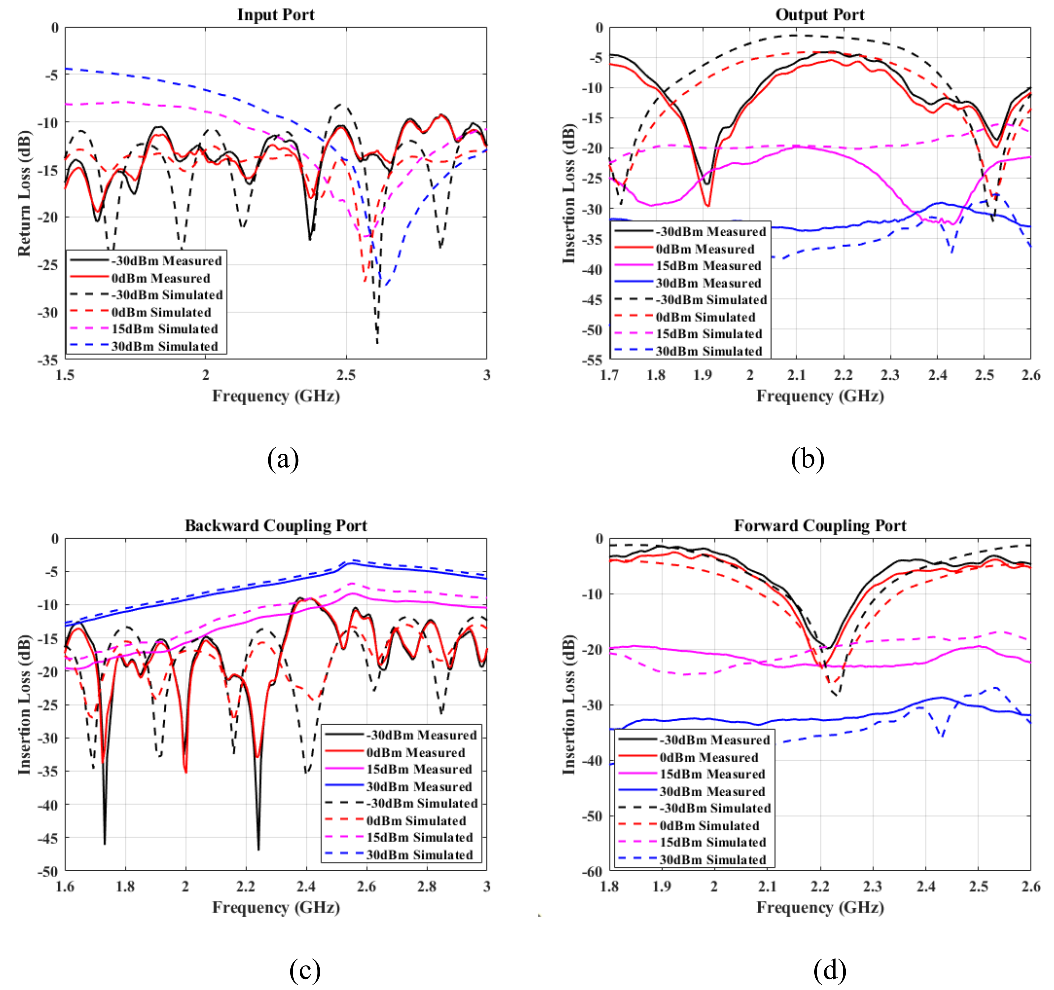

Fig. 7.20. Simulated and measured results of the proposed M-FBNMN (16-UC), (a) return loss at the input port, (b) insertion loss at port 2, (c) insertion loss at port 3, and (d) insertion loss at port 4.

7.5.2.2 Output and Backward Coupling

The PCB layout and fabricated prototype of the 16-UC design for output and backward coupling are shown in Fig. 7.21. The top side features MIMCs, MTLs, and diodes, while the bottom side consists of a GND plane. The proposed 4-port coupler is dual-band, operating at 1.6 GHz and 2.1 GHz for output and backward coupling. Similar to the forward and backward configuration, this circuit also comprises 16 UCs, each of which includes two Schottky diodes connected to the MTLs and an MIMC. The diodes in adjacent UCs are oriented differently to enable power flow in both directions.

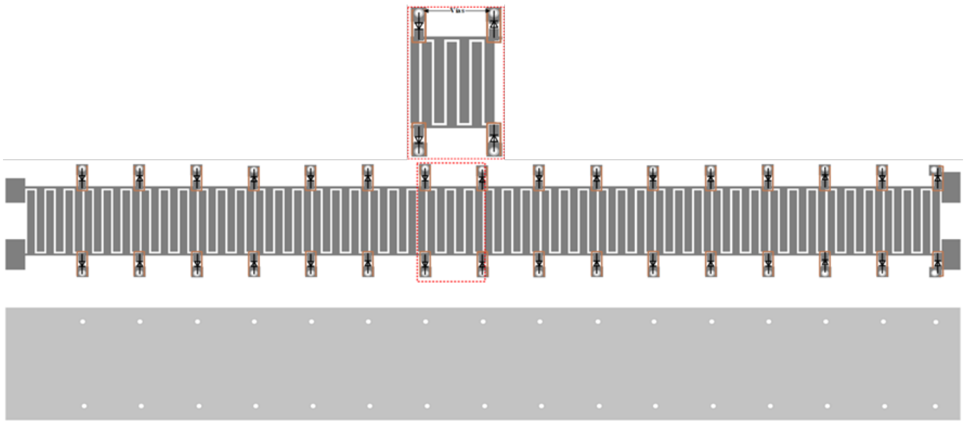

(a)

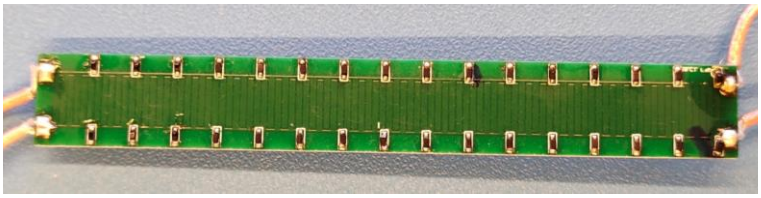

(b)

Fig. 7.21. (a) PCB layout, (b) fabrication prototype of the proposed output/backward coupler (16-UC configuration).

A CW signal is applied to the input of the proposed system, and port 2 and port 4 serve as a differential soil moisture sensor when the input power level is low. However, the CW signal is delivered to port 3 for a high-power input signal at port 1. The proposed passive system requires minimal power to measure soil moisture for smart agriculture. When low-power is applied through a signal generator at port 1 (P1), the system can detect soil moisture levels by measuring the permittivity changes using port 2 (P2) and port 4 (P4), leveraging changes in the frequency response of the applied continuous wave (CW) signal. These permittivity changes can be correlated to Volumetric Water Content (VWC). When high power is applied at P1, the proposed system acts as a switch and transfers the signal to port 3 (P3) with minimum insertion loss. In this mode, the system acts as a transmitter to send the information wirelessly to a remote receiver or gateway. This two-in-one capability of the proposed device allows for an efficient and cost-effective system to integrate sensing and communication.

A test configuration, illustrated in Fig. 7.22, is utilized to evaluate the performance of the suggested dual-band passive coupler for low and high power. As seen in Fig. 7.22(a), a VNA is used for low-power analysis to measure the S-parameters from –30 to 0 dBm. Following the calibration, all ports of the proposed dual-band coupler were connected to the VNA, and frequency responses were recorded at various power levels. The equipment used for high-power analysis is illustrated in Fig. 7.22(b). To produce high-power CW output signals with a power range of 0 to +30 dBm, a signal generator was used to create a CW RF signal fed to the amplifier with high gain. The amplifier's output was connected to port 1 of the dual-band coupler, and the signal analyzer was used to evaluate the output power at the coupler's other ports. A 20 dB attenuator was connected to the input of the signal analyzer to protect the apparatus from high-power RF signals.

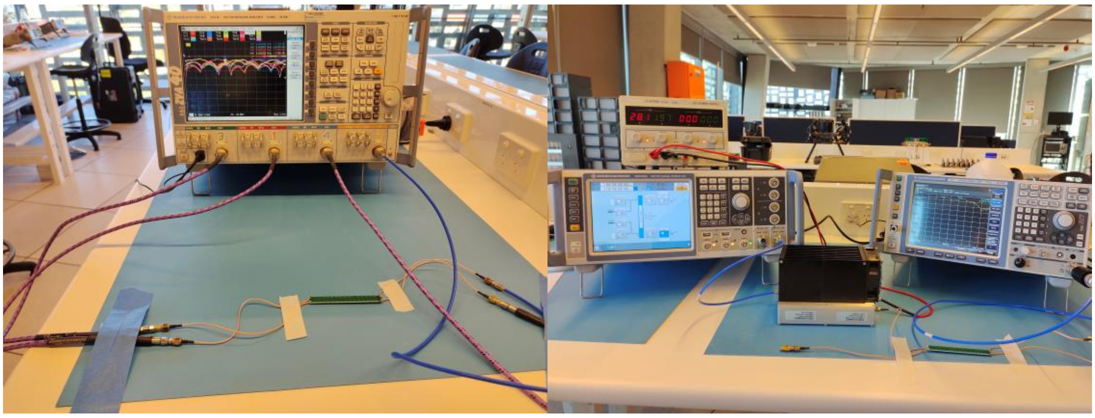

(a) (b)

Fig. 7.22. Test setup to measure the performance of the proposed output/backward coupler (16-UC configuration), (a) low-power analysis, (b) high-power analysis.

Power is swept from –30 to +30 dBm to evaluate the low and high-power performance of the proposed dual-band coupler. The corresponding simulated and measured results are displayed in Fig. 7.23. The suggested coupler exhibits output and backward coupling resonances at 1.6 and 2.1 GHz. At low power (–30 dBm), the output port (port 2) transfers all the power with minimal insertion loss, while the other ports have substantial insertion losses at 1.6 and 2.1 GHz. At port 2, the insertion losses are 0.6 dB and 1 dB at 1.6 GHz and 2.1 GHz, respectively, with isolation better than 25 dB. A sine and cosine function are visible at ports 2 and 4 (Fig. 7.23). The backward coupling port, however, receives all the power at high power, whereas the insertion losses at other ports are considerable. The insertion losses at port 2 and port 3 for low and high powers, as well as the high isolation between the ports, are displayed in Fig. 7.23(b-d). Both simulation and measurement results show good agreement, validating the performance of the structure. Therefore, the proposed design is suitable for a dual-band T/R switch for low-power IoT applications.

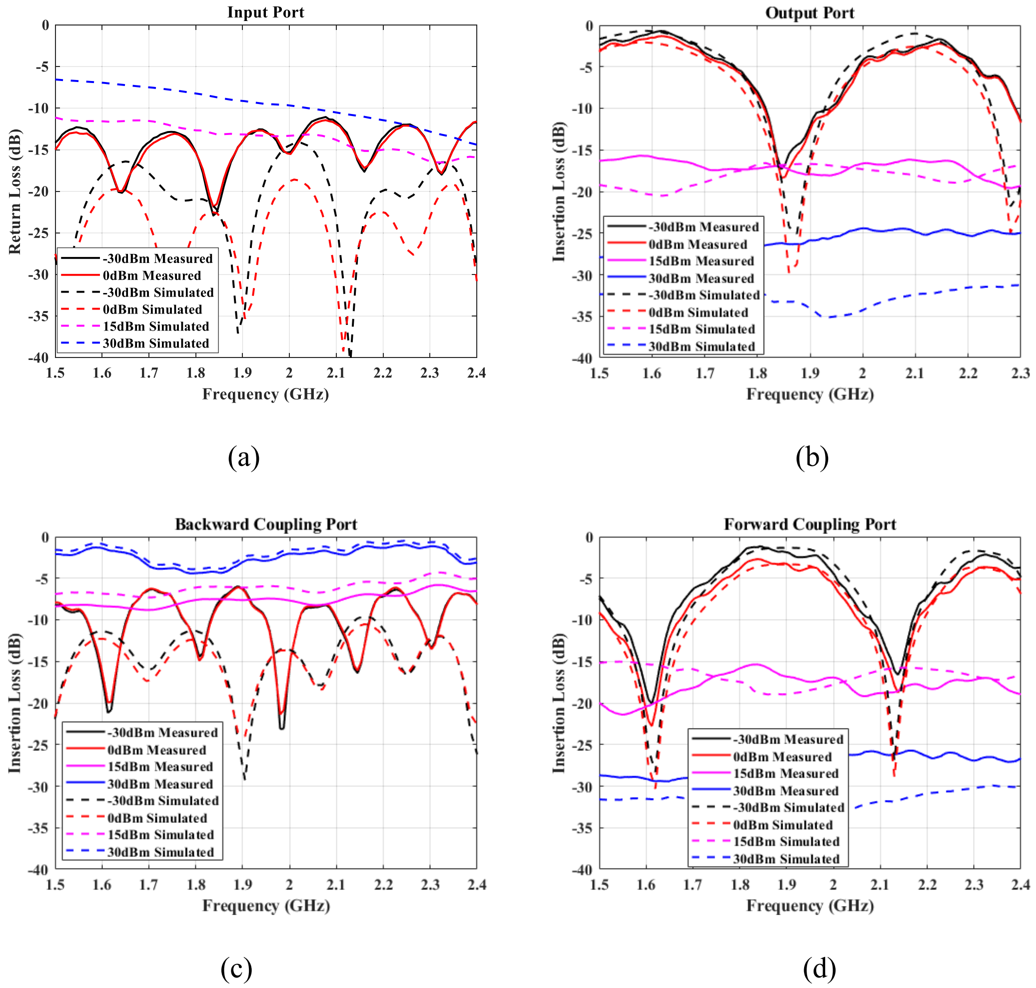

Fig. 7.23. Simulated and measured results of the proposed output/backward coupler (16-UC configuration), (a) return loss at the input port, (b) insertion loss at port 2, (c) insertion loss at port 3, and (d) insertion loss at port 4.

7.6 Integrated WPT, Sensing and Communication System

The proposed integrated Wireless Power Transfer (WPT), sensing, and communication system is illustrated in Fig. 7.24. In WPT mode, high power is captured through an antenna at port 3, which can be stored in a supercapacitor or battery connected to port 1. In sensing mode, low power is applied to port 1, and the relative magnitude (V_{MAG}) at the output ports determines the VWC. The ratio detector (AD8302 [99]) can be utilized to compare the magnitude of both outputs. In transmission (Tx) mode, high power is applied to port 1, enabling port 3, and the measured data can be sent to the access point via port 3.

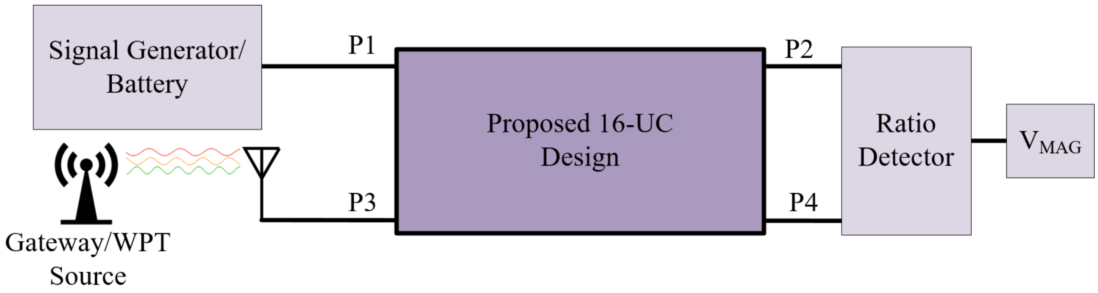

Fig. 7.24. Integration of WPT, sensing and communication.

In the proposed 16-UC structure, the repetition of UCs produces recurring responses, as shown in Fig. 7.25. The outputs at port 2 and port 4 are in quadrature, representing sine and cosine functions. When the output at port 2 reaches its maximum, port 4 shows a minimum, and vice versa. The ratio of these sine and cosine outputs is utilized to realize a differential sensor. At high power in Tx mode, the measured VWC data can be transferred from port 3 to the access points. The communication link is wideband and works from 1.5 to 3 GHz with low insertion loss, as shown in Fig. 7.26.

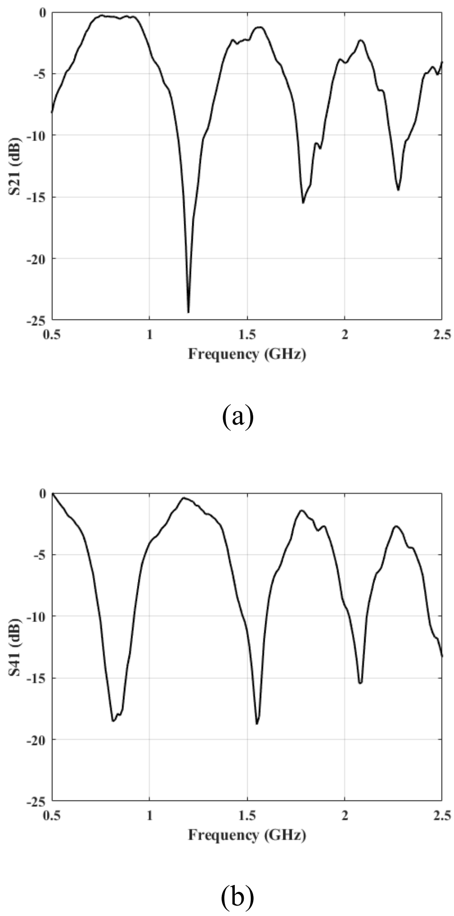

Fig. 7.25. Periodic response of the proposed 16-UC design, (a) S_{21} and (b) S_{41}.

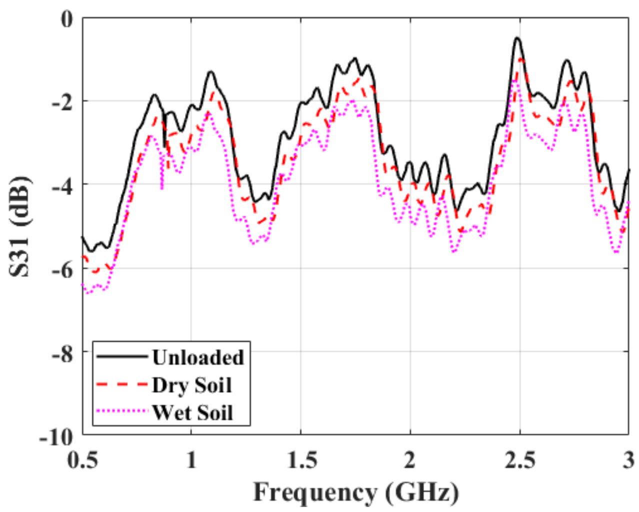

Fig. 7.26. Insertion loss at port 3 (+30 dBm) for different VWCs.

7.6.1 Simulated and Measured Results of the Integrated Sensor

The dual output (port 2 and port 4) of the proposed 16-UC structure at low power enables a differential integrated soil moisture sensor for smart agriculture. Differential sensors measure the difference in soil moisture between two outputs and provide relative data rather than just an absolute value. This relative output of both ports can be used to mitigate the environmental effects (temperature and humidity), resulting in precise measurements.

To validate the concept, the performance of the integrated differential sensor is tested at a single frequency band for different VWCs. To analyze the integrated soil moisture differential sensing of the proposed 16-UC design, a measurement setup is used, as illustrated in Fig. 7.27. A block of $92 \times 12 \times 40$ mm^3 is printed using a 3D printer as a soil container. To measure the frequency responses with different VWCs, a 4-port vector network analyzer (R&S VNA-ZVA40) is used, as illustrated in Fig. 7.27(a). All four ports of the VNA were calibrated using a Short-Open-Load-Through (SOLT) to ensure accurate measurements. The frequency changes at the output ports are utilized to estimate the VWC in the soil. The frequency responses of the structure at different VWCs can be correlated to the permittivity of soil, which can be transformed into soil moisture using TABLE 6.1.

The permittivity of the soil under test (SUT) depends on various factors, including soil moisture, mineral content, soil type and other impurities. Higher VWC leads to larger permittivity values, meaning that wet soil will have greater permittivity. Ensuring homogeneity in the SUT is necessary for accurate measurement results. The measurement system must be calibrated for each specific SUT, and any alteration in the SUT, such as the addition of impurities, requires recalibration. To maintain homogeneity, pure sand is used to prepare the test samples [246].

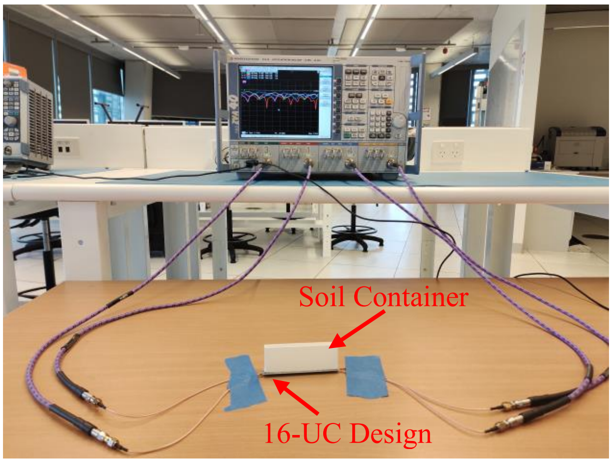

(a)

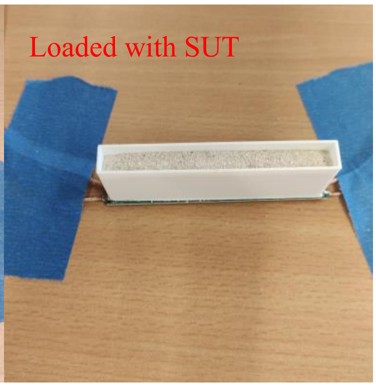

(b) (c)

Fig. 7.27. (a) Soil moisture measurement setup at low power level, (b) unloaded system, (c) system loaded with soil.

The proposed system is adaptable and can be calibrated to measure other soil types, including clay and loam. Besides soil, the proposed multi-function structure is capable of measuring the permittivity of any material in general. The typical range of soil moisture lies between 0 (dry) and 30% (fully wet), where 30% VWC causes saturation for sand, which can cause harm to the plant roots. Managing VWC within this range ensures efficient water resource usage, especially in Australia, where water conservation is essential. The simulated and measured results are shown in Fig. 7.28. The structure resonates at 900 MHz when SUT is not placed on the surface of the structure (Fig. 7.27(b)). The SUT is placed in the soil container and gradually increases the soil moisture with a step size of 5%. The resonance frequency shifts towards the left with a higher value of VWC. Higher moisture causes a high value of permittivity of SUT, which reduces the resonance frequency. For 0 to 30% VWC, the resonance frequency changes from 900 to 587 MHz. Both the simulated and measured frequency responses show close agreement, indicating the validity of the proposed structure. Three measurements were carried out with the same SUTs to assess the repeatability. For each measurement, a constant frequency shift has been observed with a maximum error of ±3.5 MHz, indicating the reliability of the structure and test setup.

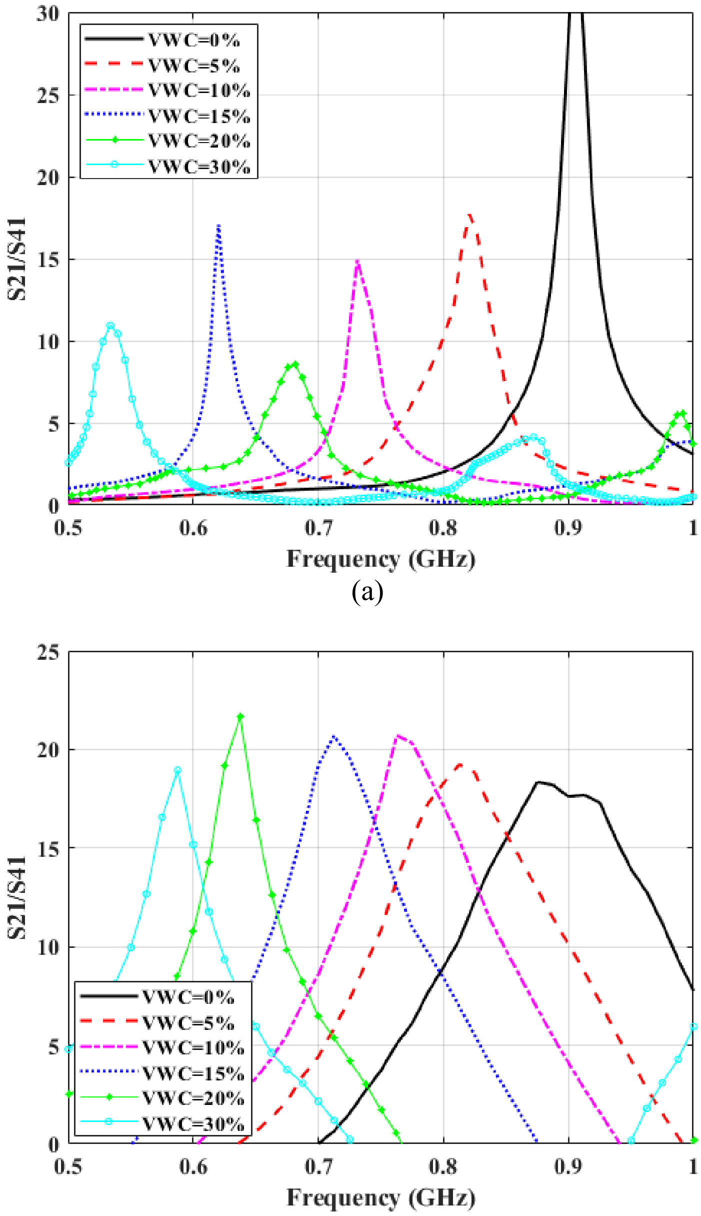

(b)

Fig. 7.28. Simulated and measured frequency responses of the proposed structure for various VWCs, (a) simulated, (b) measured.

To analyze the measurement error, a standard device, TEROS 12 [255], is utilized to measure and compare the VWC as shown in Fig. 7.29(a). By conducting multiple tests with both devices, a maximum of 3.5% error was observed for VWC, which ranged from 0 to 30%. The comparison of both devices is shown in Fig. 7.29(b).

(a)

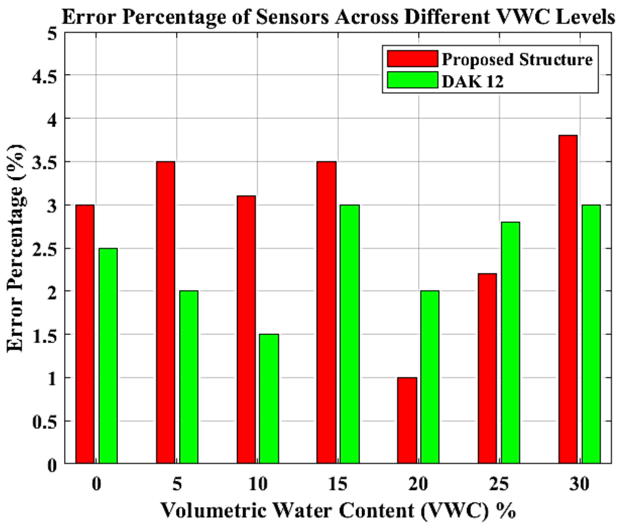

(b)

Fig. 7.29. (a) Measurement using TEROS 12 sensor, (b) error percentage (%).

7.7 Conclusion

Three different configurations of a 4-port symmetrical coupler are presented in this chapter. The proposed structures introduced in this study provide a compact, passive solution for transmission and reception applications. The suggested designs are agile and don't require biasing or control circuitry to function. This enhances their energy efficiency and makes them ideal for battery-powered IoT devices. Operating at single and dual bands, the structures utilize 32 anti-parallel Schottky diodes to enable bidirectional signal flow and achieve high isolation between low and high-power ports. Each configuration offers flexible signal routing, with low-power inputs leading to output/forward coupling and high-power inputs producing backward coupling, all without the need for external biasing. The 16-UC configuration also enables a low-power integrated differential soil moisture sensor for smart agriculture applications. This innovative technique demonstrates the potential for optimizing passive switching circuits, enhancing both performance and operational simplicity. The compact design and planar geometry make them easily integrable with other electronic components, while also reducing the overall system size for space-constrained applications. Moreover, they offer low insertion loss, which ensures better signal quality and performance when compared to bulkier switches.

8

8 Conclusion and Future Works

8.1 Conclusion

I have developed various RF structures in this thesis to integrate Wireless Power Transfer (WPT), sensing and communication for smart agriculture.

In Chapter 2, a comprehensive literature review is conducted on WPT and soil moisture sensing. The review examines existing methodologies and challenges to identify research gaps. This chapter establishes the unexplored areas in WPT and precision agriculture.

In Chapter 3, two compact rectennas are presented for WPT application. A miniaturized patch antenna is designed using a 3-Turns Complementary Spiral Resonator (3-CSR) at 1.8 GHz. To validate the simulation results, the proposed antenna is fabricated and measured. Additionally, a rectifier circuit and a matching network are designed and simulated at –10 dBm input power for high Radio Frequency to Direct Current (RF-to-DC) conversion efficiency. The rectenna achieved an efficiency of 53.6 % at –10 dBm. A pixelated rectenna operating at 2.5 GHz is also developed using the Binary Particle Swarm Optimization (BPSO) algorithm. The rectenna features a pixelated receiving antenna, which is carefully optimized to match the complex impedance of the rectifier diode, eliminating the need for a matching circuit. The optimization is performed using the BPSO algorithm. With an efficiency of 37% at an input power of 0 dBm and 64% at +12 dBm, the proposed rectenna shows significant promise for RF energy harvesting (RFEH) and WPT applications in low-power devices.

In Chapter 4, a compact Multi-Service Antenna (MSA) is presented for sensing and wireless communication using a reconfigurable complementary spiral resonator. The MSA consists of a modified patch and a 3-CSR. Two PIN diodes are integrated with the 3-CSR to realize a multi-service structure. The proposed antenna can operate in three modes: dual-band Joint Communication and Sensing Antenna (JCASA), dual-band antenna, and single-band antenna. In the JCASA mode, the first band (0.95–0.97 GHz) is used for sensing to precisely measure the permittivity, while the second band (1.53–1.56 GHz) is allocated for communication. In mode-2 and 3, the proposed MSA operates as a dual-band and single-band antenna, respectively. The proposed structure is fabricated and measured to validate its performance, and a favorable agreement is observed between the simulation and measurement results. Based on the experimental results, the proposed design is suitable for measuring soil moisture in precision farming, determining the permittivity of materials within the range of 1–20, and implementing single or dual-band antenna applications.

In Chapter 5, the proposed system consists of an Ultra-Compact Soil Moisture Sensor (UCSMS) for soil moisture measurement and a Pattern Reconfigurable Antenna (PRA)for communication to realize sensing and communication. A Complementary Spiral Resonator (CSR) is used with a microstrip transmission line to achieve miniaturization. The proposed UCSMS operates at low frequencies, 180 MHz for 3-CSR, 102 MHz for 4-turn CSR, and 86 MHz for 5-turn CSR making it suitable for covering a large volume of soil. The PRA operates at the 2.45 GHz WLAN band, facilitating the transmission of information to the base station. Integration of four varactor diodes with the communication antenna enables pattern reconfiguration, generating six distinct radiation patterns with different bias conditions. This feature makes the system suitable for smart agriculture across diverse geographical landscapes. In standby mode, the PRA can also be utilized for WPT applications to store power in a battery. This stored power can be utilized to bias the diodes to achieve reconfiguration. The UCSMS with 3-CSR and the PRA have been fabricated and measured, demonstrating a close agreement between the simulated and measured results. The sensor is adaptive and capable of measuring the permittivity of various materials within the range of 1–23.

To mitigate the environmental effects, a compact dual-band Soil Moisture Sensor (SMS) is presented for smart agriculture applications in Chapter 6. The versatility of the proposed wireless sensor allows it to operate in single and dual-band configurations. The 900 MHz band is employed for homogenous soil Volumetric Water Content (VWC) analysis in the single-band configuration. In comparison, the 500 MHz band is utilized for dual-band analysis, facilitating precise measurements and environmental compensation in soil. The proposed sensor comprises a 3-CSR, achieving compactness at a low resonance frequency, rendering the design apt for covering larger soil volumes. Three varactor diodes have been incorporated across 3-CSR to enable switching between the frequency bands. A Directional Coupler (DiC) is integrated into the input port of the sensor to create a dual-port configuration, and a 20 dB gain amplifier is connected to the input port to offset DiC and path losses. Integrating a dual-band sensor, DiC, and amplifier enhances the system's suitability for accurate VWC measurements, eliminating the need for an external portable VNA. Furthermore, the low resonance frequencies of the sensor enable it to cover a large VUT, resulting in cost efficiency as fewer sensors will be needed to cover the farming area. Sensors with and without amplifiers were fabricated and tested. A close agreement between simulated and measured results suggests the validity of the sensor's performance. A Vötschtechnik Environmental Chamber creates a realistic environment for evaluating the sensor's performance in real-world conditions. Integrating a dual-band SMS, DiC, and amplifier enables the realization of precise remote monitoring for smart farming in a real-world environment.

Finally, in Chapter 7, a smart coupler is presented to integrate WPT, sensing, and communication. A 4-port passive coupler is designed and developed, which acts as a transmit/receive (T/R) switch for the integration of the developed subsystems. Three configurations have been proposed in this work for output/backward coupling and forward/coupling. The 16-unit cell configuration also enables a low-power integrated differential soil moisture sensor for smart agriculture applications. Each configuration comprises metamaterial-based interdigital capacitors to achieve better coupling as compared to the coupled transmission lines, Schottky diodes to switch the port, and transmission lines for connectivity. The proposed couplers have been fabricated and tested, showing strong agreement between the simulated and measured results. These couplers exhibit low insertion loss for the signal and high isolation between the ports.

8.2 Contributions

Various prototypes have been developed in this research to achieve the objectives, and the following contributions have been made.

1. Miniaturized rectenna systems have been developed for WPT applications.
2. A multi-service patch antenna structure is designed and developed with dual functions:
    a. As a sensor
    b. As an antenna
3. An ultra-compact passive soil moisture sensor is developed for in-depth VWC analysis. A pattern-reconfigurable antenna is developed for communication to realize joint sensing and communication.

4. A multi-band soil moisture sensor is developed to mitigate the temperature and humidity variations effects to improve the accuracy in a practical environment.
5. Three non-linear passive couplers are developed to integrate WPT, sensing, and communication. The developed couplers are smart, act as a T/R switch and automatically switch the input signal without any DC biasing.

8.3 Future Works

In continuation of this thesis, the following future works can be done to improve the reliability and functionality of the system in a practical environment. By addressing these future work areas, the research can contribute to advancing smart agriculture technologies, leading to more efficient, sustainable, and productive agricultural practices.

8.3.1 Advanced Sensing and Monitoring

The research in advanced sensing and monitoring technology emphasizes enhancing sensor accuracy and integration across various applications for future advancements. Real-time transmission and analysis of data can be facilitated by combining communication technologies with IoT frameworks to establish responsive and flexible monitoring systems. These advancements are vital in sectors where immediate and accurate data are essential for optimizing operations and making informed decisions, such as smart infrastructure management, promoting precision agriculture and monitoring environmental conditions. Moreover, the sensing capabilities can be enhanced by incorporating factors such as monitoring nutrient levels, including Nitrogen (N), Phosphorus (P), and Potassium (K), detecting pests, tracking temperature variations, and observing other environmental conditions. This would improve the effectiveness and dependability of the system in scenarios.

8.3.2 Scalability and Network Integration

Scalability and network integration are critical for the practical deployment of IoT and smart agriculture solutions. Future research could explore methods to ensure that the developed sensors and antennas can be easily scaled up for large-scale agricultural applications. This includes investigating the interoperability of these devices with existing network infrastructures and protocols. Standard interfaces and communication protocols must be developed to enable smooth incorporation into larger IoT ecosystems. To improve the resilience and coverage of wireless sensor networks in agricultural environments, mesh network deployment and other scalable networking technologies should be researched. An extensive study can be done to scale the system of large-scale farm deployments without any battery dependency to enable seamless communication and data exchange between multiple sensor nodes.

8.3.3 AI Integration

One viable way to improve the performance and efficiency of sensing and communication systems is by integrating artificial intelligence (AI). In order to maximize system efficiency, future work may concentrate on creating AI-driven models that assess sensor data in real-time. This comprises adaptive control systems that dynamically modify sensor parameters in response to environmental circumstances and predictive maintenance, in which AI algorithms anticipate possible faults before they happen. AI is also capable of data fusion, merging data from several sensors to produce more thorough and precise insights into agricultural conditions. The dependability and efficiency of smart agriculture systems would significantly increase with the development of these AI-driven technologies. Deep learning and other AI techniques can be explored to enhance the design and performance of developed systems.

8.3.4 Real-World Deployment

The ultimate objective of these technological developments is their use in actual agricultural environments. Extensive field testing should be part of future research to confirm the created systems' functionality, dependability, and performance. In order to customize the solutions to particular crops, farming methods, and local conditions involves working with farmers and agricultural specialists. It will also be essential to research how these technologies affect crop productivity, resource efficiency, and environmental sustainability over the long run. A successful deployment would also need to address pragmatic issues like power supply, communication, and data management in the field. The practical use of these technologies will yield insightful input for additional development and enhancement of the systems. Extensive field testing can be done in an agricultural area, and developed systems can be deployed and implemented in a real-world environment to validate the performance and robustness of the proposed sensing and communication systems.

BIBLIOGRAPHY

[1] S. Sinha, "State of IoT 2024: Number of connected IoT devices growing 13% to 18.8 billion globally," ed: Retrieved from IoT Analytics: https://iot-analytics.com/number-connected …, 2024.

[2] N. Sharma and D. Panwar, "Green IoT: Advancements and Sustainability with Environment by 2050," in *2020 8th International Conference on Reliability, Infocom Technologies and Optimization (Trends and Future Directions)(ICRITO)*, 2020: IEEE, pp. 1127-1132.

[3] X. Fafoutis, A. Elsts, A. Vafeas, G. Oikonomou, and R. Piechocki, "On predicting the battery lifetime of iot devices: experiences from the sphere deployments," in *Proceedings of the 7th international workshop on real-world embedded wireless systems and networks*, 2018, pp. 7-12.

[4] R. Shadid, S. Noghanian, and A. Nejadpak, "A literature survey of wireless power transfer," in *2016 IEEE International Conference on Electro Information Technology (EIT)*, 2016: IEEE, pp. 0782-0787.

[5] L. Xie, Y. Shi, Y. T. Hou, and A. Lou, "Wireless power transfer and applications to sensor networks," *IEEE Wireless Communications,* vol. 20, no. 4, pp. 140-145, 2013.

[6] N. Shariati, "Sensitive ambient RF energy harvesting," *RMIT University,* 2015.

[7] "Low-Power Humidity and Temperature Digital Sensor." https://www.ti.com/document-viewer/HDC2080/datasheet/GUID-5AB554A1-5F5B-4CF8-B0D0-9590654E767A#TITLE-SNAS678SNAS6781218 (accessed 23 August, 2024).

[8] M. P. Aparicio, A. Bakkali, J. Pelegri-Sebastia, T. Sogorb, and V. Bou, "Radio frequency energy harvesting-sources and techniques," *Renew. Energy Util. Syst. Integr,* 2016.

[9] [Online]. Available: https://www.nxp.com/docs/en/data-sheet/NXH3670UK.pdf

[10] T. D. P. Perera, D. N. K. Jayakody, S. K. Sharma, S. Chatzinotas, and J. Li, "Simultaneous wireless information and power transfer (SWIPT): Recent advances and future challenges," *IEEE Communications Surveys & Tutorials,* vol. 20, no. 1, pp. 264-302, 2017.

[11] B. Hansen *et al.*, "Current status of and future opportunities for digital agriculture in Australia," *Crop and Pasture Science,* 2022.

[12] M. Roopaei, P. Rad, and K.-K. R. Choo, "Cloud of things in smart agriculture: Intelligent irrigation monitoring by thermal imaging," *IEEE Cloud computing,* vol. 4, no. 1, pp. 10-15, 2017.

[13] Y. E. Hamouda and C. Phillips, "Optimally heterogeneous irrigation for precision agriculture using wireless sensor networks," *Arabian Journal for Science and Engineering,* vol. 44, pp. 3183-3195, 2019.

[14] F. Viani, M. Bertolli, M. Salucci, and A. Polo, "Low-cost wireless monitoring and decision support for water saving in agriculture," *IEEE sensors journal,* vol. 17, no. 13, pp. 4299-4309, 2017.

[15] X. Yu, P. Wu, W. Han, and Z. Zhang, "A survey on wireless sensor network infrastructure for agriculture," *Computer Standards & Interfaces,* vol. 35, no. 1, pp. 59-64, 2013.

[16] R. Keshavarz, J. Lipman, D. M. M. P. Schreurs, and N. Shariati, "Highly Sensitive Differential Microwave Sensor for Soil Moisture Measurement," *IEEE Sensors Journal,* vol. 21, no. 24, pp. 27458-27464, 2021, doi: 10.1109/JSEN.2021.3125718.

[17] R. Keshavarz and N. Shariati, "High-Sensitivity and Compact Time Domain Soil Moisture Sensor Using Dispersive Phase Shifter for Complex Permittivity Measurement," *IEEE Transactions on Instrumentation and Measurement,* vol. 71, pp. 1-10, 2021.

[18] P. Pal, S. Tripathi, and C. Kumar, "Single Probe Imitation of Multi-Depth Capacitive Soil Moisture Sensor Using Bidirectional Recurrent Neural Network," *IEEE Transactions on Instrumentation and Measurement,* vol. 71, pp. 1-11, 2022, doi: 10.1109/TIM.2022.3156179.

[19] W. J. Wu, W. S. Zhao, D. W. Wang, B. Yuan, and G. Wang, "Ultrahigh-Sensitivity Microwave Microfluidic Sensors Based on Modified Complementary Electric-LC and Split-Ring Resonator Structures," *IEEE Sensors Journal,* vol. 21, no. 17, pp. 18756-18763, 2021, doi: 10.1109/JSEN.2021.3090086.

[20] K. S. Parvathi and S. R. Gupta, "Ultrahigh-sensitivity and compact EBG-based microwave sensor for liquid characterization," *IEEE Sensors Letters,* vol. 6, no. 4, pp. 1-4, 2022.

[21] M. Amiri, M. Abolhasan, N. Shariati, and J. Lipman, "Soil moisture remote sensing using SIW cavity based metamaterial perfect absorber," *Scientific Reports,* vol. 11, no. 1, p. 7153, 2021.

[22] T. Fernández-Caramés and P. Fraga-Lamas, "Teaching and Learning IoT Cybersecurity and Vulnerability Assessment with Shodan through Practical Use Cases," *Sensors,* vol. 20, p. 3048, 05/27 2020, doi: 10.3390/s20113048.

[23] N. Gondchawar and R. Kawitkar, "IoT based smart agriculture," *International Journal of advanced research in Computer and Communication Engineering,* vol. 5, no. 6, pp. 838-842, 2016.

[24] A. Tzounis, N. Katsoulas, T. Bartzanas, and C. Kittas, "Internet of Things in agriculture, recent advances and future challenges," *Biosystems engineering,* vol. 164, pp. 31-48, 2017.

[25] F. Yildiz, "Potential Ambient Energy-Harvesting Sources and Techniques," *Journal of technology Studies,* vol. 35, no. 1, pp. 40-48, 2009.

[26] J. W. Stevens, "Optimized thermal design of small ΔT thermoelectric generators," SAE Technical Paper, 0148-7191, 1999.

[27] A. S. Holmes, G. Hong, K. R. Pullen, and K. R. Buffard, "Axial-flow microturbine with electromagnetic generator: design, CFD simulation, and prototype demonstration," in *17th IEEE International Conference on Micro Electro Mechanical Systems. Maastricht MEMS 2004 Technical Digest*, 2004: IEEE, pp. 568-571.

[28] N. Shariati, W. S. T. Rowe, and K. Ghorbani, "RF Field Investigation and Maximum Available Power Analysis for Enhanced RF Energy Scavenging," in *2012 42nd European Microwave Conference*, 29 Oct.-1 Nov. 2012 2012, pp. 329-332, doi: 10.23919/EuMC.2012.6459223.

[29] I. Zhou *et al.*, "Internet of things 2.0: Concepts, applications, and future directions," *IEEE Access,* vol. 9, pp. 70961-71012, 2021.

[30] G. Santhanamari, B. Dharshini, S. Kousalya, and R. Akash, "Radar Based Target Detection and Classification," in *2023 International Conference on Intelligent Systems for Communication, IoT and Security (ICISCoIS)*, 2023: IEEE, pp. 412-416.

[31] M. A. Ullah, R. Keshavarz, M. Abolhasan, J. Lipman, K. P. Esselle, and N. Shariati, "A Review on Antenna Technologies for Ambient RF Energy Harvesting and Wireless Power Transfer: Designs, Challenges and Applications," *IEEE Access,* vol. 10, pp. 17231-17267, 2022, doi: 10.1109/ACCESS.2022.3149276.

[32] A. M. Almohaimeed, R. E. Amaya, J. A. Lima, and M. C. Yagoub, "An adaptive power harvester with active load modulation for highly efficient short/long range RF WPT applications," *Electronics,* vol. 7, no. 7, p. 125, 2018.

[33] S. Ladan, N. Ghassemi, A. Ghiotto, and K. Wu, "Highly efficient compact rectenna for wireless energy harvesting application," *IEEE microwave magazine,* vol. 14, no. 1, pp. 117-122, 2013.

[34] A. Raza, R. Keshavarz, and N. Shariati, "Miniaturized Patch Rectenna Using 3-Turn Complementary Spiral Resonator for Wireless Power Transfer," in *2021 IEEE Asia-Pacific Microwave Conference (APMC)*, 2021: IEEE, pp. 455-457.

[35] M. Migalin, R. Keshavarz, and N. Shariati, "mm-Wave Polarization Insensitive Spiral Antenna for 5G Energy Harvesting Applications," in *2022 Wireless Power Week (WPW)*, 5-8 July 2022 2022, pp. 417-421, doi: 10.1109/WPW54272.2022.9853925.

[36] M. Ali, G. Yang, and R. Dougal, "A new circularly polarized rectenna for wireless power transmission and data communication," *IEEE Antennas and wireless propagation letters,* vol. 4, pp. 205-208, 2005.

[37] S. Liu, D. Yang, Y. Chen, S. Huang, and Y. Xiang, "Broadband dual circularly polarized dielectric resonator antenna for ambient electromagnetic energy harvesting," *IEEE Transactions on Antennas and Propagation,* vol. 68, no. 6, pp. 4961-4966, 2020.

[38] M. A. Ullah, R. Keshavarz, M. Abolhasan, J. Lipman, and N. Shariati, "Low-profile dual-band pixelated defected ground antenna for multistandard IoT devices," *Scientific Reports,* vol. 12, no. 1, p. 11479, 2022.

[39] S.-H. Chang and W.-J. Liao, "A broadband LTE/WWAN antenna design for tablet PC," *IEEE Transactions on Antennas and Propagation,* vol. 60, no. 9, pp. 4354-4359, 2012.

[40] W.-S. Chen and W.-C. Jhang, "A planar WWAN/LTE antenna for portable devices," *IEEE Antennas and Wireless Propagation Letters,* vol. 12, pp. 19-22, 2012.

[41] Y.-L. Ban, S.-C. Sun, P.-P. Li, J. L.-W. Li, and K. Kang, "Compact eight-band frequency reconfigurable antenna for LTE/WWAN tablet computer applications," *IEEE Transactions on Antennas and propagation,* vol. 62, no. 1, pp. 471-475, 2013.

[42] X. Zhu and Y. Sun, "A new coupled-loop antenna for eight-band LTE/WWAN operation in ultra-thin laptop computer," *Progress in Electromagnetics Research C,* vol. 42, pp. 229-238, 2013.

[43] Y.-L. Ban, et al, "Compact coupled-fed wideband antenna for internal eight-band LTE/WWAN tablet computer applications," *Journal of Electromagnetic Waves and Applications,* vol. 26, pp. 2222-2233, 2012.

[44] N. a. J. Amani, A., "Internal uniplanar antenna for LTE/WWAN/GPS/GLONASS applications in tablet/laptop computers," *IEEE Antennas and Wireless Propagation Letters,* vol. 14, pp. 1654-1657, 2015.

[45] C. Deng, Y.-j. Xie, and P. Li, "CPW-fed planar printed monopole antenna with impedance bandwidth enhanced," *IEEE Antennas and Wireless Propagation Letters,* vol. 8, pp. 1394-1397, 2009.

[46] X. L. Liang, S. S. Zhong, and W. Wang, "UWB printed circular monopole antenna," *Microwave and optical technology letters,* vol. 48, no. 8, pp. 1532-1534, 2006.

[47] S.-S. Zhong, X.-L. Liang, and W. Wang, "Compact elliptical monopole antenna with impedance bandwidth in excess of 21: 1," *IEEE Transactions on Antennas and Propagation,* vol. 55, no. 11, pp. 3082-3085, 2007.

[48] D. Tran, P. Aubry, A. Szilagyi, I. Lager, O. Yarovyi, and L. Ligthart, "On the design of a super wideband antenna," in *Ultra wideband*: IntechOpen, 2010, pp. 399-426.

[49] Y. Dong, W. Hong, L. Liu, Y. Zhang, and Z. Kuai, "Performance analysis of a printed super-wideband antenna," *Microwave and Optical Technology Letters,* vol. 51, no. 4, pp. 949-956, 2009.

[50] K.-R. Chen and J.-S. Row, "A compact monopole antenna for super wideband applications," *IEEE Antennas and Wireless Propagation Letters,* vol. 10, pp. 488-491, 2011.

[51] V. Waladi, N. Mohammadi, Y. Zehforoosh, A. Habashi, and J. Nourinia, "A novel modified star-triangular fractal (MSTF) monopole antenna for super-wideband applications," *IEEE antennas and wireless propagation Letters,* vol. 12, pp. 651-654, 2013.

[52] B. A. Cetiner, G. R. Crusats, L. Jofre, and N. Biyikli, "RF MEMS integrated frequency reconfigurable annular slot antenna," *IEEE Transactions on Antennas and Propagation,* vol. 58, no. 3, pp. 626-632, 2009.

[53] E. Erdil, K. Topalli, M. Unlu, O. A. Civi, and T. Akin, "Frequency tunable microstrip patch antenna using RF MEMS technology," *IEEE transactions on antennas and propagation,* vol. 55, no. 4, pp. 1193-1196, 2007.

[54] L. Hinsz and B. D. Braaten, "A frequency reconfigurable transmitter antenna with autonomous switching capabilities," *IEEE Transactions on antennas and propagation,* vol. 62, no. 7, pp. 3809-3813, 2014.

[55] P.-Y. Qin, A. R. Weily, Y. J. Guo, T. S. Bird, and C.-H. Liang, "Frequency reconfigurable quasi-Yagi folded dipole antenna," *IEEE transactions on antennas and propagation,* vol. 58, no. 8, pp. 2742-2747, 2010.

[56] H. Jiang, M. Patterson, C. Zhang, and G. Subramanyam, "Frequency tunable microstrip patch antenna using ferroelectric thin film varactor," in *Proceedings of the IEEE 2009 National Aerospace & Electronics Conference (NAECON)*, 2009: IEEE, pp. 248-250.

[57] S.-S. Oh, Y.-B. Jung, Y.-R. Ju, and H.-D. Park, "Frequency-tunable open-ring microstrip antenna using varactor," in *2010 International Conference on Electromagnetics in Advanced Applications*, 2010: IEEE, pp. 624-626.

[58] H. F. Abutarboush *et al.*, "A reconfigurable wideband and multiband antenna using dual-patch elements for compact wireless devices," *IEEE Transactions on Antennas and Propagation,* Article vol. 60, no. 1, pp. 36-43, 2012, doi: 10.1109/TAP.2011.2167925.

[59] S. Chagharvand, M. R. Hamid, M. R. Kamarudin, and J. R. Kelly, "Wide and multi-band reconfigurable Vivaldi antenna with slot-line feed," *Telecommunication Systems,* Article vol. 65, no. 1, pp. 79-85, 2017, doi: 10.1007/s11235-016-0213-z.

[60] W. A. Awan *et al.*, "A miniaturized wideband and multi-band on-demand reconfigurable antenna for compact and portable devices," *AEU-International Journal of Electronics and Communications,* vol. 122, p. 153266, 2020.

[61] I. H. Idris, M. R. Hamid, K. Kamardin, and M. K. A. Rahim, "A multi to wideband frequency reconfigurable antenna," *International Journal of RF and Microwave Computer-Aided Engineering,* vol. 28, no. 4, p. e21216, 2018.

[62] H. F. Abutarboush *et al.*, "A reconfigurable wideband and multiband antenna using dual-patch elements for compact wireless devices," *IEEE Transactions on Antennas and Propagation,* Article vol. 60, no. 1, pp. 36-43, 2012, Art no. 6018254, doi: 10.1109/TAP.2011.2167925.

[63] G. H. a. B. Huff, J.T., "Integration of packaged RF MEMS switches with radiation pattern reconfigurable square spiral microstrip antennas," *IEEE Transactions on Antennas and Propagation,* vol. 5, no. 42, pp. 464-469, 2006.

[64] A. G. e. al., "A dual linearly polarized MEMS-reconfigurable antenna for narrowband MIMO communication systems," *IEEE Trans. Antennas Propag.,* vol. 58, no. 1, pp. 4-16, 2010.

[65] P. M. D. Piazza, M. D'amico, and K. Dandekar, "Experimental analysis of pattern and polarization reconfigurable circular patch antennas for MIMO antennas," *IEEE Trans. Antennas Propag.,* vol. 59, no. 5, pp. 2352-2362, 2010.

[66] M. W. Young, S. Yong, and J. T. Bernhard, "A Miniaturized Frequency Reconfigurable Antenna With Single Bias, Dual Varactor Tuning," *IEEE Transactions on Antennas and Propagation,* vol. 63, no. 3, pp. 946-951, 2015, doi: 10.1109/TAP.2015.2388776.

[67] W. A. Awan, S. I. Naqvi, N. Hussain, A. Zaidi, A. H. Naqvi, and A. Hameed, "Electrically Small Frequency Reconfigurable Antenna for Heterogeneous Applications," in *2020 International Conference on UK-China Emerging Technologies (UCET)*, 20-21 Aug. 2020 2020, pp. 1-3, doi: 10.1109/UCET51115.2020.9205472.

[68] L. M. Feldner, C. T. Rodenbeck, C. G. Christodoulou, and N. Kinzie, "Electrically Small Frequency-Agile PIFA-as-a-Package for Portable Wireless Devices," *IEEE Transactions on Antennas and Propagation,* vol. 55, no. 11, pp. 3310-3319, 2007, doi: 10.1109/TAP.2007.908815.

[69] M. Fallahpour, M. T. Ghasr, and R. Zoughi, "Miniaturized Reconfigurable Multiband Antenna For Multiradio Wireless Communication," *IEEE Transactions on Antennas and Propagation,* vol. 62, no. 12, pp. 6049-6059, 2014, doi: 10.1109/TAP.2014.2364293.

[70] M. Borhani, P. Rezaei, and A. Valizade, "Design of a Reconfigurable Miniaturized Microstrip Antenna for Switchable Multiband Systems," *IEEE Antennas and Wireless Propagation Letters,* vol. 15, pp. 822-825, 2016, doi: 10.1109/LAWP.2015.2476363.

[71] H. A. Majid, M. K. A. Rahim, M. R. Hamid, N. A. Murad, and M. F. Ismail, "Frequency-Reconfigurable Microstrip Patch-Slot Antenna," *IEEE Antennas and Wireless Propagation Letters,* vol. 12, pp. 218-220, 2013, doi: 10.1109/LAWP.2013.2245293.

[72] S. Zhu, D. G. Holtby, K. L. Ford, A. Tennant, and R. J. Langley, "Compact Low Frequency Varactor Loaded Tunable SRR Antenna," *IEEE Transactions on Antennas and Propagation,* vol. 61, no. 4, pp. 2301-2304, 2013, doi: 10.1109/TAP.2013.2239952.

[73] M. Rao and K. Sarabandi, "A Tunable, High-Gain, Very Low-Profile Composite Monopole Antenna for Low-Frequency Applications," *IEEE Transactions on Antennas and Propagation,* vol. 66, no. 7, pp. 3286-3294, 2018, doi: 10.1109/TAP.2018.2826653.

[74] H. Kang and S. Lim, "Electrically Small Dual-Band Reconfigurable Complementary Split-Ring Resonator (CSRR)-Loaded Eighth-Mode Substrate Integrated Waveguide (EMSIW) Antenna," *IEEE Transactions on Antennas and Propagation,* vol. 62, no. 5, pp. 2368-2373, 2014, doi: 10.1109/TAP.2014.2308532.

[75] F. Ferrero, A. Chevalier, J. M. Ribero, R. Staraj, J. L. Mattei, and Y. Queffelec, "A New Magneto-Dielectric Material Loaded, Tunable UHF Antenna for Handheld Devices," *IEEE Antennas and Wireless Propagation Letters,* vol. 10, pp. 951-954, 2011, doi: 10.1109/LAWP.2011.2167118.

[76] D. Piazza, Mookiah, P., d'Amico, M. and Dandekar, K.R., "Experimental analysis of pattern and polarization reconfigurable circular patch antennas for MIMO systems," *IEEE Transactions on Vehicular Technology,* vol. 59, no. 5, pp. 2352-2362, 2010.

[77] Y. J. G. P. Quin, A. R. Weily, and C. Liang, "A pattern reconfigurable U-Slot antenna and its applications in MIMO systems," *IEEE Trans. Antennas Propag.,* vol. 60, no. 2, pp. 516-528, 2012.

[78] J. S. R. S. H. Chen, and K. L. Wong, "Reconfigurable square-ring patch antenna with pattern diversity," *IEEE Trans. Antennas Propag.,* vol. 55, no. 2, pp. 472-475, 2007.

[79] S. J. W. a. T. G. Ma, "A wideband slotted bow-tie antenna with reconfigurable CPW-to slotline transition for pattern diversity," *IEEE Trans. Antennas Propag.,* vol. 56, no. 2, pp. 327-334, 2008.

[80] Y. M. J. Sarrazin, S. Avrillon, and S. Toutain, "Pattern reconfigurable cubic antenna," *IEEE Trans. Antennas Propag.,* vol. 57, no. 2, pp. 310-317, 2009.

[81] A. S. D. D. Patron, and K. R. Dandekar, "Optical control of reconfigurable antennas and application to a novel pattern-reconfigurable planar design," *IEEE J. Lightw. Technol.,* 2014.

[82] S.-Y. Y. T. Zhang, and Yong Wang., "Design of radiation-pattern- recongurable antenna with four beams," *IEEE Antennas and Wireless Propagation Letters,* vol. 14, pp. 183-186, 2015.

[83] V. N. a. C. W. Jung., "Radiation-pattern recongurable an- tenna for medical implants in medradio band."

[84] W. L. a. H. Wong., "Polarization recongurable wheel-shaped antenna with conical-beam radiation pattern," *Microwaves, Antennas and Propag., IET,* vol. 9, no. 12, pp. 1331-1336, 2015.

[85] C. M. L. a. C. W. Jung., "Radiation-pattern-recongurable antenna using monopole-loop for tbitex wristband"," *Antennas and Wireless Propag. Lett.,* vol. 14, pp. 269-272, 2015.

[86] S. X. Y. Bai, C. Liu, X. Shuai, and B. Wang, "`Design of pattern reconfigurable antennas based on a two-element dipole array model," *IEEE Trans. Antennas Propag.,* vol. 61, no. 9, pp. 4867-4871, 2013.

[87] L. Santamaria, F. Ferrero, R. Staraj, and L. Lizzi, "Slot-Based Pattern Reconfigurable ESPAR Antenna for IoT Applications," *IEEE Transactions on Antennas and Propagation,* vol. 69, no. 7, pp. 3635-3644, 2021, doi: 10.1109/TAP.2020.3044399.

[88] L. Santamaria, F. Ferrero, R. Staraj, and L. Lizzi, "Electronically Pattern Reconfigurable Antenna for IoT Applications," *IEEE Open Journal of Antennas and Propagation,* vol. 2, pp. 546-554, 2021, doi: 10.1109/OJAP.2021.3073104.

[89] Z. Ding, R. Jin, J. Geng, W. Zhu, and X. Liang, "Varactor Loaded Pattern Reconfigurable Patch Antenna With Shorting Pins," *IEEE Transactions on Antennas and Propagation,* vol. 67, no. 10, pp. 6267-6277, 2019, doi: 10.1109/TAP.2019.2920282.

[90] S. D. Assimonis, Fusco, V., Georgiadis, A. and Samaras, T., "Efficient and sensitive electrically small rectenna for ultra-low power RF energy harvesting," *Scientific reports,* vol. 8, no. 1, pp. 1-13, 2018.

[91] W. Lin, Ziolkowski, R.W. and Huang, J., "Electrically small, low-profile, highly efficient, huygens dipole rectennas for wirelessly powering internet-of-things devices," *EEE Transactions on Antennas and Propagation,* vol. 67, no. 7, pp. 3670-3679, 2019.

[92] R. W. Ziolkowski, "Electrically small antenna advances for current 5G and evolving 6G and beyond wireless systems," *Antenna and Array Technologies for Future Wireless Ecosystems,* pp. 335-391, 2022.

[93] Z. Zhang, M. Li, Q. Dai, and R. W. Ziolkowski, "Superdirective, Electrically Small, Endfire-Radiating Huygens Quadrupole Antenna," *IEEE Transactions on Antennas and Propagation,* 2024.

[94] Q. Lin, M.-C. Tang, M. Li, and R. W. Ziolkowski, "Electrically small, wideband, circularly polarized, inductive grid-array metasurface antenna," *IEEE Transactions on Antennas and Propagation,* vol. 71, no. 5, pp. 4546-4551, 2023.

[95] Z. Wu, M.-C. Tang, T. Shi, and R. W. Ziolkowski, "Two-port, dual-circularly polarized, low-profile broadside-radiating electrically small Huygens dipole antenna," *IEEE Transactions on Antennas and Propagation,* vol. 69, no. 1, pp. 514-519, 2020.

[96] X. Chen, M.-C. Tang, D. Yi, and R. W. Ziolkowski, "An interdigitated structure-based, electrically small dipole antenna with enhanced bandwidth," in *2020 IEEE International Symposium on Antennas and Propagation and North American Radio Science Meeting*, 2020: IEEE, pp. 355-356.

[97] C. M. Kruesi, R. J. Vyas, and M. M. Tentzeris, "Design and development of a novel 3-D cubic antenna for wireless sensor networks (WSNs) and RFID applications," *IEEE Transactions on Antennas and Propagation,* vol. 57, no. 10, pp. 3293-3299, 2009.

[98] S. Lim, R. L. Rogers, and H. Ling, "A tunable electrically small antenna for ground wave transmission," *IEEE Transactions on Antennas and Propagation,* vol. 54, no. 2, pp. 417-421, 2006.

[99] "AD8302." https://www.analog.com/en/products/ad8302.html#part-details (accessed October, 2024).

[100] J. Choi, F. T. Dagefu, B. M. Sadler, and K. Sarabandi, "Electrically small folded dipole antenna for HF and low-VHF bands," *IEEE Antennas and Wireless Propagation Letters,* vol. 15, pp. 718-721, 2015.

[101] A. Erentok and R. W. Ziolkowski, "An efficient metamaterial-inspired electrically-small antenna," *Microwave and Optical Technology Letters,* vol. 49, no. 6, pp. 1287-1290, 2007.

[102] M. Amiri, F. Tofigh, N. Shariati, J. Lipman, and M. Abolhasan, "Review on metamaterial perfect absorbers and their applications to IoT," *IEEE Internet of Things Journal,* vol. 8, no. 6, pp. 4105-4131, 2020.

[103] M. Amiri, F. Tofigh, N. Shariati, J. Lipman, and M. Abolhasan, "Miniature tri-wideband Sierpinski–Minkowski fractals metamaterial perfect absorber," *IET Microwaves, Antennas & Propagation,* vol. 13, no. 7, pp. 991-996, 2019.

[104] F. Tofigh, M. Amiri, N. Shariati, J. Lipman, and M. Abolhasan, "Polarization-insensitive metamaterial absorber for crowd estimation based on electromagnetic energy measurements," *IEEE Transactions on Antennas and Propagation,* vol. 68, no. 3, pp. 1458-1467, 2019.

[105] R. Keshavarz and N. Shariati, "Low profile metamaterial band-pass filter loaded with 4-turn complementary spiral resonator for WPT applications," in *2020 27th IEEE International Conference on Electronics, Circuits and Systems (ICECS)*, 2020: IEEE, pp. 1-4.

[106] M. Amiri, F. Tofigh, N. Shariati, J. Lipman, and M. Abolhasan, "Ultra wideband dual polarization metamaterial absorber for 5G frequency spectrum," in *2020 14th European Conference on Antennas and Propagation (EuCAP)*, 2020: IEEE, pp. 1-5.

[107] F. Tofigh, M. Amiri, N. Shariati, J. Lipman, and M. Abolhasan, "Low-frequency metamaterial absorber using space-filling curve," *Journal of Electronic Materials,* vol. 48, pp. 6451-6459, 2019.

[108] E. Ahamed, R. Keshavarz, D. Franklin, and N. Shariati, "Software-defined Programmable Metamaterial Lens System for Dynamic Wireless Power Transfer Applications," *IEEE Transactions on Antennas and Propagation,* 2024.

[109] M. Polivka, A. Holub, M. Vyhnalik, and M. Svanda, "Impedance properties and radiation efficiency of electrically small double and triple split-ring antennas for UHF RFID

applications," *IEEE Antennas and Wireless Propagation Letters,* vol. 12, pp. 221-224, 2013.

[110] M.-C. Tang and R. W. Ziolkowski, "A study of low-profile, broadside radiation, efficient, electrically small antennas based on complementary split ring resonators," *IEEE Transactions on Antennas and Propagation,* vol. 61, no. 9, pp. 4419-4430, 2013.

[111] A. Raza, R. Keshavarz, E. Dutkiewicz, and N. Shariati, "Compact Multiservice Antenna for Sensing and Communication Using Reconfigurable Complementary Spiral Resonator," *IEEE Transactions on Instrumentation and Measurement,* vol. 72, pp. 1-9, 2023, doi: 10.1109/TIM.2023.3300466.

[112] W. Lin and R. W. Ziolkowski, "Electrically small Huygens antenna-based fully-integrated wireless power transfer and communication system," *IEEE Access,* vol. 7, pp. 39762-39769, 2019.

[113] M.-C. Tang, H. Wang, and R. W. Ziolkowski, "Design and testing of simple, electrically small, low-profile, Huygens source antennas with broadside radiation performance," *IEEE transactions on antennas and propagation,* vol. 64, no. 11, pp. 4607-4617, 2016.

[114] A. F. Alsager, "Design and Analysis of Microstrip Patch Antenna Arrays," Electrical Engineering– Communication and Signal processing, University College of Borås, 2011.

[115] J. Zaid, Farahani, M. and Denidni, T.A., "Magneto-dielectric substrate-based microstrip antenna for RFID applications," *IET Microwaves, Antennas & Propagation,* vol. 11, no. 10, pp. 1389-1392, 2017.

[116] Y. Y. Kyi, Guo, L. and Lu, J., "Miniaturization ofA Patch Antenna Using Magneto-dielectric Material," *IEEE International Symposium on Antennas and Propagation (ISAP),* pp. 1433-1436, 2012.

[117] L. Yousefi, Mohajer-Iravani, B. and Ramahi, O.M., "Enhanced Bandwidth Artificial Magnetic Ground Plane for Low-Profile Antennas," *IEEE Antennas and Wireless Propagation Letters,* vol. 6, pp. 289-292, 2007.

[118] F. Farzami, Forooraghi, K. and Norooziarab, M., "Miniaturization of a Microstrip Antenna Using a Compact and Thin Magneto-Dielectric Substrate " *IEEE Antennas and Wireless Propagation Letters,* vol. 10, pp. 1540-1542, 2011.

[119] A. a. S. Foroozesh, L., "Size Reduction of a Microstrip Antenna with Dielectric Superstrate Using Meta-Materials: Artificial Magnetic Conductors versus Magneto-Dielectrics," *2006 IEEE Antennas and Propagation Society International Symposium,* pp. 11-14, 2006.

[120] S. M. Han, Min, K.S. and Kim, T.G., "Study on miniaturization and broadband of patch antenna using magneto-dielectric substrate," *IEEE 2008 Asia-Pacific Microwave Conference,* pp. 1-4, 2008.

[121] A. Louzir, Minard, P. and Pintos, J.F., "Parametric Study on the Use of Magneto-dielectric Materials for Antenna Miniaturization," *2010 IEEE Antennas and Propagation Society International Symposium,* pp. 1-4, 2010.

[122] X. M. Yang, Sun, Q.H., Jing, Y., Cheng, Q., Zhou, X.Y., Kong, H.W. and Cui, T.J., "Increasing the Bandwidth of Microstrip Patch Antenna by Loading Compact Artificial Magneto-Dielectrics," *IEEE Transactions on Antennas and Propagation,* vol. 59, no. 2, pp. 373-378, 2010.

[123] J. Lee, Lee, J., Min, K. and Cheon, Y., "Miniaturized Antennas With Reduced Hand Effects in Mobile Phones Using Magneto-Dielectric Material," *IEEE Antennas and Wireless Propagation Letters,* vol. 13, pp. 935-938, 2014.

[124] K. Han, Swaminathan, M., Pulugurtha, R., Sharma, H., Tummala, R., Yang, S. and Nair, V., "Magneto-Dielectric Nanocomposite for Antenna Miniaturization and SAR Reduction," *IEEE Antennas and Wireless Propagation Letters,* vol. 15, pp. 72-75, 2015.

[125] W. Lin and R. W. Ziolkowski, "Electrically small, single-substrate huygens dipole rectenna for ultracompact wireless power transfer applications," *IEEE Transactions on Antennas and Propagation,* vol. 69, no. 2, pp. 1130-1134, 2020.

[126] N. Zhu, Ziolkowski, R.W. and Xin, H., "A metamaterial-inspired, electrically small rectenna for high-efficiency, low power harvesting and scavenging at the global

positioning system L1 frequency," *Applied Physics Letters,* vol. 99, no. 11, p. 114101, 2011.

[127] S. S. R. Rishi, "mpedance Matching Techniques for Microstrip Patch Antenna," *Indian Journal of Science and Technology,* vol. 10, no. 28, pp. 1-16, 2017.

[128] D. M. Pozar, *Microwave engineering*. John wiley & sons, 2011.

[129] I. D. Bougas, M. S. Papadopoulou, A. D. Boursianis, K. Kokkinidis, and S. K. Goudos, "State-of-the-art techniques in RF energy harvesting circuits," in *Telecom*, 2021, vol. 2, no. 4: MDPI, pp. 369-389.

[130] M. Arrawatia, M. S. Baghini, and G. Kumar, "RF energy harvesting system from cell towers in 900MHz band," in *2011 National Conference on Communications (NCC)*, 2011: IEEE, pp. 1-5.

[131] "Voltage Doubler- Circuit Diagram, Half-Wave & Full-Wave." https://www.electricalvolt.com/voltage-doubler/ (accessed 27/07, 2024).

[132] N. Shariati, W. S. Rowe, J. R. Scott, and K. Ghorbani, "Multi-service highly sensitive rectifier for enhanced RF energy scavenging," *Scientific reports,* vol. 5, no. 1, p. 9655, 2015.

[133] N. Shariati, W. S. Rowe, and K. Ghorbani, "Highly sensitive rectifier for efficient RF energy harvesting," in *2014 44th European Microwave Conference*, 2014: IEEE, pp. 1190-1193.

[134] N. Nikkhah, R. Keshavarz, M. Abolhasan, J. Lipman, and N. Shariati, "Efficient dual-band single-port rectifier for RF energy harvesting at FM and GSM bands," in *2022 Wireless Power Week (WPW)*, 2022: IEEE, pp. 141-145.

[135] N. Shariati, W. S. Rowe, and K. Ghorbani, "Highly sensitive FM frequency scavenger integrated in building materials," in *2015 European Microwave Conference (EuMC)*, 2015: IEEE, pp. 68-71.

[136] F. Sarı and Y. Uzun, "A comparative study: Voltage multipliers for RF energy harvesting system," *Communications Faculty of Sciences University of Ankara Series A2-A3 Physical Sciences and Engineering,* vol. 61, no. 1, pp. 12-23, 2019.

[137] P. Rengalakshmi and R. Brinda, "Rectifier for RF energy harvesting," *International Journal of Computer Applications,* vol. 143, no. 10, pp. 14-17, 2016.

[138] S. S. Sarma, S. Chandravanshi, and M. J. Akhtar, "Triple band differential rectifier for RF energy harvesting applications," in *2016 Asia-Pacific Microwave Conference (APMC)*, 2016: IEEE, pp. 1-4.

[139] C. R. Valenta and G. D. Durgin, "Harvesting wireless power: Survey of energy-harvester conversion efficiency in far-field, wireless power transfer systems," *IEEE Microwave Magazine,* vol. 15, no. 4, pp. 108-120, 2014.

[140] S. Ahmed, Z. Zakaria, M. Husain, I. Ibrahim, and A. Alhegazi, "Efficient feeding geometries for rectenna design at 2.45 GHz," *Electronics Letters,* vol. 53, no. 24, pp. 1585-1587, 2017.

[141] K. Bhatt, S. Kumar, P. Kumar, and C. C. Tripathi, "Highly efficient 2.4 and 5.8 GHz dual-band rectenna for energy harvesting applications," *IEEE Antennas and Wireless Propagation Letters,* vol. 18, no. 12, pp. 2637-2641, 2019.

[142] J. Shen, W. Zhang, C. Wu, X. Wu, E. Fang, and X. Liu, "A Compact Duplexing Rectenna With Wireless Power Transfer and Harmonic Feedback Capabilities," *IEEE Antennas and Wireless Propagation Letters,* vol. 22, no. 7, pp. 1751-1755, 2023, doi: 10.1109/LAWP.2023.3262706.

[143] M. Chang, Y. Li, J. Han, H. Liu, and L. Li, "A Compact Polarization-Insensitive Rectenna With Harmonic Suppression for Wireless Power Transfer," *IEEE Antennas and Wireless Propagation Letters,* vol. 23, no. 1, pp. 119-123, 2024, doi: 10.1109/LAWP.2023.3319317.

[144] X. Cai, W. Geyi, and Y. Guo, "A Compact Rectenna With Flat-Top Angular Coverage for RF Energy Harvesting," *IEEE Antennas and Wireless Propagation Letters,* vol. 20, no. 7, pp. 1307-1311, 2021, doi: 10.1109/LAWP.2021.3078548.

[145] S. C. Wang, M. J. Li, and M. S. Tong, "A High-Performance Rectenna for Wireless Power Transfer in CubeSats," *IEEE Antennas and Wireless Propagation Letters,* vol. 19, no. 12, pp. 2197-2200, 2020, doi: 10.1109/LAWP.2020.3027504.

[146] Z. Dan, Z. He, H. Lin, and C. Liu, "A Patch Rectenna With an Integrated Impedance Matching Network and a Harmonic Recycling Filter," *IEEE Antennas and Wireless Propagation Letters,* vol. 21, no. 10, pp. 2085-2089, 2022, doi: 10.1109/LAWP.2022.3190879.

[147] J. Siden, X. Zeng, T. Unander, A. Koptyug, and H.-E. Nilsson, "Remote moisture sensing utilizing ordinary RFID tags," in *SENSORS, 2007 IEEE*, 2007: IEEE, pp. 308-311.

[148] W. Wagner, K. Scipal, C. Pathe, D. Gerten, W. Lucht, and B. Rudolf, "Evaluation of the agreement between the first global remotely sensed soil moisture data with model and precipitation data," *Journal of Geophysical Research: Atmospheres,* vol. 108, no. D19, 2003.

[149] R. Ding *et al.*, "Soil Moisture Sensing with UAV-Mounted IR-UWB Radar and Deep Learning," *Proceedings of the ACM on Interactive, Mobile, Wearable and Ubiquitous Technologies,* vol. 7, no. 1, pp. 1-25, 2023.

[150] Y. Feng, Y. Xie, D. Ganesan, and J. Xiong, "Lte-based low-cost and low-power soil moisture sensing," in *Proceedings of the 20th ACM Conference on Embedded Networked Sensor Systems*, 2022, pp. 421-434.

[151] Z. Chang, F. Zhang, J. Xiong, J. Ma, B. Jin, and D. Zhang, "Sensor-free soil moisture sensing using lora signals," *Proceedings of the ACM on Interactive, Mobile, Wearable and Ubiquitous Technologies,* vol. 6, no. 2, pp. 1-27, 2022.

[152] W. Jiao, J. Wang, Y. He, X. Xi, and F. Wang, "SoilTAG: Fine-Grained Soil Moisture Sensing Through Chipless Tags," *IEEE Transactions on Mobile Computing,* vol. 23, no. 03, pp. 2153-2170, 2024, doi: 10.1109/tmc.2023.3253135.

[153] J. Wang, L. Chang, S. Aggarwal, O. Abari, and S. Keshav, "Soil moisture sensing with commodity RFID systems," in *Proceedings of the 18th International Conference on Mobile Systems, Applications, and Services*, 2020, pp. 273-285.

[154] C. Josephson, M. Kotaru, K. Winstein, S. Katti, and R. Chandra, "Low-cost in-ground soil moisture sensing with radar backscatter tags," in *Proceedings of the 4th ACM SIGCAS Conference on Computing and Sustainable Societies*, 2021, pp. 299-311.

[155] J. Ding and R. Chandra, "Towards low cost soil sensing using Wi-Fi," in *The 25th Annual International Conference on Mobile Computing and Networking*, 2019, pp. 1-16.

[156] K. Finkenzeller, *RFID handbook: fundamentals and applications in contactless smart cards, radio frequency identification and near-field communication*. John wiley & sons, 2010.

[157] K. S. Rao, P. V. Nikitin, and S. F. Lam, "Antenna design for UHF RFID tags: A review and a practical application," *IEEE Transactions on antennas and propagation,* vol. 53, no. 12, pp. 3870-3876, 2005.

[158] S.-M. Yu, P. Feng, and N.-J. Wu, "Passive and semi-passive wireless temperature and humidity sensors based on epc generation-2 uhf protocol," *IEEE Sensors Journal,* vol. 15, no. 4, pp. 2403-2411, 2014.

[159] R. Mirzavand, M. M. Honari, and P. Mousavi, "N-ZERO direct conversion wireless sensor based on six-port structures," in *2017 IEEE MTT-S International Microwave Symposium (IMS)*, 2017: IEEE, pp. 1225-1227.

[160] M. M. Honari, H. Saghlatoon, R. Mirzavand, and P. Mousavi, "An RFID sensor for early expiry detection of packaged foods," in *2018 18th International Symposium on Antenna Technology and Applied Electromagnetics (ANTEM)*, 2018: IEEE, pp. 1-2.

[161] H. Saghlatoon, R. Mirzavand, M. M. Honari, and P. Mousavi, "Sensor antenna transmitter system for material detection in wireless-sensor-node applications," *IEEE Sensors Journal,* vol. 18, no. 21, pp. 8812-8819, 2018.

[162] R. Mirzavand and P. Mousavi, "A zero-power sensor using multi-port direct-conversion sensing," *IEEE Sensors Journal,* vol. 18, no. 22, pp. 9243-9250, 2018.

[163] R. Xu *et al.*, "Dual-band circularly polarized antenna with two pairs of crossed-dipoles for RFID reader," *IEEE Transactions on Antennas and Propagation,* vol. 69, no. 12, pp. 8194-8203, 2021.

[164] R. Caso, A. Michel, M. Rodriguez-Pino, and P. Nepa, "Dual-band UHF-RFID/WLAN circularly polarized antenna for portable RFID readers," *IEEE Transactions on Antennas and Propagation,* vol. 62, no. 5, pp. 2822-2826, 2014.

[165] J. Ahn, H. Jang, H. Moon, J.-W. Lee, and B. Lee, "Inductively coupled compact RFID tag antenna at 910 MHz with near-isotropic radar cross-section (RCS) patterns," *IEEE Antennas and Wireless Propagation Letters,* vol. 6, pp. 518-520, 2007.

[166] K. Zannas, H. El Matbouly, Y. Duroc, and S. Tedjini, "A flipping uhf rfid sensor-tag for metallic environment compliant with etsi/fcc bands," *IEEE Transactions on Antennas and Propagation,* vol. 69, no. 3, pp. 1283-1292, 2020.

[167] B. D. Braaten, "A novel compact UHF RFID tag antenna designed with series connected open complementary split ring resonator (OCSRR) particles," *IEEE Transactions on Antennas and Propagation,* vol. 58, no. 11, pp. 3728-3733, 2010.

[168] L. Mo and C. Qin, "Planar UHF RFID tag antenna with open stub feed for metallic objects," *IEEE Transactions on Antennas and Propagation,* vol. 58, no. 9, pp. 3037-3043, 2010.

[169] N. Khalid, R. Mirzavand, H. Saghlatoon, M. M. Honari, and P. Mousavi, "A Three-Port Zero-Power RFID Sensor Architecture for IoT Applications," *IEEE Access,* vol. 8, pp. 66888-66897, 2020, doi: 10.1109/ACCESS.2020.2985711.

[170] T. Athauda and N. Karmakar, "Chipped Versus Chipless RF Identification: A Comprehensive Review," *IEEE Microwave Magazine,* vol. 20, no. 9, pp. 47-57, 2019, doi: 10.1109/MMM.2019.2922118.

[171] B. S. Cook, J. R. Cooper, and M. M. Tentzeris, "An inkjet-printed microfluidic RFID-enabled platform for wireless lab-on-chip applications," *IEEE Transactions on microwave theory and techniques,* vol. 61, no. 12, pp. 4714-4723, 2013.

[172] S. Preradovic, I. Balbin, N. C. Karmakar, and G. F. Swiegers, "Multiresonator-Based Chipless RFID System for Low-Cost Item Tracking," *IEEE Transactions on Microwave Theory and Techniques,* vol. 57, no. 5, pp. 1411-1419, 2009, doi: 10.1109/TMTT.2009.2017323.

[173] G. S. Vardhan, N. Sivadasan, and A. Dutta, "QR-code based chipless RFID system for unique identification," in *2016 IEEE International Conference on RFID Technology and Applications (RFID-TA)*, 21-23 Sept. 2016 2016, pp. 35-39, doi: 10.1109/RFID-TA.2016.7750744.

[174] A. Ramos, D. Girbau, A. Lazaro, and S. Rima, "IR-UWB radar system and tag design for time-coded chipless RFID," in *2012 6th European Conference on Antennas and Propagation (EUCAP)*, 26-30 March 2012 2012, pp. 2491-2494, doi: 10.1109/EuCAP.2012.6205939.

[175] H. Saghlatoon, R. Mirzavand, M. M. Honari, and P. Mousavi, "Sensor antenna for dielectric constant measurement of materials in contact with the structure," in *2019 13th European Conference on Antennas and Propagation (EuCAP)*, 2019: IEEE, pp. 1-3.

[176] R. Rezaiesarlak and M. Manteghi, "Complex-natural-resonance-based design of chipless RFID tag for high-density data," *IEEE Transactions on Antennas and Propagation,* vol. 62, no. 2, pp. 898-904, 2013.

[177] M. S. Bhuiyan, A. Azad, and N. Karmakar, "Dual-band modified complementary split ring resonator (MCSRR) based multi-resonator circuit for chipless RFID tag," in *2013 IEEE Eighth International Conference on Intelligent Sensors, Sensor Networks and Information Processing*, 2013: IEEE, pp. 277-281.

[178] H. R. Bogena, J. A. Huisman, B. Schilling, A. Weuthen, and H. Vereecken, "Effective calibration of low-cost soil water content sensors," *Sensors,* vol. 17, no. 1, p. 208, 2017.

[179] M. P. Goswami, B. Montazer, and U. Sarma, "Design and Characterization of a Fringing Field Capacitive Soil Moisture Sensor," *IEEE Transactions on Instrumentation and Measurement,* vol. 68, no. 3, pp. 913-922, 2019, doi: 10.1109/TIM.2018.2855538.

[180] I. Cappelli *et al.*, "Battery-Less HF RFID Sensor Tag for Soil Moisture Measurements," *IEEE Transactions on Instrumentation and Measurement,* vol. 70, pp. 1-13, 2021, doi: 10.1109/TIM.2020.3036061.

[181] A. d. Santos *et al.*, "A Reconfigurable Multisensor Based on Printed Circuit Board Technology for Measuring Moisture Content and Temperature in Stored Grain," *IEEE Transactions on Instrumentation and Measurement,* vol. 71, pp. 1-10, 2022, doi: 10.1109/TIM.2022.3170979.

[182] W.-J. Wu and W.-S. Zhao, "A Quality Factor Enhanced Microwave Sensor Based on Modified Split-Ring Resonator for Microfluidic Applications," *IEEE Sensors Journal,* vol. 22, no. 23, pp. 22582-22590, 2022.

[183] S. Goswami, K. Sarmah, A. Sarma, K. K. Sarma, and S. Baruah, "Design considerations pertaining to the application of complementary split ring resonators in microstrip antennas," in *Emerging Innovations in Microwave and Antenna Engineering*: IGI Global, 2019, pp. 25-56.

[184] R. Marqués, F. Martin, and M. Sorolla, *Metamaterials with negative parameters: theory, design, and microwave applications*. John Wiley & Sons, 2011.

[185] M. Amiri, M. Abolhasan, N. Shariati, and J. Lipman, "RF-Self-Powered Sensor for Fully Autonomous Soil Moisture Sensing," *IEEE Transactions on Microwave Theory and Techniques,* 2022.

[186] C. L. Yang, C. S. Lee, K. W. Chen, and K. Z. Chen, "Noncontact Measurement of Complex Permittivity and Thickness by Using Planar Resonators," *IEEE Transactions on Microwave Theory and Techniques,* vol. 64, no. 1, pp. 247-257, 2016, doi: 10.1109/TMTT.2015.2503764.

[187] C. S. Lee and C. L. Yang, "Complementary Split-Ring Resonators for Measuring Dielectric Constants and Loss Tangents," *IEEE Microwave and Wireless Components Letters,* vol. 24, no. 8, pp. 563-565, 2014, doi: 10.1109/LMWC.2014.2318900.

[188] X. Han *et al.*, "Microwave sensor loaded with complementary curved ring resonator for material permittivity detection," *IEEE Sensors Journal,* vol. 22, no. 21, pp. 20456-20463, 2022.

[189] A. Ebrahimi, W. Withayachumnankul, S. Al-Sarawi, and D. Abbott, "High-sensitivity metamaterial-inspired sensor for microfluidic dielectric characterization," *IEEE Sensors Journal,* vol. 14, no. 5, pp. 1345-1351, 2013.

[190] M. Alibakhshikenari *et al.*, "A Comprehensive Survey of “Metamaterial Transmission-Line Based Antennas: Design, Challenges, and Applications”," *IEEE Access,* vol. 8, pp. 144778-144808, 2020, doi: 10.1109/ACCESS.2020.3013698.

[191] C. H. Tseng and C. L. Chang, "A Broadband Quadrature Power Splitter Using Metamaterial Transmission Line," *IEEE Microwave and Wireless Components Letters,* vol. 18, no. 1, pp. 25-27, 2008, doi: 10.1109/LMWC.2007.911981.

[192] M. Gil, J. Bonache, and F. Martin, "Metamaterial filters: A review," *Metamaterials,* vol. 2, no. 4, pp. 186-197, 2008.

[193] R. Marqués, F. Medina, and R. Rafii-El-Idrissi, "Role of bianisotropy in negative permeability and left-handed metamaterials," *Physical Review B,* vol. 65, no. 14, p. 144440, 2002.

[194] S. Mohammadi and M. H. Zarifi, "Differential microwave resonator sensor for real-time monitoring of volatile organic compounds," *IEEE Sensors Journal,* vol. 21, no. 5, pp. 6105-6114, 2020.

[195] S. Gopalakrishnan, J. Waimin, N. Raghunathan, S. Bagchi, A. Shakouri, and R. Rahimi, "Battery-less wireless chipless sensor tag for subsoil moisture monitoring," *IEEE sensors journal,* vol. 21, no. 5, pp. 6071-6082, 2020.

[196] T. Alam and M. Cheffena, "Integrated Microwave Antenna/Sensor for Sensing and Communication Applications," *IEEE Transactions on Microwave Theory and Techniques,* vol. 70, no. 11, pp. 5289-5300, 2022.

[197] R. Keshavarz, A. Abdullah, and N. Shariati, "Autonomous Nonlinear Passive Transmit-Receive Switch for Compact IoT Devices: A Three-Port Agile Network," *arXiv preprint arXiv:2407.14759,* 2024.

[198] R. Keshavarz, D. L. Sounas, S. Keshavarz, and N. Shariati, "Enabling Wireless Communications, Energy Harvesting, and Energy Saving by Using a Multimode Smart Nonlinear Circuit (MSNC)," *IEEE Transactions on Instrumentation and Measurement,* 2024.

[199] A. Raza, R. Keshavarz, and N. Shariati, "Precision Agriculture: Ultra-Compact Sensor and Reconfigurable Antenna for Joint Sensing and Communication," *IEEE Transactions on Instrumentation and Measurement,* 2024.

[200] A. Kord, D. L. Sounas, and A. Alù, "Low-loss broadband magnetless circulators for full-duplex radios," in *2018 IEEE/MTT-S International Microwave Symposium-IMS*, 2018: IEEE, pp. 506-509.

[201] X. Wu and X. Liu, "A magnetless 4-port circulator and its microstrip implementation," *IEEE Transactions on Circuits and Systems II: Express Briefs,* vol. 69, no. 3, pp. 969-973, 2021.

[202] A. Kord, D. L. Sounas, and A. Alu, "Pseudo-linear time-invariant magnetless circulators based on differential spatiotemporal modulation of resonant junctions," *IEEE Transactions on Microwave Theory and Techniques,* vol. 66, no. 6, pp. 2731-2745, 2018.

[203] Y. Ha, C. H. Choi, and N. J. Shah, "Development and Implementation of a PIN-Diode Controlled, Quadrature-Enhanced, Double-Tuned RF Coil for Sodium MRI," *IEEE Transactions on Medical Imaging,* vol. 37, no. 7, pp. 1626-1631, 2018, doi: 10.1109/TMI.2017.2786466.

[204] D. N. Elluru *et al.*, "Design of an Absorptive High-Power PIN Diode Switch for an Ultra-Wideband Radar," *IEEE Journal of Microwaves,* vol. 2, no. 2, pp. 286-296, 2022, doi: 10.1109/JMW.2021.3138889.

[205] A. Singh and M. K. Mandal, "Parasitic Compensation and Hence Isolation Improvement of PIN Diode-Based Switches," *IEEE Transactions on Circuits and Systems II: Express Briefs,* vol. 68, no. 1, pp. 97-101, 2021, doi: 10.1109/TCSII.2020.3000587.

[206] L. Yuan, Z. Wang, W. Wei, and X. Han, "High-frequency broadband RF transmit-receive switch for pulsed magnetic field NMR," *IEEE Transactions on Instrumentation and Measurement,* vol. 72, pp. 1-9, 2023.

[207] J. Xu, S. Yao, Y. Song, J. Li, and Y. Jiang, "A Balanced T/R Switch for Wideband NMR Front-End," *IEEE Transactions on Circuits and Systems II: Express Briefs,* vol. 71, no. 5, pp. 2834-2838, 2024, doi: 10.1109/TCSII.2023.3348798.

[208] A. Poh and Y. P. Zhang, "Design and Analysis of Transmit/Receive Switch in Triple-Well CMOS for MIMO Wireless Systems," *IEEE Transactions on Microwave Theory and Techniques,* vol. 55, no. 3, pp. 458-466, 2007, doi: 10.1109/TMTT.2006.890510.

[209] Y. P. Zhang, Q. Li, W. Fan, C. H. Ang, and H. Li, "A Differential CMOS T/R Switch for Multistandard Applications," *IEEE Transactions on Circuits and Systems II: Express Briefs,* vol. 53, no. 8, pp. 782-786, 2006, doi: 10.1109/TCSII.2006.876379.

[210] Y. Yin, B. Chi, Z. Xia, and Z. Wang, "A Reconfigurable Dual-Mode CMOS Power Amplifier With Integrated T/R Switch for 0.1–1.5-GHz Multistandard Applications," *IEEE Transactions on Circuits and Systems II: Express Briefs,* vol. 61, no. 7, pp. 471-475, 2014, doi: 10.1109/TCSII.2014.2327343.

[211] W. Wen, L. Sang, and M. Chan, "A wide-band T/R switch using enhanced compact Waffle MOSFETs," *IEEE Microwave and Wireless Components Letters,* vol. 16, no. 5, pp. 287-289, 2006, doi: 10.1109/LMWC.2006.873495.

[212] J. Jiang and R. R. Mansour, "VO 2-based Transmit/Receive Switch," in *2020 50th European Microwave Conference (EuMC)*, 2021: IEEE, pp. 534-537.

[213] S. Keshavarz, H. M. Kadry, and D. L. Sounas, "Four-port Spatiotemporally Modulated Circulator with Low Modulation Frequency," in *2021 IEEE Texas Symposium on Wireless and Microwave Circuits and Systems (WMCS)*, 18-20 May 2021 2021, pp. 1-4, doi: 10.1109/WMCS52222.2021.9493276.

[214] D. W. Sinkovits and M. S. Conradi, "Improved rejection of transmitter noise: a convenient scheme with resonant crossed diodes," *Journal of Magnetic Resonance,* vol. 171, no. 1, pp. 11-14, 2004.

[215] V. P. Singh, M. N. Kumar, M. A. K. Misra, and P. Kuncha, *IoT Communication protocols*. GCS PUBLISHERS, 2023.

[216] V. Rovelli, "Energy efficiency in intermittent computing systems through static frequency scaling techniques," 2023.

[217] R. M. Khattab and A. A. T. Shalaby, "Metamaterial-Based Broadband Branch-Line Coupler and its Application in a Balanced Amplifier," in *2021 International Conference on Electronic Engineering (ICEEM)*, 3-4 July 2021 2021, pp. 1-7, doi: 10.1109/ICEEM52022.2021.9480615.

[218] I. Munina, I. Vendik, and V. Crnojevic-Bengin, "Design of 0-dB reconfigurable directional coupler using metamaterial structure," in *2013 7th International Congress on Advanced Electromagnetic Materials in Microwaves and Optics*, 2013: IEEE, pp. 139-141.

[219] A. R. Katko, A. M. Hawkes, J. P. Barrett, and S. A. Cummer, "RF Limiter Metamaterial Using p-i-n Diodes," *IEEE Antennas and Wireless Propagation Letters,* vol. 10, pp. 1571-1574, 2011, doi: 10.1109/LAWP.2011.2182490.

[220] R. Islam and G. V. Eleftheriades, "Compact Corporate Power DividerUsing Metamaterial NRI-TLCoupled-Line Couplers," *IEEE Microwave and Wireless Components Letters,* vol. 18, no. 7, pp. 440-442, 2008, doi: 10.1109/LMWC.2008.924915.

[221] A. F. Azarnaminy, M. Ou, and R. R. Mansour, "PCM-Based Reconfigurable Acoustic Resonators and Filters: For Potential Use in RF Front-End Applications," *IEEE Microwave Magazine,* vol. 25, no. 2, pp. 48-67, 2024.

[222] R. Keshavarz, Y. Miyanaga, M. Yamamoto, T. Hikage, and N. Shariati, "Metamaterial-inspired quad-band notch filter for LTE band receivers and WPT applications," in *2020 XXXIIIrd General Assembly and Scientific Symposium of the International Union of Radio Science*, 2020: IEEE, pp. 1-4.

[223] I. J. Bahl, *Lumped elements for RF and microwave circuits*. Artech house, 2022.

[224] X. She and Y. Chow, "Interdigital microstrip capacitor as a four-port network," in *IEE Proceedings H Microwaves, Antennas and Propagation*, 1986, vol. 3, no. 133, pp. 191-197.

[225] N. Dib, Q. Zhangb, and U. Rohde, "New CAD model of the microstrip interdigital capacitor," *Active and passive electronic components,* vol. 27, no. 4, pp. 237-245, 2004.

[226] L. Zhou and F. Xu, "A Miniaturized Branch Coupler Based on Substrate Integrated Coaxial Line Loaded Interdigital Capacitor," in *2021 International Conference on Microwave and Millimeter Wave Technology (ICMMT)*, 23-26 May 2021 2021, pp. 1-3, doi: 10.1109/ICMMT52847.2021.9617853.

[227] L. Bin, Z. Huimin, Z. Bo, X. Hui, and W. Yi, "A novel design of miniaturized power divider and branch coupler using interdigital circuit," in *2015 9th European Conference on Antennas and Propagation (EuCAP)*, 13-17 April 2015 2015, pp. 1-4.

[228] R. Keshavarz and M. Movahhedi, "A compact and wideband coupled-line coupler with high coupling level using shunt periodic stubs," *Radioengineering,* vol. 22, no. 1, p. 323, 2013.

[229] J. Cihlar and F. T. Ulaby, "Dielectric properties of soils as a function of moisture content," 1974.

[230] P. Zhang, H. Yi, H. Liu, H. Yang, G. Zhou, and L. Li, "Back-to-back microstrip antenna design for broadband wide-angle RF energy harvesting and dedicated wireless power transfer," *IEEE access,* vol. 8, pp. 126868-126875, 2020.

[231] R. Keshavarz and N. Shariati, "Highly sensitive and compact quad-band ambient RF energy harvester," *IEEE Transactions on Industrial Electronics,* vol. 69, no. 4, pp. 3609-3621, 2021.

[232] M. Wang, Y. Fan, L. Yang, Y. Li, J. Feng, and Y. Shi, "Compact dual-band rectenna for RF energy harvest based on a tree-like antenna," *IET Microwaves, Antennas & Propagation,* vol. 13, no. 9, pp. 1350-1357, 2019.

[233] S. Hemour and K. Wu, "Radio-frequency rectifier for electromagnetic energy harvesting: Development path and future outlook," *Proceedings of the IEEE,* vol. 102, no. 11, pp. 1667-1691, 2014.

[234] M. S. Islam, M. T. Islam, M. A. Ullah, G. K. Beng, N. Amin, and N. Misran, "A modified meander line microstrip patch antenna with enhanced bandwidth for 2.4 GHz ISM-band Internet of Things (IoT) applications," *IEEE Access,* vol. 7, pp. 127850-127861, 2019.

[235] W. Tu, S. Hsu, and K. Chang, "Compact 5.8-GHz Rectenna Using Stepped-Impedance Dipole Antenna," *IEEE Antennas and Wireless Propagation Letters,* vol. 6, pp. 282-284, 2007, doi: 10.1109/LAWP.2007.898555.

[236] M. Arrawatia, M. S. Baghini, and G. Kumar, "Differential Microstrip Antenna for RF Energy Harvesting," *IEEE Transactions on Antennas and Propagation,* vol. 63, no. 4, pp. 1581-1588, 2015, doi: 10.1109/TAP.2015.2399939.

[237] S. Chandravanshi, S. S. Sarma, and M. J. Akhtar, "Design of Triple Band Differential Rectenna for RF Energy Harvesting," *IEEE Transactions on Antennas and Propagation,* vol. 66, no. 6, pp. 2716-2726, 2018, doi: 10.1109/TAP.2018.2819699.

[238] H. Sun, Y. Guo, M. He, and Z. Zhong, "A Dual-Band Rectenna Using Broadband Yagi Antenna Array for Ambient RF Power Harvesting," *IEEE Antennas and Wireless Propagation Letters,* vol. 12, pp. 918-921, 2013, doi: 10.1109/LAWP.2013.2272873.

[239] M. A. Ullah, R. Keshavarz, M. Abolhasan, J. Lipman, and N. Shariati, "Multi-Service Compact Pixelated Stacked Antenna with Different Pixel Shapes for IoT Applications," *IEEE Internet of Things Journal,* 2023.

[240] Y. Kuwahara, "Multiobjective optimization design of Yagi-Uda antenna," *IEEE Transactions on Antennas and Propagation,* vol. 53, no. 6, pp. 1984-1992, 2005.

[241] K. Parsaei, R. Keshavarz, R. M. Boroujeni, and N. Shariati, "Compact Pixelated Microstrip Forward Broadside Coupler Using Binary Particle Swarm Optimization," *IEEE Transactions on Circuits and Systems I: Regular Papers,* vol. 70, no. 12, pp. 5265-5274, 2023, doi: 10.1109/TCSI.2023.3314621.

[242] D. Wang, D. Tan, and L. Liu, "Particle swarm optimization algorithm: an overview," *Soft computing,* vol. 22, pp. 387-408, 2018.

[243] S. Mirjalili and A. Lewis, "S-shaped versus V-shaped transfer functions for binary particle swarm optimization," *Swarm and Evolutionary Computation,* vol. 9, pp. 1-14, 2013.

[244] J. D. Baena, R. Marqués, F. Medina, and J. Martel, "Artificial magnetic metamaterial design by using spiral resonators," *Physical review B,* vol. 69, no. 1, p. 014402, 2004.

[245] I. J. Bahl and D. K. Trivedi, *A Designer's Guide to Microstrip Line*. 1977, pp. 174-175.

[246] "Bagged Product Supplies." https://baggedproductsupplies.com/ (accessed.

[247] "DAK 12." https://speag.swiss/products/dak/dak-probes/ (accessed 29 January, 2024).

[248] "TDR-315L." https://hydroterra.com.au/product/ict-tdr-315l-time-domain-reflectometry-soil-water-content-conductivity-temperature-sensor/ (accessed 29 January, 2024).

[249] Y. I. Leshchanskii, G. Lebedeva, and V. Shumilin, "The electrical parameters of sandy and loamy soils in the range of centimeter, decimeter, and meter wavelengths," *Radiophysics and Quantum Electronics,* vol. 14, no. 4, pp. 445-451, 1971.

[250] J. Guo, Y. Tang, Y. Wu, C. Zhu, and J. Huang, "Embeddable Soil Moisture Content Sensor Based on Open-End Microwave Coaxial Cable Resonator," *IEEE Sensors Journal,* vol. 23, no. 12, pp. 13575-13584, 2023, doi: 10.1109/JSEN.2023.3266665.

[251] L. A. P. Silva, F. d. A. B. Filho, and H. D. d. Andrade, "Soil Moisture Monitoring System Based on Metamaterial-Inspired Microwave Sensor for Precision Agriculture Applications," *IEEE Sensors Journal,* vol. 23, no. 19, pp. 23713-23720, 2023, doi: 10.1109/JSEN.2023.3307652.

[252] M. Zekri and L. R. Parsons, "Determination of field capacity in a Florida sandy soil and drainage time at different depths," *HortTechnology,* vol. 9, no. 2, pp. 258-261, 1999.

[253] P. Salter and F. Haworth, "The available-water capacity of a sandy loam soil: I. A critical comparison of methods of determining the moisture content of soil at field capacity and at the permanent wilting percentage," *Journal of Soil Science,* vol. 12, no. 2, pp. 326-334, 1961.

[254] S. H. Jackson, "Comparison of calculated and measured volumetric water content at four field sites," *Agricultural water management,* vol. 58, no. 3, pp. 209-222, 2003.

[255] "TEROS 12." https://metergroup.com/products/teros-12/ (accessed 29 August, 2024).

[256] "Climate Test Chamber." https://www.simultech.com.au/climate-test-chamber-global-simulator-chambers (accessed 29 January, 2024).

[257] A. Aquino, C. G. Juan, B. Potelon, and C. Quendo, "Dielectric Permittivity Sensor Based on Planar Open-Loop Resonator," *IEEE Sensors Letters,* vol. 5, no. 3, pp. 1-4, 2021, doi: 10.1109/LSENS.2021.3055544.

[258] D. A. Fleri and L. D. Cohen, "Nonlinear Analysis of the Schottky-Barrier Mixer Diode," *IEEE Transactions on Microwave Theory and Techniques,* vol. 21, no. 1, pp. 39-43, 1973, doi: 10.1109/TMTT.1973.1127912.

[259] R. Keshavarz, A. Mohammadi, and A. Abdipour, "A Quad-Band Distributed Amplifier With E-CRLH Transmission Line," *IEEE Transactions on Microwave Theory and Techniques,* vol. 61, no. 12, pp. 4188-4194, 2013, doi: 10.1109/TMTT.2013.2288939.